# PREDICTION OF RAIL DAMAGE ON UNDERGROUND-METRO LINES

# PELIN BOYACIOGLU

A thesis submitted to the University of Huddersfield in partial fulfilment of the requirements for the degree of Doctor of Philosophy

The University of Huddersfield

September 2018

Copyright statement

# Abstract

Safety and reliability of rails primarily depend on detection, monitoring and maintenance of rolling contact fatigue (RCF) defects. Since when they are undetected and untreated, they can further propagate and increase the risk of rail failures. Thereby, infrastructure managers (IMs) tend to detect these cracks at an early stage in order to manage this risk. After detection, the growth of these cracks should be monitored and efficient maintenance should be carried out to prolong the rail life. However, this requires reliable and sufficient field data with accurate prediction models of RCF damage and its counterpart damage mechanism; wear. Although the current models, which are particularly used on real track conditions, focus on mainline routes and were often validated using rail surface observations, lesser emphasis has been placed on underground-metro system tracks and the use of non-destructive testing (NDT) measurements particularly the crack depth which is a key parameter in the assessment of crack severity and maintenance planning.

In recent years, London Underground (LUL) has put additional effort to improve their rail inspection practices to support the optimisation of their rail maintenance strategy. Besides the use of several different NDT techniques, the magnetic flux leakage based sensor is used to measure the depth of detected cracks. Research suggested that this rail inspection data could be used to improve the accuracy of damage predictions. With the help of successive measurements, the severity of damage could be quantified and the changes in RCF estimations and its interaction with wear over time could be demonstrated. It was proposed that this should increase the confidence in prediction models for maintenance planning and help to support future maintenance optimisation.

Owing to use of different NDT techniques, a significant volume of field defect data was collected and examined in detailed during the research to understand the dominant damage mechanisms and the influential factors promoting RCF crack growth. It was found that severe damage is not limited to mainline and freight routes, with rails on metro lines also suffering from a high number of cracks. In addition, the various track data consisting of wheel-rail profile measurements, track geometry, vehicle speed diagrams and traffic information were also submitted. This provided a good opportunity to build detailed vehicle dynamics simulations for the selected lines to be further studied on LUL.

The Whole Life Rail Model (WLRM) and the Shakedown Map were selected as predictive models since, they can integrate with vehicle dynamics simulations. However, when the main input of WLRM; 'Tγ' was initially applied to LUL tracks, it was found that while, it successfully showed the effect of significant factors, it resulted in over-and under-estimation of the RCF damage in several locations. Therefore, the research investigated the interaction between the model parameters and their comparison on sites with and

without reported RCF defects to find an optimum solution. The results indicated certain distinctions and hence, new wear and RCF damage prediction methods were developed using a combined Shakedown Map and Tγ approach.

Both of the methods were applied to selected LUL RCF monitoring sites. Whilst the wear method was applied to predict the loss in cross-section area of the rail, the new RCF crack depth prediction model was validated using the MRX-RSCM crack depth measurements. The location and severity of both damage types were successfully predicted. To observe and predict the changes in RCF damage including the interaction of wear over successive measurement intervals brought novelty to the study. In addition, the accuracy of predictions was improved on sites with various track characteristics such as high and low rail of checked and unchecked curved track section and tangent tracks.

# Table of Contents

# List of Figures

# List of Tables

# Dedications and Acknowledgements

First and foremost, I would like to express my deepest appreciation to my supervisor Dr. Adam Bevan for his continuous support, guidance and help throughout my research. It has been always a privilege to have such a nice and patient supervisor.

Secondly, I would like to convey my sincere gratitude to Institute of Railway Research (IRR) of University of Huddersfield and Rail Safety and Standards Board (RSSB) for the funding of this research project and providing my scholarship throughout my study. I also would like to thank Prof. Simon Iwnicki for giving me this opportunity and great support! Additionally, many thanks to David Crosbee, Cassandra Woodhouse, Dr. Phil Shackleton and Paul Molyneux-Berry from IRR for their help.

Thirdly, I owe special thanks to London Underground for providing a significant volume of data and collaboration. Many thanks to Andy Vickerstaff for his enthusiasm to my project, Christine Baldwin, Mathew Lee and Dennis Webber-Johnston for guiding me during my site visit and also Jonathan Bray and Stephen Long from Tubelines. In addition, I would like to thank MRX Technologies; Dr. Stephanie Klecha for her help. I am very grateful for all their support and I highly appreciate the opportunity to work with you.

Fourthly, I would like to thank all my former colleagues and friends for the joy, friendship, support and encouragement. Many thanks to all the good memories which we shared, they helped me to get through the hard times during my research. The list is so long but, I must write some of the names; Meyrem Kutlu, Dr. Ibrahim Catalkaya, Dr. Burcu Ozdemir and Dr. Ismail Emrah Kilic. Whenever I've needed, they were always there!! Furthermore, many thanks to Dr. Ozlem Bak, Victoria-Serdar Arslan, Ban-Bakthiar Ames, Liza-Fabio Della Mora, Guler-Joel Suss, Mehmet Emin Kanpak and Barbara Binder. I feel very lucky to meet such wonderful friends in Huddersfield.

Finally, I would like to thank and dedicate my PhD research to my family, Nebahat, Mustafa Asim and Guvenc Boyacioglu, my grandmother Neriman Dogruol who made her five year old granddaughter's wish come true by waiting two hours in Alsancak train station for my first railway journey to Bayindir/izmir. Many thanks for all your love, care support, understanding, help and patience(!). Also, very special thanks to my former managers in the Marmaray Project, Dr. Haluk Ibrahim Ozmen and Dr. Zeynep Sindel Buket, as they are part of my family. Thanks for always believing in me. I'm hugely indebted to you for your trust and encouragement.

# List of Abbreviations

ATO – Automatic Train Operation

BAK – Bakerloo line

BH – Bullhead

BRR – British Rail Research

CEN - Comité Européen de Normalisation

DB- Deutsche Bahn (German Railways)

EN – European Norm

EPFM- Elasto-Plastic Fracture Mechanics

FB – Flat Bottom

FE - Finite Element

FM – Friction Modifier

GB – Great Britain

GDU – Grease Distribution Unit

HCF – High Cycle Fatigue

JLE – Jubilee Line Extension

JNP – Jubilee, Northern and Piccadilly Lines

JUB – Jubilee line

ICRI – International Collaboration Research Initiative

IM - Infrastructure Manager

LEFM- Linear Elastic Fracture Mechanics

LCF- Low Cycle Fatigue

LCS – Location Coding System

LUL – London Underground

MBD – Multi-body Dynamics

NB - Northbound

NDT – Non-Destructive Testing

MGT – Million Gross Tonnes

MRX-RSCM – MRX Rail Surface Crack Measurement

RCF – Rolling Contact Fatigue

SB – Southbound

TRV – Track Recording Vehicle

UIC - International Union of Railways

UK – United Kingdom

WEL – White Etching Layer

WLRM – Whole Life Rail Model

# List of Symbols

Tγ – Wear Number (N)

$T_x$, $F_{long}$ – Creep force in longitudinal direction (N)

$T_y$, $F_{lat}$ – Creep force in lateral direction (N)

$\gamma_x$ – Creepage in longitudinal direction (-)

$\gamma_y$ – Creepage in lateral direction (-)

$M_z$ – Spin moment (Nm)

$\omega_z$ – Spin creepage (rad/m)

k – Shear yield limit (N/mm²)

$F_N$, N – Normal force at the wheel-rail contact (N)

S – Sliding distance (m)

H – Hardness (HV)

a – Semi width of contact patch in longitudinal direction (mm)

b - Semi width of contact patch in lateral direction (mm)

P(x) – Contact pressure (N/mm²)

$P_0$ – Maximum contact pressure (N/mm²)

E – Elastic modulus (N/mm²)

$\vartheta$ – Poisson's ratio (-)

$\sigma$ – Tensile stress (N/mm²)

$\tau$ – Shear stress (N/mm²)

$\rho$ – Residual stress (N/mm²)

$q$ – Tangential stress (N/mm²)

$\mu$ – Friction coefficient (-)

T/N – Traction coefficient (-)

R – Equivalent radius (mm)

# Publications

This dissertation shares part of its contents with the following publications:

Boyacioglu, P., Bevan, A. & Vickerstaff, A. (2017). Prediction of RCF Damage on Underground Metro Lines, ICRT 2017: Railway Development, Operations and Maintenance. American Society of Civil Engineers (ASCE). p 207-225 18p.

Boyacioglu, P., Bevan, A., & Vickerstaff, A. (2018). Use of NDT Inspection Data to Improve Rail Damage Prediction Models. 8th International Conference on Railway Engineering (ICRE 2018), London, UK.

# Chapter 1  Introduction

The introduction of high speed lines, higher axle loads in freight traffic along with the increased passenger demand and shorter headways in railway operations, make rails more vulnerable to damage. Wear and rolling contact fatigue (RCF) are two of the key damage mechanisms observed in rails. Rails are exposed to cyclic loading during traffic operations and the high contact forces in the wheel-rail interface cause cracks to initiate in the railhead. After initiation of these cracks, several factors stemming from material characteristics, varying operational and environmental conditions cause them to grow further. If they are left undetected and untreated, the propagation of these defects can lead to premature rail replacements and/or rail breaks. Therefore, RCF cracking is crucial for the railway industry worldwide as they are one of the major risk factors influencing the maintainability and operational safety of tracks. In addition, rail damage maintenance (e.g. inspections, repairs and grinding) is very costly and time consuming for the Infrastructure Managers (IMs).

In order to meet the increased traffic demand and provide a safe operation at reduced whole-life cycle costs, the rails have to provide long-term performance. Developing accurate and efficient tools for the prediction of rail damage is a prerequisite for optimisation of maintenance and (re)investment. This requires reliable and sufficient field defect monitoring data in order to help to understand the existing RCF mechanism in rails and to support the damage prediction modelling studies. However, this contains certain challenges such as limitations in rail inspection devices sometimes reduce the reliability of field defect data and the changing operational and environmental conditions in rail traffic make it difficult to monitor the crack propagation from field observations. In addition, the complex crack growth mechanism affects the rate of propagation and therefore, the depth of each crack varies based on its development path and initiation angle from the surface.

## 1.1 Research aims and objectives

Although RCF is considered to be a major factor affecting the maintainability and safety of the tracks in heavy-haul and high-speed railway lines, due to excessive axle loads and higher speeds in these routes, it is also a crucial concern for underground-metro systems. While rail damage in conventional mainline routes has been primarily investigated within previous studies (Girsch and Heyder, 2003; Li et al. 2008; Olofsson and Nilsson, 2002) there has been less emphasis placed on the development of RCF cracking in these metro systems. However, with the changing track characteristics, the high traffic demand as well as the reduction in the available maintenance times, means that the management of RCF cracks is also of vital importance on these lines.

The main aim in this research is to investigate rail damage mechanisms on underground-metro systems. RCF and wear damage were examined in detail on selected lines of the London Underground (LUL) network using field defect data and rail profile measurements. In addition, the crack propagation on selected sites was investigated by analysing crack depth data obtained from consecutive measurements using the MRX Rail Surface Crack Measurement (MRX-RSCM) non-destructive inspection device. Variations in key wheel-rail contact parameters at selected RCF sites were investigated to improve the accuracy of damage prediction modelling. This was achieved by accomplishing the following objectives:

1. Understand the dominant damage mechanisms on the studied lines and identify the key factors that promote RCF crack growth by analysing the field defect data.
2. Evaluate the effectiveness of current rail damage prediction model under the influence of significant factors particularly observed on metro lines and the comparison of its predictions with the field defect data.
3. Investigate the variations in the key contact parameters between the sites with and without reported RCF defects in order to identify the conditions that are contributing to the observed damage and propose improvements to rail damage prediction models.
4. Validate the proposed model predictions using NDT measurements and provide guidance/suggestions on future maintenance strategy

## 1.2 Contribution to knowledge

The research contributes to current knowledge by answering some of the important questions in the existing literature. Firstly, a comprehensive study was carried out to investigate the prevalent damage mechanisms on metro tracks. A large volume of field data was examined such as rail inspection outputs in terms of both RCF cracking and wear and including their maintenance history. In addition, various track data was also received containing track geometry, vehicle speed profile and traffic information. Compared to other modelling studies, this was very beneficial and provided the research an opportunity to build detailed vehicle dynamics route simulations.

Secondly, the main model which was used in this research to predict the damage is the Whole Life Rail Model (WLRM). This model was selected as it has been implemented and validated in real-case studies and it allows to investigate how different vehicle types, speeds, wheel and rail profiles and track geometries affect rail wear and RCF formation by integrating vehicle dynamics simulation outputs in its model framework. Even though the model produced successful predictions at a number of sites on the Great Britain (GB) rail network, it has not been developed/validated on routes with significantly different operating conditions. In this research, the WLRM was implemented on the metro lines of

London Underground (LUL). The effect of significant factors on its input; wheel-rail contact energy (Tγ) were demonstrated and its correlation with field defect data was conducted.

Thirdly, contrary to previous modelling studies, this research compared the key damage prediction parameters between the sites where RCF cracking was previously reported and having no reported RCF defects in order to improve the accuracy of estimations. The results showed certain variations between different sites and hence, a new methodology was developed to predict both RCF and wear damages by using a combined Shakedown Map and Tγ approach.

Fourthly, the use of advanced technology for the measurement of crack depth in rails, such as the MRX-RSCM inspection device, brings novelty to the research. Previous validation studies mainly relied on comparing the surface damage observations (e.g. crack length and density) with simulations' results. In this research, this was further improved by using the crack depth measurements, which is a significant parameter in assessing the severity of cracking and defining the maintenance requirements. The detection outputs, including: crack depth measurements and surface damage map, provided an opportunity to investigate the influence of changing contact conditions on crack propagation. In addition, they helped to develop a new RCF crack depth prediction model which was also further validated on selected 'RCF Monitoring Sites' with various track characteristics such as high and low rails on checked and un-checked curves and tangent tracks.

Finally, the comprehensive field data analysis and the improvement in the accuracy of RCF and wear damage predictions especially on consecutive inspection cycles can provide an opportunity to support the future maintenance optimisations and move to condition-based maintenance on LUL.

## 1.3 Structure of the thesis

This thesis consists of nine chapters. Whilst Chapter 1 provides the research's aim, objectives and its contribution to current knowledge, Chapter 2 clarifies the RCF and wear damage mechanisms and introduces the current prediction models from the existing literature. The selected models, e.g. WLRM and Shakedown Map, are explained in detail with their assumptions and findings from previous related studies.

Chapter 3 describes the characteristics of the network studied and contains a further literature review regarding the problems observed on other metro systems and LUL. The third section of the chapter includes detailed analysis of the field crack data. The dominant damage mechanisms, critical track sections and key influential factors on the studied lines are examined in this chapter.

Chapter 4 presents the wheel-rail contact calculations in VAMPIRE vehicle dynamics simulation software. It also includes a review of existing contact models and their effect on rail damage modelling. Additionally, this chapter contains a description of the preparation of the vehicle dynamics route simulations and the factors which were taken into account in the input files.

Chapter 5 demonstrates the applicability of the WLRM on the metro lines of LUL. The effect of significant factors on Tγ (such as curve radius, friction, different track irregularity levels and wheel-rail profile shapes) are presented in the first section. The second section evaluates the effectiveness of the model by comparing the model input parameter with the field crack data. The key areas that potentially cause discrepancies in the predicted damage on the studied lines are also detailed in this chapter.

Chapter 6 describes the methodology which was adopted in this research. The interaction between the selected damage prediction modelling parameters and their influence on the observed damage are provided in the first and second section of this chapter. The results from these sections led to the development of a combined Shakedown Map and Tγ approach in the damage predictions. The third section explains these new proposed models for both RCF and wear damages.

Chapter 7 presents the application of the new wear damage prediction method. The selection of representative data and the number of simulation conditions considered in the analysis as well as the sites used in validations are initially described in this chapter. The model predictions were compared to the wear measurements on these selected sites.

Chapter 8 provides the application of the new RCF damage prediction method. The predicted location and severity (depth) of cracks were compared with MRX-RSCM outputs from consecutive measurements. The areas which showed good and poor correlations are identified and suggestions for improvement are given. It also includes guidance on using the proposed models to support maintenance optimisation on the LUL.

Chapter 9 concludes the thesis by summarising the findings in the different stages of the research and by addressing the objectives. Additionally, recommendations are given for future research work.

The structure of the thesis is illustrated in Figure 1.1.

**Introduction**
- Research's aim and objectives
- Contribution to knowledge

**Literature Review**
- RCF and wear damage
- Current damage prediction models and their gaps
- WLRM
- Shakedown Map

**Field Defect Data Analysis**
- London Underground and the characteristics of the studied lines
  - Bakerloo and Jubilee lines
- Literature review on other metro systems and LUL
- Field defect data analysis

**Route Simulations**
- Wheel-rail contact modelling in Vampire
- Review of other existing models
  - Their effect on rail damage modelling
- Preparation of vehicle dynamics route simulations

**Evaluation of WLRM for use on LUL**
- The effect of significant factors on 'signed Tγ'
  - Curve radius, friction, different track irregularity levels and wheel-rail profile shapes
- Route RCF damage predictions
  - Comparison of predicted locations with field defect data

**Methodology**
- The relationship between the damage prediction parameters (Shakedown Map and Tγ)
- Their comparison and effect on observed damage
- Combined Shakedown Map and Tγ approach in RCF and eear damage predictions

**Wear Damage Prediction**
- Application of wear damage prediction method
- Validation of model results using MiniProf measurements at selected sites

**RCF Damage Prediction**
- Application of RCF damage (crack depth) prediction method
- Validation of model results using MRX-RSCM measurements
  - Crack depth data and surface damage map in consecutive intervals
- Guidance on maintenance optimisation

**Conclusions**
- Conclusions
- Recommendations for future work

Figure 1.1: The structure of the thesis

# Chapter 2   Literature Review

This chapter gives an overview of the existing literature related to the research topics presented in this thesis. The first section gives a brief explanation about wheel-rail contact, RCF, wear and the interaction between these two damage mechanisms. The second section explains the inspection of RCF defects and introduces the prevalent non-destructive testing techniques, including the MRX-RSCM inspection device. The novelty of this device, its measurement outputs and the previous validation studies are also presented. The current RCF damage prediction models and the gaps in these approaches are explained in the third section of this chapter. The reasons for the selection of the WLRM and Shakedown Map approaches, their methodology, assumptions and the previous findings in the related studies are also highlighted.

## *2.1  Wheel-rail contact*

As the RCF damage is a consequence of wheel-rail contact, it is firstly introduced in the thesis. When the wheel travels on the rails, the contact generates various conditions. For instance, while the rail and wheel profile shapes influence their position and other related geometrical parameters, the differences between the forward velocity and circumferential velocity of the wheels as well as the friction between two contacting surfaces causes creepage, affecting adhesion and movement of the trains. The wheel-rail contact calculations are generally described by the following for sub problems:

1)   Geometrical Problem
2)   Normal Problem
3)   Kinematical Problem
4)   Tangential Problem

In the geometrical problem, the contact positon, size and area are calculated depending on the wheel rail profile shapes and the contact pressure is found in the normal problem. The most widely used method is the Hertzian theory which uses three common cases; line, circular and elliptical contacts. As can be seen in Figure 2.1, each body in these contact differs such as while two cylinders are used in the line contact, spheres and ellipsoids are used in the circular and elliptical contacts, respectively. They are rigid non-conforming surfaces, pressing to each other and meet at a point where the normal distance between them is minimum (Ayasse & Chollet, 2006).
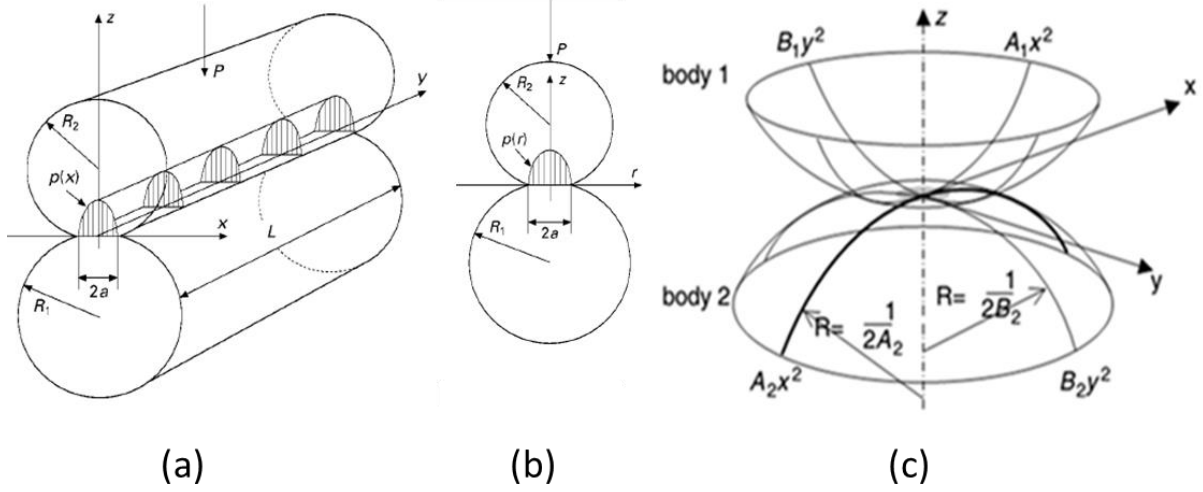
Figure 2.1: Hertzian Contacts; line contact (a) and circular point contact (b) (Lewis & Olofsson, 2009) and elliptical (c) (Ayasse & Chollet, 2006)

To illustrate an example, the elliptical contact calculation is given which has curvatures with two different radii. The contacting surfaces of the bodies are demonstrated by $z_1 = (x, y)$ and $z_2 = (x, y)$ for the wheel and rail, respectively and have two principal curvatures:

$$z_1 = A_1 x^2 + B_1 y^2 \tag{2.1}$$

$$z_2 = A_2 x^2 + B_2 y^2 \tag{2.2}$$

where $A$ is the longitudinal and $B$ is the lateral curvature. In the railway case, these curvatures are shown in the below Figure 2.2 and are represented as follows:
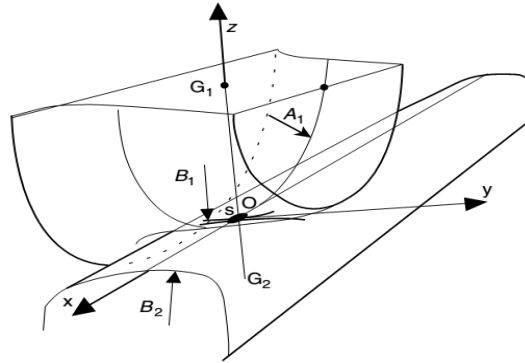


Figure 2.2: Hertzian contact demonstration in the wheel-rail application (Ayasse & Chollet, 2006)

Wheel:

$$\frac{d^2 z_1}{dx^2} = 2A_1 \approx \frac{1}{r_n} \tag{2.3}$$

$$\frac{d^2 z_1}{dy^2} = 2B_1 \approx \frac{1}{R_{wx}} \tag{2.4}$$

Rail:

$$\frac{d^2 z_2}{dy^2} = 2B_2 \approx \frac{1}{R_{rx}} \tag{2.5}$$

The longitudinal curvature of the rail ($A_2$) is generally neglected since, the rail is straight which make its radius infinite. But, the radius of the longitudinal curvature in the wheel ($A_1$) is taken as normal radius of the wheel $r_n$ (usually rolling radius of the wheel). The

radii of the lateral curvatures are found ($R_{wx}$ and $R_{rx}$) from the transverse profiles of the wheel and rail.

The relative vertical distance between the bodies is calculated by the sum of the two bodies:

$$z_1 + z_2 = d = Ax^2 + By^2 \qquad (2.6)$$

$$A = \frac{1}{2r_n} \qquad (2.7) \qquad \text{and} \qquad B = \frac{1}{2}(\frac{1}{R_{wx}} + \frac{1}{R_{rx}}) \qquad (2.8)$$

Hertz proposed a semi-ellipsoid pressure distribution over an elliptic contact patch area with semi-axes a and b. Hence the pressure distribution over this patch is:

$$p(x,y) = P_0 \sqrt{1 - \left(\frac{x}{a}\right)^2 - (\frac{y}{b})^2} \qquad (2.9)$$

where Po is the maximum contact pressure and it is calculated from applying Normal contact force $F_N$ to the semi-ellipsoid.

$$P_0 = \frac{3F_N}{2\pi ab} \qquad (2.10)$$

The semi-axes a and b are dependent on the geometry of the bodies in contact and Normal force which are calculated as follows:

$$a = m \left(\frac{3}{4}\frac{F_Z}{E^*}\frac{1}{A+B}\right)^{\frac{1}{3}} \qquad (2.11)$$

$$b = n \left(\frac{3}{4}\frac{F_Z}{E^*}\frac{1}{A+B}\right)^{\frac{1}{3}} \qquad (2.12)$$

where $E^*$ is the equivalent Elastic modulus $E_1$, $E_2$, and $v_1$, $v_2$ are the Elastic moduli and Poisson's ratios of each body in the contact.

$$\frac{1}{E^*} = \frac{1-v_1^2}{E_1} = \frac{1-v_2^2}{E_2} \qquad (2.13)$$

Inevitably, these parameters vary in line and circular contacts (Lewis & Olofsson, 2009). For instance, the semi-axes a and maximum contact pressure $P_0$ are found from the below formulas:

Line contact; $a = \left(\frac{4PR}{\pi E^*}\right)^{1/2}$ (2.14) $\qquad$ and $\qquad$ $P_0 = \frac{2P}{\pi al}$ (2.15)

Circular contact; $a = \left(\frac{3PR}{\pi E^*}\right)^{1/3}$ (2.16) $\qquad$ and $\qquad$ $P_0 = \frac{3P}{2\pi a^2}$ (2.17)

On the contrary to elliptical contact, the line contact (*l*; cylinder length) and circular contact have single radius in each body in which the equivalent radius $R$ is calculated as follows:

$$\frac{1}{R} = \frac{1}{R_1} + \frac{1}{R_2} \qquad (2.18)$$

Although it has been commonly used, the Hertzian theory contains the following assumptions:

1) Each body in the contact area are linearly elastic, isotropic and homogeneous.
2) The bodies are assumed to be perfectly smooth which causes frictionless contact.
3) The half-space assumption is valid in the theory which means that the size of the contact area is significantly smaller than the dimensions of each body. This assumption is also described as both of the rail and wheel generate a rigid and non-conforming contact.
4) The curvatures of the surfaces in contact are constant.

However, these assumptions are often violated in the real case profiles. In order to increase accuracy, several methods have been developed which are summarised in Chapter 4.1.1.

In the kinematical and tangential problems, this aforementioned creepage and the related forces are calculated, respectively. When the wheels travel at velocity V, they are also subject to torque T which enables the angular velocity of the wheel w and in turn creates the circumferential velocity c = wr (r:radius of the wheel). The difference between these two velocities causes a deviation from the pure rolling motion which is called as creepage. Creepage is generated in the contact patch in three directions: longitudinal, lateral and spin. The longitudinal creepage $(\gamma_x)$ is the deviation in relative velocity in the longitudinal direction and the lateral creepage $(\gamma_y)$ is similarly defined as the relative velocity in lateral direction. The spin $(\omega)$ is the relative angular motion between wheel $(w_{w,z}$ in $z$ direction) and rail $(w_{r,z}$ in $z$ direction) about an axis normal to the contact patch. Figure 2.3 presents the creepage and velocity directions (Dollevoet, 2010).
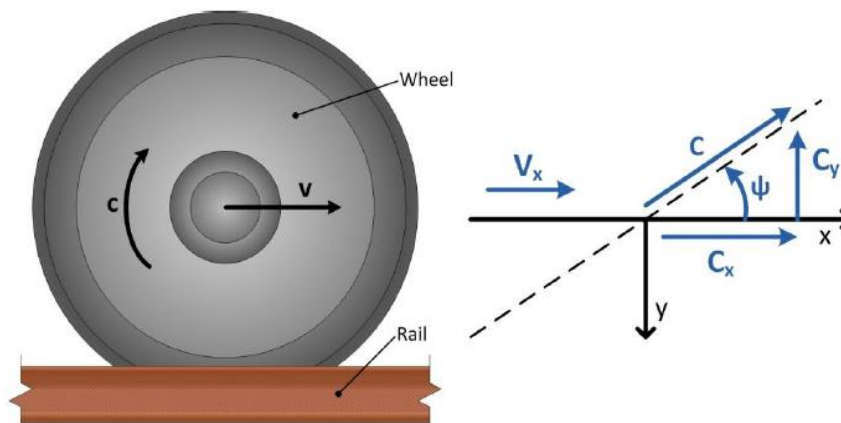


Figure 2.3: Creepage and velocity directions at the wheel-rail contact (Dollevoet, 2010)

$$V_{roll} = rolling\ velocity = 1/2(V + C) \qquad (2.19)$$

$$\gamma_x = \frac{V_x - C_x}{V_{roll}} \qquad (2.20)$$

$$\gamma_y = \frac{V_y - C_y}{V_{roll}} \tag{2.21}$$

$$w_z = \frac{w_{w,z} - w_{r,z}}{V_{roll}} \tag{2.22}$$

where $\Psi$ is the yaw angle of the wheelset relative to the track. The forces arising from this relative motion in the contact patch are defined as creep forces and there have been again many different methods to calculate which are detailed in Chapter 4.1.2.

## *2.2 Development of RCF damage*

When a rail section is exposed to repeated loading, its response can be described by four loading regimes as illustrated in Figure 2.4 (Johnson, 2000). When the yield stress of the rail material is not exceeded, the elastic response takes place. But, with the increased loading, cyclic shear-induced dislocations cause plastic deformation and generate slip bands surrounded by less affected material. This difference creates residual stresses within the material after the contact is unloaded and they will help to delay further plastic deformations. When they are combined with the strain hardening of the plastically deformed material, it enables the material to support much higher loads than its elastic limit. This response is called elastic shakedown.
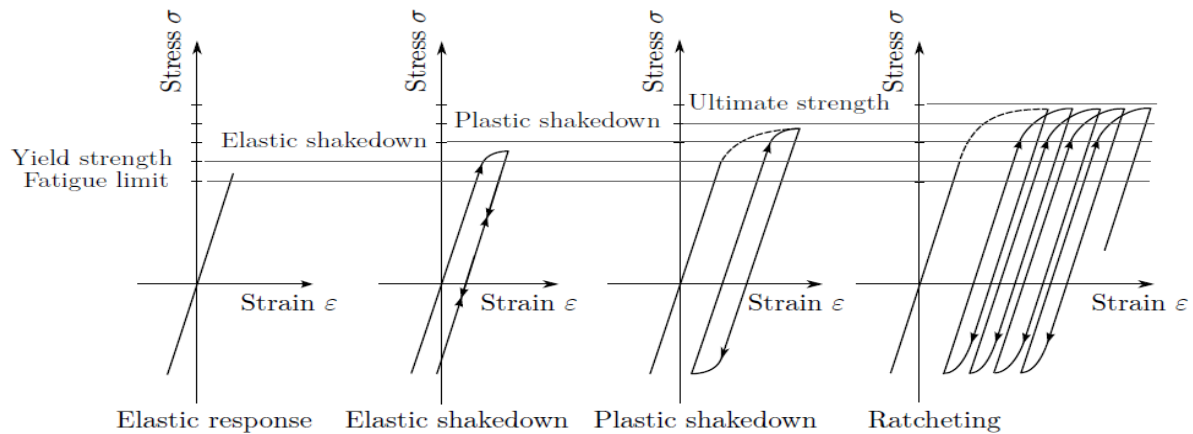


Figure 2.4: Material response to cyclic loading (Johnson, 2000)

When the load is greater than the elastic shakedown limit, there will be plastic flow with each cycle. Under plastic shakedown, the cyclic stress-strain curve becomes stabilised closed loop with no accumulation. However, the higher increase in loading conditions cause incremental (uni-directional) accumulations by every load passage. This process is called as ratchetting and it continues until the ductility of the material is exhausted. When this is exceeded, it may cause the removal of material from the surface as wear debris or initiation of cracks in the railhead (Kapoor, Beynon, Fletcher, & Loo-Morrey, 2004).

After the initiation of a crack, its further propagation is mainly driven by the contact stresses as well as bending and shear stresses arising from the load during the passage of the wheel. When these stresses are combined with thermal stresses, due to restrained

elongation of continuously welded rails and residual stresses developed from manufacturing process, cracks can grow further and increase in length (Schilke, Larijani, & Persson, 2014) .

The life of a crack is defined by its development path. However, it is very difficult to predict the crack development path as the aforementioned stresses are influenced by several factors such as different wheel-rail contact conditions, vehicle configurations, traffic, track and environmental factors. Moreover, rail material characteristics play a major role in the point of crack initiation and the direction of crack growth.

Rail material type, its chemical composition, steel grade and the kind of metallurgical processing and/or the heat treatment method adopted during manufacturing are some of the key elements which influence rail microstructure. The current EN standards include a range of pearlitic steel grades with varying hardnesses between 200 HBW and 400 HBW. But, although some of the rails have similar hardness levels, their microstructure can differ based on the aforementioned changes which in turn affect their performance during railway operations (Bevan, Jaiswal, Smith, & Ojeda Cabral, 2018). Nevertheless, the steel grade R260 is one of the most dominant rail types used in mainline and metro systems.

In addition to the complex nature of the crack development, the number of cracks initiated differs depending on the material and loading condition (Schilke et al., 2014). There are various types of RCF crack related damage which are observed in railway lines: head checks, squats, shelling, longitudinal vertical and horizontal cracking are different type of cracks which are formed from the aforementioned factors (Zerbst, Lundén, Edel, & Smith, 2009).

The crack development is usually defined by three phases, as demonstrated in Figure 2.5. The crack initiation takes place in the first phase. Then, the crack slowly expands in the second phase and increases its growth rate until rail fractures in the final phase.
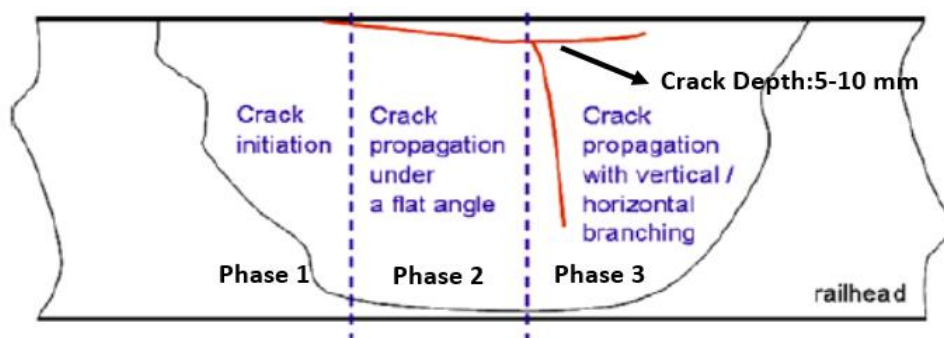


Figure 2.5: Three phases in crack development (Plu, Bondeux, Boulanger, & Heyder, 2009)

Numerous studies have been conducted to find explanatory concepts to understand this RCF phenomenon. However, it is still unclear which of the above factors lead to which type of crack initiation and how they affect the crack propagation. After initiation, crack

development path varies and it is usually defined by its surface and sub-surface length, depth and its angle from the surface.

One of the studies which investigated microstructure of rails stated that the depth of the plastically deformed surface layer and the level of alignment of the microstructure altered depended on the contact loading and the rail steel grade. When the load was applied repeatedly in similar directions, the plastic deformation followed this direction. However, the material properties of the steel ceased to be isotropic when the rail is plastically deformed and became anisotropic which resulted in different resistance to crack propagation and the study found that the cracks grew along the direction which had lowest resistance (Larijani, 2014). Figure 2.6 displays the difference while there is a random distribution indicating the isotropy under undeformed material (Figure 2.6 (a)), the plastic deformation starts to re-orient and align, made the material anistropic (Figure 2.6 (b)).



(a)                                                                                    (b)
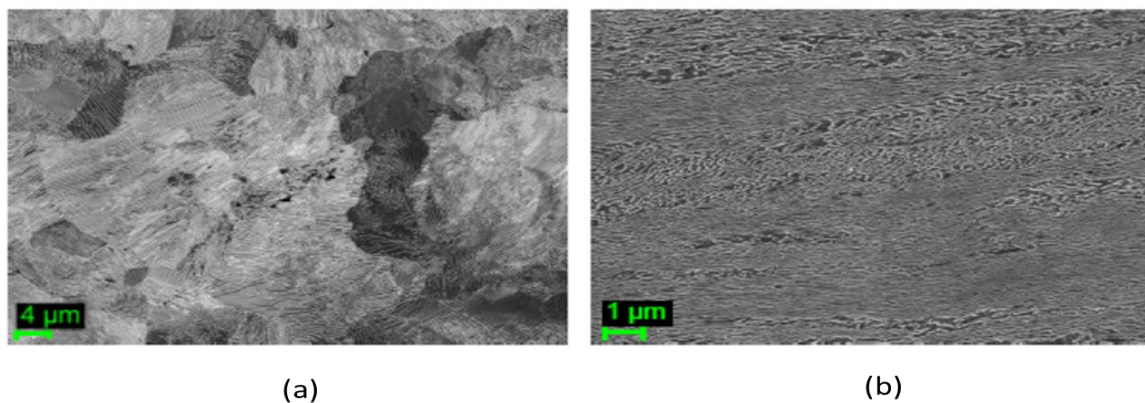
Figure 2.6: Differences in material microstructure under undeformed (a) and deformed (b) states (Larijani, 2014)

Crack initiation and growth and the influence of the rail microstructure to its surrounding cracks have been investigated using test rig and field sample test results (Schilke et al., 2014). The crack followed the plastically deformed layer allowed it to propagate in only one direction. But, after reaching the boundary of this layer, its path was determined by the loading and the stochastic weaknesses of material. It was also identified that branching occurs for the cracks which had the shortest distance to each other. Cracks propagated together and the main crack reached deeper points then a single crack. Figure 2.7 displays the cracking in this field sample of a UIC 900 A grade rail located on the curve track. Whereas Figure 2.7 (a) shows the schematical representation of the transverse plastic flow (solid lines) and the border of the plastically deformed region (dashed line), the typical crack (b) and the crack branching (c) observed on this sample.

In a separate study, the concept of crack shielding in multiple closed head check cracks showed that two cracks cannot grow close to each other since, the one which had a higher crack growth rate would shield the slower crack (Tillberg, Larsson, & Runesson, 2009).
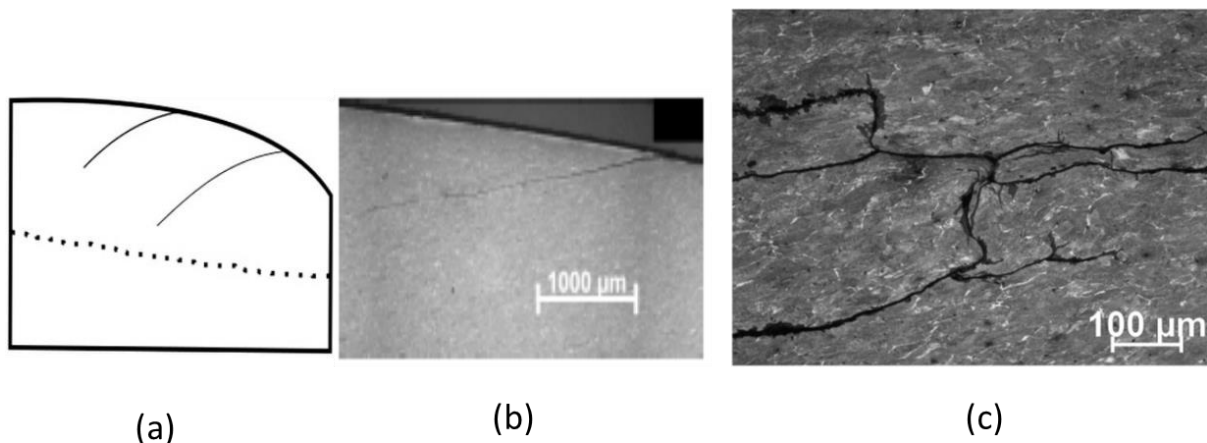
Figure 2.7: Schematical representation of plastic flow (a), surface crack (b) and crack branching (c) in the field sample of UIC900A grade rail (Schilke et al., 2014)

## 2.2.1 Wear and its interaction with RCF

High wheel-rail contact forces do not only cause cracks to initiate, but also lead to wear on the rail surface. In general, wear is defined as the loss or displacement of material from a contacting surface (Olofsson, Zhu, Abbasi, Lewis, & Lewis, 2013). While material loss might be in the form of a debris, material displacement may occur as a result of transfer of material by adhesion or local plastic deformation.

There are different types of wear mechanisms that can generate between contacting bodies, such as the wheel and rail, which are summarised below (Lewis & Olofsson, 2009):

*Oxidative wear* is a process where an oxide layer of the material is detached from the surface. It occurs under low contact conditions.

*Adhesive wear* takes place at microscopic surface asperities where the contact occurs between the surfaces. When the contact surfaces in these regions move relative to each other, the material is broken away by either brittle or ductile fracture. After the material at the original points of contact has broken, contact will occur at new surface asperities.

*Abrasive wear* is generated due to relative motion of either harder asperities, which is known as two-body abrasive wear, or hard particles such as those formed from different contaminants trapped between the surfaces, which is known as three-body abrasive wear. These third body particles can consist of remaining material of the surface that have already worn away and oxidised or may include hard contaminants (Carroll, 2006).

*Thermal wear* occurs as a result of frictional heating at the contact. This surface heating causes to a softening or melting of the material. The heated material can thereafter be displaced as it resembles a viscous fluid.

*Delamination wear* mainly results from the accumulation of plastic deformation due to high number of wheel passages, thin sheets of wear debris are detached from the surface.

The above different mechanisms lead to changes in the wear rate/regime. Commonly, there are three wear rates: mild, severe and catastrophic. Whereas mild wear is often associated with oxidative wear, severe wear is caused by adhesive wear. Increased temperatures at the contact and material softening in this region result in catastrophic wear regime (Olofsson et al., 2013). The mild wear led to smoother surfaces whereas, severe wear gave rise to rougher surfaces.

The service life of a rail is generally defined by when fracture occurs (RCF cracking reaches severe conditions) and/or when the amount of combined wear (head and side wear) exceeds the maximum limits (Ben-Akiva, 1996). The limits may change for different type of traffic and track sections. For instance, on LUL, the maximum allowable crack depth is defined as 7 mm and the maximum side wear is 4mm under 6mm of headwear (LUL, 2015). Traditionally, wear in rails is defined with reference to three different locations of measurement profile which are also presented in Figure 2.8.

1) Top (Head)/Vertical Wear (W1): The amount of material worn at the railhead surface (vertical axis of the rail)
2) Side Wear (W2): The material worn at 90° to the vertical axis in the gauge point (according to European Norm Standards, it is 14 mm below the top of rail)
3) Gauge Corner Wear (W3): The wear at 45° to the vertical axis.
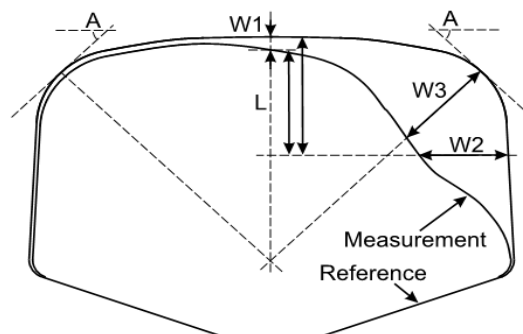


Figure 2.8: Rail wear measurement (Greenwood-Engineering, 2010)

Even though the wear is produced by several different mechanisms, ratchetting and high plastic deformation accumulations can lead to both RCF and wear. Under this condition, the initial stages of their development are very similar, however they will interact each other in a highly complex manner. Figure 2.9 shows a section from the 900A rail disc in which the large unidirectional plastic deformations and surface cracks were evident under ratchetting. However, the competition between wear and RCF was also demonstrated as the initiated cracks were continuously truncated by worn material depth of 220 μm (Donzella, Mazzù, & Petrogalli, 2009).
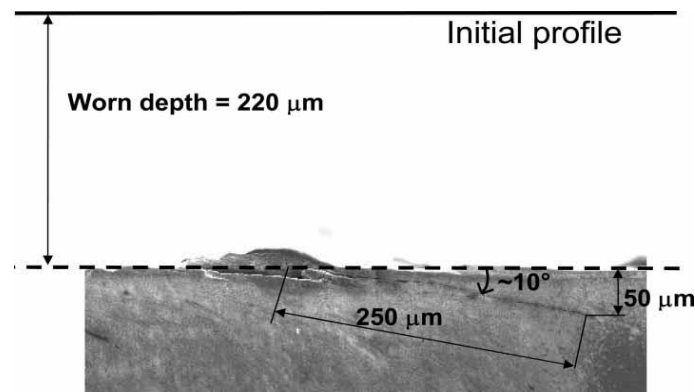
Figure 2.9: Truncation of a crack due to wear on the 900A rail disc under ratchetting (Donzella et al., 2009)

While wear may dominate and cracks simply wear away in some cases, the wear rates may be low in different circumstances, allowing cracks to propagate. Nevertheless, excessive wear may be also critical and can give rise to undesirable conditions such as it may decrease the service life of a rail and lead to a modification in rail and wheel profiles which in turn affect the wheel-rail contact positions. The optimal strategy in material removal was described by the term called 'Magic Wear Rate' (E. Magel, 2011). This aimed to remove the existing and incipient cracks with the combined amount of natural and artificial (grinding) wear. Although the technological advances in the rail manufacturing such as changes in chemical composition and heat treatment processes have resulted in steels with higher hardness and yield strength which make them more resistant to crack initiation and wear, the problem of RCF cracks continues to exist in railways. The increased wear resistance means that the surface initiated cracks are no longer removed through wear. In other words, low wear rates cause initiated cracks to develop in the plastically deformed rail steel and those may grow deeper into the rails. In addition to this, the lower wear rate means that any unfavourable rail gauge corner shapes remain for longer than seen with softer steel rails which will reach a conformal shape more rapidly (E. Magel, Roney, Kalousek, & Sroba, 2003).

## 2.3 Rail inspection and non-destructive testing (NDT) techniques

In order to reduce the risk of rail failures, infrastructure managers (IMs) generally endeavour to eliminate rail defects at an early stage. Since they influence safety and quality of operation and increase operating expenses, rail inspection becomes crucial. IMs predominantly carry out visual inspection to assess the surface condition of the rail and use non-destructive testing (NDT) to detect rail defects. They primarily use ultrasonic testing, eddy current and magnetic induction measurements.

In ultrasonic inspection, a beam of ultrasonic energy generated by a piezoelectric element is transmitted into the rail. The reflected (scattered) energy of the transmitted beam is then detected using a collection of transducers. It was often stated that the standard ultrasonic sensors have poor ability in detecting surface initiated cracks (< 4mm) and

cannot accurately detect critical defects masked by spalled rail or shallow defects (Papaelias, Roberts, & Davis, 2008). In order to overcome this problem, multiple transducers need to be employed at different angles to increase the detection ability of these cracks which is demonstrated in Figure 2.10.
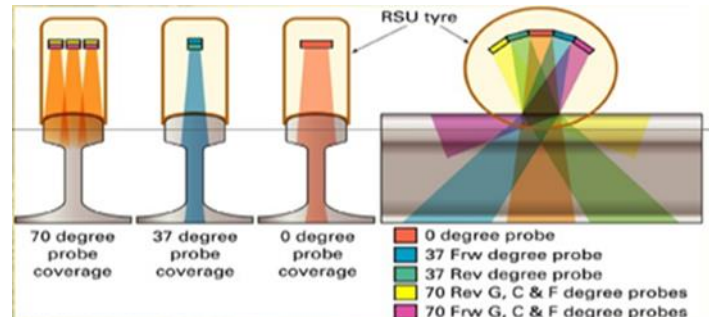


Figure 2.10: Multiple ultrasonic transducers positioned at various angle (Innotrack, 2008b)

Eddy current technology is also widely used in rail industry. The sensors consist of one exciting and one sensing coil which detects the eddy currents generated from magnetic field. When there is a near-surface defect, currents are causing fluctuations and giving rise to changes in the impedance. Although it is stated that this system has a better performance than ultrasonic inspection, it is sensitive to changes in the distance between the coils and the target. Thus, it is strongly influenced by the lift-off variations which means that certain surface defects can still be missed during inspection (Innotrack, 2008b). In addition, eddy current measurements give an indication for the depth of the cracks by using a predefined crack initiation angle to estimate the crack depth.

Rail inspection with magnetic induction or (magnetic flux leakage), permanent magnets or DC electromagnets are utilised to generate a magnetic field. Sensors close to the railhead measure changes in the magnetic field (leakage in magnetic flux) to identify the location and severity of defect in the rail. Even though this technique has demonstrated a higher accuracy in detecting the near-surface and surface-breaking defects, its performance has been adversely affected by increases in inspection speeds which stem from the reduction in the magnetic flux density (Papaelias et al., 2008).

Over the last few years, the limitations in current methods have led researches to develop different techniques for the inspection of rail condition. These new technologies include: Field Gradient Imaging, Alternating Current Field Measurement, and Electromagnetic Acoustic Transducers. Even though these systems have showed good performance in detecting cracks, they can be adversely affected from grinding marks and lift off variations. The use of automated visual inspection systems is also a recent development which has been utilised in railways. High speed cameras are mounted on test trains and used to capture high quality video images that are analysed on-line using customised image analysis software. The system is able to measure the condition of the rail head surface, wear percentage, gaps along the rail and corrugation. Nonetheless, it cannot accurately

detect rail cracks. The detection of cracks requires a more reliable data and the movement of the cameras sometimes causes blurred images which reduce the resolution of the images. Therefore, real-time data evaluation is not possible in this system and an off-line analysis is needed to identify any defective areas.

Visual inspection is still one of the primary methods used to verify the detections carried out by the more advanced techniques and to assess the severity of the cracks. The crack depth, which is a critical parameter in the assessment of the severity of a crack, could not be detected reliably by most of the recent inspection tools. However, it is crucial for track maintenance to decide if it is a current risk that requires immediate removal or will become a risk in the future. Previously, the crack severity classification is largely based on surface length rather than depth. Figure 2.11 was developed in order to determine RCF severity classification. A large sample of rails were sectioned and the RCF cracks were examined to define a correlation between length and depth of a crack (Glavin, Aspebakken, & Besch, 1989). As shown, if the surface length of a crack is larger than 20 mm, it corresponds to heavy severity and the possibility of the crack growing further increases rapidly.
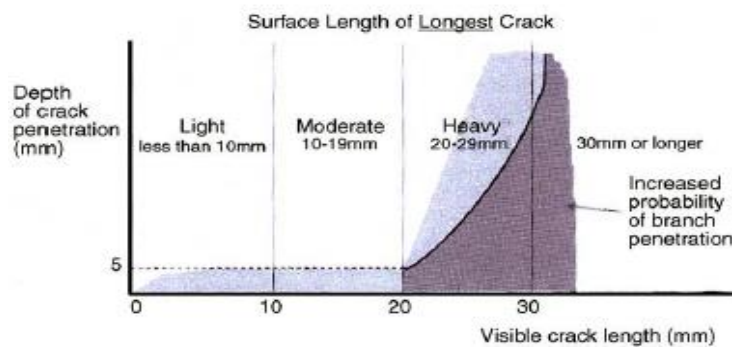


Figure 2.11: Correlation of crack penetration with visible crack length (Glavin et al., 1989)

In a more recent study, the observed crack depths were plotted against the observed surface crack length for different type of rail steel grades (Innotrack, 2009a). It was found, for rail steel grade R220 that for observed surface crack lengths of less than 17 mm the crack depth was not longer than 5 mm, but for greater surface crack lengths, the depth increased up to a maximum of 10 mm. However, it was also noted that there was no direct correlation between surface length and crack depth for all the rail steels investigated. The position of the rail whether it was on curved, transition or straight track along with the different rail steels changed the crack growth angle which led to different crack depths regardless of its surface length.

In order to validate the correlation presented in Figure 2.11, the recent study analysed the crack shapes by multi-slice axial sectioning. Each axial slice of the rail, shown in Figure 2.12, a representation of the observed cracks in the transverse plane was made. This revealed that there is considerable variability in the shape of the cracks even for 'moderate'

severity cracks (Garnham, Fletcher, Davis, & Franklin, 2011). The results from this UK study were compared with the data obtained from German (Deutsche Bahn-DB) and Canadian rail networks. Visual surface crack length and vertical crack depth of UK/DB were relatively in good agreement but, the observations from the Canadian rail network deviated due to the different traffic conditions experienced by these rails. The study also stated that the singular vehicle characteristics led to regular RCF crack patterns.
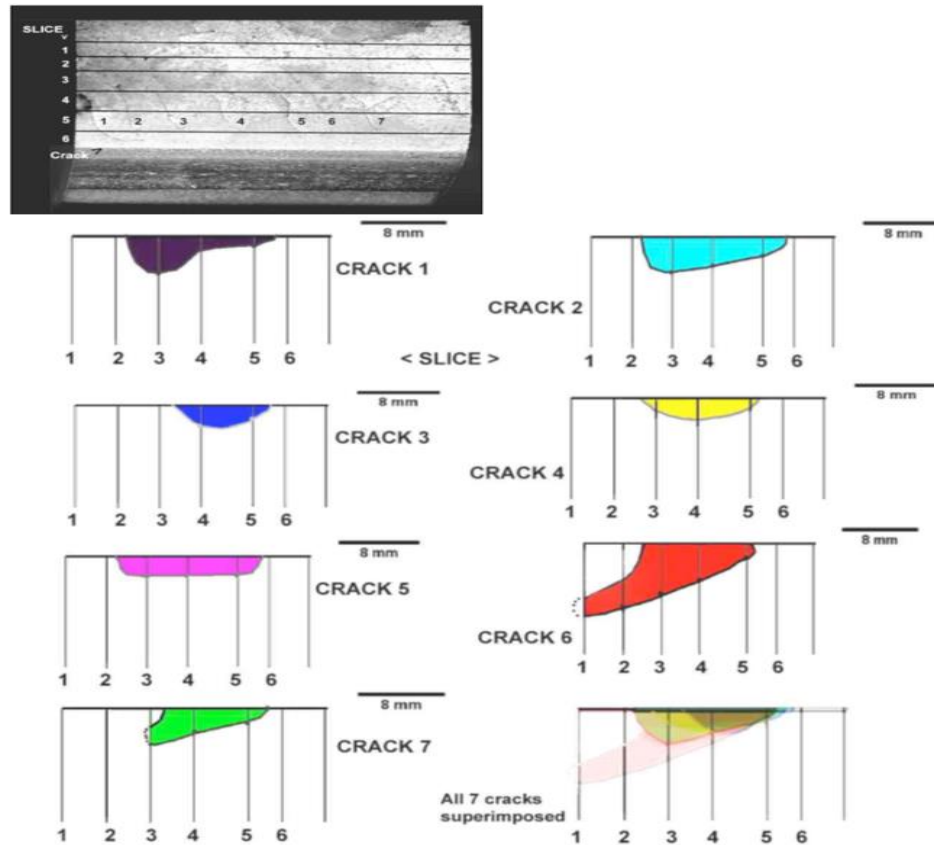


Figure 2.12: Vertical sections through a series of RCF cracks in a rail (Garnham et al., 2011)

## 2.3.1 MRX-RSCM crack measurement

One of the latest technologies for crack detection is the MRX Rail Surface Crack Measurement (MRX-RSCM) system (developed by MRX Technologies). The MRX-RSCM system uses magnetic flux leakage to measure crack depths up to 7 mm into the railhead and also gives an opportunity to estimate the presence of subsurface damage. When there are no defects, the flux lines travel undisturbed through the railhead. But in rails with defects, the flux cannot travel as easily and some flux leaks. Sensors measure the depth from changes in strength of the flux lines which is also named as artifact depth (MRX, 2011).

With the help of 19 sensors positioned 5 mm apart to each other as shown in Figure 2.13 and 2.5 mm longitudinal detection interval, 5 x 2.5 mm grids are generated on the top

surface demonstrating the severity of damage by the help of pre-defined colour scale. The system measures crack depths and outputs the maximum in each 1m interval.

Totally, the RSCM technology enables the following measurements:

- Crack depth (0-7 mm)
- Crack (longitudinal) track position (crack locations on the line, distance (km))
- Crack (lateral) position on the rail head surface (close to gauge or field side of the rail. etc, 0-95 (5*19) mm
- Indicative shape of the crack
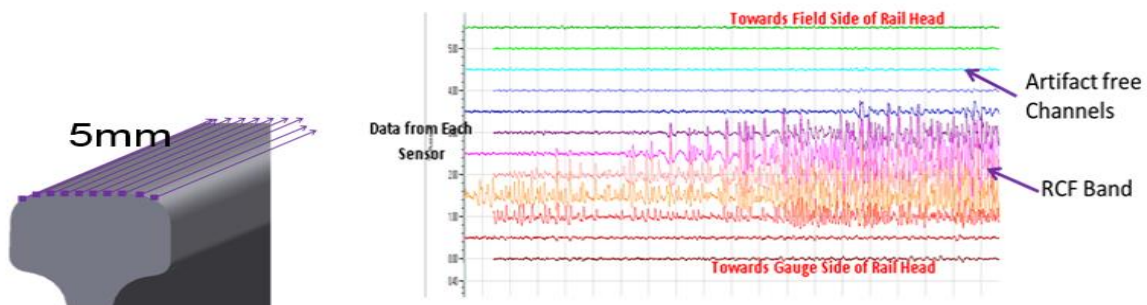


Figure 2.13: Sensor positions and measurements (MRX, 2011)

Figure 2.14 shows the real-time display data on the RSCM Operator Propelled Unit for a spalling type of RCF crack. Whereas the "Artifact/Crack Depth" graph on the left side of Data Display plots the deepest crack depth along the measured track, the "Rail View" graph (also named as Surface Damage Map in the measurement outputs) shows the crack location on the 1 m segment of rail head surface. The type and severity of a RCF crack in the Rail View screen can be predicted from the Damage Colour Scale. For instance, while a dark blue colour demonstrates a light/minor damage, a red colour shows a more severe/deep damage.
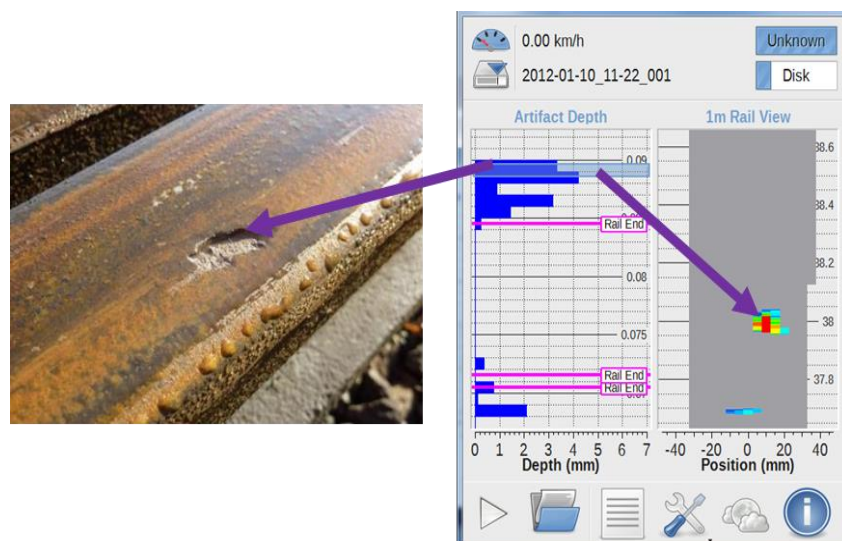


Figure 2.14: Example of the MRX-RSCM output (Klecha, 2013)

In order to validate the MRX-RSCM crack measurements, a number of examinations were conducted. The laboratory conditions showed that the system provided a good correlation for the cracks between 1.5-5 mm depth. It classified the rail section as severe damage when there was spalling (or flaking off) of material on the rail surface. Both flash-butt and alumino-thermit welds were distinguished, as it showed the highest severe damage warning in these locations (Kaewunruen, 2015).

However, further validation studies which were carried out under International Collaborative Research Initiative (ICRI) project revealed significant differences between crack depth measurements using the MRX-RSCM and Draisine systems and rail sectioning results. Draisine is an inspection tool which uses eddy currents to inspect rail flaws. It measured the crack length and calculated the crack depth based on assumed crack angle which was defined as 25° in the study. After measurements of cracks in the specified regions, the rail sections were removed from the track. The rail cross sections were cut and examined under electron microscope. The success of Draisine was mainly dependent on the pre-defined crack initiation angle. When the angles were smaller than 25°, it overestimated the damage depth. Similarly, the MRX-RSCM also provided unsatisfactory validation, as it measured 50-75% higher than the actual crack depth. Nonetheless, it was mentioned that 1 m depth output interval may be responsible for this inaccuracy as the length of rail samples were shorter (E. Magel, 2016).

## 2.4 RCF damage prediction modelling

The phenomenon of RCF has been investigated for many years. Various models were developed by applying different techniques and laboratory tests were conducted to understand the reasons behind the problem. In this thesis, the RCF damage prediction models have been divided into three main groups, as presented in Figure 2.15. The first group is the crack initiation models which primarily focus on predicting the initiation time and investigate whether the initiated cracks are able to pass the critical limit. This helps to understand whether the cracks removed by wear (and/or grinding) or they have the potential to propagate further. Secondly, the propagation models are mostly concentrated on calculating the crack growth rate in further stages of crack development. Finally, the models mainly focus on predicting the location of cracking on large railway networks to find the critical sites. Crack locations are defined by longitudinally which means the distances along the lines and laterally over railhead.
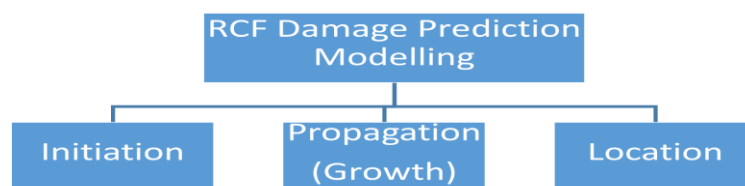


Figure 2.15: Three main types of RCF damage prediction modelling

Similar to phases given in the RCF crack development, the crack growth rate changes in both the initiation and propagation stages (Kapoor, Schmid, & Fletcher, 2002). Figure 2.16 illustrates the crack propagation rate in respect to the increase in crack size. Additionally, the factors which have an influence on the crack growth rate are presented.
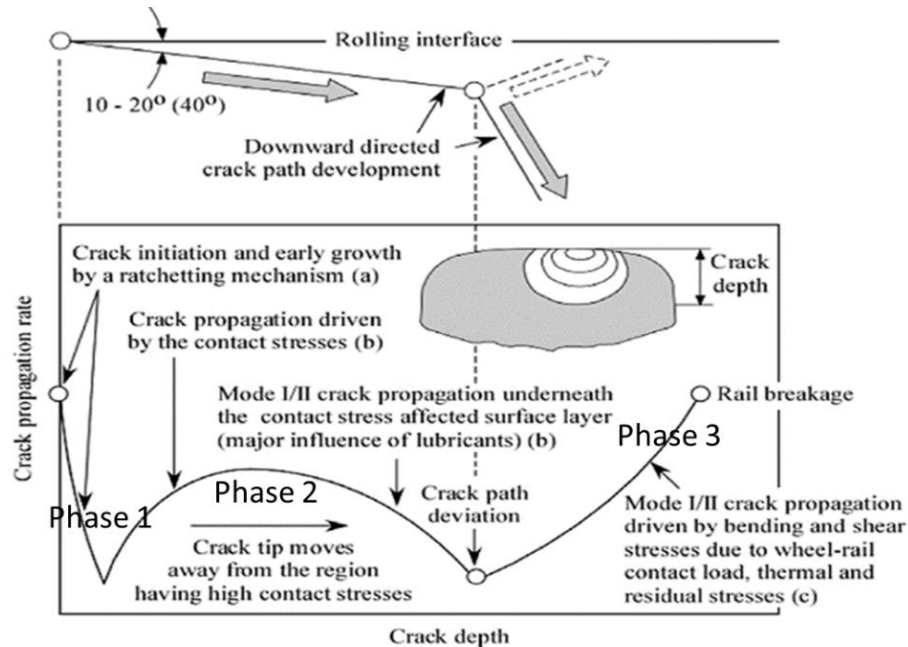


Figure 2.16: Phases in the crack propagation rate (Kapoor et al., 2002)

In addition to failure of the grains in the railhead due to ductility exhaustion and large plastic deformations, the white etching layer (WEL) may be also formed resulting from severe plastic deformations and/or high temperature rises under the phase 1 (Carroll & Beynon, 2007). At the end of this phase, the cracks are initiated which corresponds to a crack length of approximately 3-5 grains (0.1-0.5 mm). Transition to the second phase of crack development occurs when the crack growth is driven by shear mode contact stresses. During this phase, the crack becomes long enough to be affected by additional crack growth mechanisms. Lubrication and water are very crucial in this stage as they dramatically influence the stress state. When the crack becomes larger and the crack tip moves away from the high stress region, the crack propagation slows down. The influence of the compressive longitudinal residual stresses, which are also a consequence of plastic flow produced by contact loading, are also modified in the phase 2. If these stresses are located close to the rail surface, then their effect will reduce as the crack propagates. The reduction in these stresses makes the rail bending stresses more significant at longer crack lengths and encourages the development of branch cracks, which may penetrate in to the rail head at an angle of 55° – 65°. Thus, rail bending stresses dominate during phase 3 crack growth. As it can be also seen in Figure 2.16, the crack propagation rate is largely defined by the modes in fracture mechanics (Lewis & Olofsson, 2009).

One of the most popular crack initiation models is the Brick (Dynarat) model. This was developed to predict crack initiation as well as wear. A cross section of a rail was modelled as a mesh of elements (or bricks) parallel to the direction of traction. Each element in the mesh was assigned material properties such as initial shear yield stress and critical plastic shear strain for failure. The plastic shear strain increment per cycle was calculated from the difference between the maximum orthogonal shear stress and the shear yield stress. When the accumulated strain in an element reached its critical value, the element failed and was marked as 'weak'. With respect to this, the model could show the points where the material fails at the surface as wear debris or remains as part of the material structure and forms crack-like defects. The depth of crack initiation was determined from the number and orientation of weak elements in the mesh as expressed as percentage damage depth in the model such as 1% and 10% damage depth (Franklin & Kapoor, 2007).

Another crack initiation model is the overall wheel-rail contact and damage model (OCD) which is a combination of extended creep force (ECF) and the approximate wear and damage (AWD) models (Six et al., 2017). The structure and the steps of the model is shown in Figure 2.17. In the first step, the ECF model calculates the contact shear stress distribution required for the AWD model considering the tribological effects such as roughness, temperature and/or fluids. Then, the plasticity model calculated the plastic shear strain distributions $\alpha_Z$ from the bulk stress model results; $\sigma(x,y,z)$ and $\tau(x,y,z)$. Later, the damage model estimates the RCF crack initiation and wear model predicts the depth of removed material from the surface. It was stated that (microscopic) cracks either lead to the formation of flakes or wedge-like structures depending on the distribution of angular plastic shear strain. Whereas flakes can lead to wear, wedge like structures can contribute either wear and/or RCF which can ultimately form macroscopic fatigue cracks. The model results provided good agreement with a full-scale test rig results in which gauge corner cracking was observed after 100,000 cycles.
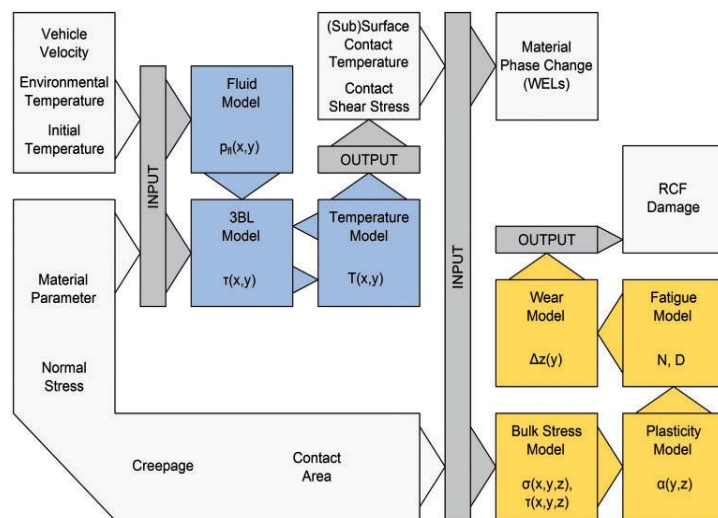


Figure 2.17: The steps and the sub-models in the overall OCD model approach (Six et al., 2017)

In the RCF crack growth modelling, the cracks were described by the three distinct regimes: micro-structurally short cracks, physically short and long cracks. Each crack regime had a fracture mechanics based approach to characterise crack propagation behaviour: micro-structural fracture mechanics (MFM), elastic-plastic fracture mechanics (EPFM) and linear-elastic fracture mechanics (LEFM). Although numerous investigations were conducted to determine whether the EPFM or LEFM was applicable in the propagation of shorter cracks, it is still a controversial issue. Whereas some researchers believed that the LEFM was applicable since the rail has shaken down to elastic steady state which did not lead to high increments in bulk plastic strains, the others questioned the fact that there was large plastic zone compared to crack length in the short crack regime (from Phase 1 to 2) which causes crack growth in elastic-plastic regime rather than linear-elastic (Ringsberg & Bergkvist, 2003).

As it was previously mentioned, defining the critical crack size in the modelling is important and from a maintenance perspective, this would include the identification of the crack size which cannot be removed by wear or grinding. Therefore, the interaction of wear and RCF is significant in the crack growth. Previous models which account for wear rate showed three different levels for both crack initiation and propagation stages (Ringsberg, 2005). As it is demonstrated in Figure 2.18, when the wear rate is at the Level 1, the crack formation is not generated. The slightly lower rate at Level 2 may remove the initiating cracks faster than they form, hence the crack growth is restricted. When the wear rate is very low, the crack growth cannot be prevented which generally occurs in harder rail steels due to their higher wear resistance.
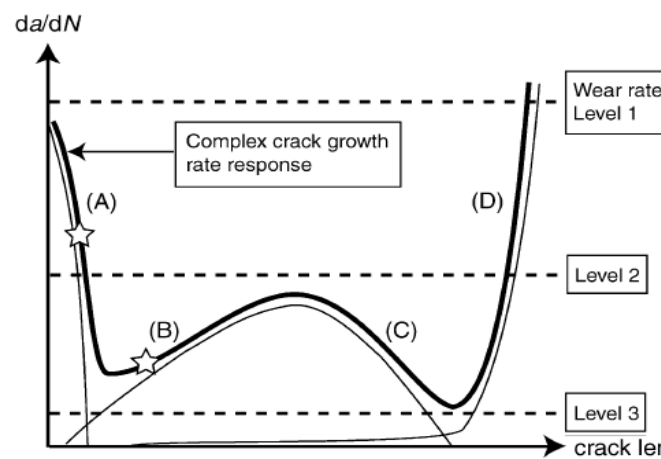


Figure 2.18: The influence of wear rate on crack propagation (Ringsberg, 2005)

Crack propagation models can be differed according to the dimension of the wheel-rail contact and the initial crack defined in the modelling. While some researchers considered line contact (2D) modelling, others have used 3D elliptical contact models. The crack dimension described in these models changes in terms of depth, sub-surface length and crack inclination angle. Additionally, 3D models have been recently started to study

in which semi-circular or semi-elliptical cracks have been assumed. There are also studies which have used 2.5D modelling, which is a combination of 3D elliptical contact patch with a 2D crack model.

Ringsberg (2005) created a 2D FE model to analyse the propagation of short cracks in a set of twin disc tests. As a consequence of laboratory tests, he found that the LEFM was not appropriate to describe the RCF crack behaviour since, the local conditions of crack growth near the crack tip were greatly affected by the adjacent material deformation and response. Thus, the EPFM was conducted using the results from FE model for four crack lengths: 0.05, 0.1, 0.2 and 0.4 mm with selected crack inclination angle of 20°. The results showed that all of the cracks extended by the mode II shear growth mechanism and the direction of the three shortest cracks were almost parallel to each other but, the longest crack in the study had the lowest propagation rate and turned in an upwards direction.

For the cracks in Phase 2, the influence of fluid is playing a major role in the determination of crack growth. The laboratory tests which were conducted to investigate this phenomenon found that three possible mechanisms were generated by this fluid effect (Way, 1935). In modelling, these three following mechanisms as demonstrated in Figure 2.19 are usually taken into account to calculate crack propagation rates.

I)    Fluid might lubricate the crack faces which means that the crack is propagating in mode II by the cyclic shear stresses caused by repeated rolling contact.

II)   Hydraulic pressure mechanism; fluid forced to prise apart the crack faces which generates mode I stress intensities at the crack tip.

III)  Fluid entrapment mechanism; crack mouth closes or contact patch can seal it and the fluid inside the crack applies a pressure towards the tip.
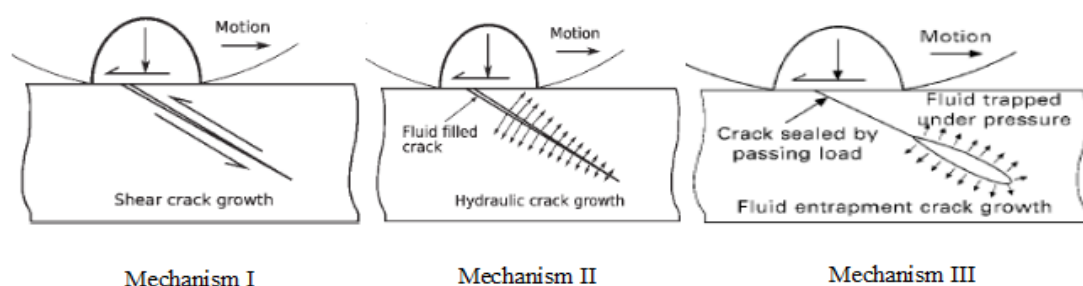


Figure 2.19: Mechanisms of the fluid effect used in the RCF modelling (Lewis & Olofsson, 2009)

One of the first models which was developed to analyse the effect of fluid on crack growth considered the three above mechanisms (Bower, 1988). The 2D model of a surface initiated crack was generated with a sufficiently long crack in order to use LEFM principles and with a crack angle of 25°. In the first mechanism, stress intensities at the tip of the crack were calculated using dislocation method to present the load as it moved over the surface (Keer & Bryant, 1983). It was found that the sequence of slip, stick, opening and

closure was dependent on neither the inclination nor the length of the crack. However, the direction of traction changed the crack growth as the driving traction produced greater stress intensities than the braking traction. The second mechanism was studied by taking the hydraulic pressure equal to the Hertzian pressure of the half width contact. The crack growth rates were rapid but the model was unable to demonstrate the influence of the direction of traction. Thirdly, the crack was filled with fluid just before the contact reached the crack mouth and afterwards, crack mouth was sealed when contact passed over it. Both mode I and II stress intensities should be calculated as the fluid kept part of the crack open (mode I) and reduced the friction forces acting on the crack faces (mode II). It was concluded that the driving traction again generated large stress intensities but the braking traction showed an opposite effect.

In the F&B (Fletcher & Beynon) model, the 2.5D modelling technique which gave the opportunity of changing the contact position over the crack was used to describe the effect of rail grinding or re-profiling of the running surface. Figure 2.20 shows the influence of 3D contact patch on the 2D semi-elliptical cracks. While the cracks "A" and "B" could be covered by the contact which made the Fluid Mechanisms II and III applicable, the cracks "C" and "D" cannot be fully sealed by the contact patch. The stress intensities were calculated using Green's functions in order to reduce the computation time. Although the method helped to convert the stresses along the line of an inclined surface breaking crack in to a stress intensity factor, the F&B model extended it to semi-elliptical/circular cracks by using a geometry factor. Regarding the lubrication effect, only the first mechanism was taken into account and the friction of the crack faces was varied in the model. In the no-offset case, the stress intensity factors (and hence crack growth rate) were greater for elliptical contact patches with high ellipticity (a/b) levels. But, the offset contacts showed that even the small offset of the contact by 1.6 mm (corresponds to 40% of crack radius) produced a 10 % reduction on the predicted shear mode stress intensity factor. For the 3.1 mm offset, the crack growth rate was decreased by 80% which is very common in reality by changing the cross sectional profile through grinding (Fletcher & Kapoor, 2006).
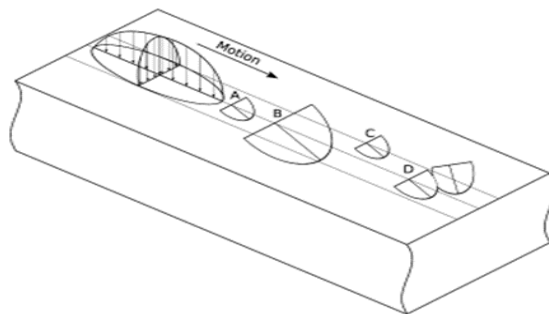


Figure 2.20: Influence of 3D contact patch on semi-elliptical crack (Fletcher & Kapoor, 2006)

The F&B model was further studied to investigate the hydraulic pressure and fluid entrapment mechanisms on crack growth. In the study, full-scale testing was also

conducted to analyse fluid penetration. Rainwater was simulated using water carrying a fluorescent dye to allow its presence inside the cracks in order to detect it in the destructive examination. At the end of the experiments, it was found that the fluid could penetrate into the cracks without contact loads or traction of a passing wheel. Therefore, they stated that the idea of crack having to be opened by passing wheels to allow water in was violated. The modelling results demonstrated that fluid pressurisation increased the crack growth rate relatively higher than the no-fluid case. This second mechanism had a greater impact on the small cracks (which had less than 4-5 mm of radii) and the wear rate was lower thus, the cracks continued to propagate and crack truncation could not be observed. However, the fluid pressure did not apply to larger cracks since, the contact may not seal these larger crack sizes. Again, the shear mode crack growth model was studied which produced lower crack growth rates even from the wear rate hence, provides a stable crack propagation for larger cracks (Fletcher, Hyde, & Kapoor, 2008).

One of the earlier works done by the 3D modelling technique with semi-elliptical cracks used the Body Force Method to calculate the stress intensity factors (Kaneta & Murakami, 1991). The crack face was divided into 128 triangular sub-regions. The weighting functions indicating the magnitude of body forces at each sub-region. The hydraulic pressure was taken as equal to the contact pressure at the crack mouth and decreased linearly along the length of crack and reached zero at the crack tip. It was found that the direction of surface traction, the distance of contact to the crack mouth and the crack inclination angle strongly controlled the fluid seepage into the crack. In the shear mode growth, crack was extended when driving traction became larger and crack face friction was low while, the tensile mode crack growth induced by hydraulic pressure was occurred at the deepest point for smaller cracks. When the crack depth became higher, the crack growth occurred at the tip of the mouth which led to arrow head shape crack development.

The 3D modelling approach using FE analysis was also studied to examine the crack propagation in squat type defects. Both small and large crack sizes: 12.46 mm and 44.80 mm were taken into account in the study. It was found that the direction of surface traction and friction played an important role in the crack growth rate as well as crack branching. The length of the crack was also crucial as while larger cracks were more prone to crack branching and transverse defects, small cracks were liable to spalling especially in the dry condition (Bogdański & Brown, 2002). They also studied the fluid entrapment mechanism by applying iterative numerical procedure. During iterations, the pressure in the crack faces was gradually increased in each step which caused a separation of crack faces and an expansion of the area. In each iteration, the volume inside the crack was enlarged however, the pressure was kept constant until the area of open cracks stopped widening. After reaching the "state of equilibrium" condition, the three fracture modes were

calculated for each step. The fluid entrapment was only valid until the contact centre reached the centre of the crack. In this position, fluid squeezed out from the crack which led to a decrease in the opening mode, but an increase in shear mode causing the system passing to fluid mechanism I. In the study, 3D and 2D model results were also compared and found that crack growth rates were much larger in 2D models. Hence, for fluid mechanism II and III, rate reduction factors 0.25 and 0.16 had to apply to the 2D results (Bogdański & Lewicki, 2008).

Crack branching was also studied by mixed-mode fracture mechanics which was applied to crack tip to demonstrate the deviation in crack growth. A numerical analysis was made to compute the dominant modes in crack growth according to the consecutive wheel positions with respect to crack location. The three phases occurred in the analysis; the first phase was a mixed of I and II modes, a pure mode II and mode I generated on the second and third phases, respectively. The study found that branching initiated after the crack length reached 4.2 mm. The occurrence of crack branching further studied in the dry and wet conditions as it is displayed in Figure 2.21. In the dry condition, the higher rolling surface friction which increased greater tangential loads enhanced crack opening and branching in the beginning however, the high crack face friction increased crack locking and high wear on the surface removed the initiated cracks. Conversely, crack growth rates were decreased in the wet condition and no branching was occurred in the starting phase, but low crack face friction increased the sliding in the crack faces which resulted in larger crack growth rates. Additionally, the influence of residual stresses on crack growth rate was investigated. Whereas the positive residual stresses increased the crack extension rate due to an enhancement of crack opening and branching, the negative residual stresses led to a reduction in crack opening and sliding which affected the branching and crack growth rate adversely (Dubourg & Lamacq, 2002).
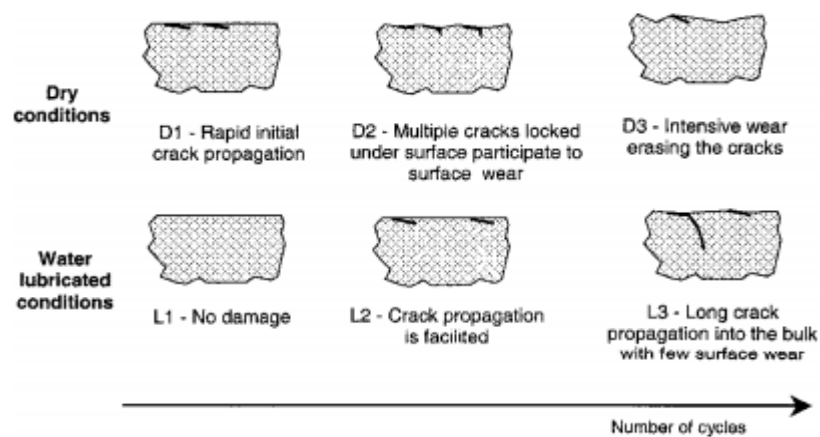


Figure 2.21: Schematic representation of damage under dry conditions and water lubrication (Dubourg & Lamacq, 2002)

The effect of multiple crack interaction on crack growth was analysed considering only the bending stresses. The distance between the cracks was selected as 5 mm and the crack inclination angle was taken as 30° to represent shallow angled RCF cracks which were usually observed in Phase 3 crack propagation (driven mostly by bending stresses). The single cracks with varying inclination angles were also modelled to compare the results. Naturally, the single cracks showed the widest opening and no shielding was occurred from the tensile stresses. On multiple cracks, larger widening took placed at the end of series regardless of the numbers of cracks modelled in the analysis. Therefore, the stress intensities were calculated for the central cracks to show the influence of neighbouring cracks. All stress intensities in each mode were found to be lower than the single crack case. In addition, it was shown that the material between cracks was relieved of stress in the longitudinal direction but, the material at either end of the series was highly stressed (Fletcher, Hyde, & Kapoor, 2004).

Besides the above models, there are models which are used to predict RCF damage locations over long distances. They can be easily integrated with vehicle dynamics simulations and hence the models' input parameters can be calculated for various operating conditions and track characteristics. The common models are the Whole Life Rail Model (WLRM) and Shakedown Map which are clarified in the subsequent sections.

## 2.4.1 Gaps in the RCF damage prediction models

During the review of currently available RCF crack initiation and propagation models several gaps were identified. The crack growth models which were explained in the previous sections were mainly fracture mechanics based approaches and hence, they required certain parameters of an initiated crack such as size, shape and orientation. Additionally, the dominant modes and stresses in these models were mainly determined as a result of laboratory testing which were often undertaken through the use of twin-disc testing. In these models, the effect of fluid was investigated as it was pronounced that this had a major impact on crack propagation rates. This was generally incorporated into the models by changing the friction levels in the rolling surface and inside the crack faces. The impact of wear and/or grinding in some of the models was also studied to find the influence of wear rate on crack development and the effect of change in wheel-rail contact position on crack growth rate.

However, these factors considered in the current approaches were not sufficient to scrutinise the RCF problem. Each phase in the crack growth rate in Figure 2.16 may be affected by various factors stemming from changing operational characteristics. Firstly, divergent traffic conditions such as freight and passenger operations result in different speeds and vehicle configurations with various wheel profiles, axle loads and bogie characteristics. Secondly, track characteristics such as curve radii and cant deficiency

values significantly affect the wheel-rail contact size and position. Although these factors have an impact on crack growth rate, they were sometimes overlooked in the models.

Specifically, the contact pressure which was commonly taken as 1500 MPa in the models did not always reflect the real conditions as it reaches larger values on high tonnage routes or it may reduce due to two-point contact condition which is mostly occur in the curved track sections. In addition, the wear which was occasionally incorporated into the models to demonstrate its influence on crack truncation can have greater impacts on the crack development process.

These assumptions in the aforementioned models had to be made due to usage of Finite Element (FE) modelling technique in the calculations. Although it provides the detailed analysis of stress and strain distributions under wheel-rail contact, it is cumbersome to establish and is not appropriate to describe the significant variation in operating conditions observed in reality. Furthermore, the models aimed to demonstrate the effect of fluid mechanisms II and III on crack growth were making numerous calculations and iterations in order to showed how fluid goes inside the crack. However, the findings from full-scale testing showed that the water would be present in cracks from the first wheel of a passing vehicle (Fletcher et al., 2008). Hence, this extensive number of iterations might become unnecessary in describing this fluid mechanism.

As a consequence, a more rapid approach is required for the prediction of RCF damage on large railway networks. These models should be easily integrated with vehicle dynamics simulations in order to calculate wheel-rail contact positions and forces for various kind of operating environments and traffic networks. In this research, the relatively rapid methods "Whole Life Rail Model" (WLRM) and Shakedown Map were selected.

## 2.5  Using Tγ in the RCF and wear damage predictions

The Tγ approach was first put forward as a hypothesis in the year 1978 (Allen, 1978). The net tangential force of the wheelset and the work done in a contact was derived by using the torque balance on the wheels. According to this hypothesis, the net tangential force which was derived from the torque balance was equal to the force on the wheelset and it is the drag force which pulls vehicle to move forward direction. This force which is the Tγ was calculated from the sum of the products of the creepage and creep forces for the longitudinal, lateral and spin components. Therefore, the work done on a wheelset was equal to the distance multiplied by this tangential force.  It was assumed that the energy which led to this work must be dissipated in some form such as noise and/or heat, but it was argued that the majority of the energy would be released by wearing the wheel-rail contact surfaces. For this reason, the parameter Tγ is also called as Wear Number.

$$T\gamma = T_x\gamma_x + T_y\gamma_y + M_z w_z \qquad (2.23)$$

where $T_x$, $T_y$ and $\gamma_x, \gamma_y$ are the tangential creep forces and the corresponding creepages in the longitudinal and lateral directions respectively, and $M_z$ and $w_z$ are the spin moment and the corresponding spin creepage respectively.

Although the parameter was initially used to predict wear, it was later proposed that the energy generated in the contact patch could also result in a RCF damage and hence the WLRM was developed.

## 2.5.1 WLRM damage function

One of the well-known approaches used in the prediction of rail damage, particularly the initiation and location of RCF cracks, is the Whole Life Rail Model (WLRM). The model predicts the RCF damage severity and the interaction of wear on the crack development process (e.g. wear removes RCF damage), based on the increase in contact energy parameter Tγ. Therefore, the model describes the regions where wear would be the dominant mechanism and the regions where RCF damage would be more likely to accumulate. Figure 2.22 shows the development of WLRM Damage Function from the regions of RCF and Wear damage separately (Dembosky, 2004).
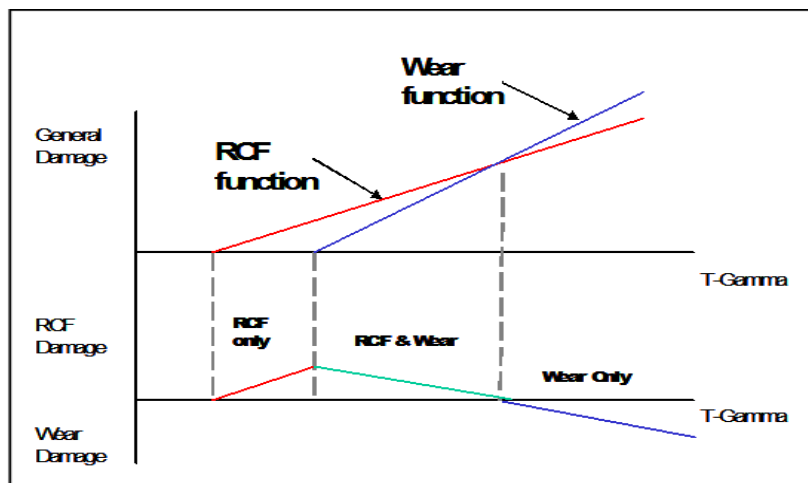


Figure 2.22: Combination of wear and RCF functions in the WLRM (Dembosky, 2004)

The WLRM was developed as a consequence of several studies that were conducted following the Hatfield Rail Accident in 2000. This accident played a crucial role in RCF studies, as the cause of the derailment was a broken rail that resulted from the propagation of head check defects. Although the cracks were observed and the rail replacement in the accident region had been scheduled, the cracks led to fracture before their removal (Grassie, 2005). To better understand the crack development mechanism and to support the manage and mitigation of the problem, RCF cracks at several sites on the GB railway network were investigated. These studies enabled a detailed understanding of crack patterns observed in the rails and the influence of track geometry, vehicle and traffic characteristics and contact conditions on the initiation and growth of the damage.

The data collected from the site investigations was considered in the development of the WLRM through the use of vehicle dynamics simulations. Several vehicle types, with different bogie and suspension characteristics, real track geometry conditions and various wheel and rail profiles were modelled to calculate the variations in Tγ. The values were correlated with the site observations to develop the WLRM damage function. This damage index generated from the developed damage function is a non-dimensional number which accumulates based on the number of cycles (or axle passes) given in the model.

In order to test and validate the WLRM, the model predictions were linked to the actual RCF conditions seen on site, particularly surface crack length, position and orientation (Burstow, 2004). Figure 2.23 which was one of the outputs of this study displays the comparisons of damage indices and surface crack lengths for left and right rails at tangent track site in the Ruscombe study site (UK). The largest surface crack lengths can be associated with the higher damage indices in several locations of the track. But, there are still places where the model could not accurately predict the RCF damage.
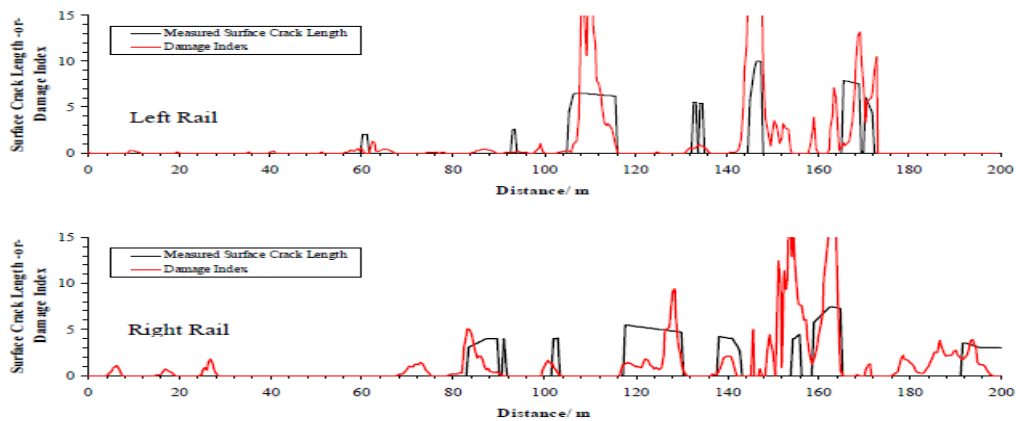


Figure 2.23: Comparison of damage index and surface crack length for left and right rails at Ruscombe study site (Burstow, 2004)

Following the site validation, several revisions to the WLRM damage function were implemented and the model took its final form as shown in Figure 2.24. The damage function is divided into three regions. In the low energy level, which is defined at a fatigue threshold of 15 J/m (N), the energy at the wheel-rail contact is insufficient to generate damage and therefore the predicted damage is zero. When this number is exceeded (first region), the model shows positive RCF damage index values which referred to as "RCF Only" type of damage and it reaches a peak damage value at 65 J/m (N). In the second region, which is defined as "RCF and Wear", the energy levels (> 65 J/m (N)) increase and wear begins to dominate but the wear is not sufficient to remove the initiated cracks entirely. In the third region where Tγ values become higher than wear/RCF balance point of 175 J/m (N), the predicted damage passes through zero to negative values. In this region, the wear rate dominates the cracks growth in the higher energy levels and the wear becomes sufficient to remove initiated cracks (Bevan, 2011).
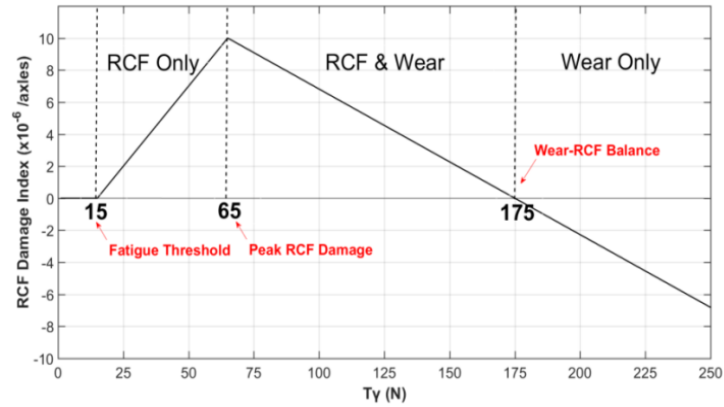
Figure 2.24: WLRM RCF damage function (Bevan, 2011)

It should be also noted that the Tγ in this model is also referred to as 'signed Tγ' which based on the assumption that RCF in rails is generated under only traction direction, while braking direction leads to wheel damage. It was shown during previous modelling studies and experiments that RCF cracks could continue to propagate under fluid effect when the longitudinal creep force was acting in a traction direction which is indicated by a force on the rail, opposite to the direction of travel and wheel's longitudinal creep as shown in Figure 2.25. Traction force at the wheel-rail contact moved over the crack and cause fluid (entrapment) inside the crack to apply pressure towards the tip. Thus, the model only considers the regions where the longitudinal force on the rail is opposite to the direction of traffic (on the wheel, similar direction to traffic) and predicts the damage based on its value. In the previous studies, the spin component of the Tγ was often neglected due to computational limitations during that time and it was assumed that its contribution would be very small. However, recent simulation tools can calculate this and studies have taken into account accordingly (Bevan, 2011; Dirks et al., 2015).
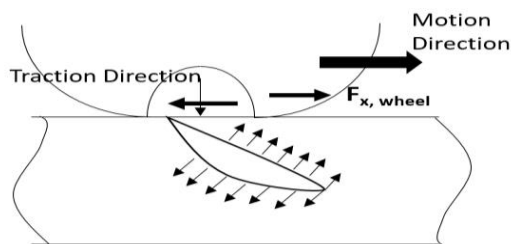


Figure 2.25: Influence of fluid on the crack propagation.

## 2.5.1.1 The assumptions in the WLRM RCF damage function and its previous applications

Although the current form of the WLRM was successfully applied and validated using real case studies to predict RCF damage, the model contains several assumptions which made it less accurate when it was implemented on routes with different characteristics to those used during the original validation of the model. These can be divided into three groups.

Firstly, the term Tγ is still a hypothesis suggesting the net tangential force rotating the wheelset was transformed into an energy causing RCF and wear at the wheel-rail surface by neglecting other outputs such as noise, heat and etc. The previous WLRM results provided good indications where the sites were more susceptible to RCF cracking. Quantification of Tγ at the contact patch correlated with the depth that ratchetting developed in the material. However, as the further propagation depended on factors such as fluid pressurisation (or entrapment), thermal and residual stresses, it was mentioned that it might become inapplicable to predict these phases. Therefore, some studies combined with crack growth models. One of the studies found that crack growth rate increases with the Tγ, but it was uncertain which conditions were leading to further extension after ratchetting. Similarly, the brick model showed a good correlation particularly for values of Tγ below 65 N. However, the higher Tγ values that showed a larger wear rate did not provide good agreement with the brick model and site conditions where a decrease in RCF initiation risk was not observed (Burstow, Fletcher, Franklin, & Kapoor, 2008).

Secondly, the previous works predominantly used VAMPIRE vehicle dynamics software in the WLRM computations. Although VAMPIRE is a very rapid simulation tool to provide creepages and creep forces for a wide range of different contact conditions, the calculated results were the global outputs of the wheel-rail contact. The usage of Hertzian theory and Kalker's pre-calculated look-up tables in the wheel-rail contact problem lowers the accuracy of results and do not show the distribution of forces (local output). These limitations are clarified in the Chapter 4 of this thesis.

Thirdly, the assumptions which were made in the development of WLRM can cause certain drawbacks. Firstly, due to use of "Signed Tγ", the WLRM gave reasonably good validation especially in respect to classic high rail RCF, but it often disregarded the low rail damage (Evans, Lee, & Hon, 2008). Therefore, the study suggested that the creep force angles between 0° and 90° may also cause RCF and Figure 2.26 was developed.

Since the WLRM was previously used and validated on the mainline routes of GB railway network, the breaking points (thresholds) of the model may require modification when considering different vehicle/track characteristics and operating conditions. When the longitudinal creep force direction of each contact on these mainline tracks was analysed, it can be seen that the flange contact is usually in the traction direction on the high rail. Thereby, the previous WLRM studies have mostly taken into account the signed Tγ values at the wheel flange/gauge corner contacts at the outer wheel of the leading axle. For instance, the high Tγ (>=175 N) generated at this contact was defined to be responsible for the side wear in rails (Burstow, 2006). However, the creep force directions and the Tγ might vary under different railway systems. In these conditions, the dominant wear

damage which can be occurred by the several aforementioned mechanisms might be observed as a result of smaller Tγ values. The study which compared the RCF and wear in high speed and heavy-haul lines showed that on the contrary to high speed lines where the wear volume was reduced and RCF damage became severe, the plastic deformation became critical with greater axle loads which increased the wear volume in the freight lines (Zhong, Hu, Shen, Wang, & Lius, 2011).
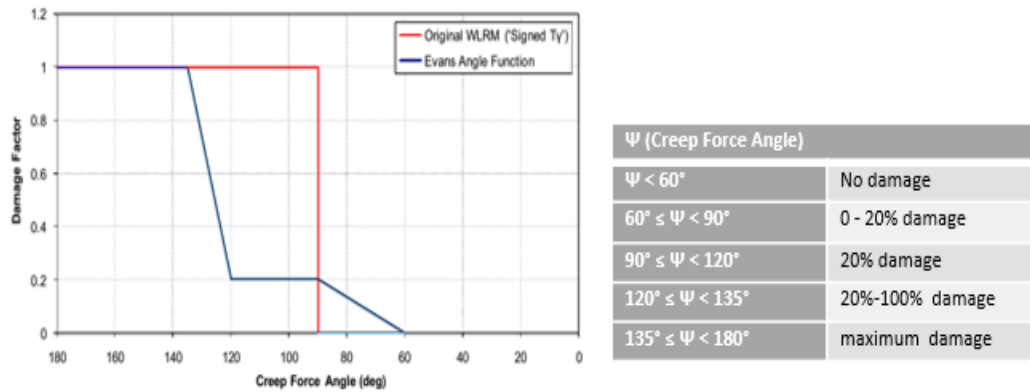


Figure 2.26: 'Signed Tγ" in the WLRM and Evans Angle Function (Bevan, 2011)

The WLRM was developed based on the performance of R260 rail material and high coefficient of friction (μ = 0.45) was selected since the actual friction conditions on track were unknown and it was decided to incorporate the worst case scenario into the model. Since IMs have recently tended to use harder steel grades and apply lubrication in critical track sections in order to manage RCF defects, the influence of using them should be further analysed and considered in the model. Regarding the use of alternative rail steels, the influence of material properties on the model was accounted theoretically. It was assumed that hardness of alternative steels can lead to different wear/RCF balance points on the model and the elongation parameter can provide an indication of peak damage and the first slope of the model ductility (Burstow, 2009). Figure 2.27 demonstrates the proposed WLRM damage function for alternative steels. However, it should be noted that the validation of these models has been in still in progress.
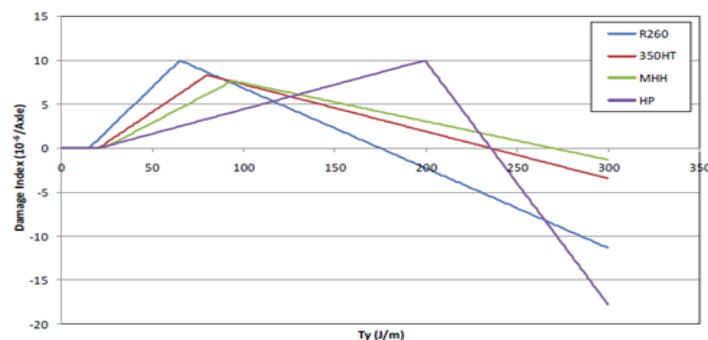


Figure 2.27: Proposed WLRM damage function for alternative rail steels (Burstow, 2009)

## 2.5.2  Wear predictions using Tγ and a different approach: Archard function

The Tγ was initially used in predicting wear. One of the earlier studies was performed using a laboratory rig and field measurements, aimed to provide a relationship between Tγ and wear damage for both rails and wheels. A large volume of wear data from the field was collated to find the wear rate and to establish a correlation between Tγ. The spin component in this study was initially neglected since, it was stated that its contribution to wear number was very small. As a result of full scale rig laboratory experiments, the following relationship was found which is as follows:

If Tγ < 200 N, Mild Wear

If Tγ > 200 N, Severe Wear                                                                (2.24)

The study calculated the wear rates for both rail and wheels which was expressed as a cross-sectional area loss of the rail produced by the passage of a certain number of vehicles. The results presented below were for rails only (McEwen & Harvey, 1986).

$$Tγ < 100 \text{ N, rail wear rate} = 5.0 \times Tγ \times 10^{-4} \quad mm^2/10^3 \text{ axles}$$

$$100 < Tγ < 200 \text{ N, rail wear rate} = 5.0 \times 10^{-2} \quad mm^2/10^3 \text{ axles}$$

$$Tγ > 200 \text{ N, rail wear rate} = (2.5 \times Tγ - 322) \times 10^{-3} \quad mm^2/10^3 \text{ axles}$$

$$\text{Lubricated Condition; rail wear rate} < 6.0 \times 10^{-3} \quad mm^2/10^3 \text{ axles} \qquad (2.25)$$

In the subsequent study, the laboratory results were validated using field data. The wear number predictions that were computed from curving program outputs compared with the measured wear rates from a wide variety of track locations. Although the correlation between Tγ and curvature was rather sparse particularly at sharper curves, this study showed that the mild wear rate prediction for the moderate/shallow curves was similar to laboratory results. The field measurements showed less severe wear rates than those seen in the laboratory experiments which stem from an application of lubrication in sharper curved tracks (Harvey & McEwen, 1986).

This model was later called the British Rail Research (BRR) Wear Function shown graphically in Figure 2.28 which demonstrates both the mild, transitional and severe wear rates. One of the first well-known studies that used this model's principle was to predict wear on wheels (Pearce & Sherratt, 1991). The predicted wheel profiles and the conicity vs distance plots calculated from vehicle dynamics simulations were compared to data obtained from long-running profile wear experiments. Although the route models in the analysis consisted of typical alignment sections (e.g. tangent and curved tracks), a relatively good agreement was achieved in the study.
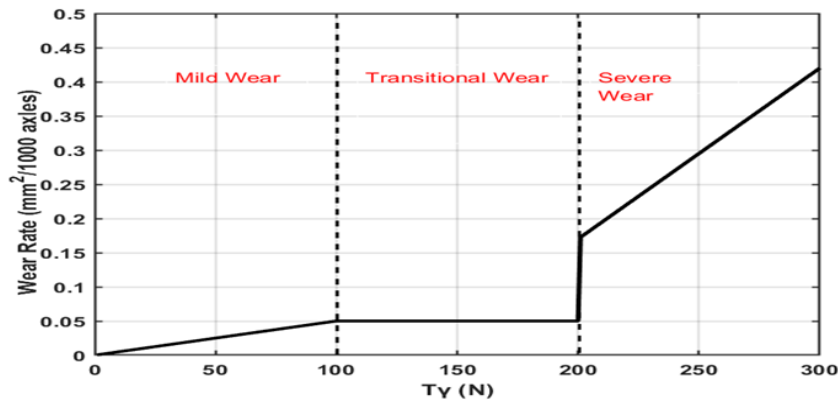
Figure 2.28: BRR wear function (McEwen & Harvey, 1986)

In the following years, this model has been adapted to include the Tγ/A parameter, where A is the nominal contact area. As it was mentioned previously, there are several kinds of wear mechanisms that are responsible for different wear rates in rails. In order to understand the influential factors, a large number of laboratory experiments have been carried out across several studies. It was mentioned that creep force, creepage and Hertzian contact area were the main parameters affecting the wear rates. A linear relationship was found between the wear rate (in terms of weight loss per unit nominal contact area in unit distance rolled) and the parameter Tγ/A (Bolton, Clayton, & McEwen, 1982). The successive study confirmed the relationship between wear rate and Tγ/A and conducted metallurgical examinations to analyse the specimens from the laboratory tests (Bolton & Clayton, 1984). There are three different types of wear rates. Whereas the type I wear rate was more related to surface oxidation and a metallic flake formation, the type II wear was characterised by the wider range of flake deformation and adhesive wear. In type III, a large volume of material loss was observed.

Figure 2.29 shows the results of the Tγ/A based wear model from the previous studies. It can be seen that the materials in different wear tests almost result in similar behaviour such as the increase in Tγ/A gave rise to higher wear rates (Lewis et al., 2010). In addition, it shows different wear rates; mild, severe and catastrophic for R8T and R7T wheel steels. The effect of different wear rates on both surface and subsurface was investigated and it was observed on the surface effects that while the oxidative wear occurred at low Tγ/A values, the ratchetting process became dominant as Tγ/A values increased in the experiments. Similarly, the observation of subsurface morphologies revealed that a larger amount of plastic deformation was generated at higher levels of Tγ/A. The further increase in Tγ/A values (catastrophic regime) led to the development of RCF cracks on the worn surfaces and the direction of them changes downwards to form larger cracks.

However, it was noticed in the further experiments' results that the sudden changes in wear rate were caused by the severity of loadings: normal load, sliding velocity or surface temperature. The wear rate followed a similar pattern with the creep curve in that the first

transition wear occurred at the transition point from partial slip to full slip. But, the temperature calculations for the contact demonstrated that the large increase in wear rates seen at the second wear transition might result from a thermally induced reduction in yield strength and other material properties.
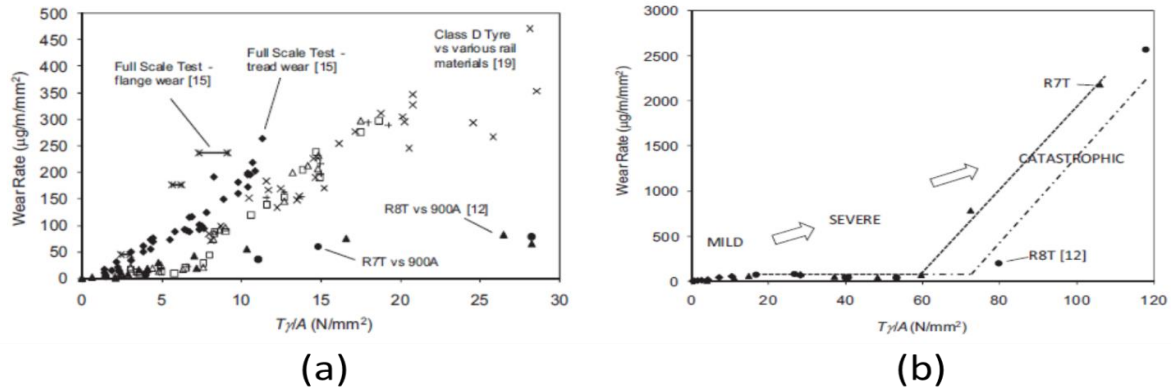


Figure 2.29: The Tγ/A wear model results from several studies (a) and the different wear regimes for R8T and R7T wheels (b) (Lewis et al., 2010)

Furthermore, it was mentioned that while the Tγ method helped to show the transitions in wear rates and could reflect the changes of other contact parameters such as pressure and slip by moving the values on the wear curve, it did not demonstrate their individual contributions on wear. In order to take into account, the mapping method was used which calculated the wear based on Archard's function. The volume of wear *V* is calculated from the following formula where *k* is a non-dimensional wear coefficient, *N* is the normal force, *s* is the sliding distance and *H* is the hardness of the softer material at the contact.

$$V_{wear} = k \frac{N*s}{H}$$
(2.26)

The wear coefficient *k* is found from the wear map based on the sliding velocity *v* and contact pressure *P*. The wear map demonstrated in Figure 2.30 was developed using a mixture of twin-disc and pin-on-disc testing methods using R7 wheel material and 900A grade rail material. It also shows the specific regions where tread and flange contacts generally occur. It was mentioned that while tread contacts located in the mild to severe wear regime, the flange contacts were in the severe to catastrophic regimes which matched with the field observations (Olofsson et al., 2013).

Despite a large number of studies being conducted, the wear transitions and rates defined in these models are valid only for dry conditions. The effect of different mechanisms and third body materials such as lubricants and water were not considered. Recently, twin-disc testing study was carried out to compare the wear characteristics under dry, water and grease lubricated conditions of R260 rail against R8T wheel material (Hardwick, Lewis, & Eadie, 2014). Figure 2.31 shows the Tγ/A results for these three conditions. It can be seen that the wear rates were considerably lower compared to dry case and it was stated that

higher energy levels were required to achieve the severe-catastrophic wear regimes for water and grease contacts. Nevertheless, much work are needed to establish new models.
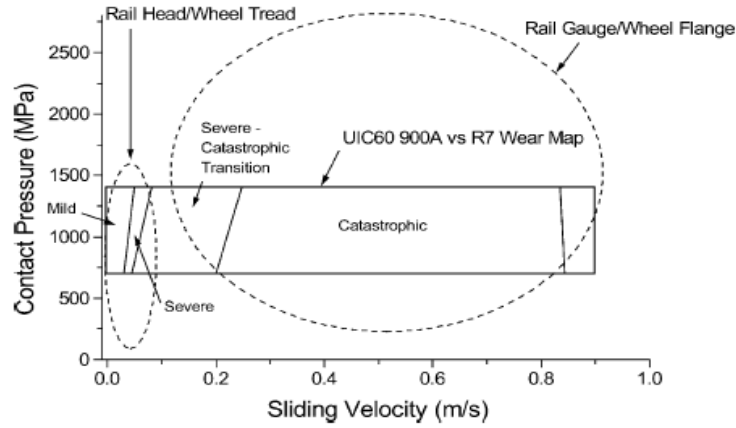


Figure 2.30: Rail steel wear map for UIC60 900A (Lewis & Olofsson, 2004)
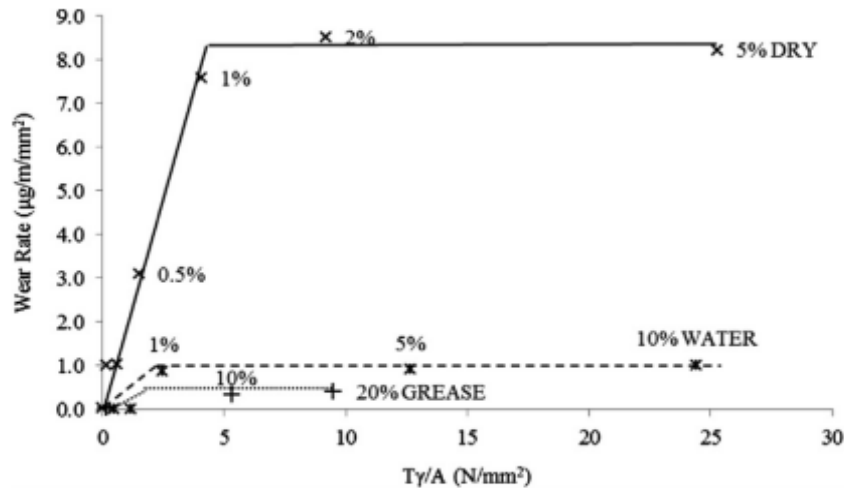


Figure 2.31: Wear rates at low Tγ/A values under dry, water and grease lubricated conditions for R260 rail against R8T wheel material (Hardwick et al., 2014)

## 2.6 Shakedown map

The Shakedown Map was developed based on different material responses explained in Chapter 2.2 for both line and point contacts. In order to model the ratchetting, the non-linear kinematic hardening law had been incorporated into a theory of elastic plastic rolling and sliding contact (Bower & Johnson, 1991).

### 2.6.1 Calculation of a rolling-sliding line contact

In the calculations of a line contact, an elastic cylinder with $R$ radius with an elastic perfectly plastic half space was assumed which is also shown in Figure 2.32.
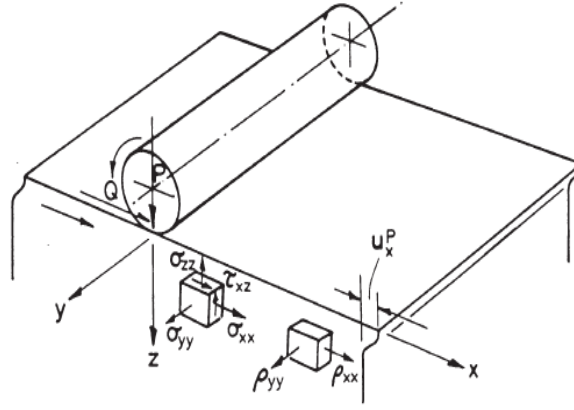
Figure 2.32: Rolling/Sliding contact of a cylinder with an elastic perfectly-plastic half space (Johnson, 1989)

The semi-width of contact a and the contact pressure *P* were calculated using the Hertzian principles Equations 2.14 and 2.15 which was previously introduced in Chapter 2.1. The elastic contact stresses $\sigma_{xx}$, $\sigma_{yy}$ and $\sigma_{zz}$ were given as (Johnson, 2000).:

$$\sigma_{xx} = -(\tfrac{P_0}{a})\{(a^2 - 2z^2)\sqrt{a^2 + z^2} - 2z\} \tag{2.27}$$

$$\sigma_{zz} = -(\tfrac{P_0}{a})\sqrt{(a^2 + z^2)} \tag{2.28}$$

$$\sigma_{yy} = \vartheta(\sigma_{xx} + \sigma_{zz}) \tag{2.29}$$

Since Oz is an axis of symmetry, the shear stress $\tau_{zx}$ equals to zero and hence, the principal stresses

$$\sigma_1 = \sigma_{xx} \tag{2.30}$$

$$\sigma_3 = \sigma_{zz} \tag{2.31}$$

$$\sigma_2 = \vartheta \, (\sigma_{xx} + \sigma_{zz}) \tag{2.32}$$

When these stresses were considered at the surface (*x=z=0*), the principal stresses became $\sigma_1 = \sigma_3 = -P_0$ and $\sigma_2 = -2\vartheta P_0$ and when they substituted into the Tresca criterion, yield occurred when $P_0$ reached the value $\sigma_y/(1 - 2\vartheta)$.

$$|\sigma_1 - \sigma_3| = |\sigma_{xx} - \sigma_{zz}| = \sigma_y = 2k \tag{2.33}$$

Thus, the principal shear stress $\tau_1 = 1/2(\sigma_1 - \sigma_2)$ has a maximum value of $0.30P_o$ at a depth of about $z = 0.78a$. This means that in the rolling condition of a line contact, yield will initiate at the point (0, 0.78) which is below the surface

$(P_0)_y = 1.67\sigma_y = 3.3k$ (Tresca criterion) $\quad (P_0)_y = 1.79\sigma_y = 3.1k$ (Von-Mises criterion) (2.34)

However, when residual stresses were introduced, it was expected the half-space to remain plain in rolling condition. Owing to this fact, they became independent of x and y directions $\rho_{xy} = \rho_{yz} = 0$ and $\rho_{zz} = \rho_{zx} = 0$. Thus, the $\rho_{xx}(z)$ and $\rho_{yy}(z)$ was stated to be vary only on the *z* direction.

To find the lower bound of the Shakedown Map, Melan's theorem was used and $\rho_{yy}(z)$ was selected to ensure that $(\sigma_{yy} + \rho_{yy})$ was the intermediate principal stress. In order to define the lower bound in which yield was not to be exceeded by the Tresca criterion:

$$(\sigma_1 - \sigma_3)^2 = \{(\sigma_{xx} + \rho_{xx}) - \sigma_{zz}\}^2 + 4\tau_{zx}^2 \leq 4k^2 \tag{2.35}$$

It was stated that this condition could be justified by taking $(\tau_{zx})_{max} = k$ and $\rho_{xx} = \sigma_{zz} - \sigma_{xx}$. In the elastic contact stress field, $(\tau_{zx})_{max} = 0.25P_0$ at $x = \pm0.87a$, $z = 0.5a$ provided the lower bound to the shakedown limit.

$$P_0^s \geq 4k \tag{2.36}$$

In the calculation of an upper bound, the Koiter's Theorem was used to demonstrate the effect of accumulation of plastic strains. The incremental plastic displacement ΔuP was assumed to generate under shear at a depth of h below the surface. The work by the elastic stresses was then computed as $\tau_{zx}$ΔuP and the plastic dissipation is kΔuP. By Koiter's theorem, the incremental collapse (ratchetting) will occur when

$$\tau_{zx}\Delta uP \geq k\Delta uP \tag{2.37}$$

Therefore, the optimum band to the shakedown limit was obtained by selecting $h = 0.5a$ at which $\tau_{zx}$ has its maximum value $0.25P_0$ which also corresponded to

$$P_0^s \leq 4k \tag{2.38}$$

When the upper and lower bound values were compared, it was apparent that they were both equal to $P_0^s = 4k$.

However, although the friction traction was not considered in the rolling contact, it was taken into account in the sliding contact which equals to

$$q(x) = \mu\, P_0\sqrt{1 - (x - a)^2}\;;\quad \mu \text{ is friction coefficient} \tag{2.39}$$

Under this condition, the combined effect of both pressure p(x) and q(x) should be taken into account. Contrary to rolling contact, the maximum value was slightly increased and located more close to the surface. At the surface, the stress state became hydrostatic due to normal pressure and there was no tendency to yield (except for the negligible plastic flow in the lateral direction). Therefore, only the stresses under frictional traction q(x) were considered:

$$\sigma_{xx}(x,0) = -2\mu x/a \qquad\qquad -a \leq x \leq a \tag{2.40}$$

$$\sigma_{yy}(x,0) = -2\vartheta\mu x/a \qquad\qquad -a \leq x \leq a \tag{2.41}$$

$$\sigma_{zz}(x,0) = 0 \qquad\qquad -a \leq x \leq a \tag{2.42}$$

$$\tau_{zx}(x,0) = -q(x) = -\mu P_0\sqrt{1 - \left(\tfrac{x}{a}\right)^2} \tag{2.43}$$

The principal shear stress $\tau_1(x,0)$ in the plane of deformation which is given by

$\tau_1(x, 0) = \frac{1}{2}(\sigma_3 - \sigma_1) = \frac{1}{2}\sqrt{(\sigma_{zz} - \sigma_{xx})^2 + 4\sigma_{zx}^2} = \mu P_0$. The results showed that the yield was initiated simultaneously at all the points in the contact surface $\tau_1 = k$,

$$(P_0)_y/k = 1/\mu \qquad (2.44)$$

Figure 2.33 was developed considering both rolling and sliding line contact. The Shakedown Map demonstrated that under sliding conditions, both the elastic and shakedown limits were equal which means that they are not dependent on the material hardening. In addition, it showed that at μ=0.25, the critical stress moved from subsurface to surface.
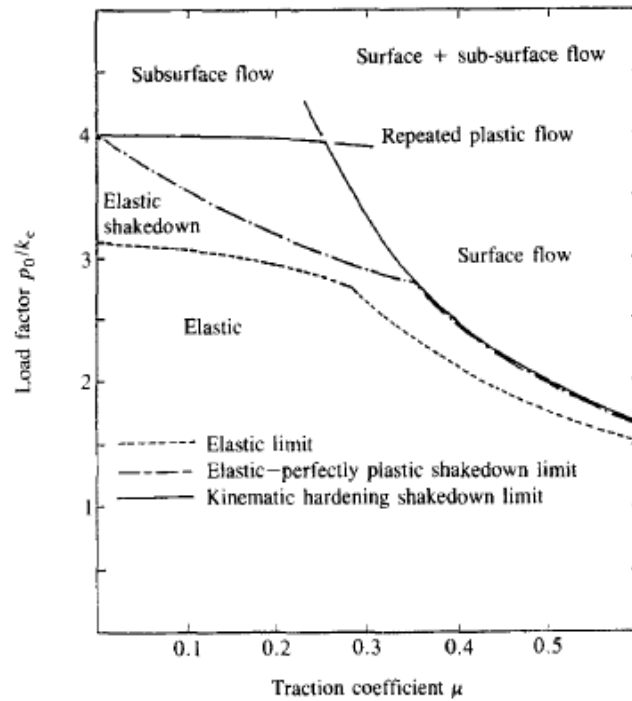


Figure 2.33: Shakedown Map in a line contact for a perfectly plastic and kinematic hardening material (Johnson, 1989)

The presented shakedown theory in the above assumed that full slip takes place between the cylinder and half-space. However, under partial-slip condition which means when the traction coefficient (T/N) is lower than the friction μ (mostly occurred in the dry conditions), the lines displayed in the Shakedown Map changes. Whereas for low friction, there were less differences between the partial and full-slip, a higher impact on the maximum shear stress was calculated for higher friction (Bower & Johnson, 1991). Figure 2.34 shows the Shakedown Map with partial slip. It can be concluded that the partial slip lowered the shakedown limits and hence made these contacts became more damaging. Moreover, the effect of kinematic hardening on low values of μ demonstrated that it had a crucial role in finding the yield limit under subsurface stresses.
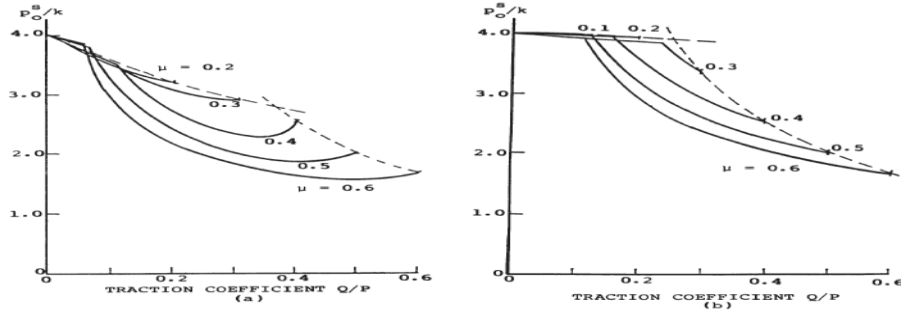
Figure 2.34: Shakedown Maps with partial slip: a)Elastic-perfect-plastic b)Kinematic hardening (Johnson, 1990)

## 2.6.2 Calculation of a rolling-sliding point contact

To find the shakedown limits for rolling and sliding point contacts, the Hertzian contact pressure was again used which is calculated from Equation 2.10. Under sliding conditions (Ponter, Hearle, & Johnson, 1985);

$$q(x,y) = \mu P_0 \sqrt{1 - \left(\frac{x}{a}\right)^2 - \left(\frac{y}{b}\right)^2} \tag{2.45}$$

It was stated that the calculations were more difficult for point contacts than line contacts since six components of residual stresses should be considered in the analysis which is displayed in Figure 2.35. Whereas a complete surface layer of uniform depth was displayed relative to the subsurface in line contacts, only material close to the contact area was displaced and left underformed material on either side of the track in point contact case.
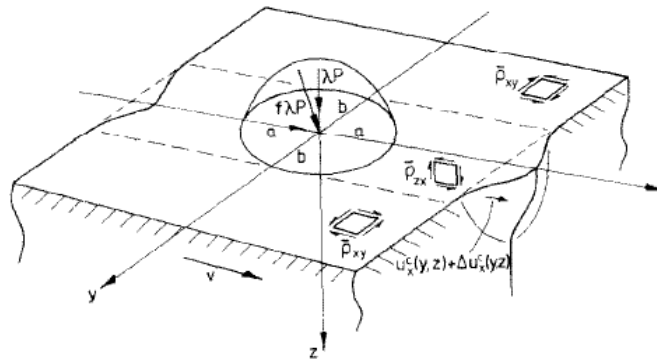


Figure 2.35: Rolling/Sliding contact of a point with an elastic perfectly-plastic half space (Ponter et al., 1985)

The displacement field caused to a self-equilibrating system of residual stresses $\rho_{xy}(y,z)$ and $\rho_{yz}(y,z)$. It was mentioned that this difference in point contacts led to two types of plastic deformation:

1) The incremental growth of plastic deformation as it was previously called as ratchetting.

2) A repeated closed cycle of alternating plasticity took place which generated beneath the surface with no incremental growth. This state was called as plastic shakedown.

63

Figure 2.36 demonstrates the shakedown limits for point contacts. While the y-axis is the load factor with represented by $\lambda P_0/k$ ($\lambda$ is the shape factor), the x-axis is the traction coefficient given represented as $f$, $\mu$ or $T/N$ in the literature.

$$\lambda P_0 / k = \frac{3F_N}{2\pi abk} \tag{2.46}$$

$$f = \mu = \frac{T}{N} = \sqrt{F_{lat} + F_{long}} \Big/ F_N \tag{2.47}$$

where $F_{lat}$ is the lateral tangential force, $F_{long}$ is the longitudinal tangential force *and* $F_N$ is the normal load. In this case, it was stated that when the traction coefficient exceeded 0.3, yield initiated at the surface.
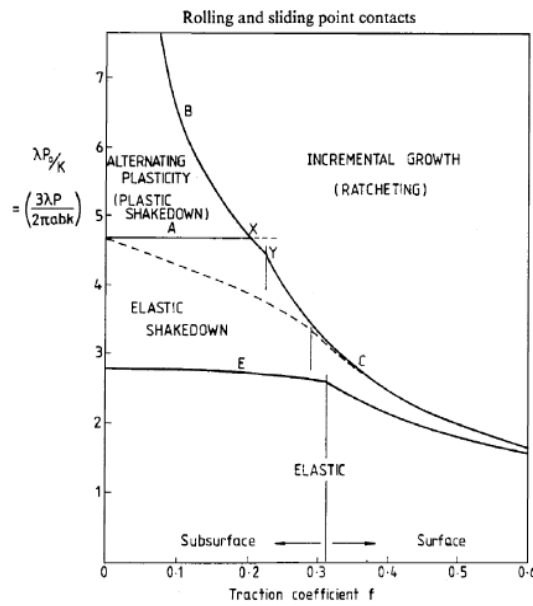


Figure 2.36: Shakedown Map on a circular (point) contact (Ponter et al., 1985)

The plastic shakedown was located between the curves A and B in Figure 2.36. As it was previously mentioned, a fully contained enclave of material below the surface encountered a closed cycle of plastic strain, but the surrounding undeforming material prevented the progressive strain growth. Regarding the ratchetting limit, it was found that the point contact at the surface was subjected to the same-damaging non-proportional cycle of stress as it was experienced in line contacts. The X and Y were found as 0.203 and 0.227, relatively. Also, the dashed line represents the shakedown limit calculated by considering the aforementioned Melan's theorem which applied for line contact.

Furthermore, it was mentioned that the given Shakedown Map was applicable for particularly point contacts which have larger lateral width than its longitudinal semi axis ($b \geq a$) and circular contact ($a=b$). In order to address this issue, the effect of different ellipticity levels ($a/b$) was investigated (Ponter, Chen, Ciavarella, & Specchia, 2006). Figure 2.37 shows that the shakedown limit monotonically decreased with b/a. It was found that the *b/a=4* was closest to the line contact. Although there were larger variations

observed between the different ellipticity levels under low traction coefficient values, the shakedown limit became almost similar at *μ=0.4*.
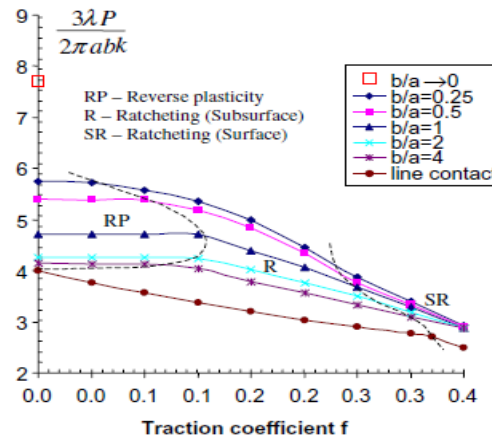


Figure 2.37: Shakedown Map for point contact with different ellipticity levels (Ponter et al., 2006)

It should be noted that a different type of material response takes place under repetitive load passages. Even though some passages will exceed the shakedown limit and cause plastic deformation to accumulate, the other passages as well as the surface displacement resulting from this previous exceedance might affect the shakedown limit. These potential modifications in the shakedown limit either lead material to a reversion to a shakedown state or continue to increase ratchetting.

## 2.6.3 The assumptions in the Shakedown Map and its previous applications

The Shakedown Map and ratchetting limit are an efficient method to define the material's response to the applied forces and provides an indication of the propensity to generate surface and sub-surface damage. But, the model was developed based on certain theoretical assumptions:

1) Hertzian contact theory: Although it has certain assumptions which were detailed in the Chapter 2.1, the Shakedown Map extended the Hertzian contact theory by including the inelastic material response and rolling friction (Ringsberg, 2001).
2) The sliding contact case was in full slip and the effect of partial-slip condition was mainly neglected. Nevertheless, while partial slip condition showed a higher influence on line contacts, it showed a lesser effect on point contacts (Dirks & Enblom, 2011).
3) It was mainly applicable for particularly point contacts which have larger lateral width than its longitudinal semi axis (*b≥a*) and circular contact (*a=b*).

In one of the earlier studies, Beagley (1976) linked the transition between mild and severe wear by the help of the Shakedown Map. It was stated that the traction coefficient of 0.32

played a crucial role as it was indicated as the transition point from subsurface to surface deformation. On lubricated surfaces, the T/N was less than 0.32 and hence the maximum shear stress occurred below the surface. Additionally, the wear was experienced particularly under high contact stresses and it became more critical than cracks as it was often encountered at the rail flange contact in rail traffic operations.

Another study used the Shakedown Map to determine the failure mechanism and the related RCF prediction model for different type of material responses. When the material is below the elastic shakedown limit, the failure would occur eventually by high cycle fatigue (HCF) mechanism. As it was expected, no cracks were initiated for the simulated magnitudes of contact pressure and friction coefficient. However, if it was above this limit and inside the plastic shakedown limit, the material was defined to be failed by Low Cycle Fatigue (LCF). In this regime, lower number of cycles were generated to initiate crack development than HCF. The model results for the ratchetting mechanism showed the severity of this regime since the cracks were generated at the lowest number of cycles (Ringsberg, Loo-Morrey, Josefson, Kapoor, & Beynon, 2000). In the subsequent study, the site observations revealed that the large shear deformations of the material microstructure in the zone of head checks occurred as a consequence of both ratchetting and LCS mechanisms. The HCF produced less visible damage on the surface of damaged rails (Ringsberg, 2001).
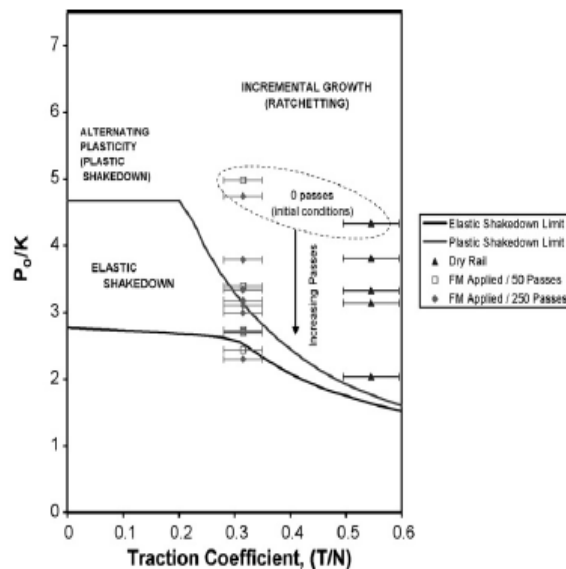


Figure 2.38: Shakedown Map for dry and FM conditions (Eadie et al., 2008)

A more recent study demonstrated the effect of friction modifiers (FM) on the rail damage by using the Shakedown Map. As it is presented in Figure 2.38, the dry conditions led to more severe deformations (ratchetting) than the FM conditions. While the ratchetting mechanism gave rise to wear and head check crack formation, the FM applications delayed the onset of head checking (Eadie et al., 2008).

One of the well-known applications of the shakedown theory is the Surface Fatigue Index (FI$_{surf}$). It was calculated from the horizontal projection of the shortest distance between contact points and the ratchetting limit. (Ekberg, Kabo, & Andersson, 2001). As the equation of the boundary curve for surface flow (ratchetting) in the Shakedown Map is

$$v = \frac{1}{f} = \frac{1}{T/N}$$
(2.48)

Then, the surface fatigue index becomes;

$$FI_{surf} = f - \frac{1}{v} = f - \frac{2\pi abk}{3F_N}$$
(2.49)

Previous studies were conducted to validate this model using twin-disc and full-scale testing. It can be seen in Figure 2.39 that the RCF was predicted for all the test conditions with the exception of wet twin-disc cases in which the (FI$_{surf}$) value was given as negative. During the experiments, the higher FI$_{surf}$ values led to early crack initiation. However, it was stated that the further detection of cracks was not reliable as the wear removed the initiated cracks. It should be noted that the FI$_{surf}$ was applicable for surface initiated damage, another parameter the surface fatigue index FI$_{sub}$ was also developed in which the cracks were assumed to initiate at depths approximately 3 mm from the surface (Ekberg, Åkesson, & Kabo, 2014).
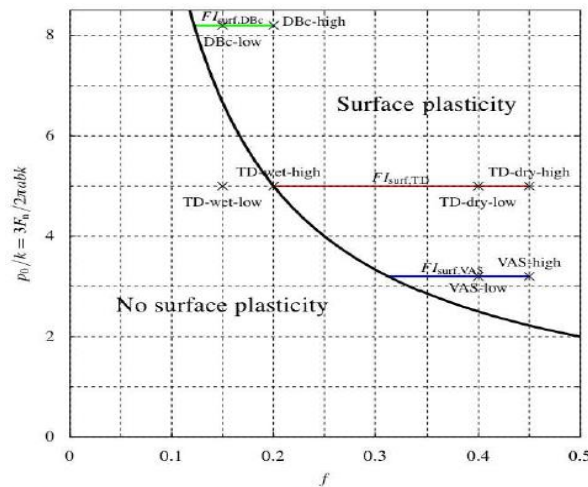


Figure 2.39: The surface fatigue index (*FI$_{surf}$*) results for the studied test conditions (Innotrack, 2009b)

FI$_{surf}$ and WLRM predictions were compared in a number of studies. One of the studies stated that the damage index provided a better correlation to the reality than the FI$_{surf}$, as it underestimated some of the damage (Stichel, Mohr, Ågren, & Enblom, 2008). In tighter curves, the damage index became negative showing the larger wear rate over crack initiation but, in these areas, the FI$_{surf}$, had the highest values (more distant to ratchetting limit). It was later stated that although the FI$_{surf}$ might underestimate the RCF prediction for high creepages due to limitation of traction coefficient values by the maximum friction coefficient, the damage index might overestimate as it was previously observed in the laboratory experiments that for high creepages (> 5%), the RCF life was unaffected by creepage.

Recently, new models: Stress Index (SI) and Energy Index (EI) have been developed by incorporating the longitudinal and lateral shear stresses to these models (Dirks, Enblom, Ekberg, & Berg, 2015).

$$SI = \sqrt{\tau_{zx}(x,y)^2 + \tau_{zy}(x,y)^2} - k \qquad (2.50)$$

$$EI(x,y) = \tau_{zx}(x,y) * \left(\gamma_x - (\varphi * y)\right) + \tau_{zy}(x,y) * \left(\gamma_y + (\varphi * x)\right) \qquad (2.51)$$

where $\tau_{zx}(x,y)$ and $\tau_{zy}(x,y)$ are respectively the longitudinal and lateral shear stresses in the cell element of $x$ and $y$ directions. $\gamma_x, \gamma_y$ are the creepages and $\varphi$ is the spin moment. These new models were also extended by the crack propagation model in order to predict crack depth for small crack sizes. In the study, the model results were correlated with measured crack depths and surface crack lengths on a curve of the Dutch railways. It was found that while EI provided better predictions regarding crack depth estimations, the SI was superior in surface length. Nonetheless, it was mentioned that further validation was required considering a range of operational conditions as the models were only applied on a single curve.

## 2.7 Conclusions and discussions

In this chapter, the definition of RCF, wear and the interaction between these two damage mechanisms are given. In order to manage RCF crack growth and to reduce the risk of rail failure, it was noted that the further processes of both of the damages should be predicted since, wear (as well as grinding) can truncate the size of existing cracks. However, to understand these damaging conditions better in rails and to increase the accuracy of current prediction models, it was suggested that reliable and sufficient field monitoring defect data is essential. Therefore, current inspection methods and NDT techniques are also provided in the chapter with their strength and limitations.

The crack data acquired by the MRX-RSCM rail inspection device was selected for use in this research due to its novelty in crack depth measurement. Although it provided satisfactory results in certain studies, further validation studies revealed that it over-predicted the crack depths. In order to overcome these problems and increase the reliability of field crack data in the research, several measures were taken which are detailed in Chapters 3 and 8.

Additionally, the current RCF and wear damage prediction models are summarised along with their benefits and assumptions. When the influential mechanisms in crack development as well as wear were reviewed, it was noticed that there are several factors affecting damage in rails. Nevertheless, plastic deformation accumulation (including uni-directional strain; ratchetting) is commonly responsible. The existing detailed RCF crack growth models mainly utilised FE modelling which provided the opportunity to build 2D/3D

contact-crack models. However, even though this helps to understand comprehensively the changes in stresses and find the crack growth rates under the effect of several factors such as different fluid mechanisms, it requires high computational times to solve a number of cases. In addition, certain parameters of an initiated crack (e.g. size, shape and orientation) should be pre-defined. Therefore, when the damage predictions over long distances such as London Underground were considered, this modelling technique becomes impractical to apply and investigate a wide range of operating conditions with changing traffic, track geometry characteristics and wheel-rail profiles.

The two common approaches used in the prediction of damage initiation and location are the WLRM and Shakedown Map. Both of them can be used in combination with vehicle dynamics simulations and by the help of these tools, it is possible to efficiently calculate different wheel-rail contact parameters and inputs of these models: $T\gamma$, T/N and load factor (contact stress) for numerous operating conditions. Although they provided satisfactory results in previous studies and validated using laboratory testing and field observations, they contain certain assumptions (as clarified in Chapters 2.5.1.1 and 2.6.3) and the accuracy of estimations were sometimes reduced. Both of the models predict the RCF damage based on plastic deformation accumulation. However, while the Shakedown Map gives an indication of its severity and may only be used for qualitative analysis, the energy term can be quantified in the WLRM to show the incremental plastic deformation. Nevertheless, due to effect of several factors on further crack propagation such as fluid, thermal and residual stresses, it was previously mentioned that the WLRM should be used in combination with crack growth rate models (in longer crack depths).

A number of studies were conducted to compare damage index and $FI_{surf}$. It was concluded that the $FI_{surf}$ might underestimate the damage due to limitation of traction coefficient values by the maximum friction coefficient (as it often predicted the RCF under dry conditions) whereas, the damage index might overestimate since, the high creepages did not always lead to increased RCF risk. In addition, the higher $FI_{surf}$ values did not have a good correlation with the negative damage index, as wear removed the initiated cracks.

Moreover, the input parameter of the WLRM: $T\gamma$ (and $T\gamma/A$) was also used in the wear rate predictions. It was observed that the ratchetting process became dominant as $T\gamma/A$ increased but its further increase led to the development of RCF cracks on worn surfaces. In the later studies, it was mentioned that the energy parameter was not individually considered the influence of other contact parameters in wear rates and hence, the Archard's function that considers the contact stress and sliding velocity have been started to utilise in wear damage prediction studies. However, it should be noted that the wear transitions and rates defined in these models are valid only for dry conditions. Although

recent testing studies were carried out considering third body materials, much work is required to establish new models.

In the light of all the facts mentioned above, the research initially used WLRM in the RCF damage predictions. The assumptions and deficiencies of the WLRM particularly, the 'signed Tγ' were addressed and tried to improve in the study. For instance, one of the key issues that while the WLRM has been used at a number of sites in the mainlines of GB network, it has not been tested on routes with different characteristics such as metro-underground systems. Owing to changes in vehicle and track characteristics on London Underground network, it was suggested that the model may require modifications. Additionally, the Shakedown Map parameters were also taken into account in the subsequent steps of the research.

Furthermore, the literature review demonstrated that even though crack depth is a key parameter in the crack severity, previous laboratory test findings and model results were primarily used in the validation of crack growth rate prediction studies and surface observations were largely used in the WLRM studies. A conversion factor (aspect ratio) has been recently applied to estimate the crack depth. However, as it can be expected from the complex crack growth behaviour, a single aspect ratio might produce inaccurate predictions for every crack (Burstow, 2004). Therefore, contrary to previous studies, this research suggested to use MRX-RSCM crack depth measurements in the model validation. Although it might be unsuitable to correlate the contact surface energy term Tγ with crack depth, the research used this parameter to accumulate damage rate between different sets of measurements.

# Chapter 3   Site Selection and Field Crack Data Analysis

During the development and validation of RCF damage prediction models, it is important to observe the development of cracks in the field. Since the research aimed to quantify the growth of RCF cracks, the availability of repeatable rail inspection data played a key role in the site selection. In addition, it was also necessary to have reliable data to describe the infrastructure and vehicle characteristics such as: track geometry, vehicle configuration, wheel-rail profiles and traffic conditions.

London Underground (LUL) currently uses various NDT methods to inspect the condition of the railhead in order to optimise their maintenance methods (Vickerstaff, 2015, 2016). Owing to the opportunity of significant volumes of field data and consecutive MRX-RSCM crack depth measurements, two lines from the LUL network were selected for detailed investigation in the research. LUL provided the field defect data for these selected lines along with the profile and track geometry measurements and the maintenance history information including the rail replacement dates and track lubricator positions.

In this chapter, the operating and track conditions of the two lines are initially described and the problems which were mentioned in the previous LUL and other metro-underground systems studies are summarised.

Furthermore, the chapter includes a detailed review of rail inspection data. The field defect was analysed to find the dominant damage mechanisms and the critical track sections. In addition, several correlations were made with the track data to identify the influential factors promoting RCF crack growth in the selected lines.

## 3.1  London Underground

London Underground is the oldest and one of the busiest metro railway networks in the world. It carried nearly 1.5 billion passengers in 2015. Its history dates back to 1863 when the world's first underground railway, the Metropolitan line, was opened to service from Paddington to Farringdon (TfL, 2017).

The population growth and rapid development have led the city to expand its metro network over the years. Currently, it consists of 11 lines with 270 stations. In order to provide an efficient service to this high traffic demand, LUL has been carrying out major repairs to the rolling stock and upgrading systems. For instance, new automatic signalling systems were installed in some of the lines to allow Automatic Train Operation (ATO). However, previous studies conducted on metro-underground systems (given in the next

section of this chapter) and from discussions held with LUL demonstrated that the change of driving mode (from manual to ATO mode) increased the number of RCF cracks on the lines. To investigate this effect on RCF cracks, which results in higher traction/braking forces, two lines were selected in the research with one operated under manual mode (Bakerloo line) and the other under ATO mode (Jubilee line).

### 3.1.1 Bakerloo line

The Bakerloo line was originally named by the combination of Baker Street and Waterloo Railway Line and opened to service in 1906. Throughout the years, the line has gone through a number of changes and is now made up of 25 stations and a total length of approximately 23.2 km, as illustrated in Figure 3.1. The line includes a mixture of deep tube (Queen's Park to Elephant & Castle) and surface running sections which are solely operated by the Mk II 1972 Stock trains.
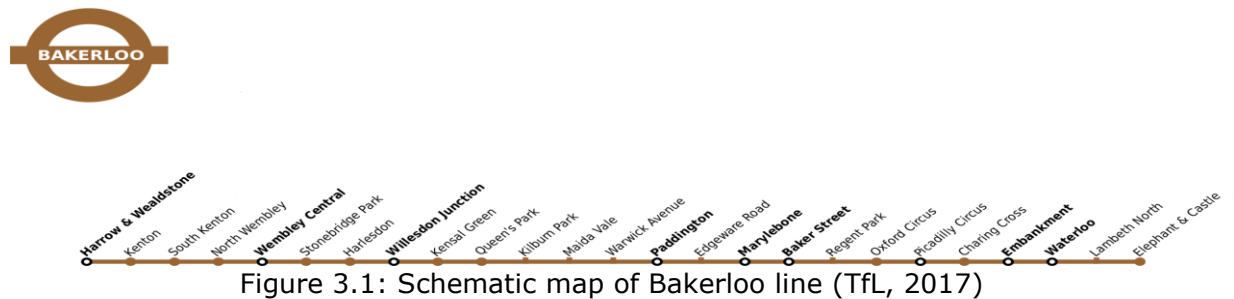


Figure 3.1: Schematic map of Bakerloo line (TfL, 2017)

Bakerloo line is declared to be ninth busiest line in the entire network (Hopkinson, 2016). Figure 3.2 shows the annual tonnage levels for the Bakerloo Southbound (SB) line defined in Million Gross Tonnes (MGT) and Total MGT, which includes the passenger loading. It can be seen that the busiest section of the line is between Marylebone and Oxford Circus Stations. Also, Figure 3.2 defines the Track Loading parameter which classifies each track section according to its maintenance priority level and usage and is calculated as follows:

$$L = (TV^2)/1000 \qquad\qquad (3.1)$$

where L is the track loading, T is the total MGT (tonnes) and V is the permitted speed (mph).

Table 3.1: Classification per track loading on LUL

| Track Loading | Classification |
|---|---|
| L>60 | A* |
| 30<L<60 | A |
| 15<L<60 | B |
| L<15 | C |
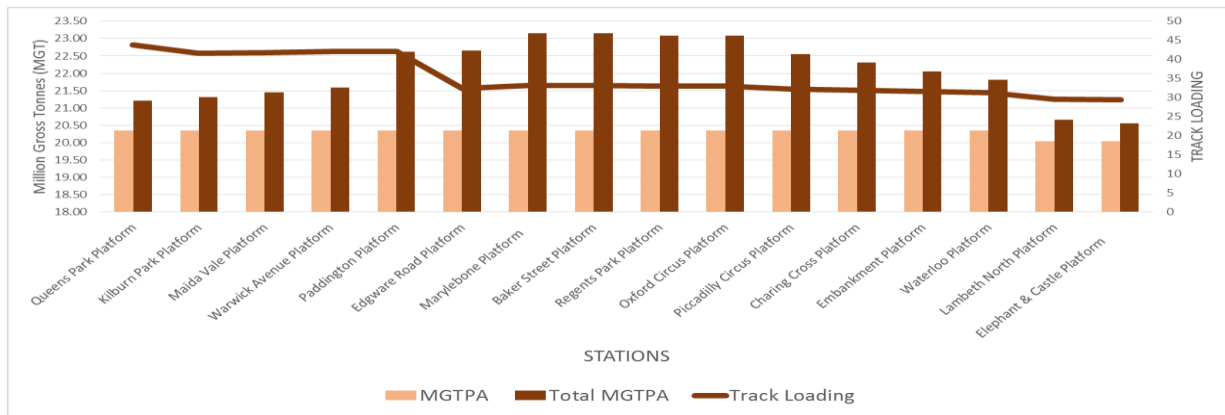
Figure 3.2: Track tonnage levels in Bakerloo Southbound line

The tunnel cross section is a deep bored cylindrical cast iron tunnel with a single track which has an internal radius of about 1.83 m and the tracks are constructed of conventional LUL type which is non-ballasted concrete slab track with bull-head (BS 95lb) rail supported on hard wood sleeper by cast iron chairs spaced at 0.95 m intervals (Chatterjee et al., 2003). Recently, flat bottom CEN 56E1 rails have also been installed in several sections of the line. Due to old trackwork, infrastructure and insufficient tunnel clearance, the maximum running speed ranges between 45 km/h and 55 km/h. As mentioned, the Bakerloo line is currently operated under manual mode and therefore this has reduced permitted speed levels. However, the distance between the stations is short, with a mean distance of only 400 m.

The track geometry on the Bakerloo line consists of sharp curves with a minimum curve radius of 85 m. Check rails are installed on curves for radius smaller than 200 m. As it can be seen in Figure 3.3, check rails were located to the inside of low rails in these curves. When the track gauge is at nominal distance (1435 mm), the flangeway clearance between low rail and check rail becomes 47 mm. The purpose of a check rail on these sharp curves is mainly to reduce the risk of flange climb derailment and failure of track components by distributing the lateral wheel-rail forces.
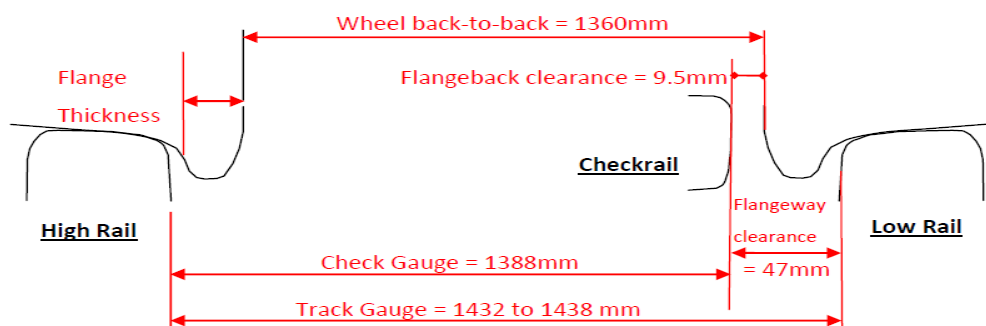


Figure 3.3: Nominal track system dimensions including check rail positions

In the Bakerloo line, the station platforms are also generally located in these check-railed curves. Figure 3.4 shows the Waterloo station which has a curved platform. The actual

73

cant level is mainly affected by the curve radius, but also the location of the curves in relation to the platforms. In the majority of cases, a cant of 100 – 120 mm is implemented, but is increased to 150 mm for a 125 m curve radius. The low running speeds and the high actual cant values decrease the level of cant deficiency to 10 – 50 mm. In some sections, cant excess is also present on the line.


Figure 3.4: The curved platform in the Waterloo station

The section between Elephant & Castle and Queen's Park is managed by Transport for London (TfL) and the remaining sections are under the control of Network Rail (NR) therefore, the aforementioned 11 km-long track section was modelled in this research.

### 3.1.2 Jubilee line

To reduce congestion on the Metropolitan and Bakerloo Lines, the Jubilee Line was opened to operation in 1979. Later, the Jubilee Line Extension (JLE) was proposed and construction started in 1993. This project  connected the section from Green Park to Stratford in 1999 (Mitchell, 2003). The final configuration of the line is presented in Figure 3.5.


Figure 3.5: Schematic map of Jubilee line (Tfl, 2016)

The total length of the Jubilee line, including the JLE, is approximately 36.5 km and 13 of the 27 stations are underground stations. The majority of the line runs over-ground, the middle section is located under the ground level between the surface tracks. From Stanmore to Finchley Road, the tracks are ballasted tracks and run parallel to Metropolitan line between Finchley Road and Wembley Park. Then, the line enters the tunnel section before Finchley Road station and exits before reaching Canning Town station. The tunnel sections are mainly divided into two sections: while, the old section has conventional LUL type of tracks (as aforementioned in the Bakerloo line), the JLE extension was constructed with a low vibration slab track system as illustrated in Figure 3.6. The ballasted tracks with

concrete sleepers were implemented from Canning Town to Stratford where the Jubilee Line runs parallel to Docklands Light Railway (DLR). Similar to Bakerloo line, two types of rail profiles were installed, but the CEN 56E1 are predominantly used in the JLE section. At the beginning of the operation, the 1972 Tube Stock trains were utilised. This stock was later replaced by 1983 and 1996 Stock trains, respectively. Although the 1996 Stock was delivered as six-car train sets, a seventh car was added to all of the trains in 2005.



Figure 3.6: Track super-structure in Jubilee Line Extension (Mitchell, 2003)

The Jubilee line is operated under ATO mode with a maximum running speed of 90 km/h in several locations. The line carries a high volume of passengers and it is pronounced to be the third busiest line in London Underground network (Hopkinson, 2016) with an annual average track tonnage of 29 MGT, compared to 22 MGT on the Bakerloo line. The changes in track tonnage are shown in Figure 3.7, which illustrates that the highest total tonnage takes place between Westminster and Canary Wharf section.
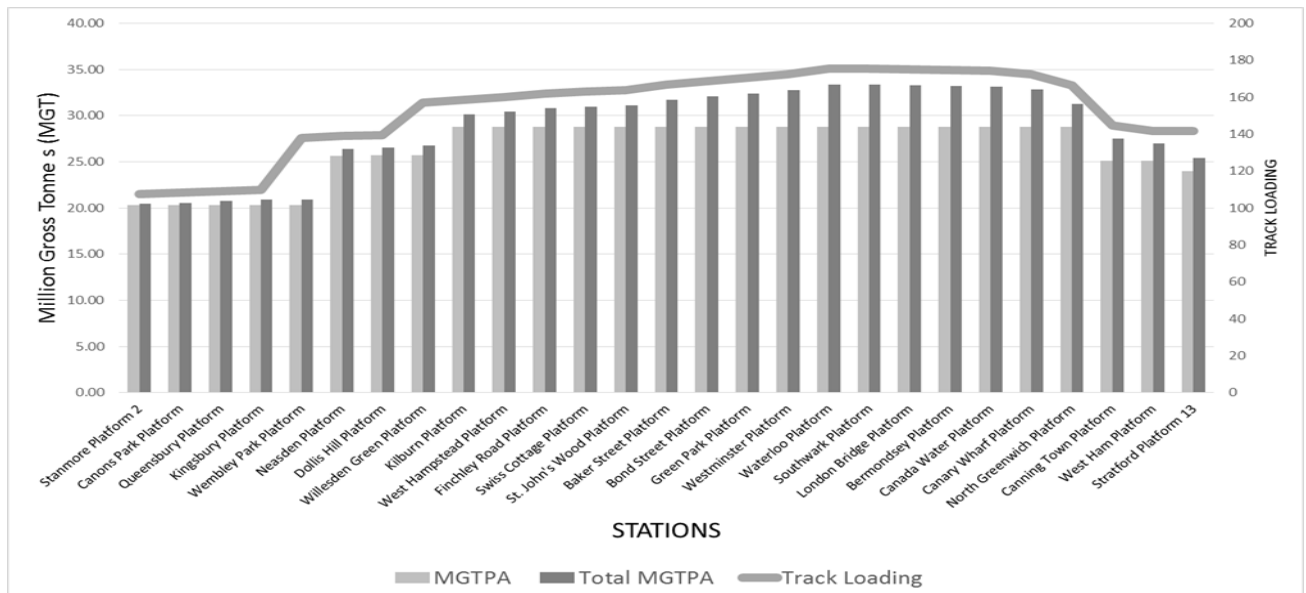


Figure 3.7: The track tonnage levels in Jubilee Southbound line

The Jubilee line also has curvaceous track geometry but, it has a higher minimum curve radius of 250 m. Therefore, checks rails are not required for this line and most of the

platforms are located on straight sections of track. The actual cant value varies along the line, but due to increased running speeds the cant deficiency becomes higher and reaches a maximum of 80 – 85 mm in the JLE section.

## 3.2 RCF cracking in metro-underground systems and London Underground

The public expectation from the rail mass transit is significantly demanding; the railways should provide a reliable, comfortable, safe and un-interrupted service. However, these requirements put a huge demand on the performance of the wheel-rail interface and make the damage prediction and preventive maintenance crucial. A study of RCF cracks on the German (DB) rail network pointed out a significant difference between the mainline and metro systems. Heyder et al. (2014) stated that the uniform loading generated by a homogenous fleet of vehicles produced stresses concentrated within a narrow contact region (running band) on railhead and this led to rapid crack growth in suburban rapid transit systems which was also responsible for the early crack initiation in these lines.

The study which was undertaken at Vienna Underground stated that the track tonnage in metro lines were in the same range as conventional main railway lines (Valenta, Varga, & Loibnegger, 2013). It was concluded that the susceptibility of RCF cracking in rails did not depend solely on track tonnage, axle-load and speed; rail material, wheel profile and vehicle characteristics also played a key role.

Another study in the Vienna Underground investigated the so-called "surface break-out" type defects which generally occurred in curved track sections. But, in this case, those were located in curved tracks just before the stations. This is where the metro trains severely decelerate and hence the forces increased on the outer rail of the track (Fischmeister et al., 2009). The study also mentioned that when the rails were subjected to homogeneous traffic, they showed uniform crack spacings and generated regular RCF crack growth patterns.

Similarly, a study which analysed the RCF cracks in Attiko Metro in Athens through non-destructive evaluation and metallographic sectioning found that the larger number of cracks were observed in the curve sections as well as braking sections before the stations. These cracks had a depth of approximately 4 mm, but the crack subsurface lengths were varied between 20 and 50 mm stemming from the various crack initiation angles (Haidemenopoulos et al., 2006).

The earlier investigations conducted for LUL confirmed some of the aforementioned findings and suggested some critical points. It was revealed that the severity of the cracking substantially increased when a new rolling stock was introduced on the lines (Scott, 2009). When the rail profile measurements were analysed, it was found that

flattening had occurred on the low rails of sharp curves (inner rails of the tracks) with low cant deficiency values. The high actual cant implementation caused larger resultant forces on the low rails which in turn increased the damage risk in these areas. This finding was very crucial particularly for the lines where ATO was implemented as the vehicle speeds were increased to provide larger cant deficiency values.

The recent study which investigated the reported defects on LUL put forward a significant difference from the previous studies. In 2006, approximately 600 squats were recorded by JNP (Jubilee, Northern and Piccadilly lines) Division, but the majority of them were observed on Jubilee and Northern lines in which the new rolling stock was brought into service (Grassie, Fletcher, Hernandez, & Summers, 2011). When their defect records were evaluated, it was noticed that the 45% of the defects observed in the most 10 critical sites which were located in open track sections rather than tunnel sections. Further metallurgical examinations revealed that some characteristics of the reported squats differed, as these defects were initiated by the excessive wheelslip in poor adhesion areas, approaching signals on open track sections and resulted in thermal damage to the rails. Hence, a new name was given and called as studs: squat-type of defects. Moreover, the observations demonstrated that the studs did not propagate further. As it is shown in Figure 3.8, their superficial appearance looked similar when they exceeded certain size. And they were both recorded outside the tunnels but, squats were mostly found in traction sections and studs were located in high traction as well as particularly in braking sections. While the squats frequently occurred in straight and moderate curve track sections, studs may also be seen on sharp curves and on both high and low rails. On the contrary to squats, which had relatively lower crack growth rate and initiated at the gauge corner side of the rail, studs may develop within the first 10 MGT of traffic and generate in the middle or field side of the running band.
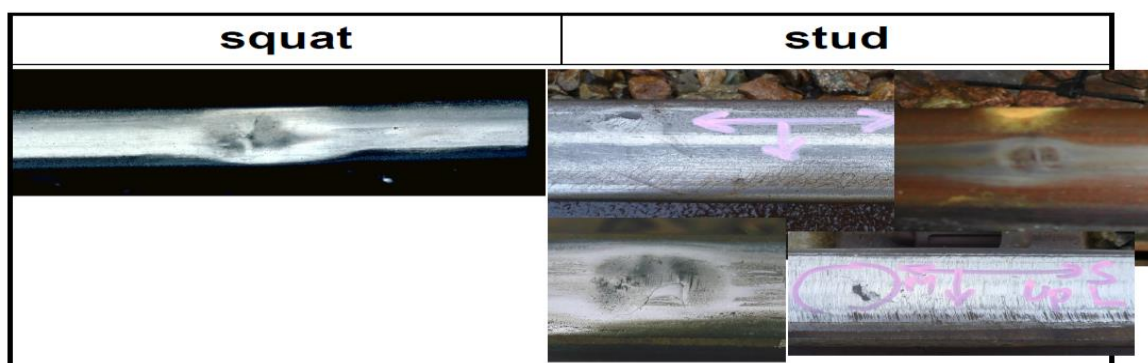


Figure 3.8: Superficial appearance of a well-developed squat and stud defects (Grassie, 2011)

## 3.3 Field crack data analysis

Previous railway research has generally been using a track segmentation approach for data analysis that required identification of segments on the basis of track and/or

operational conditions. The track segmentation is divided based on top-down and bottom-up approaches (Innotrack, 2008a). In the top-down method, all the collected data is grouped into track sections with the similar characteristics such as curve radius. Then, the related information; traffic and operational conditions, trackform characteristics including line defects and track failures information are gathered for each track segment. In the Bottom-Up method, all the track failures and rail defect data are collated and distributed according to their location along the line. The idea behind the bottom-up approach is that the failure modes which caused the most expensive repair and maintenance (rail replacement, grinding, etc.) in the past may lead to similar activities in the future. The steps of this data analysis approach is presented in Figure 3.9.

The bottom-up approach was used in the data analysis step of this research. Firstly, defect information obtained from the defect data sheet and MRX-RSCM measurements were evaluated to understand the dominant crack mechanisms and to assess their severity. Secondly, track geometry and maintenance history data including rail replacement, grinding activities and lubrication application points were analysed and correlated with defect information to determine the influential factors on crack patterns and to find the critical sections.



**Processing Data/Defect Analysis**
- Current distribution along the line
- Determination of factors causing these defects
- Comparison/Correlation of these defects between other sections in the similar networks or other routes

**Track Data Collection**
- Track Geometry
- Trackwork Construction
- Traffic Data
- Maintenance History

**Rail Defect Information**
- Inspection Method
- Severity
- Location

Figure 3.9: Steps in the field crack data analysis

### 3.3.1 Rail inspection in London Underground

LUL currently uses NDT devices, such as ultrasonic and/or magnetic flux leakage (MRX-RSCM) sensors. In addition, they carry out visual inspections to verify these measurements and in particular to identify defects which may have been missed by the NDT techniques or have been rectified in order to define potential risks to generate rail failures. The defects are recorded in the rail defect form that includes the information such as date and type of inspection, rail defect type (code number), severity, location,

repair/maintenance technique and the minimum actions which have to be taken before its removal. Depending on the severity of crack and risk level, the type of repair or maintenance was determined from the LUL's standards. For example, while the low-priority (depth<5mm) defects are recommended for planned monitoring and maintenance, such as grinding, minimal repair and rail welding, the high-priority defects (depth≥5mm) require a more rapid rail replacement with minimum actions such as speed limits and emergency clamps in the highly critical defect (LUL, 2013). The defect reports are listed in defect data sheets for each railway line on LUL.

### 3.3.2 Bakerloo and Jubilee lines defect data sheet

The defect data sheets analysed in this research contained the recorded information between the years 2013 – 2015. When the inspection methods in identifying the defects were compared in Figure 3.10, it was noticed that the ultrasonic testing was the primary technique used in these two lines. However, it was also noted that approximately 25% and 5% of the total defects on Bakerloo and Jubilee lines respectively were recorded as ultrasonically untestable. This means that the level of damage on the surface of the rails prevented ultrasonic detection.
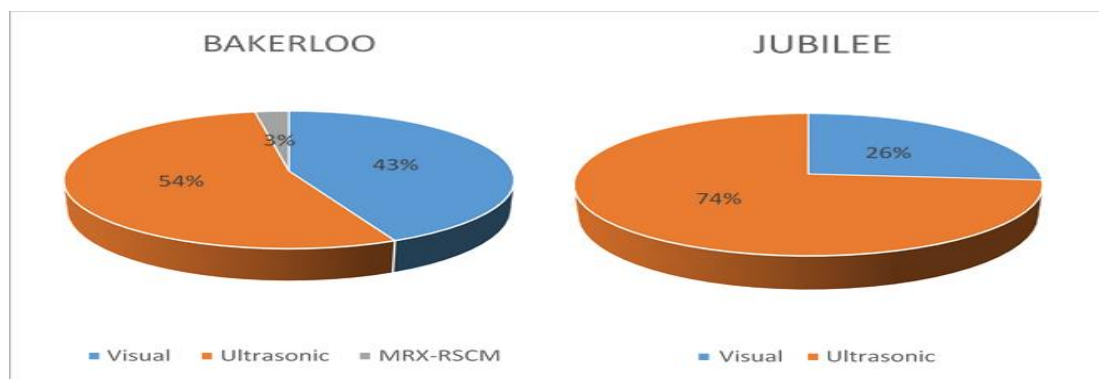


Figure 3.10: Rail inspection method in the Bakerloo and Jubilee lines

LUL records the observed defects using a Code Number which is defined according to principles given in the UIC 712 Rail Defects Leaflet. This code gives three primary information about the defects;

1) Defect zone whether they are generated on the welds (if the rails are connected by a joint/fishplates; rail-end), switch and crossings (S&Cs) and mid-rails (plain track) which represents the intermediate sections between rail-end/welds and/or S&Cs.
2) Defect position inside the rail, head, web and foot of the rail.
3) Defect type such as squats, shelling, corrugation and etc.

The code usually consists of three or four digits. Whilst the first two digits represent the defect zone and rail position, respectively, the last one/two digits give information about the defect type and further details. For example, the code 227 represents the squat type of cracks inside the railhead in the mid-rail/plain track zone.
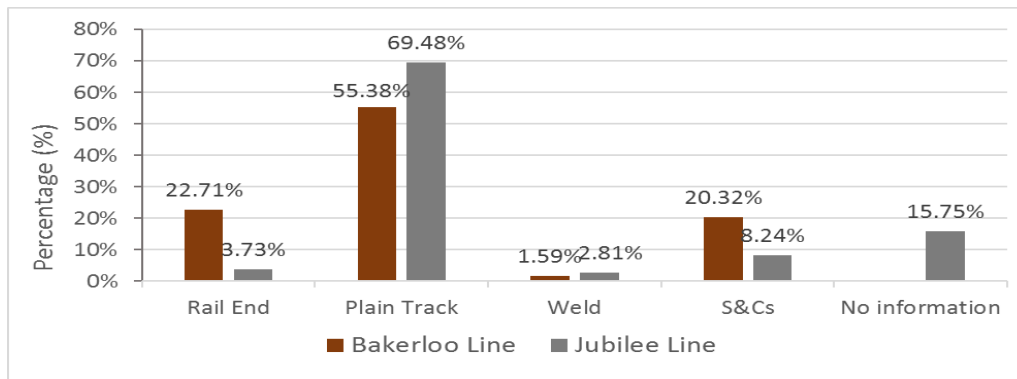
Figure 3.11: Recorded defect zones in the Bakerloo and Jubilee lines

Figure 3.11 illustrates the recorded defect zones on the selected lines. As expected, cracks were predominantly observed on plain-track sections which had a longer distance compared to other zones on the track. Rail-end and S&C zones were also under high risk of damage especially on the Bakerloo line. Since this line is a relatively old metro line, the age of turnouts and the larger proportion of bull-head type of rails, which are connected by rail joints, might account for the increase in the number of defects.

The effectiveness of rail inspection depends on the efficiency and accuracy of the inspection device and the skill and experience of the inspector. The data presented here are the outputs from the defect reports prepared by LUL inspectors and hence it might occasionally contain misinformation. For example, the defect zone or the defect type may be typed incorrectly or no information may be provided. Due to this problem, approx. 16% of the total number of observed defects on the Jubilee line had no information regarding its occurrence zone.

The RCF cracks are mainly divided into two groups: surface and subsurface-initiated defects. Whilst, the defects in the first group are mostly generated due to repeated loads and high contact forces at the wheel-rail interface, subsurface-initiated cracks are often caused by metallurgical faults such as improper heating or cooling. As it can be seen in Figure 3.12, the most prevalent type of rail damage was squats which can be frequently observed on both Bakerloo and Jubilee lines. They are often described in the literature as dark spots containing cracks with a circular arc or V-shape. Widening of the running band and localised depressions were also indicated as the by-product of this defect mechanism (E. Magel, 2011). On LUL, when the estimated length and depth of the squat defects exceed a certain value, they were recorded as squat with T/O (tache ovale) which corresponds to a transverse defect from RCF in Figure 3.12. The results indicated that approx. 10% and 25% of the total squats recorded in Jubilee and Bakerloo lines, respectively had a possibility to growth further, resulting in a transverse defect.
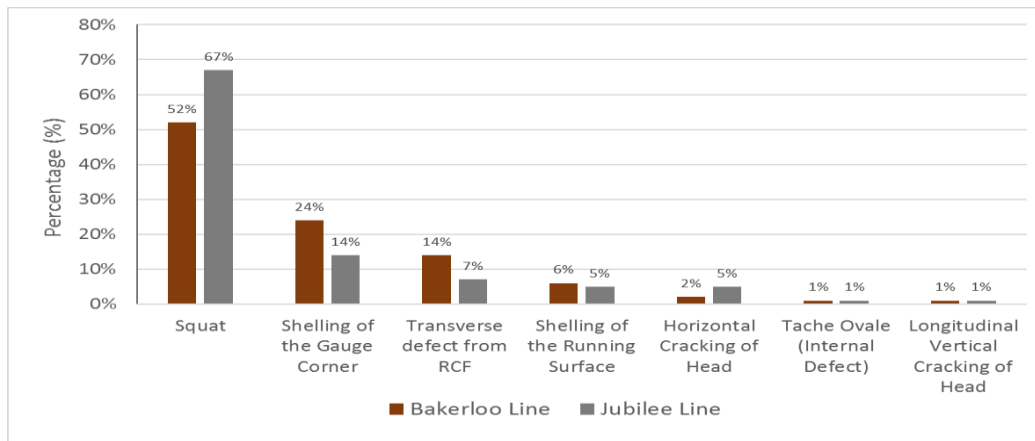
Figure 3.12: RCF defects recorded in Bakerloo and Jubilee lines

The second dominant type of rail damage was shelling which was often seen on the gauge corner and the top of running surface of the railhead. The high contact stresses leading to surface and subsurface-initiated cracks merge together to cause localised loss of structural integrity which results in shelling of the surface material in the railhead (Olver, 2005). This shows that high contact stresses are not just limited to heavy axles in freight traffic, but metro lines also suffer from high forces generated at the wheel-rail contact in combination with frequent load passages which have a significant impact on the formation of damage.

Longitudinal vertical and horizontal cracking were also recorded in the data sheets. These are progressive type of cracks which tend to separate the head into parts horizontally, parallel to the running surface or vertically through the head (UIC, 2002). Besides the surface-initiated cracks, the tache ovale type of defect which is a subsurface defect, was also reported by the maintenance team.

As expected from the finding of the stud study, a high number of squats were observed in LUL (Grassie et al., 2011). However, as aforementioned, some of these recorded squats could be stud type defects which was also declared by LUL staff. In fact, a relatively low number of wheel burns were also reported in the lines.

### 3.3.3 MRX-RSCM rail inspection

LUL has been using the MRX-RSCM device to increase the reliability of rail inspection and to measure the crack depth information. The sensor provides two measurement outputs that include a surface damage map and crack depth diagram. Figure 3.13 shows example outputs for a track section located just before a station between Regents Park and Baker Street on the Bakerloo line. The measured crack depths are presented at one meter intervals on the lower plot, whilst the upper diagram displays the rail damage on the rail head for a highlighted 50 m section of the crack depth diagram.
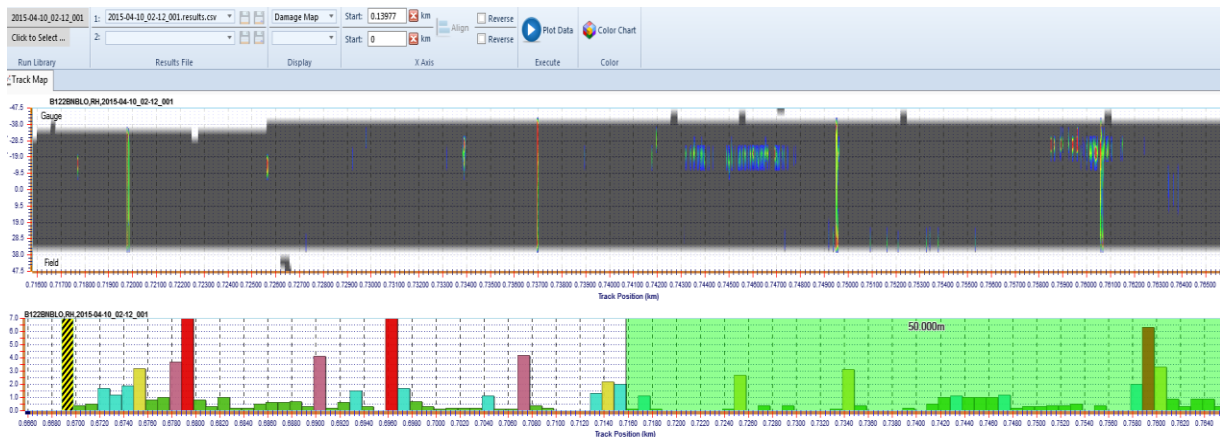
Figure 3.13: MRX-RSCM measurement output data for a track in Bakerloo line

The MRX-RSCM data for the Bakerloo line has two subsequent measurements, which were conducted in the 2014 and 2015 whereas, the Jubilee line was inspected in 2013 and 2015.

During the data analysis, a number of issues were identified. Several occasional gaps were revealed during the investigation of the distances between different measurements. For instance, the length of the Location Coding System (LCS) sections varies when two consecutive measurements were overlaid to each other and the MRX-RSCM crack data was compared with the distance in the track geometry information.

MRX-RSCM crack measurements are performed by the operator pushing the sensor along the railhead. The road wheels which are shown in Figure 3.14 are set to central position and rail wheels used to gauge when the device is on track. Due to changes in the railhead profile and the effect of slip, the road wheels cannot effectively adjust and rail wheel produces different distances for similar LCS sections. In addition, the differences in starting and stopping points increased the gap between two consecutive measurements.
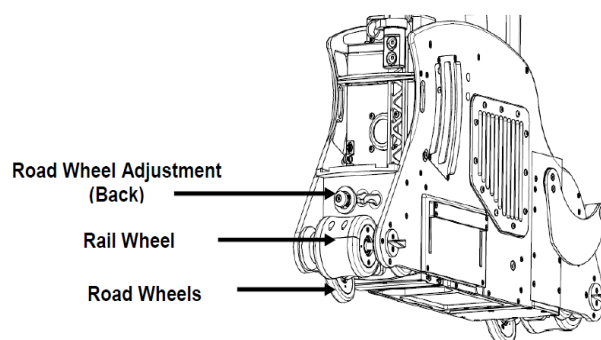


Figure 3.14: Gauging adjustment of the MRX-RSCM inspection device

Furthermore; as it is expected from the field data, the MRX-RSCM crack depth measurements were scattered along the measurement route which might mainly stem from the changes in the maintenance history of the rails throughout the lines. However, the aforementioned over-prediction problems may also play a role. Nonetheless, LUL

carried out measurements by an optimum walking speed of 5 km/h to increase the accuracy. In addition, the field crack data that were obtained from various methods such as visual inspection, ultrasonic and MRX-RSCM sensors were overlaid in order to increase the efficiency of field data analysis and eliminate the detection errors in the research.

### 3.3.4 Field crack data analysis results

The field crack data collected from defect data sheet and MRX-RSCM measurements were correlated with the track geometry and maintenance history data to identify the significant factors having an effect on crack mechanisms and determine the critical track sections.

Figure 3.15 displays the 2014 and 2015 MRX-RSCM crack depth results in 1 m interval and the defect data output for right rails in the Bakerloo Northbound (NB) line. The blue arrows demonstrate the common defect locations such as at approx. Ch. 7+000 km, 8+000 Km, 8+500 km, 10+500 km while, the orange arrows show the unmatched areas (Ch. 4+000 km and 5+000 km). Additionally, the dashed lines at Ch. 4+500 km and Ch. 7+500 km presented the areas where all the methods were in agreement. The crack depth values which clustered along the route were mainly considered in this study. However, the distance discrepancies can also be seen when the crack depth trends/platoons are compared in consecutive measurements.
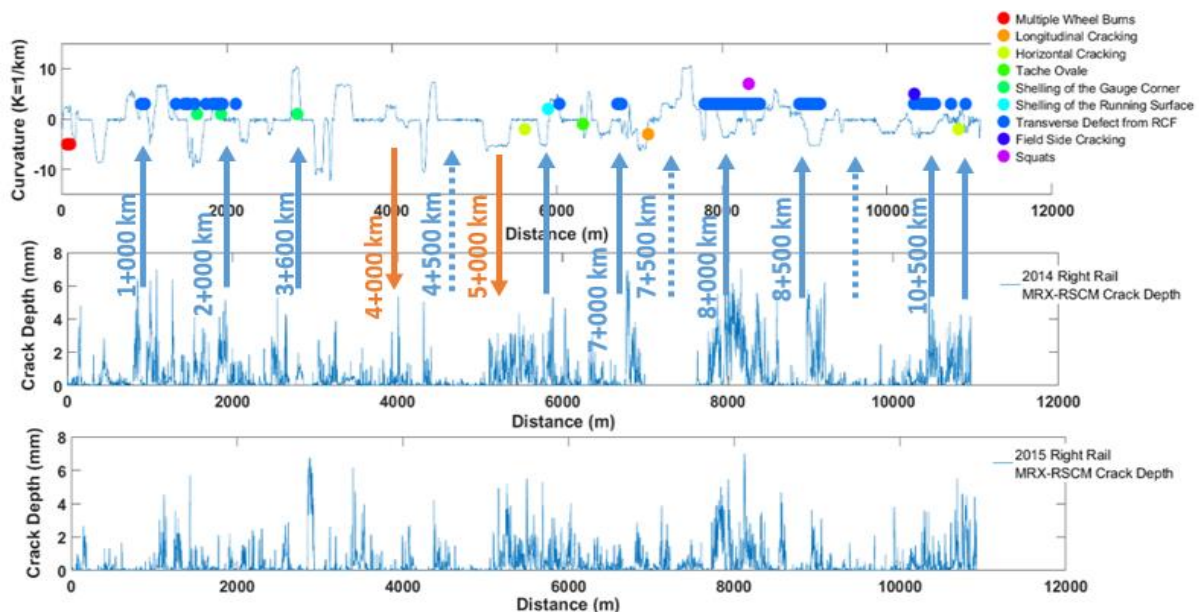


Figure 3.15: Right rail MRX-RSCM crack measurements and defects on the Bakerloo NB line (Note: 1+000 km = 1000 m)

It can be observed from Figure 3.15 that the cracks mainly occur on high rails of the curve sections and the dominant damage type is the transverse RCF defects. In contradiction to the findings in the stud-squat comparison study (Grassie et al., 2011) that stated that squats were mainly generated in the outside section, they were reported in tunnel sections and had a high tendency to increase their size. When the depth of transverse defects was

considered, it was noticed that even though they were measured as approx. 4mm at around Ch.8+000 km in 2014, they were reduced in 2015 which might stem from the grinding activity took place between the two inspections. But, the decrease in crack depth at Ch.1+000 km, Ch.2+000 km Ch.3+600 km was caused by the rail replacement in 2014.

In order to test the previous arguments regarding the effect of traction, the platform regions were particularly evaluated and it was noticed that the higher number of defects occurred in the traction areas where the trains start to accelerate after station platforms both in the Bakerloo and Jubilee lines. Although certain metro system studies highlighted the importance of braking sections, this study validated conclusions from previous RCF modelling study that forces in the driving traction produced greater stress intensities than the braking when they are exposed to the fluid effect (Bower, 1988).

The lubrication mechanism which has a primary influence on crack propagation rate was analysed, as it was primarily applied on both the check and running rails which can be seen in Figure 3.16. However, the purple circled areas in the plot displays that the defects were occurred on the lubricated regions of the Bakerloo SB line. This also supported the previous RCF modelling results stating that the fluid pressurization raised the crack growth especially for small cracks in 4-5 mm length (Fletcher et al., 2008).
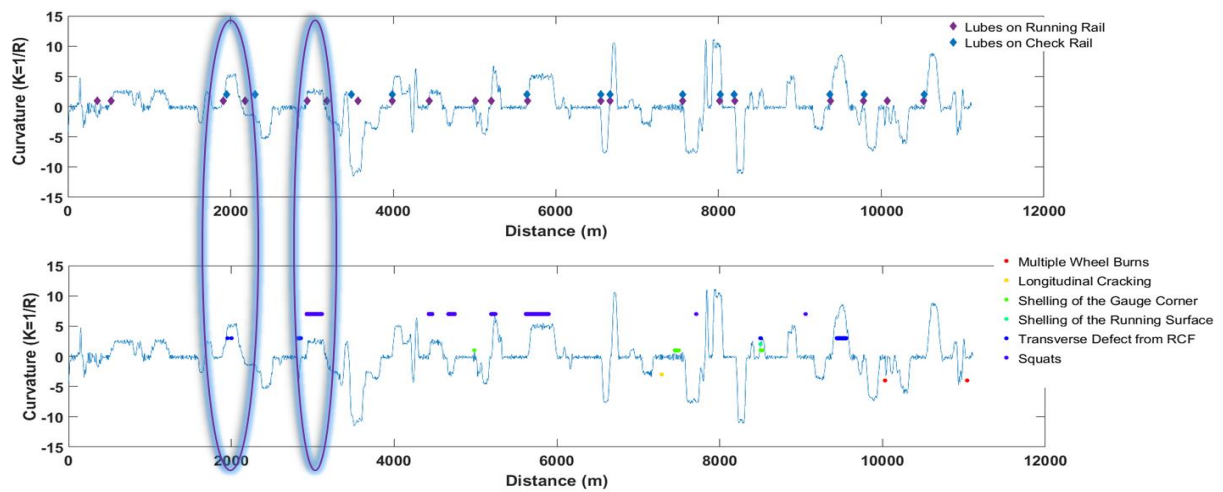


Figure 3.16: Left rail lubricator positions and the defects on the Bakerloo SB line

The defect data for left rails on the NB route of the Jubilee line are presented in Figure 3.17. The inconsistency between the defect data and MRX-RSCM measurements can be again seen in some sections but, the majority of the cracks were matched due to the greater number of reported defects in this line. The tunnel section is also marked in Figure 3.17 which starts from approx. Ch. 3+200 km and ends at Ch. 22+500 km. This demonstrates that both the open-track (Ch.23+000-35+000 km) and tunnel sections (Ch.15+000-23+000 km) were suffering from RCF cracks. There was a substantial reduction in the number of cracks in the JLE section between Ch.5+000-14+000 km, this

was noted both in the defect data and MRX-RSCM measurements. Due to a new tunnel track system (or the rail age might be smaller compared to other areas) and the low track irregularity levels stemming from the higher track stiffness levels presented in Figure 3.18.
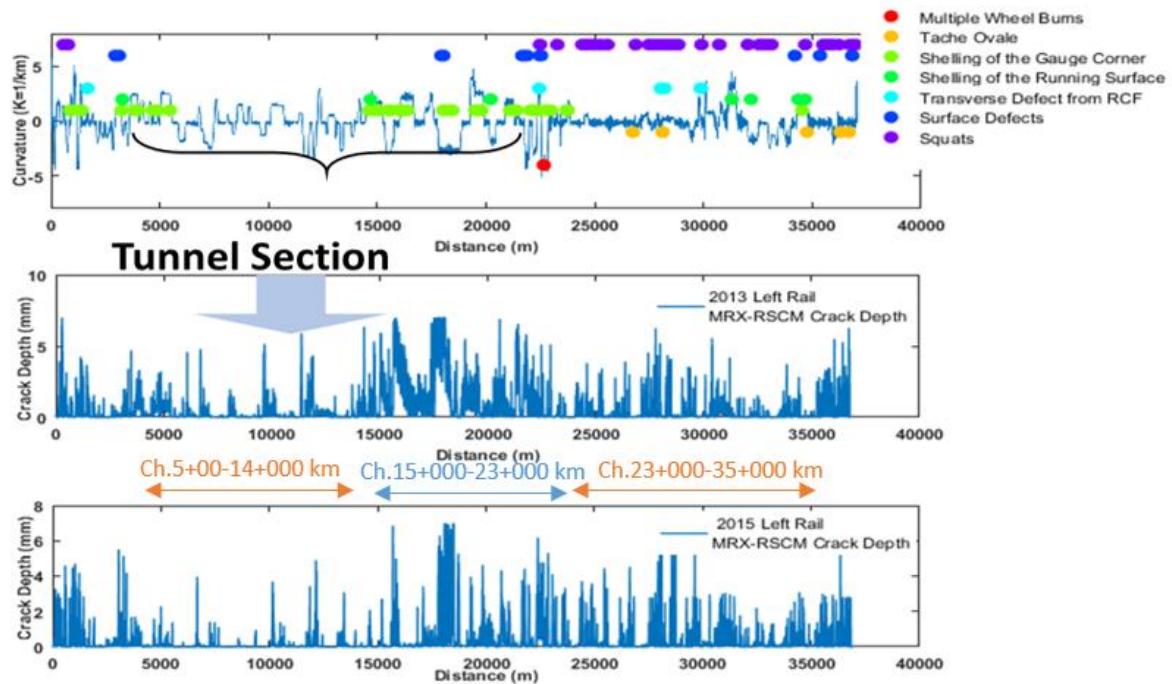


Figure 3.17: Left rail MRX-RSCM crack measurements and defects on the Jubilee NB line
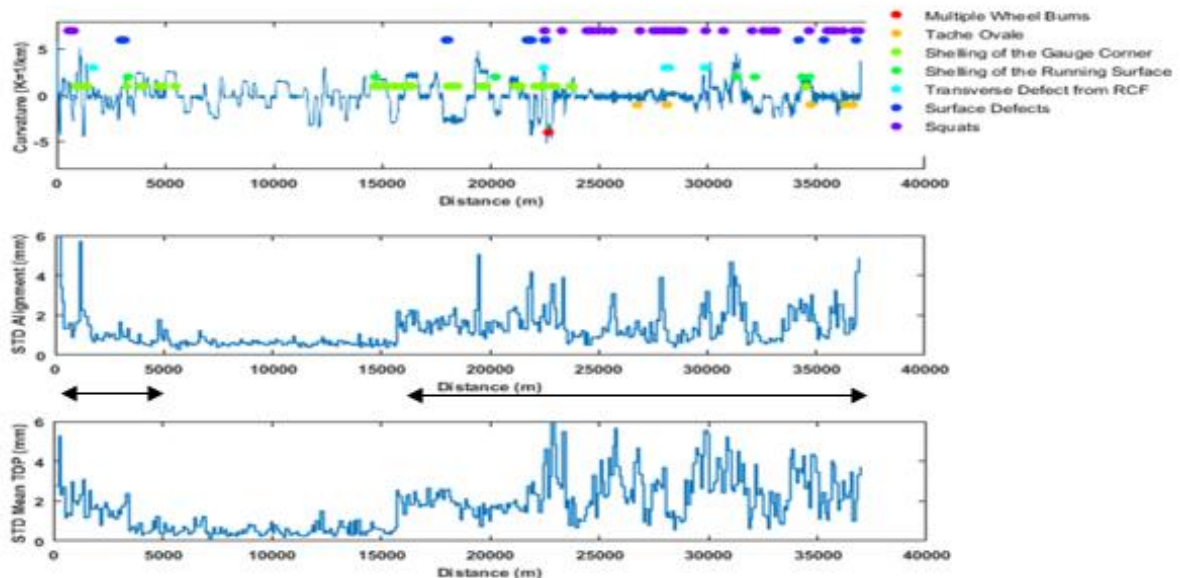


Figure 3.18: Left rail defects and the lateral and vertical track irregularity levels on the Jubilee NB line

Similar to the results of the aforementioned stud-squat comparison study (Grassie et al., 2011), the squats were mainly reported in the open regions especially in the tangent track and moderate curve sections in the Jubilee line. But, the shelling defects were predominantly observed in tunnel sections while high rails were seem to be more

susceptible to gauge corner cracking, the top of running surface shelling was mainly observed on the low rails, showed that over-canted tracks cause high contact forces.

Moreover, it was noted from the data analysis that the actual track quality levels, determined from the deviation in the lateral and vertical irregularities had an impact on crack formation. The number of defects substantially increased in ballasted track and the old track infrastructure where the standard deviations in 100 m are relatively high compared to other sections demonstrated in Figure 3.18. This outcome also supported the previous finding stating that the squats were often related to rail top surface irregularities particularly the short wave irregularities which may suggest the impact of stiffness characteristics of the track such as rail, rail pad and etc  (Li, Zhao, Esveld, Dollevoet, & Molodova, 2008).

In the study, the MiniProf wheel and rail profile measurements were also examined and noticed that the flattening was occurred similar to the findings of previous LUL study (Scott, 2009). This is particularly evident on BH rails which might be caused by the over-canted tracks on Bakerloo line, variations in track stiffness and worn wheels which moved the contact positions towards the field side of the low rail.

## *3.4  Conclusions and discussions*

This chapter presented detailed information about the study network and provided an overview of previous studies conducted for underground-metro systems and London Underground.

The operating and track characteristics of selected lines, Bakerloo and Jubilee were compared and the main differences are as follows:

- The Bakerloo line has relatively more curvaceous track geometry with a minimum curve radius of 85 m. Check rails are installed on curves which have radii smaller than 200 m. The line is operated under manual mode with an average (maximum) running speed of 50 km/h.
- The Jubilee Line consists of larger curve radii as the minimum curve radius is 250 m and hence check rails are not required. In comparison, it is operated under ATO mode and the running speed reaches to 90 km/h at several locations.

From the review of previous studies into RCF cracking on underground-metro systems, it was noted that the track tonnage levels in these lines were close to mainline routes and the higher number of defects were reported in the curved track sections particularly before stations (braking zones). Also, the previous studies in LUL highlighted the significant impact of the introduction of a new rolling stock (or upgrades to existing rolling stock, e.g. change in traction package) or a change in driving operation mode (from manual to automated systems) on RCF cracks. In a separate study, reported squats were analysed

in detail and it was found that some of them were initiated by the limited wheelslip in poor adhesion areas. Hence, they gave a new name; studs.

The acquisition and critical analysis of significant volumes of field data was also presented to understand the dominant damage mechanisms and to identify the influential factors. This included a detailed review of track, operational characteristics and maintenance actions that have a crucial impact on growth rate of the cracks. The specific observations from this analysis includes:

- Although defect data sheets contained certain problems stemming from ultrasonically untestable rails and misinformation in the visual defect forms, it was apparent that shelling and squat were the most common defects on both of the lines.

- The main differences between the Bakerloo and Jubilee lines were noticed in the squat defects. Similar to the findings in the stud-squat study; these were mostly observed in shallower curves and overground sections on the Jubilee line. However, sharper curves (R<200 m) on the Bakerloo Line were also prone to these defects and potentially had a higher risk of propagation, as 25% of total squats were recorded as transverse defects from RCF.

- Even though issues regarding the aligning of the data from consecutive MRX-RSCM measurements was encountered, this data was useful for observing the severity of RCF cracking on the entire lines. For instance, whereas the defect data sheets showed high rails were more vulnerable to rail damage in Bakerloo line, the MRX-RSCM data demonstrated the severity of cracks both in low rails and tangent tracks. On the Jubilee line, the larger number of reported defects provided a better correlation with the MRX-RSCM data. Gauge corner shelling was primarily observed on the high rail, whereas shelling on the top of running surface was observed particularly on the low rails.

- A higher number of defects were recorded in the traction areas and lubricated/over-ground sections which potentially supported the finding of the previous RCF modelling studies. The traction direction which stated to be leading fluid pressurization and entrapment mechanisms gave an increase in crack growth rates.

It should be also noted that the interpretation of the field data is very significant. In this section of the research, rail maintenance history data such as grinding and replacements were also taken into account in order to correctly understand the reasons in the crack depth reductions between the consecutive measurements and to clearly address the differences between the sites having measured/reported defects and not.

# Chapter 4   Vehicle Dynamics Route Simulations

This chapter provides a brief review of wheel-rail contact modelling and the method adopted in the VAMPIRE vehicle dynamics simulation software. The influence of different models and the selected method on damage prediction is also investigated. The preparation of the vehicle dynamic route simulations is also described in the chapter. The significant volume of data provided by LUL was again helpful in developing the detailed models of the two lines. The data such as the actual track geometry, wheel-rail profile measurements, vehicle speed and track lubricator positions were considered in the preparation of route simulations which helped to calculate the contact and the selected model input parameters that were used in the further steps of the research.

## 4.1  Wheel-rail contact modelling

The forces acting between wheel and rail generated by the contact are strongly affected by the motion of the wheelset with respect to the track. In reality, railway alignment consists of curves, gradient, cant and track irregularities which result in variations in wheel-rail contact characteristics and make their calculation more complex.

In reality, the wheel-rail contact problem changes frequently along the track which can be very computationally intensive to capture in vehicle dynamic simulations. To simplify this, a number of assumptions can be made to accelerate the simulation process. However, these simplifications can reduce the accuracy of the results and hence, they give rise to a trade-off between accuracy and computation speed. There are various computer packages which have been developed by research institutes and railway administrations around the world to calculate the dynamic behaviour of railway vehicles and the forces at the wheel-rail interface such as GENSYS, SIMPACK, NUCARS and VAMPIRE.

In this research, the VAMPIRE vehicle dynamics simulation software is used due to its computational efficiency, which allows the evaluation of a large number of parameters in a short timeframe and its success in calculating damage during previous studies. VAMPIRE has also been extensively validated against a series of full-scale experiments using load measuring wheels on locomotives, passenger and freight vehicles (Evans & Iwnicki, 2002). The wheel-rail contact calculations in VAMPIRE vehicle dynamics simulation software is described by the aforementioned four sub-problems in Chapter 2.1 and illustrated in the Figure 4.1.
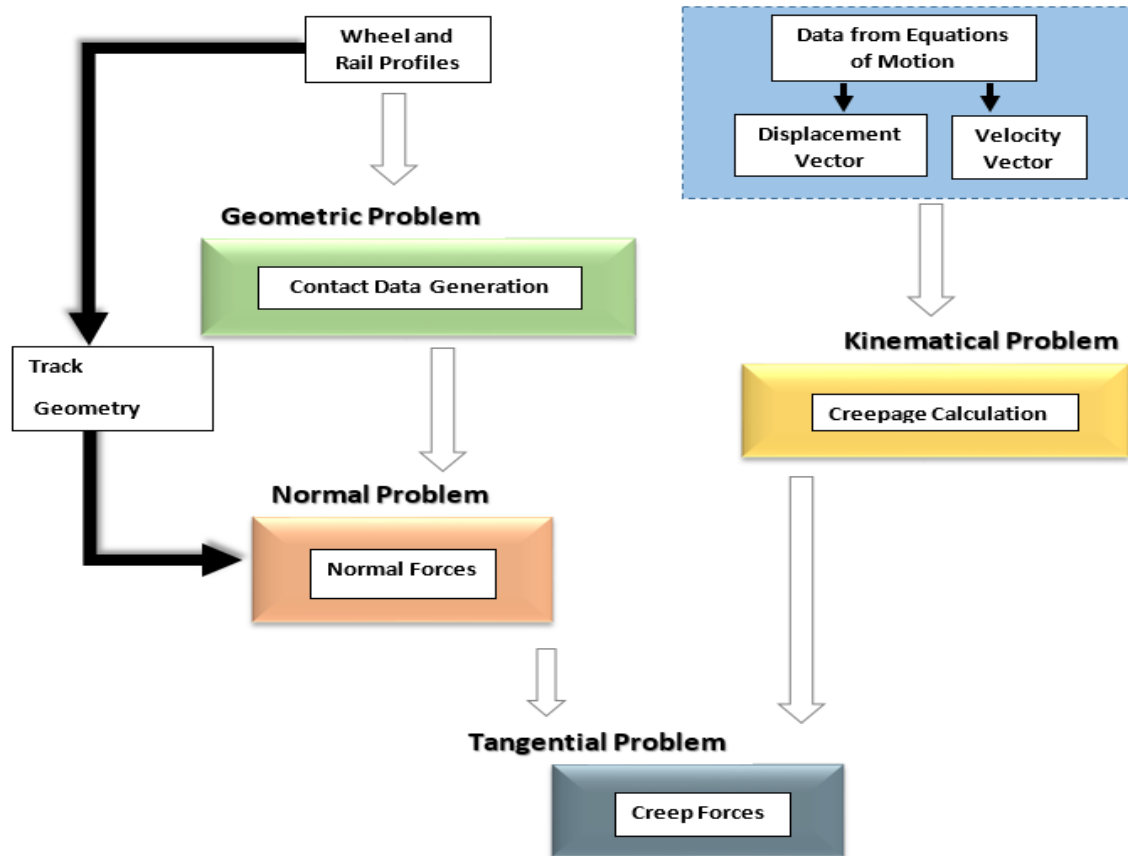
Figure 4.1: The calculation steps of wheel-rail contact problem in Vampire

## 4.1.1 Geometrical-normal problem

Geometric analysis is undertaken using the Contact Data Generation Module in VAMPIRE which takes into account the shape of the wheel and rail profiles and their relative positions without considering the vehicle motion and track geometry condition. The module calculates the wheel-rail contact data for a pair of wheel-rail profiles, with a specified track gauge, rail inclination, axle load and wheel diameter.

After the determination of the location, size and area of the contact, the contact pressure distribution within this area is calculated in the normal problem. Vampire calculates the geometrical and normal problem based on Hertz theory which was previously introduced in the Shakedown Map model (Chapter 2.5). This theory is widely used in the calculation of the contact due to its closed form solution and efficiency, which makes it attractive to the wheel-rail contact problem in vehicle dynamic simulations and has been implemented in previous RCF studies.

However, as previously mentioned in Chapter 2.1, the assumptions in the Hertzian theory are often violated in the real case profiles. For example, the assumptions of half-space and the elliptical contact area can lead to inaccurate results. Even though they may be valid in the wheel tread-rail head contacts, the wheel flange-rail gauge corner contacts might change the radii of curvatures dramatically and especially, the worn wheel and rail

profiles which might generate conformal contacts may cause these assumptions to lose their existence. A study which evaluated these assumptions found that the Hertz solution was only valid when the plastic flow did not occur and/or the contact zone did not move to regions where the curvature values become inconstant (Yan & Fischer, 2000).

Researchers have further evaluated these limitations and developed non-Hertzian contact models. In one of the earlier models, the contact patch was divided into strips and the contact pressure distribution in each strip was assumed to be elliptical in order to reduce computational costs (Knothe & Le The, 1984). In order to simplify the contact patch determination, the other researchers generally utilised virtual penetration concept in which the surface deformations were neglected and it was assumed that the bodies could rigidly penetrate into each other. For instance, Stripes theory defined the scaling factor as a function of relative radii of curvatures and hence an ellipse with different semi-axes ratio rather than a Hertzian ellipse could be obtained which makes this model more accurate than the previous models (Sichani, Enblom, & Berg, 2014).

When the wheelsets are displaced laterally, it is observed that multiple contact points are generated from the sudden jumps. This condition and the conformal contacts which lead to wider contact areas were studied by a Multi-Hertzian approach. The Multi-Hertzian models were built by using semi-elliptic or bell-shaped functions to ascertain the secondary contact points (Sichani, 2013). These models are also declared as slow compared to Hertzian case. In a more rapid approach, Pascal and Sauvage generated a single an equivalent ellipse to replace two-single contacts which computes the sum of the creep forces on each separate ellipse to find the total creep force. This approach may not be efficient in damage analysis as it did not show the real values in each affected contact and/or it may lead to larger contact patch area (Iwnicki, Björklund, & Enblom, 2009).

Despite those limitations given for Hertz theory, the rigid contact is still one of the most commonly used approaches in commercial vehicle dynamics simulations as it can be easily integrated into different codes. The occurrence of multiple contact in rigid contact can also be identified from the sudden jumps in the contact positions such as in VAMPIRE vehicle dynamics simulation (Shackleton, 2009). When the wheelsets are displaced laterally, the contact position may be seen to move across the rail crown. This condition can be remarkably noticed when they move close to flange contact positions. The Contact Data Generation module places 'L' and 'R' markers in the output (.con) files to represent when two-point or flange contact occurs on both the left and right rails. The program starts to detect the flange contact point when the contact angle is greater than 30 degrees (used as a default setting) and calculates the contact parameters of the two points based on Hertz theory. It is assumed that the applied load on the wheel tread contact shifts to flange contact and it is apportioned when there are two contacts. In some cases, the point contact

can occur at lower or higher contact angles depending on the radii of the flange root and flange face of the wheel. Therefore, each pre-calculated contact file should be checked before it is used as an input in the subsequent modelling stages.

## 4.1.2 Kinematical-tangential problem

The calculation process of the other contact parameters for the given velocities and displacements of the wheelset are performed in two stages. As aforementioned in Chapter 2.1, the creepages and the related creep forces are calculated in the kinematical and tangential problems, respectively.

Similar to Geometrical-Normal contact problem, many studies have also been conducted in this Tangential problem to propose more accurate solutions. One of the well-known model which is often named as the exact/complete theory in the literature is the CONTACT code developed by Kalker. It contains of two algorithms: NORM and TANG which were used to solve the normal and tangential problems, respectively. This theory was also depended on the half-space assumption and estimated that the bodies are homogeneous and linear elastic, but the contact geometry was not restricted to elliptical patch area. The contacting surfaces were discretized into rectangular elements and whether each element was in the adhesion (stick) and slip was determined in the code. Since this code requires a high computational effort, it is not suitable for commercial vehicle dynamics simulation tools (Zaazaa & Schwab, 2009).

In order to reduce the calculation times, Kalker developed a simplified theory and implemented it in a faster algorithm called FASTSIM. A flexibility parameter was introduced between the tangential pressure $P_T$ and elastic displacement $u$ which is a function of the global creepage vector $\xi$, the ellipse semi axes $a$, $b$ and the combined shear modulus $G$ and Poisson's ratio ($v$). The surface was described by a grid separating parallel strips in the rolling direction which is shown in Figure 4.2. Each grid point on the surface was assumed to deform independently of its neighbouring points. This deformation was caused by applied traction at that point and then the flexibility parameters were introduced for the three creepage directions.
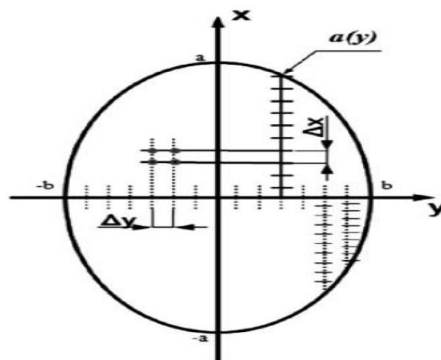


Figure 4.2: The contact patch discretisation in the FASTSIM algorithm (Zaazaa & Schwab, 2009)

To evaluate the computational efficiency between FASTSIM and CONTACT code, he also conducted comparison studies which demonstrated that while FASTSIM results were satisfactory especially for the pure creepage, it provided less accurate results in other combination of creepages. He claimed that FASTSIM was approximately 400 times faster than CONTACT code but, this rapid calculation method gave errors up to 25% in the tangential forces (Kalker, 2013). The FASTSIM was also further improved and implemented on non-Hertzian Contacts which were mainly done by introducing non-elliptic flexibility parameter or local ellipse for each grid (Ayasse & Chollet, 2006).

Each of the given sub-problems in the above can be solved with different methodologies in the literature, many alternative methods have been proposed to increase computational efficiency. They are not independent from each other and they should be evaluated simultaneously. Therefore, they require highly comprehensive methods which take several time to complete the computation for even one wheel-rail pair.

In order to speed up the simulation process and to run the long distance routes in short times, researchers proposed to use again interpolation methods in the Tangential problem which in general can be defined either by tables or specific formulas. The interpolation method was often preferred in Vehicle Dynamics simulations due to its computational efficiency and accuracy (Bosso, Spiryagin, Gugliotta, & Somà, 2013).

The creep force–creepage relationship in the Non-linear creep law of Vampire was defined in a pre-calculated multi-dimensional look-up table. This table was prepared based on the contact theory of J.J Kalker and was created using the CONTACT Program developed by Vortech Computing in the Netherlands (DeltaRail, 2014).

### 4.1.3  Impact of contact models on rail damage modelling

In rail damage modelling, it is very important to make realistic assumptions in the wheel-rail contact parameters in order to understand the effect of contact conditions on the resulting forces and rail damages such as RCF and wear. Therefore, the main purpose of contact modelling is to determine the magnitude of stresses and deformations that are generated when the two bodies are brought into contact. One of the best approaches which provides the possibility for detailed modelling of deformations is finite element (FE) analysis. This technique enables the description of complicated geometric shapes including surface roughness and non-linear material properties in the wheel-rail contact modelling. However, as aforementioned, it requires excessive computation times.

The key requirement in the application of different methods is to be integrated with the railway vehicle dynamics simulation tools. Since the contact problem should be calculated at every time step of long-distance simulations, the detailed methods are often not desirable. Recently, studies have been conducted to develop faster and more accurate

solutions for the determination of contact dimensions and the surface tangential distribution rather than global creep forces in the contact patch which are essential in the calculation of wear and RCF damage.

To assess the accuracy of different simplified contact theories used in vehicle dynamics simulations, a study was performed which compared the results of FASTSIM, Shen–Hendrick–Elkins, Polach, Vermeulen–Johnson, linear theory with saturation and USETAB (which is the aforementioned Kalker's look up tables in VAMPIRE). Considering the Hertzian based contact geometry and surface normal pressure, it was found that USETAB and FASTSIM gave errors in the longitudinal and lateral creep force calculations in the range of 5-10%, while the other methods differ 15-60% from CONTACT (Vollebregt, Iwnicki, Xie, & Shackleton, 2012).

In the Manchester Benchmark study, the position and dimension of the contact for each wheelset lateral displacement were compared using a number contact methods which were employed in the vehicle dynamics simulations. Since each simulation tool used a various technique, the study offered a valuable comparison. For instance, while the Nucars and OCREC integrated multi-Hertzian codes in their model framework, Kalker based approaches were utilised in LAGER and CONTACTPC92 models. It was stated that multi/non-Hertzian contact models calculated wider contact patch areas than those predicted by their Hertzian counterparts as it was found by Vampire (Shackleton & Iwnicki, 2008). On the contrary to the Hertzian theory which gave better results with smooth profiles (less plastic flow/wear both in the wheel and rail), non-Hertzian models were more successful in the un-smooth profiles and irregular rail geometry conditions which was particularly the case in switches and crossings.

A more recent study was performed in order to investigate the performance of the non-Hertzian contact models in the online vehicle simulations in which the computations were carried out in each time-step. The study used the advanced numerical approaches Kik–Piotrowski, Linder and Stripes in geometrical-normal contact problem and FASTSIM in the tangential problem. It was found that these models calculated lower creepages (12% lower) and creep forces (3% lower) than the Hertzian-based FASTSIM model. Another finding in the study was that that the difference in the dynamic behaviour of the vehicle between the non-elliptical methods and FASTSIM was rather small for small contact angles, however it increased dramatically for larger contact angles particularly in curved tracks. The researchers also noted that the implementation of these models will be slow and not efficient for the simulation of vehicle dynamics on extended pieces of track (Burgelman et al., 2015).

Another study calculated the Archard wear volume in wheels based on Hertzian/Elliptic with FASTSIM and Stripes theories. It was concluded that the Stripes theory redistributed

the stresses and consequently the wear with increasing curvature and it calculated relatively higher results in the flange/gauge contact wear (Enblom & Berg, 2008).

In order to show the differences between global (vehicle dynamics simulation output) and local (distributions over contact patch such as FASTSIM) computations, some of the important damage prediction parameters have been compared in several studies. A study which examined the changes in $FI_{surf}$ values found that the calculations for each cell element in the contact patch locally instead of globally led to higher results both at flange and low rail contacts. The difference increased as the curve radius decreased (Dirks & Enblom, 2011). In contrast to this finding, Pombo et al., (2011) investigated the wear depth calculations using the $T\gamma/A$ approach and stated that there was good agreement between two outputs. A maximum of 4% difference in global case caused by the changes in input parameters. However, the study also mentioned that the local approach required about twice the computational time than the global case due to post-processing of input parameters in the FASTSIM code.

Accurate determination of wheel-rail contact dimensions and computation of tangential distribution over the contact patch has gained significance in the rail damage modelling. But, these detailed models require a rigorous treatment and they are not suitable for long distance simulations where the wheel-rail pairs are frequently changing along the track. Although the VAMPIRE has relatively lower accuracy and produce global (cumulative) forces in the contact patch, it has certain advantages in the real-case simulations. For instance, numerous track irregularity levels and various contact conditions resulting from different wear patterns can be described. In addition, the friction can be altered between different contacts which can be helpful when defining the effective lubrication distance for the track-mounted lubricators. Furthermore, it was also mainly used in the previous WLRM studies. Thus, the selected breaking points in the damage model were calibrated to the global outputs. For this reason, VAMPIRE was selected in this research. But, FASTSIM was also used in conjunction with VAMPIRE in order to show the changes in Chapter 9. The Hertzian model was used in both of the programs since, it was previously stated that non-Hertizan models were not suitable to use in longer track conditions.

## 4.2 Preparation of route simulations

VAMPIRE vehicle dynamics route simulations require three main inputs; these include a vehicle model, track characteristics (such as track geometry, speed, friction levels) and wheel-rail contact files. These inputs are referenced in a Run file which also defines the type of analysis which will be conducted throughout the simulation and the output parameters that are to be computed and stored in the output file.

In this study, the transient analysis was used which calculates the response of a vehicle to the track alignment and general external forces in each time step. Figure 4.3 illustrates the steps of the transient modelling stage in VAMPIRE. A forcing file was also included in this study to apply an additional torque to the wheelsets to model the influence of traction and braking on the resulting creep forces.
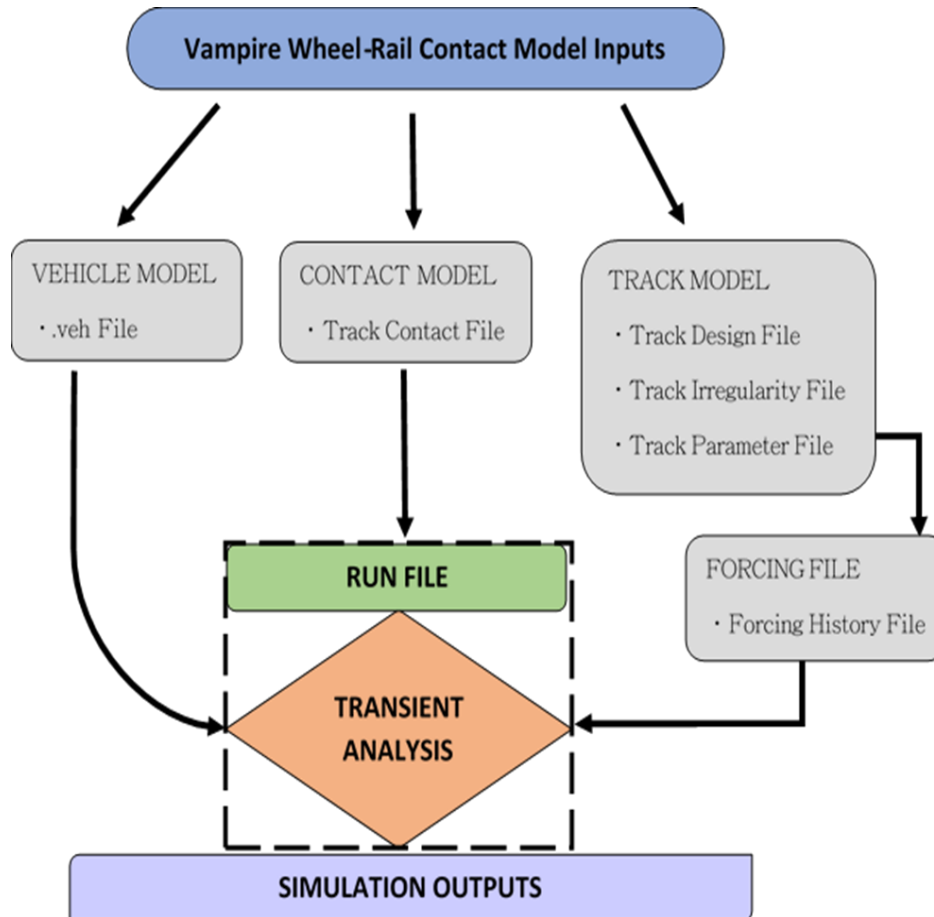


Figure 4.3: Steps of the transient modelling stage in Vampire

## 4.2.1  Vehicle model

A rail vehicle is a Multi-Body System (MBS) which includes a series of interconnected rigid or flexible bodies. Each body in the system, such as carbody or wheelset, is described by its properties including mass, moment of inertia, dimension and position in the system and connected using a combination of force elements and joints. When the system is ran over the defined track model, the force elements and joints generate applied forces and torques due to the relative motion of the bodies. Springs and dampers which are typical examples of force elements are combined via primary and secondary suspension components (Shevtsov, 2008). Figure 4.4 exhibits the VAMPIRE vehicle model assembly. In this research a model of 1972 and 1996 Stock vehicles were utilised for the Bakerloo and Jubilee lines respectively. These vehicle models were supplied by LUL for use in the research and have been previously used in a large number of wheel-rail interface studies.
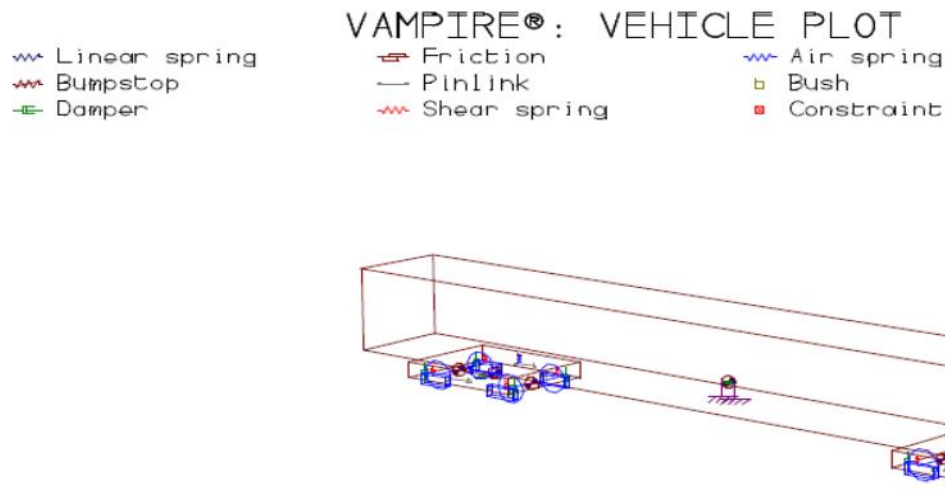
Figure 4.4: VAMPIRE vehicle model assembly

The 1972 Stock fleet was introduced in Bakerloo line as a replacement of 1938 and 1959 Stocks. The manufacturer of the rolling stock was the Metro-Cammell and it was developed based on the Victoria Line's 1967 Tube Stock. It consists of 7 car trains formed of a 4-car unit (Driving Motor (DM) – Trailer (T) - Trailer-Driving Motor) and a 3-car unit (Uncoupling Non-Driving Motor-Trailer (UNDM) - Driving Motor). Each coach/car has two bogies and each bogie has two axles.

The 1996 Stock entered service in 1997 following the opening of Jubilee line Extension. It was built by Alstom and designed for automatic train operations. Although the first fleet was composed of six-car units, a special trailer unit (ST) was included to the trains in 2005. The final configuration is as follows: DM-T-UNDM+UNDM-ST-T-DM

In the research; the three cars were taken into account on both of the lines: the front and rear motor cars with the third trailing car.

## 4.2.2 Wheel-rail contact model

As introduced in the Section 4.1.1; the Contact Data Generation Module of VAMPIRE creates output (.con) files for each rail-wheel pair. This file contains all necessary parameters describing the position and properties of the contact patch with respect to the wheelset lateral shift.

In rail damage predictions, it is very important to consider different combinations of wheel-rail profiles in order to accurately replicate real on-site conditions. In the research described here, four different scenarios were modelled to describe the wear state of both Bakerloo and Jubilee lines as detailed below:

1) New Rail - New Wheel (NN)
2) New Rail - Worn Wheels
   a. New Rail - Worn Wheel 1 (NW1): Lightly worn wheel

     b.  New Rail - Worn Wheel 2 (NW2): Moderately worn wheel

     c.  New Rail - Worn Wheel 3 (NW3): Severely worn wheel

3) Worn Rail - New Wheel (WN)

4) Worn Rail - Worn Wheels

     a.  Worn Rail - Worn Wheel 1 (WW1): Lightly worn wheel

     b.  Worn Rail - Worn Wheel 2 (WW2): Moderately worn wheel

     c.  Worn Rail - Worn Wheel 3 (WW3): Severely worn wheel

Rail cross sectional profiles were measured by LUL at a number of locations and time intervals using a MiniProf device. These profiles were received in the data collection stage of the study and reviewed to determine the actual contact conditions and level of rail wear. A number of rail profiles were selected and used as a worn rail case in the analysis. In the new rail case, the situation is complicated by the fact that the rail type changes along each of the lines. This includes a mixture of bullhead (BS 95lb) and flat-bottom (CEN 56E1) rail types.

LUL utilise two different wheel profiles, known as LT3 and LT5. Although LT3 was the original wheel profile for LUL rolling stock, the LT5 wheel profile was designed to eliminate flange contact occurrence on bullhead rails and to provide a relatively lower conicity when combined with a CEN 56E1 rail. The new and worn variants of the LT3 and LT5 wheel profiles were used for Bakerloo and Jubilee lines respectively. The wheel profile measurements which were again submitted by LUL were post-processed to select representative worn cases for use in the simulations.

The level of flange height and thickness of wheels in operation on the Bakerloo and Jubilee lines is plotted in Figure 4.5 and 4.6 below. The red points show the provided MiniProf wheel profile files. As it can be seen on the Figures, there is almost a linear relationship between flange height and thickness. This showed that although there was not a significant flange wear, the larger wear and flattening were predominantly observed on the tread which resulting in an increase in flange thickness as the datum moved down the flange. While the lubrication seemed to cause a reduction in flange wear, the low adhesion conditions may potentially increase the risk of sliding and give rise to flattening on wheels. In addition, hollow worn wheel profiles were observed on the Jubilee line which might be also stem from the excessive lubrication on the lines.
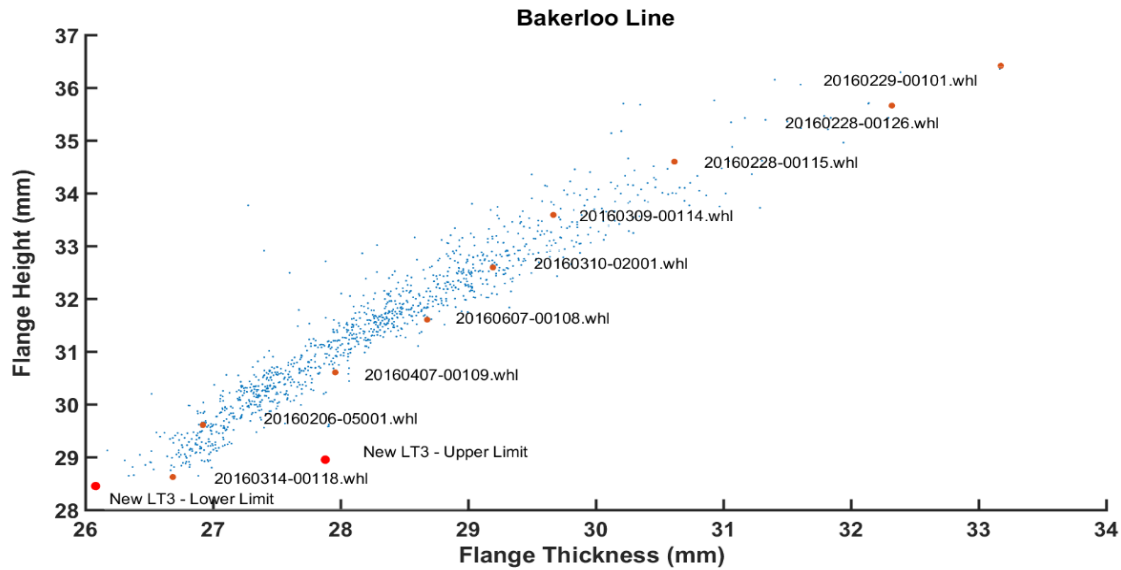
Figure 4.5: Flange thickness vs. flange height on Bakerloo line
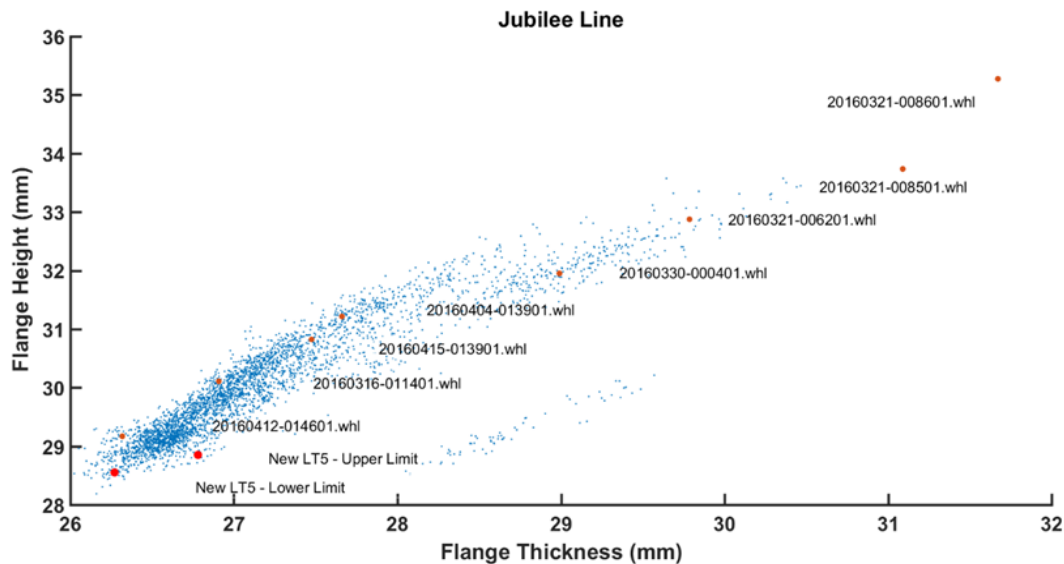


Figure 4.6: Flange thickness vs. flange height on Jubilee line

In order to identify the distribution/frequency of wheel wear, the flange height and thickness data are also presented as histogram plots in the Figure 4.7 and 4.8 for each line. Considering these distributions, the profiles listed in Table 4.1 were selected as representative of lightly, moderately and severely worn wheel cases for use in the simulations. Figures 4.9 and 4.10 illustrate the worn profile shape for each of the selected wheel profiles compared to a new LT3 and LT5 profile. For example; profiles '20160407-00109.whl' and '20160316-011401.whl' were selected as representative of a lightly worn condition as they correspond to approximately 40% and 50% of the profiles in operation on the Bakerloo and Jubilee lines respectively.
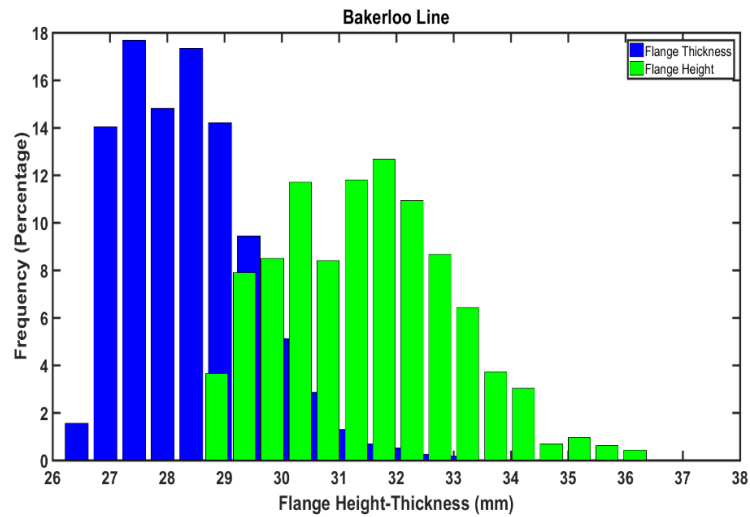
Figure 4.7: Flange thickness and height distribution on Bakerloo line
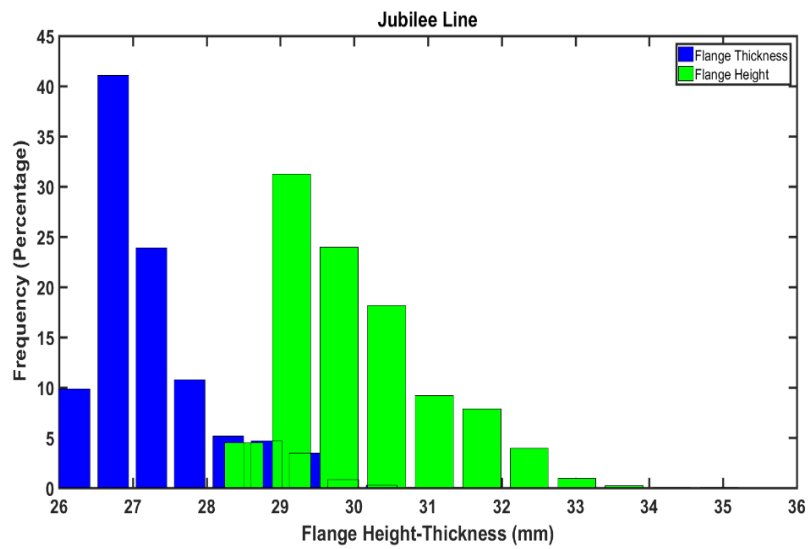


Figure 4.8: Flange height and thickness distribution on Jubilee line

Table 4.1: Selected worn wheel profiles

| | Wheel Profile Name | Flange Thickness | Flange Height | Distribution | Severity Condition |
|---|---|---|---|---|---|
| **Bakerloo** | 20160407-00109.whl | 27.96 | 30.6 | 40% | Lightly Worn |
| | 20160310-02001.whl | 29.19 | 32.59 | 40% | Moderately Worn |
| | 20160228-00126.whl | 32.32 | 35.66 | 20% | Severely Worn |
| **Jubilee** | 20160316-011401.whl | 26.15 | 30.15 | 50% | Lightly Worn |
| | 20160404-013901.whl | 27.37 | 31.23 | 30% | Moderately Worn |
| | 20160321-006201.whl | 29.22 | 32.91 | 20% | Severely Worn |
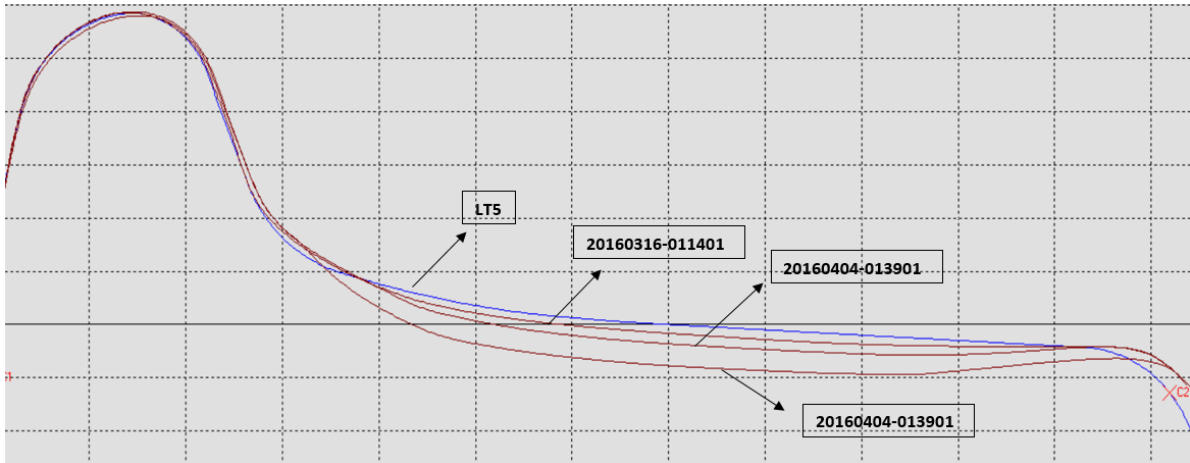
Figure 4.9: Selected worn wheel profiles compared to new LT5 profile condition – Jubilee line
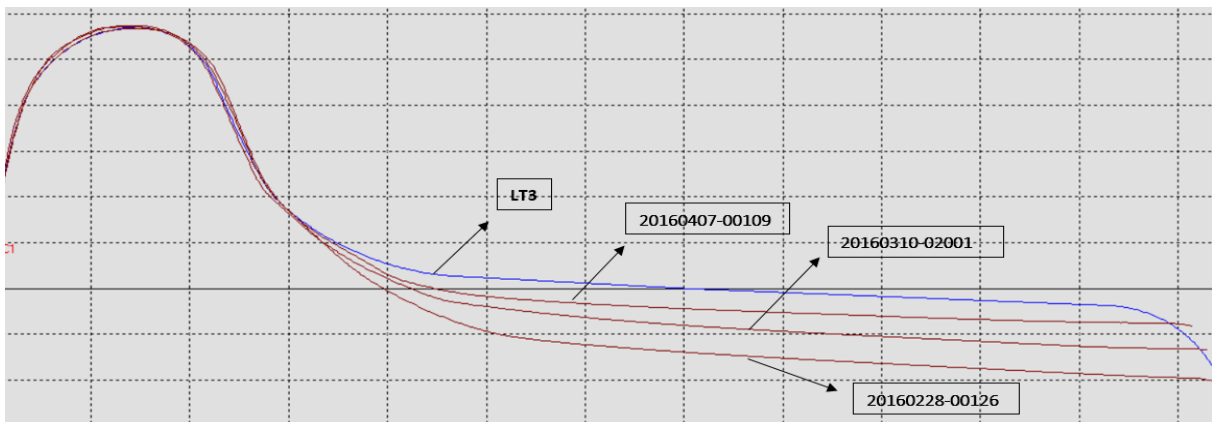


Figure 4.10: Selected worn wheel profiles compared to new LT3 profile condition – Bakerloo line

A VAMPIRE Track Contact File was prepared for each wear state defined in Table 4.1. This files defines how the wheel-rail contact data varies along the route due to changes in rail shape. The VAMPIRE transient analysis program linearly interpolates the contact data for each wheelset as it progresses along the track. The following Figure 4.11 shows an example of the contact conditions developed from different wheel and rail profile combinations along the route.
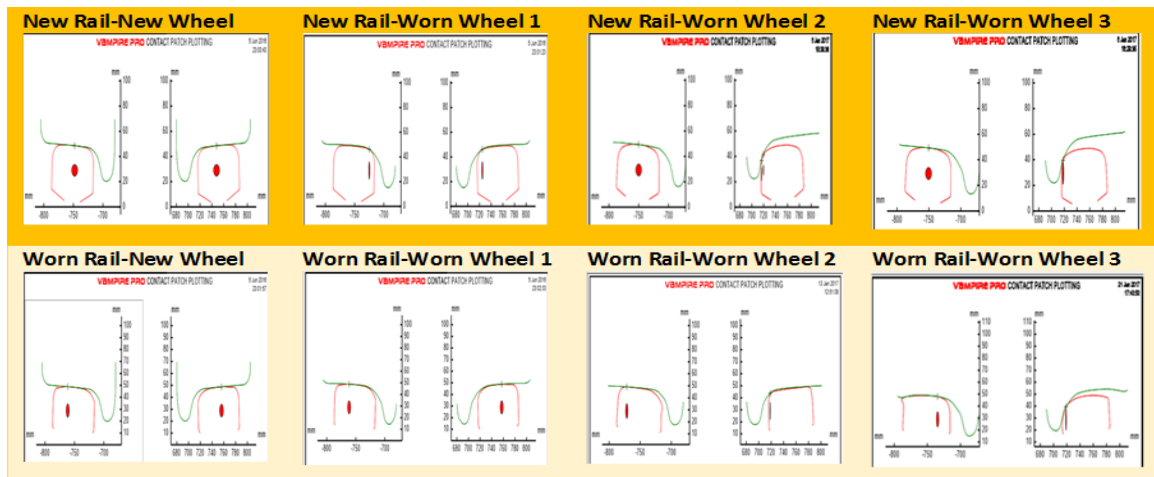


Figure 4.11: Example of the different wheel-rail contact conditions

## 4.2.3 Track model

In Vampire, track design and irregularity files can be used to represent the actual track geometry of the simulated route. Other track characteristics, such as variations in friction levels along the tracks can also be modelled. These features are very beneficial in rail damage modelling as they allow the effect of the influential factors to be studied as previously explained in this report. In this study, 4 different type of track files were prepared in order to represent the real characteristics of the tracks, including:

1) Track Design File
2) Track Irregularity File
3) Track Parameter File
4) Forcing History File

Track recording vehicles (TRVs) on LUL survey the railway lines at specified frequencies to show the actual condition of the track geometry. They collect information such as short wavelength lateral and vertical irregularities, curvature, cross-level (cant), twist, gauge and gradient. These measurements were acquired for both of Bakerloo and Jubilee lines and track irregularity files were prepared which contained the following information: curvature, lateral and vertical irregularities, cant and gauge variations.

In addition, a track design file was prepared which consisted of the vehicle speed data extracted from the Speed-Distance diagrams for each line. The characteristics of the Bakerloo line mean that check rails are present, therefore for the location of the check rails were also defined in the design file by specifying an appropriate flangeway clearances.

A track parameter file can be used in VAMPIRE to vary certain parameters with distance along a route, such as variations in track stiffness, friction levels or contact conditions. This research used a track parameter file to vary the friction levels which were changed according to the position on the railhead (e.g. wheel tread, flange and flangeback for check rails) and distance along the route.

Friction coefficient changes due to surface (material) conditions, contaminants and environment. Surface roughness, water, oil/grease, leaves, temperature and humidity can all influence the friction in various ways (E. Magel, 2017).

In this research, the friction coefficients in the track parameter file was mainly defined considering the previous studies' findings and the lubrication application on LUL. Table 4.2 shows the friction coefficients measured by hand-pushed tribometer. As it was expected, the dry rail had relatively larger values compared to contaminated conditions. Similarly, another study done by Swedish National Rail Administration stated that the friction coefficients were varied from 0.4 for dry rail to 0.1 with a blackish leaf layered rail (Olofsson, 2009).

Table 4.2: Friction coefficients measured with a salient system tribometer (Olofsson, 2009)

| Condition | Friction Coefficients |
|---|---|
| Sunshine dry rail, 19$^o$C | 0.6-0.7 |
| Recent rain, 5$^o$C | 0.2-0.3 |
| With a lot of grease on rail, 8$^o$C | 0.05-0.1 |
| Damp leaf film on rail, 8$^o$C | 0.05-0.1 |

Lubrication implementation on LUL generally depends on the "good practice" of track maintenance team and lubricator's subcontractor recommendations. They utilise vehicle and track mounted lubricators in order to mainly reduce wear and noise. Their position and type of lubricator used on each route were obtained and this mainly include the use of normal plunger operated track-mounted lubricators located on the high-rail and check-rail (Bakerloo line only) in curves. In addition, timer-based lubrication systems were installed from Green Park to Stratford and friction modifiers have been recently introduced at certain locations between Green Park and Canning Town.

In the lights of the above findings and lubrication implementation, a μ of 0.36 was selected in the tunnel sections, which is lower than the reported 0.4 range due to the success of on-board stick lubes system. Also, a lower value of μ of 0.25 was selected for the over-ground sections to take into account the environmental conditions. In areas where flange lubrication is present, the value of μ was reduced to 0.15. This also agreed with values from similar systems and previous simulation studies (Olofsson, 2009; Sinclair, 2004; Tunna, Sinclair, Perez, & Transit, 2007).

To predict the distance at which the lubrication is effective was difficult, since it depended on a number factors (Wilson, 2006):

- Application method: Normal plunged, timer based and etc.
- Type of lubricant: Additive chemicals (e.g. thickening agents, temperature control or quick drying additives).
- Frequency of Application
- Rate of Application (dose)
- Lubricator components: pump container, nozzle and hose system
- Grease consumption: depends on contact patch position, axle load and etc.

Although there are a number of studies which have been undertaken to determine this effective carry-over distance, it is still generally optimised through trial and error. In one of the oldest studies, it was stated that the ideal position for track-mounted lubricators should be at the onset of wear on the gauge face and the effective distance continued until

the gauge wear values decreased to normal limits (Frank, 1981). This finding was further analysed in a more detail during a recent study where it was concluded that this principle was more applicable for curves in the 400 – 600 m radius range (Marich, Kerr, & Fogarty, 2001). Another study postulated that the effectiveness of lubrication decayed exponentially starting from the application point (Thelen & Lovette, 1996).

Several simulations were conducted with varying friction levels to understand the influence of the lubrication. Generally, LUL positioned the high-rail lubricators at the onset of curves and the effective distance was selected starting from the application point to the point where flange contact ceased throughout the curve considering the relatively shorter curves' lengths in study network and the uncertainty in rate (dose) of application in each lubrication point.

VAMPIRE uses the pre-defined friction coefficients table to calculate creep forces based on the Kalker's relationship given in Figure 4.12. However, subsequent measurements showed a reduced initial slope (stemming mainly from contamination and surface roughness) and a falling friction (caused mainly by temperature and speed) from this curve. This may influence both wheel/rail contact parameters and vehicle dynamics behaviour (Vollebregt, 2014). Recently, more advanced friction models have been developed for use in vehicle dynamics simulations.
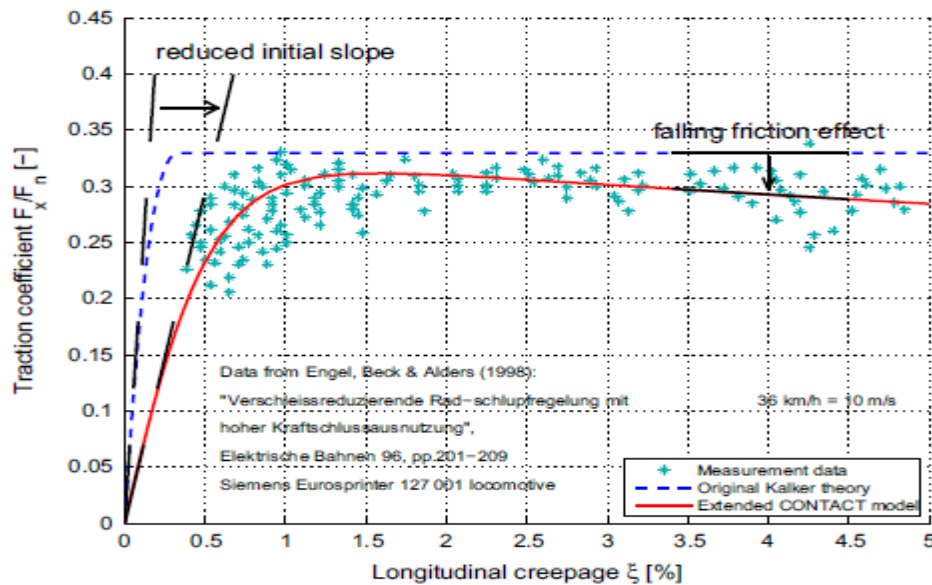


Figure 4.12: Theoretical and measured creepage-traction coefficient (creep force) relationship (Vollebregt, 2014)

## 4.2.4  Forcing history file

In order to investigate the effect of traction/braking forces on rail damage, which can be a significant factor in a metro–underground system, a forcing file was used to apply an external force to the wheelset during the simulation.

This file describes the applied torque at the wheelset due to traction/braking and was calculated from the total tractive effort required for the lead vehicle to accelerate/decelerate along the tracks and also considers the resistance forces acting in an opposite direction to the train motion. The total resistance is generally composed of the following resistance forces (Profillidis, 2000):

$$F_R = F_T + F_L \; ; \;\; F_L = F_{RIC} + F_{RIG} \tag{4.1-2}$$

where

$F_R$ = Total running resistance

$F_T$ = Train resistance

$F_L$ = Line Resistance

$F_{RIC}$ = Curve resistance

$F_{RIG}$ = Gradient resistance

## 4.2.4.1 Train resistance

The running resistance of the trains is often described with the help of the Davis' Equation which is as follows:

$$F_T = A + BV + CV^2 \tag{4.3}$$

The A, B and C are the train resistance coefficients and V is the vehicle speed (m/s). Firstly, the term $A + BV$ represents the mechanical resistance in which the coefficient A is related to the vehicle mass and the coefficient B is related to mechanical characteristics dependent on the rotation of axles, mechanical transmission and braking, etc. Finally, the third term $CV^2$ demonstrates the aerodynamic drag.

Generally, the empirical formulas which were developed by rolling stock manufacturers and railway administrations are used to solve this problem. In this research, one of the well-known formulas that was developed by Sauthoff for the suburban-passenger trains was applied. The coefficients in the formula were determined from the mass of the vehicles, a factor relevant with the number of axles, number of vehicles and a value stands for the cross-sectional area of the vehicles weighted with their aerodynamic behaviour (Brünger & Dahlhaus, 2008). The Sauthoff formula is given as:

$$F_T = (0.01 * m_w * g) + (a + c_b * (3.6 * v) + \frac{1}{Q}(0.0471) * (n_w + 2.7) * A_f (3.6 v_r)^2) \tag{4.4}$$

where $v$ =speed (m/s)

$\quad$ $v_r$ =relative speed between vehicle and air (m/s)

$\quad$ $m_w$= mass of the vehicle (kg)

$\quad$ $g$ =gravitational acceleration (9.81 m/s²)

$\quad$ $a$ = the coefficient is taken as $a = 1.9$

$\quad$ $c_b$ = factor for number of axles in vehicles ($c_b = 0.0025$ for 4 axles)

$n_w$ = number of vehicles in the train

$A_f$ = cross sectional area of vehicles (m²)

$Q$ = mass (tonnes)

Although the tunnel resistance was not considered individually, the previous research stated that for speed values lower than 100 km/h, this resistance force is highly dependent on train mass and it was one of the reasons for reducing the weight of metro rolling stock and suburban trains (Nielsen, 2016).

## 4.2.4.2  Line resistance

The line resistance was composed of curve and gradient resistances in this research. When a train passes through a curve, an additional force is applied against the running direction. This resistance is called as curve resistance and it becomes crucial in the narrower curves (Nawaz, 2015):

$$F_{RIC} = 0.01 * \frac{800}{R} \tag{4.5}$$

where $R$ = curve radius (m).

Through the flat regions, the train confronts no external force regarding the elevation differences. However, the gradient resistance appears when the train is running upwards or downwards. Whilst it becomes positive in the uphill gradient direction, it is taken as negative in the downhill gradient (Nan, 2011).

$$F_{RIG} = g * m * sin\alpha \tag{4.6}$$

where m=mass of train (tonnes)

g= gravitational acceleration

$a$ = degree of gradient

When the train motion is taken into account, the tractive effort is calculated from the below equation:

$$F_{TR} - F_R = f_P * m * \frac{dv}{dt} \tag{4.7}$$

where $F_{TR}$=Total tractive effort at wheel rim (N)

$fp$ = rotating mass factor, the rotating part of the train will also consume some effort depending on the different car units:

$$f_P = (f_{PT} * m_T + f_{PW} * m_{PW})/(m_T + m_{PW}) \tag{4.8}$$

where $f_{PT}$ = rotating mass factor for traction units

$m_T$ = weight of traction units

$f_{PW}$ = rotating mass factor for trailing units

$m_T$ = weight of trailing units

Then the applied torque (T) on wheelset is found by,

$$T = F_{TR} * R_{wheel} \qquad (4.9)$$

where $R_{wheel}$ = nominal radius of wheel.

### 4.2.4.3  Comparison of total tractive effort in the studied lines

In order to compare the total tractive effort on the studied lines, the total running resistances were firstly computed for both Bakerloo and Jubilee NB lines as demonstrated in Figure 4.13.
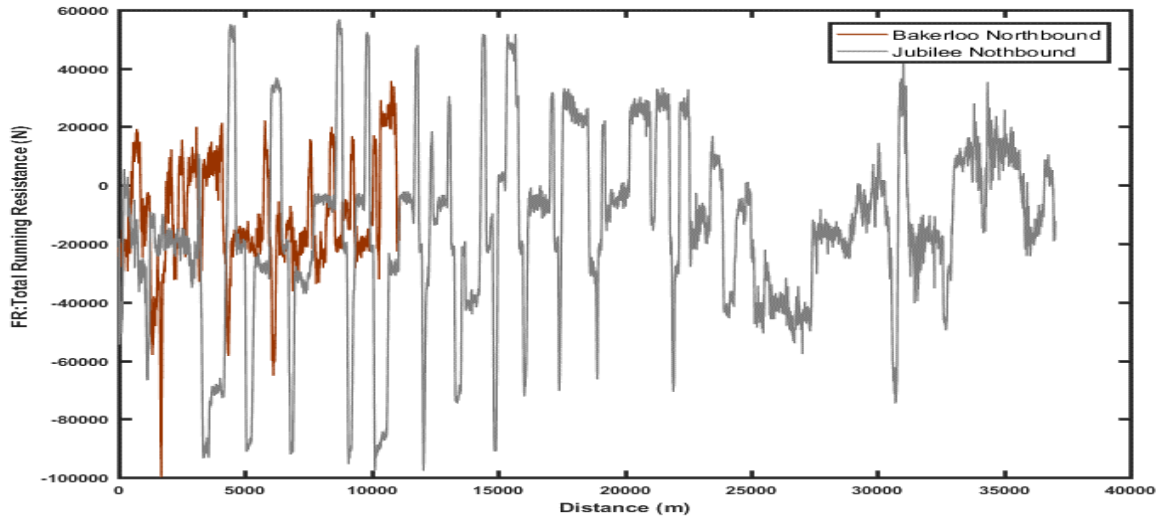


Figure 4.13: Comparison of total running resistance in Bakerloo and Jubilee NB lines

The total running resistance primarily depended on the gradient such that the resistance force became higher in the upward direction, whilst in the downward direction the resistance was negative. For instance, the instantaneous drop around Ch.1+600 km (around Waterloo Station) in Bakerloo line were caused from the tunnel elevation changes before passing underneath the Thames River. In addition, the higher running speeds and heavier vehicle mass had a significant impact on train resistance especially the larger train resistance as well as the increased gradient resistance in JLE section (between Ch.5+000-14+000 km) resulted in a larger total running resistance for the Jubilee line. Nonetheless, the small curve radii values in Bakerloo line increased the curving resistance to a greater extent and played a key role in the total resistance.

The traction forces presented in Figure 4.14 were largely influenced by acceleration/deceleration of the train movements. The highest levels (positive values) can be seen after the station platforms due to traction in these zones, the braking forces before station regions lower these values dramatically, resulting in a negative tractive effort. However, in contradiction to the expectations, which is higher running speeds and ATO mode will lead to greater traction forces, the short distance between stations affected the

acceleration and decelerations levels significantly on the Bakerloo line. The peak traction force values on the Bakerloo line became higher than the Jubilee line.
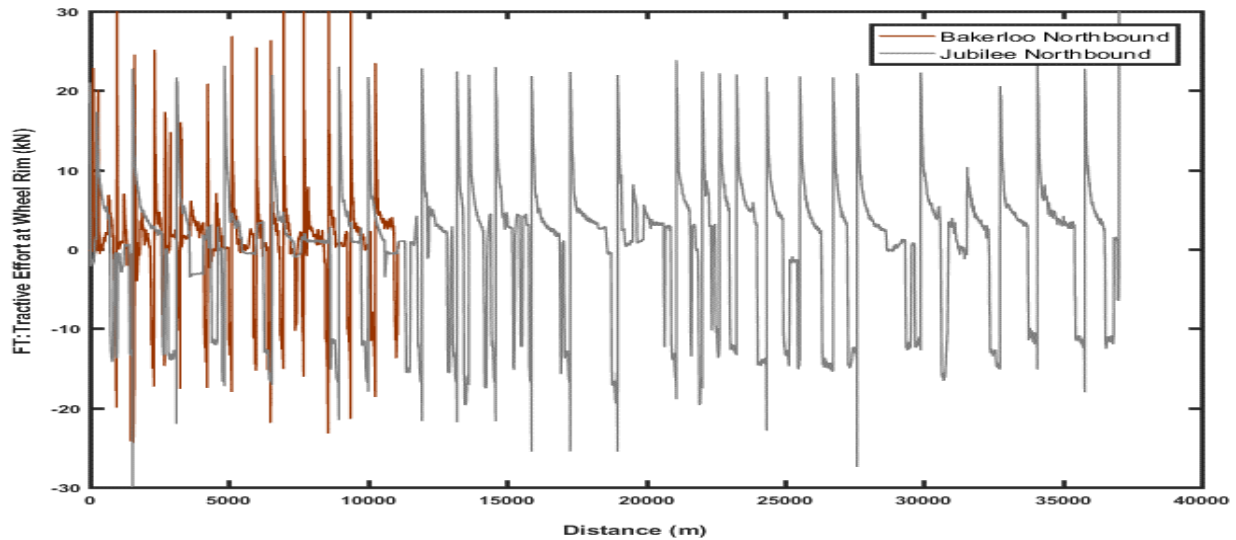


Figure 4.14: Comparison of total tractive effort in Bakerloo and Jubilee NB lines

## 4.3 Conclusions and discussions

This chapter explains the modelling which was used in the research to calculate the creepages, creep forces and other contact parameters used in the subsequent chapters. Firstly, the existing different wheel-rail contact models were reviewed, highlighting their assumptions and impact on rail damage modelling. Based on this review, the Vampire vehicle dynamic software was selected for this research due to its utilisation and success in previous WLRM studies. During these studies, the breaking points contained within the damage function were calibrated based on the global wheel-rail contact outputs, which are output from VAMPIRE. However, in order to investigate the effect of the local wheel-rail contact calculation, FASTSIM comparison was also provided in Chapter 9. However, it should be noted that the Hertzian model was used in both programs, as the previous study which applied relatively quicker non-Hertzian models stated that it may be difficult to apply on longer distances of track.

The second section of this chapter presented the preparation of the detailed route simulations for Bakerloo and Jubilee lines. The large of volume of track data was very beneficial and used as an input in the modelling. Variations in contact conditions were captured by considering both new and worn wheel-rail profiles. Worn rail profiles were measured at certain distance intervals along the lines by LUL, whereas worn wheel profiles were selected based on the distribution of flange height and thickness to represent lightly, moderate and severe worn conditions.

A Vampire track model was prepared for each route which describes the different route characteristics. This included: realistic vehicle speed profiles, actual short and long

wavelength track geometry, variations in coefficient of friction along the track to account for variations in lubrication/environmental conditions and the influence of traction/braking forces.

With respect to friction, it should be noted that even though it is influenced by factors such as surface roughness, speed, etc., the findings in previous studies and LUL's lubrication implementation were mainly considered in the development of a track parameter file. VAMPIRE computed the creep forces based on the single value of coefficient of friction and the given Kalker's creepage-creep force relationship. However, the previous measurements demonstrated that the relationship was affected by several factors.

In order to include the effect of additional traction/braking forces to simulations, which was stated to be major factor influencing rail damage on metro tracks, forcing history file was prepared from the total tractive efforts calculated for each vehicle on the studied lines. It was found that although the higher running speeds and ATO mode was expected to result in larger tractive efforts to Jubilee line, the short distances between the station significantly affected the results on Bakerloo line and made the peak values relatively higher.

# Chapter 5  Review of Influential Factors and Route RCF Damage Predictions

The WLRM was developed to predict the location of RCF cracks at a number of sites on the GB mainline railway network. Although the model has successfully predicted the location and severity of damage at a number of sites during previous studies, it has not been validated on routes with different operating conditions. When the different traffic and track characteristics of LUL are taken into account, the model may require certain modifications.

In this chapter, the influence of a number of factors on the 'signed Tγ' were investigated to evaluate the effectiveness of the model for use on LUL. Additionally, the 'signed Tγ' results produced on each line are compared with the reported defects and MRX-RSCM measurements.

## 5.1  Review of influential factors on Tγ

The Vampire route simulations have been used to evaluate the influence of additional traction/braking forces, curve radius, friction coefficient (lubrication) as well as different track irregularity levels and wheel–rail profile shapes on Tγ.

### 5.1.1 Effect of additional traction and braking forces on Tγ

Previous RCF damage studies conducted on metro-underground systems and from discussions held with LUL demonstrated that a higher number of defects were reported on track sections with high traction/braking forces. In order to understand the influence of traction/braking forces and the effect of ATO mode operation on rail damage, routes were selected with ATO (Jubilee line) and Manual (Bakerloo line) mode operation. The forcing history files, as described in Chapter 4.2.4, were included in the route simulations to allow the inclusion of the additional torque at the wheel-rail interface associated with traction/braking.

To assess the effects of the traction/braking torques on the creep forces and Tγ, a comparison was made between simulations with and without the additional traction forces. The cumulative distribution of the longitudinal creep forces at the tread and flange contacts that were primarily influenced by the torque on the wheelset are displayed in Figures 5.1 and 5.2. Although the additional torques tended to raise the longitudinal creep forces at tread contacts by approx. 6% and 4% on Bakerloo and Jubilee lines, respectively; it had relatively less influence on flange contacts. The traction/braking forces (traction coefficient) are limited by the friction coefficient which is pre-defined in the VAMPIRE simulations. The results show that while most of tread contacts did not reach the critical

limits, the lubrication on the majority of flange contacts caused a reduction in this limit and lead to slip (saturated) condition. However, it should be noted that to understand how these additional torques affect stick and slip conditions, local wheel/rail contact models, such as FASTSIM, which calculate the distribution of tangential forces within the contact patch should be used.

The positive (wheel) longitudinal creep forces in Figure 5.1, which corresponds to a negative direction on the rail, help to demonstrate the total distribution of affected regions within the current WLRM calculation (e.g. signed Tγ assumption). In this respect, 42% of the Bakerloo and 49% of the Jubilee lines were predicted to be susceptible to rail RCF damage with the remaining areas not under rail damage risk. The predicted risk became greater at flange contacts since over 60% of contacts had a longitudinal creep force in the positive direction, as presented in Figure 5.2.
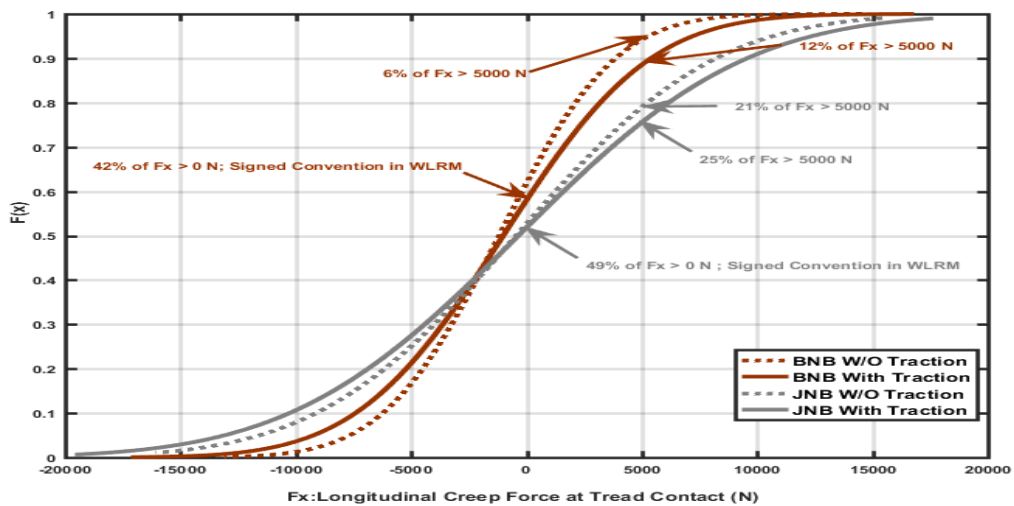


Figure 5.1: Cumulative distribution of longitudinal creep force at tread contacts on Bakerloo and Jubilee NB lines
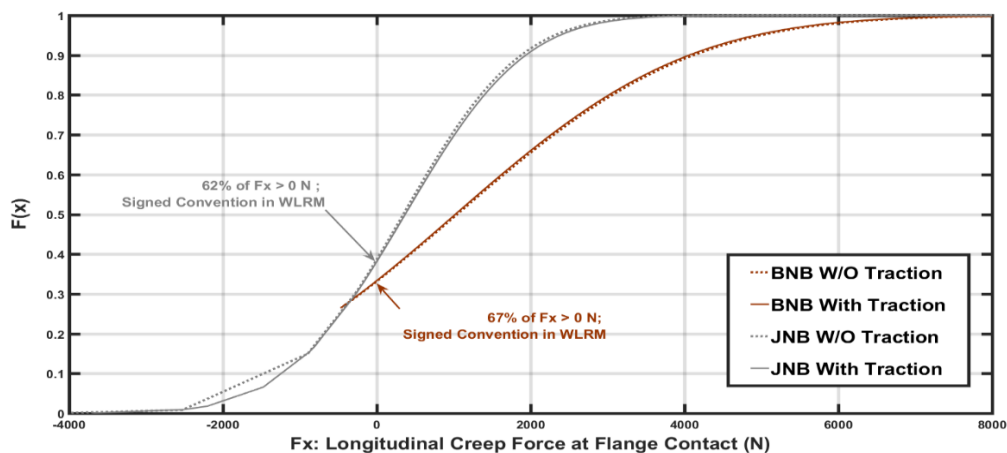


Figure 5.2: Cumulative distribution of longitudinal creep forces at flange contacts on Bakerloo and Jubilee NB lines

A comparison of Tγ values at both tread and flange contacts are presented in Figures 5.3 and 5.4. Despite the higher tractive forces on the Bakerloo line, the additional torque had a greater impact at tread contacts on the Jubilee line since they raised the results by approx. 12% in the region of peak RCF damage at a Tγ of 65 N. However, it was also noticed that while traction increased the tread contact energy on low rails (inner side of curved tracks), a slight decrease was observed on high rails (outer side of curved tracks). On sharper curves located on the Bakerloo line, the flange contacts were generally saturated contacts (full slip condition) therefore, resulted in only a small increase in energy levels. In addition, Figure 5.3 shows that approx. 70% of contacts on both lines produced energy levels that were higher than the fatigue threshold limit of 15 N. But, it should be noted that the presented energy is the 'raw Tγ' and hence the distributions were larger than compared to 'signed Tγ' case as previously mentioned. Although 65 N limit was exceeded at 50% of tread and 35% of flange contacts on Bakerloo line, 25% and 8% of contacts on the Jubilee line had higher energy levels.
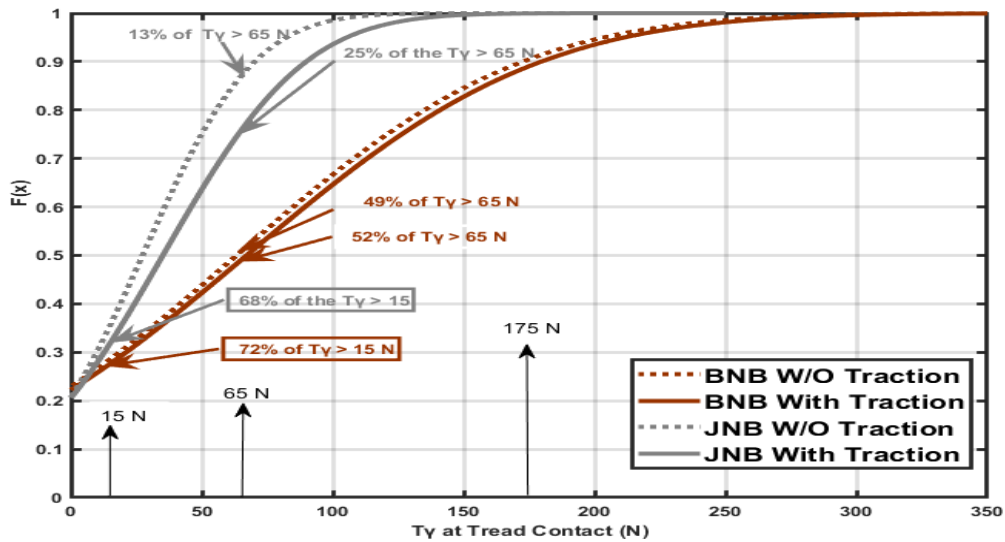


Figure 5.3: Cumulative distribution of Tγ at tread contacts on Bakerloo and Jubilee NB lines
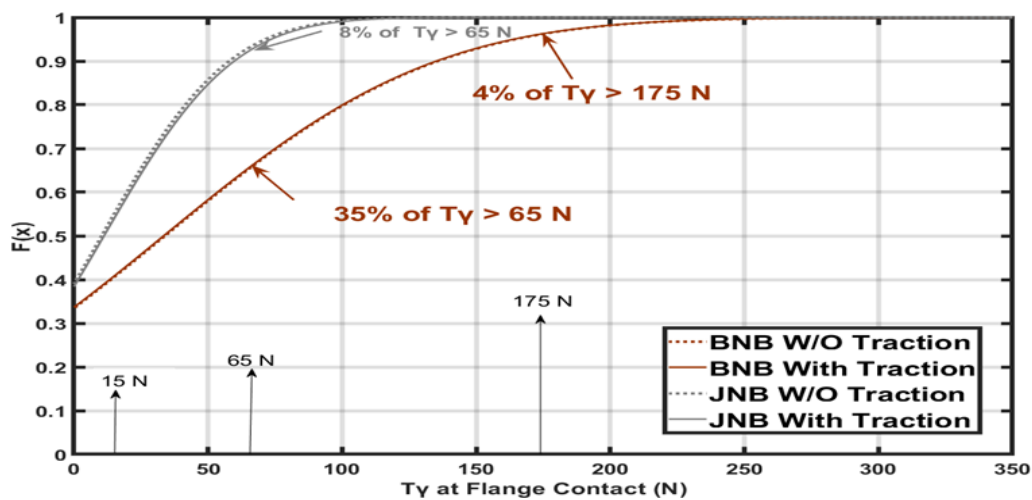


Figure 5.4: Cumulative distribution of Tγ at flange contacts on Bakerloo and Jubilee NB lines

## 5.1.2 Effect of curve radius on Tγ

Curve radius is one of the significant factors having an influence on the performance of the vehicle and hence the Tγ. Compared to mainline networks that often have minimum curve radii in the range of 300-500 m, metro systems generally consist of smaller radii curves down to 100 m. As the WLRM was validated on mainline curves of larger radii, the effect of the smaller curve radius seen on these routes on Tγ was investigated. Figure 5.5 shows the distribution of curve radius on the studied lines. The Bakerloo line consists of a large proportion of sharper curves between 100-150 m. Both lines also include a high percentage of curves in the 300-400 m radius range. Compared to the Bakerloo line, the distribution of shallower curves is relatively higher in Jubilee line.
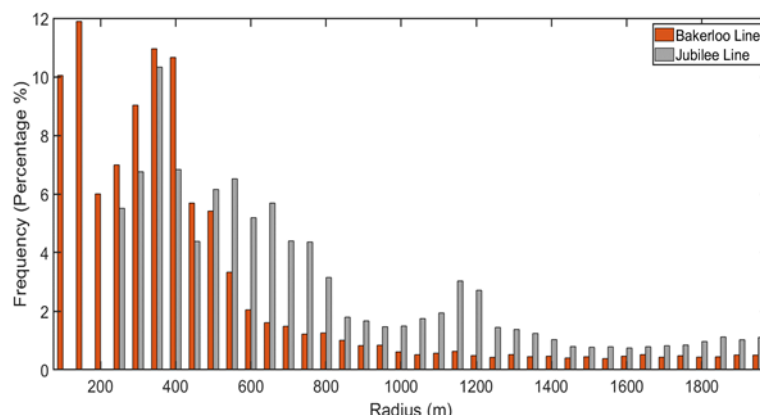


Figure 5.5: Curve distribution along the lines

The mean 'signed Tγ' values in each bin of the curve histogram were calculated and are presented in Figures 5.6 and 5.7. The former shows the mean 'signed Tγ' at flange and the latter gives tread contacts on the high rail (outer rail in curves) and low rail tread (inner rail in curves) contacts for each line. Regarding flange contacts, both of the lines generated similar energy values and wear risk at around a curve radius of 300 m, but the Bakerloo line produced higher RCF risk as the curve radius is increased. The LT5 wheel profile in Jubilee line generated lesser number of flange contact. Thus, the Tγ values were relatively smaller on this line and the number of flange contacts dramatically decreased after 900 m radius, with the exception of mean 'signed Tγ' of 85 N on the 1250 m curve.

The check rail contact in the Bakerloo line restricted the level of wheel flange contact on the high rail. In addition, the high traction forces especially in the station areas influences the direction of the creep force and result in positive forces for both low rail and tread contacts. Therefore, while flange contacts had lower energy in these curves (R<200 m), tread and low rail contacts had greater Tγ values resulting in higher levels of predicted wear than RCF damage.

In previous WLRM mainline studies, it was noted that the longitudinal creep force was often positive on high rails and negative on low rails. Therefore, while the model was often

able to demonstrate damage predictions on high rails, it usually showed no damage on low rails of mainline routes.  On LUL, the infrastructure characteristics play a key role at the wheel-rail interface and influence the "signed Tγ". Therefore, both the tread and low rail contacts on unchecked curves on the Bakerloo line produced larger 'signed Tγ' values. It can be seen in these Figures that all the contacts on the curves R<1000 m radius were under RCF risk.

The reduction at the number of the flange contacts in the Jubilee line gave rise to greater energy at the tread contacts. However, the longitudinal creep forces were mainly negative on the low rails and therefore, the 'signed Tγ' values were similar to mainline routes.

Furthermore, Figures 5.6 and 5.7 revealed that the wear was the most dominant mechanism especially on the sharper curves, while, the RCF risk became crucial for shallower curves on both lines. This might result in inaccurate predictions of rail damage since, the analysis of the field data analysis showed a higher number of squats and transverse defects were observed on the sharper curves located on the Bakerloo line. Similarly, the lower predicted damage risk on the low rail might lead to underestimation of shelling type defects observed on these rails, particularly on the Jubilee line.
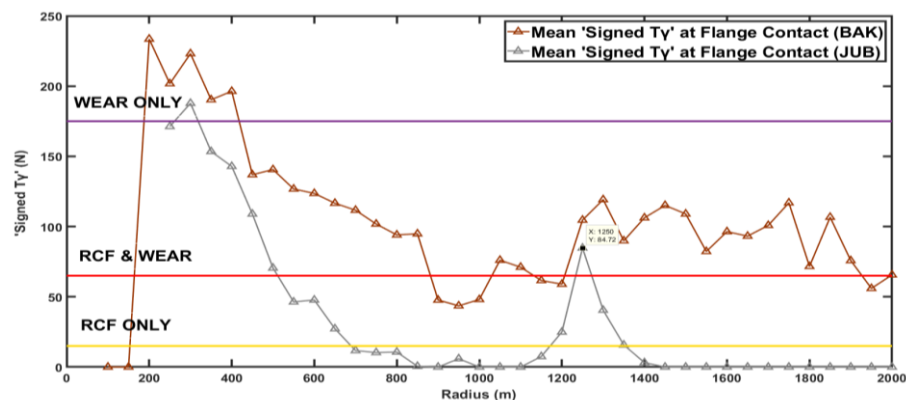


Figure 5.6: Effect of curve radius on mean 'signed Tγ' at flange contact
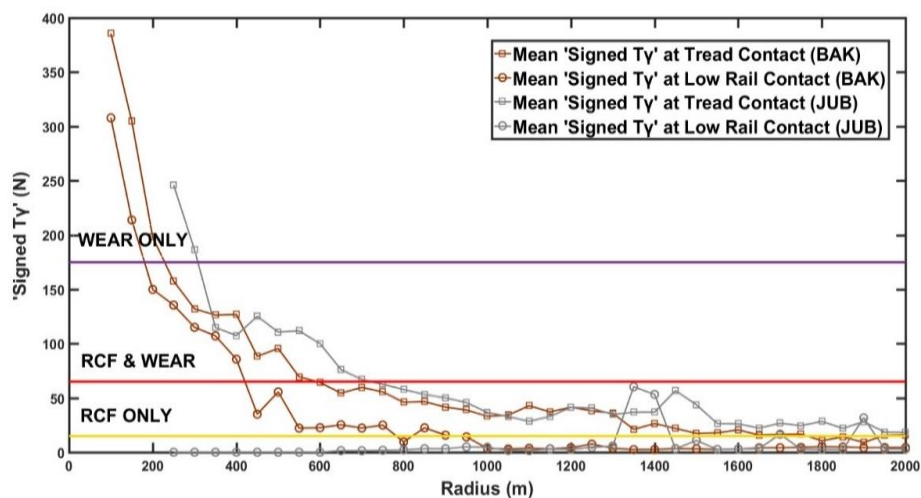


Figure 5.7: Effect of curve radius on mean 'signed Tγ' at tread and low rail contacts

## 5.1.3 Effect of friction coefficient on Tγ

The friction at the wheel-rail interface is critical in the management of wear and RCF damage, since high friction conditions lead to excessive wheel-rail wear, whereas excessive lubrication may increase the risk of crack growth. The actual friction conditions in the VAMPIRE models were described using a Track Parameter file as described in the Chapter 4, which describes how the coefficient of friction and its effectiveness vary along the route.

The original WLRM damage function was developed by selecting a high coefficient of friction as 0.45. This was primarily due to the uncertainty in the actual friction conditions on track and to incorporate the worst case scenario into the model. To demonstrate the influence of different friction levels on Tγ, the Jubilee line route simulations were conducted using different friction coefficients. Figures 5.8 and 5.9 demonstrate the mean 'signed Tγ' values for flange and low rail tread contacts, respectively. When using a μ = 0.45, the highest energy levels at both flange and tread contacts are predicted. Reducing the friction coefficient decreased the mean 'signed Tγ' and the overall damage risk. However, the reduction in wear risk due to lubrication on the tighter curves of the Jubilee line gave rise to RCF risk. This means that the lower wear rate may raise the crack growth rate and make high rails more susceptible to RCF damage risk which was also observed in the field crack data analysis.
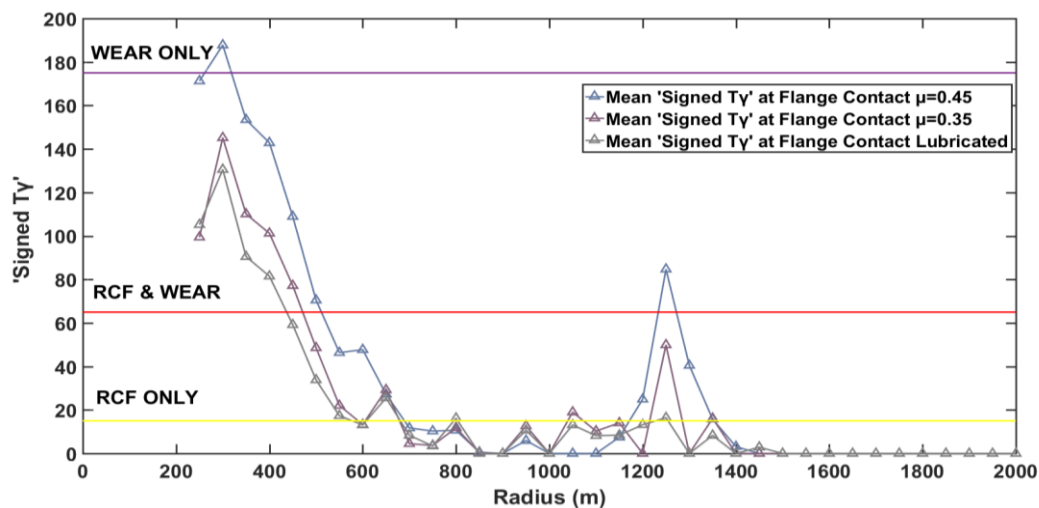


Figure 5.8: Effect of different friction conditions on mean 'signed Tγ' at flange contacts

High rail flange lubrication was shown to have an adverse effect on the low rail. When there is two-point contact on the high rail, the steering forces were distributed between tread and flange contacts. However, as the lubrication reduced longitudinal creep force (steering force) from flange contacts, the energy levels increased at the low rail contact. This might be also resulting from the change in creep force direction at this contact. For example, the mean 'signed Tγ' value of zero on the 300 m radius curve increased to 95 N.
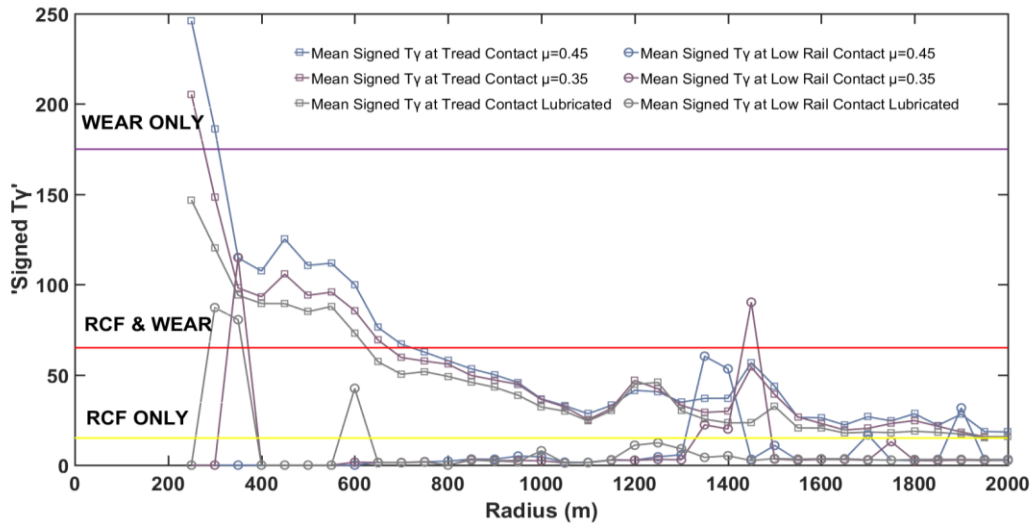
Figure 5.9: Effect of different friction conditions on mean 'signed Tγ' at tread and low rail contacts

It should be noted that VAMPIRE calculates the creep forces (accordingly Tγ) based on the given Kalker's relationship model considering pre-defined friction coefficients in the simulations. But, in reality it is affected by changes in material properties (at interfacial layer) and surface conditions such as contamination, roughness, speed and etc. Therefore, in order to obtain more accurate results, more advanced models should be used in vehicle dynamics simulations.

## 5.1.4 Effect of track irregularity on Tγ

The installation errors during track construction and deviations caused by deterioration following high number of vehicle passages lead to track irregularities in the railway lines. Measured track irregularities were obtained from LUL from a Track Recording Vehicle (TRV). This data includes outputs such as curvature, vertical and lateral track irregularities, cant and gauge variations.

The influence of track irregularities on the mean 'signed Tγ' at flange and tread-low rail contacts of Jubilee line are compared in Figures 5.10 and 5.11, respectively. Removing (No IRR) and scaling (Sc IRR) the track irregularities had little effect on the magnitude of Tγ values on the Jubilee line, but it was noted that they had a major impact on the distribution of the contact position on the railhead. For example, there was no flange contact generated with zero and scaled irregularities at shallower curve radii whereas, with irregularities flange contact occurred on 1250 m radius curve with a mean 'signed Tγ' of 85 N. Additionally, the energy and RCF risk substantially increased at the low rail contact of 1350 m radius curve.
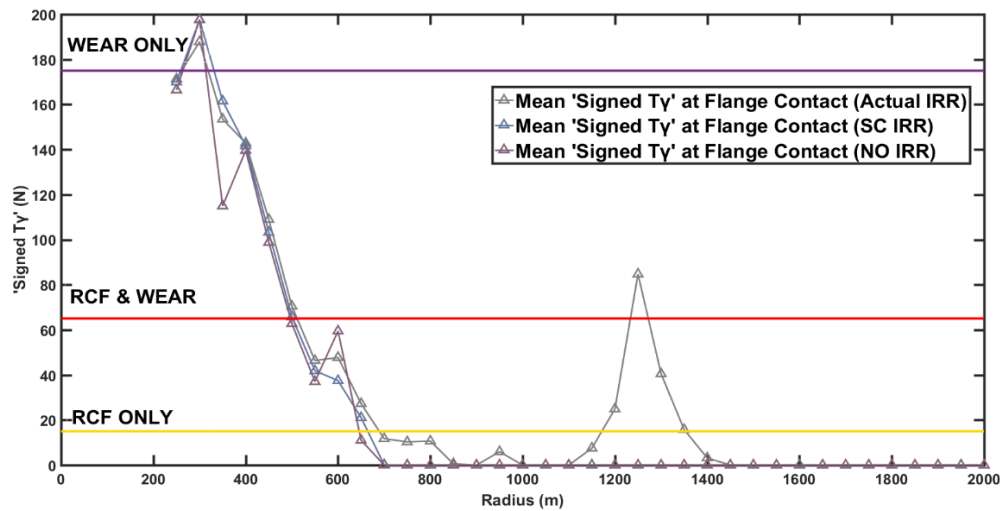
Figure 5.10: Effect of track irregularity on mean 'signed Tγ' at flange contacts
(Note: Actual IRR = measured TRV data, No IRR = No irregularities and Sc IRR = Scaled irregularities)
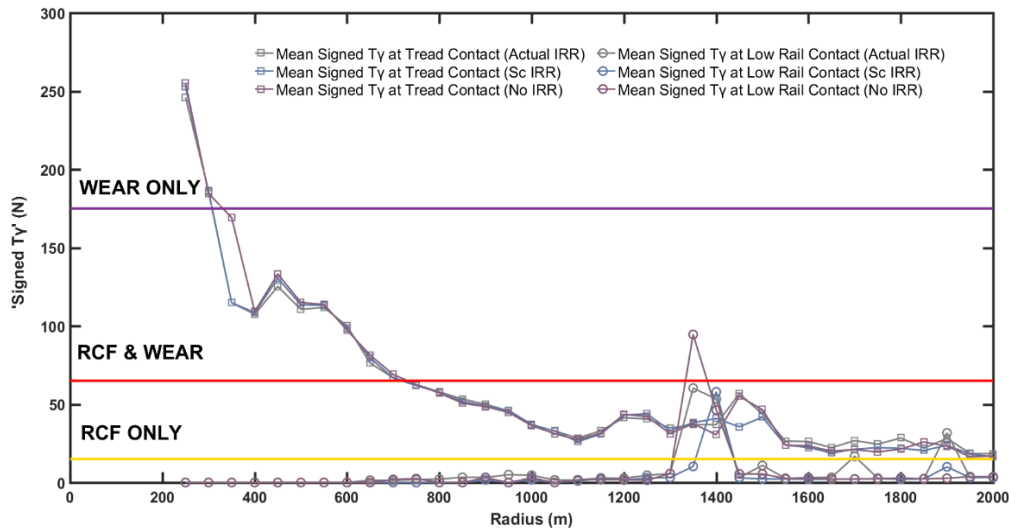


Figure 5.11: Effect of track irregularity on mean 'signed T' at tread and low rail contacts
(Note: Actual IRR = measured TRV data, No IRR = No irregularities and Sc IRR = Scaled irregularities)

## 5.1.5 Effect of different profile shapes on Tγ

In the rail damage modelling, it is important to take into account different wheel-rail profile combinations as the wheel and rail geometry play a key role in the determination of contact conditions and forces. The results provided in the previous figures were prepared considering new rail and wheel profile pairs. However, the shape of rail profile frequently changes along the route due to wear, grinding and/or renewals. Similarly, the wheel profiles also wear over time and are re-profiled at various intervals.

A comparison of the Tγ using new (NN) and worn rails with lightly (WW1), moderately (WW2) and severely (WW3) worn wheel profiles are given in Figure 5.12, 5.13 and 5.14 for flange, high rail tread and low rail tread contacts, respectively. The determination of severity of worn wheel profiles and their distribution on the Bakerloo and Jubilee lines were explained in detail in Chapter 4.2.2.

Generally, wheel and rail profiles wear to shapes that give rise to conformal contacts at the wheel-rail interface, resulting in an increase in conicity. However, due to lubrication and changes in rail-wheel material properties, the distribution of conformal contact conditions was varied throughout the routes.

As it can be seen in Figures 5.12 and 5.13, the lightly worn profile (WW1) generated a lower conicity which caused an increase in the Tγ at the flange contact and a reduction at the tread contacts, with the exception of 300-400 m curve radius range. The hollow worn wheel profiles (WW2 and WW3) had no significant influence at the tread contact, however, they led to higher levels of Tγ at the flange contact. Furthermore, results at the low rail tread contact, presented in Figure 5.14, shows that the worn cases changed the creep force direction in a very small section of the Jubilee line. Therefore, the mean 'signed Tγ' values is dramatically increased for a small number of low rail contacts.
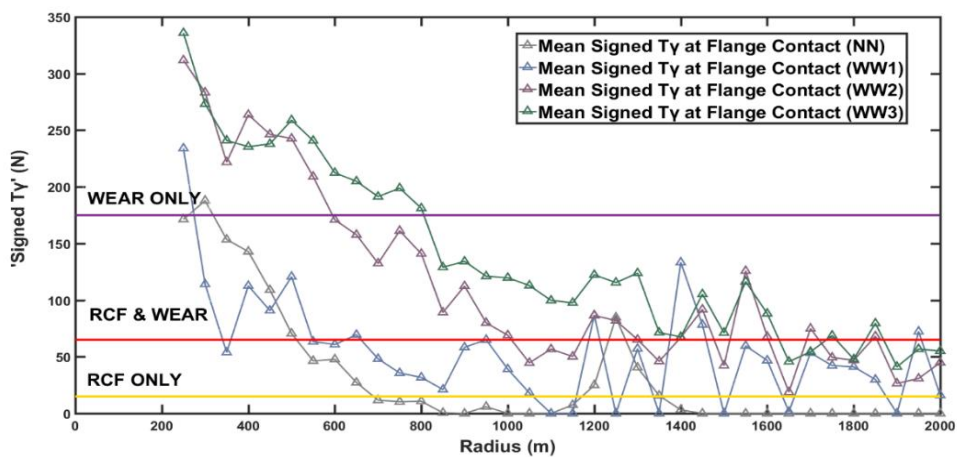


Figure 5.12: Effect of worn case on mean 'signed Tγ' at flange contact
(Note: NN=New rail and wheel profile, WW1=Worn rail and lightly worn wheel profile (1),
 WW2=Worn rail and moderately worn wheel profile (2), WW3=Worn rail and severely worn wheel profile (3))
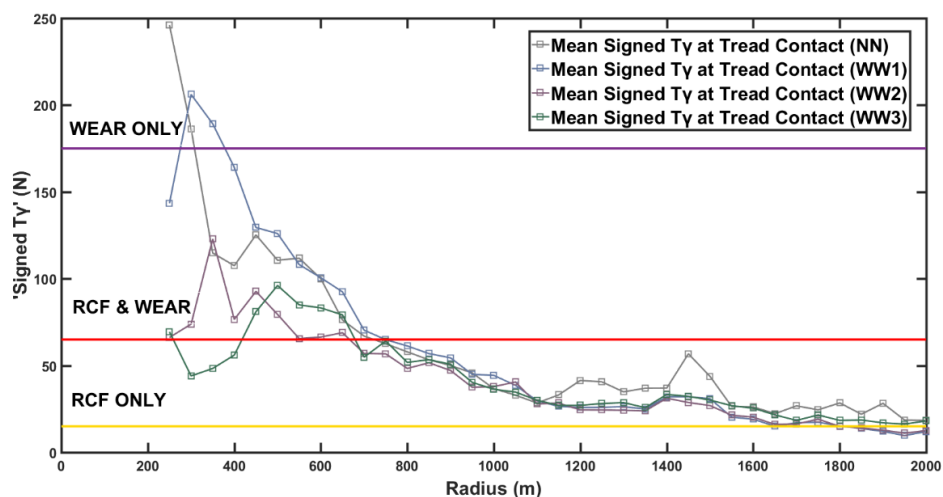


Figure 5.13: Effect of worn case on mean 'signed Tγ' at tread contact
(Note: NN=New rail and wheel profile, WW1=Worn rail and lightly worn wheel profile (1),
 WW2=Worn rail and moderately worn wheel profile (2), WW3=Worn rail and severely worn wheel profile (3))

117
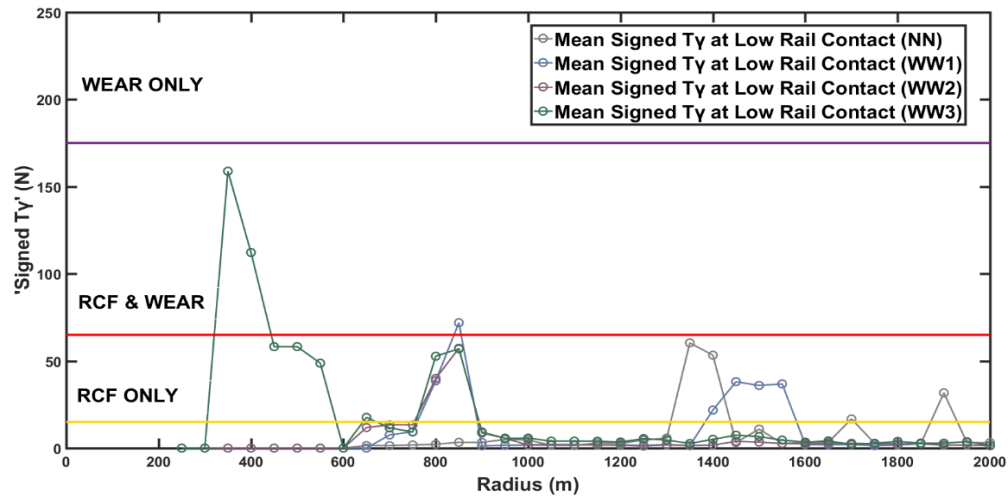
Figure 5.14: Effect of worn case on mean 'signed Tγ' at low rail contact
(Note: NN=New rail and wheel profile, WW1=Worn rail and lightly worn wheel profile (1),
 WW2=Worn rail and moderately worn wheel profile (2), WW3=Worn rail and severely worn wheel profile (3))

The comparisons presented above demonstrated the influence of different profile shapes on the prediction of rail damage. Since the vehicles have variety of worn profiles in real traffic operations, each passage of wheel will contribute to either wear/RCF or no damage risk. Therefore, the total damage predictions generated by each wheel/axle pass should be accumulated to account the interaction of wear and RCF for the life of a rail.

It should be noted that although the effect of friction, track irregularities and different profile shapes on 'signed Tγ' were presented for only the Jubilee line, similar results were also obtained for the Bakerloo line and hence they are not presented in the thesis.

## 5.2  Route RCF damage predictions

In this section, predictions of 'signed Tγ' were compared with observations and measurements of damage from site. Instead of using the Damage Index output from the WLRM, the 'signed Tγ' values calculated from the different simulation cases were used in damage prediction. Due to uncertainties in the breaking points associated with the WLRM damage function, such as the fatigue threshold and Wear-RCF balance, for use on metro systems, the computed values were compared with the field observation data in order to examine the efficiency in predicting the defect location along the route (longitudinally) and to evaluate its effectiveness in differentiating between damaged and undamaged areas. However, it should be noted that although the cracks reported as RCF related damage in the defect data sheet and MRX-RSCM was assumed to measure the RCF related cracking, thermal damage associated cracking (e.g: wheel burn and stud defects) could be recorded as fatigue-induced cracking due to similarity in their superficial appearance. In addition, while many factors are influencing the RCF developments, the reported defects highly depended on rail age (recent replacements) and grinding activities. In the research, rail maintenance history data was also considered in the correlation of damage predictions.

## 5.2.1 Bakerloo (NB) line

Since the purpose of this part of the research is to evaluate the accuracy of the damage predictions (longitudinally) along the route, the 'signed Tγ' was compared on both of the rails. In case of two-point (tread and flange) contacts which was particularly evident on the outer (high) rails of curved tracks, the Tγ values were summed to find the maximum energy produced at that distance on the lines. Figure 5.15 was developed which provides a colour contour showing the level of the summed Tγ values, while the x-axis displays the distance along the route, the track cant values (±20 mm corresponds to straight sections) is plotted on the y-axis. A summary of the other operation and track characteristics on this line are provided in the Chapter 3.1.1.
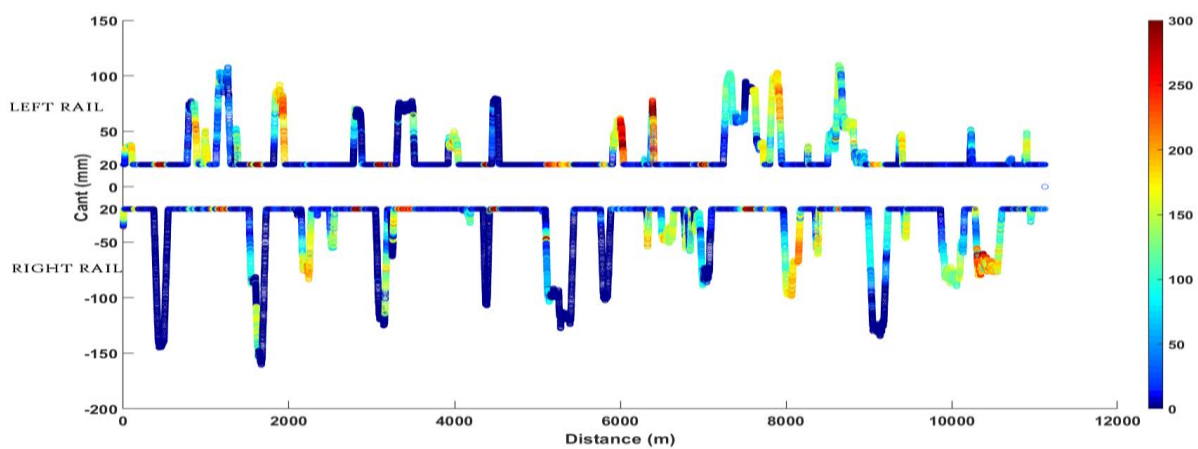


Figure 5.15: 'signed Tγ' results on the left and right-hand rails of Bakerloo NB line

The "signed Tγ" assumption demonstrated high results on both high and low rail RCF damages especially in the checked curve sections of Bakerloo (NB) line. Although flange contacts had relatively less number of occurrences and produced slightly smaller results in these sections, the higher energy at tread contacts helped to demonstrate the severity on some of the high rails. As expected from the results of the previous study, the low rails had also large values. Additionally, the station names are presented in Figure 5.15, as it was noticed that the damage predictions were influenced by the high traction/braking in these zones and the check rail and the track lubricator positions are displayed in Figure 5.16 below in order to demonstrate their impact on the 'signed Tγ' values. The large cant values and the lubrication implementation in the check rail sections had a significant impact on the Tγ values, particularly on the high rail. For example, while the non-existence of lubrication in the proximity of Waterloo station resulted in a Tγ of 150 N on the high rail, this was reduced to 100 N in the Regent's Park Platform where lubrication was applied at the beginning of the curve. Additionally, the influence of traction/braking forces were analysed which showed that both traction and braking regions were heavily affected. However, in the straight platforms, such as Charing Cross Platform, the energy became larger especially in the traction regions.
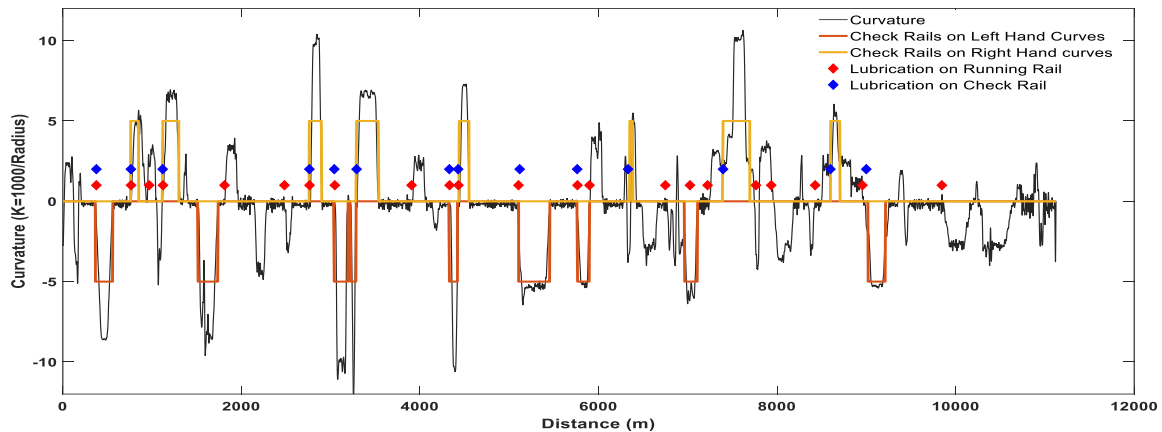
Figure 5.16: Check rail and track lubricator positions in the Bakerloo NB line

The damage susceptibility predictions were compared with the defect information and measurements obtained from the MRX-RSCM. The upper plot in Figure 5.17 included the defects measured on the right rail of the Bakerloo line whereas, the bottom plot shows the Tγ values. As indicated by the blue arrows, several locations of high 'signed Tγ' coincided with locations of reported cracks. The damage particularly on the high rails of the curve section (radius>200 m) at Ch.8+000 km and the low rails of the check rail sections at Ch.3+000 km showed good agreement with the predictions. But, the damaged regions which are indicated by orange arrows could not be predicted using the 'signed Tγ'. For instance, the cracks on the low rails around Ch.1+000 km and the tangent tracks at Ch.5+500 km. Nevertheless, the 15 N limit in the current WLRM might be appropriate to predict this damage. Another important observation is that although the two curves at Ch.10+000 km had similar curvature ranges, the transverse defects were only reported in the second curve owing to traction effect after Kilburn Park Station. Although, the energy values were high on the first curve, no defects were reported as indicted by black arrow.
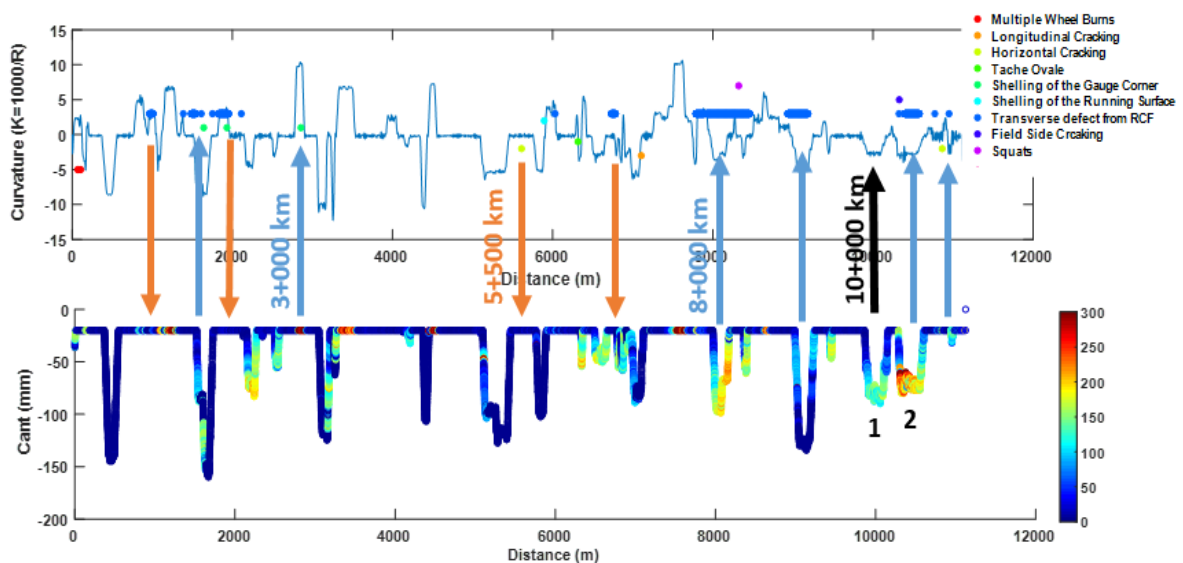


Figure 5.17: 'signed Tγ' predictions and reported defects on the right rail of the Bakerloo NB line

120

Using the MRX-RSCM crack depth data in the validation process will be more beneficial as the measurements were provided for the entire line and the crack depth is an essential parameter in the assessment of crack severity and maintenance decisions. However, discrepancies in the distance of these measurements made the validation difficult, as detailed in Chapter 3.3.3. Figure 5.18 illustrates the MRX-RSCM measurements in 2014 and 2015 on the right rail of the Bakerloo line and their comparison with the Tγ levels. Some of the blue and orange arrows were highlighted to demonstrate the matched locations with the defect data. For example, the MRX-RSCM inspection device also detected transverse defects at around Ch.8+000 km and the reported horizontal cracking at Ch.5+500 km. However, the low Tγ generated in the latter section cannot predict this damage.
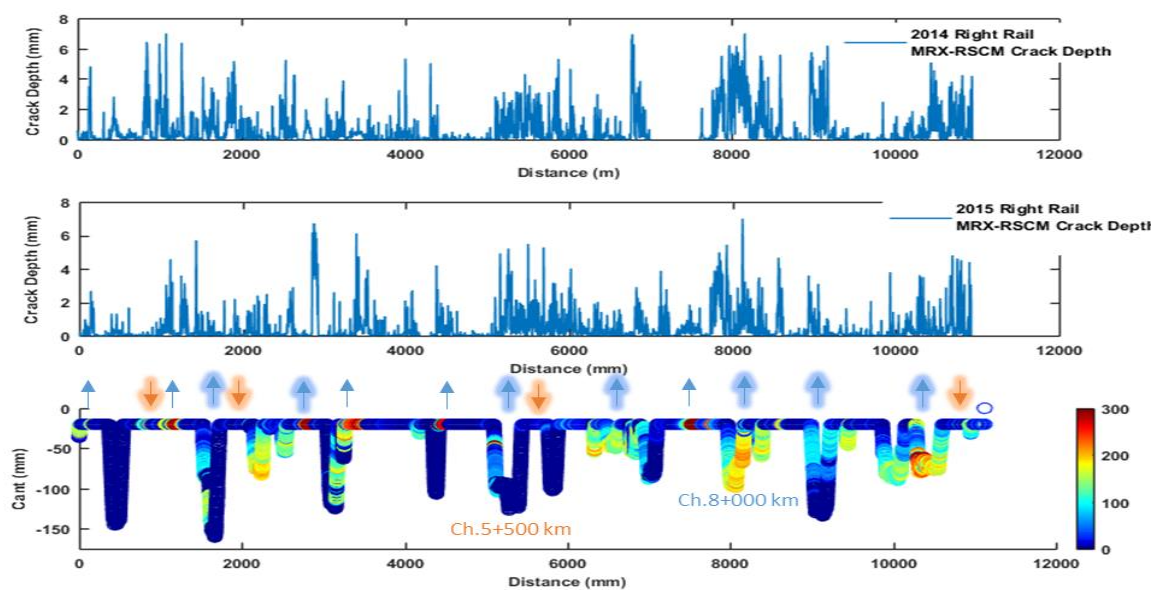


Figure 5.18: 'signed Tγ' predictions and MRX-RSCM measurements on the right rail of the Bakerloo NB line

The observed defects on the left rail of the Bakerloo line provided relatively better correlations with the Tγ levels as illustrated in Figure 5.19 below. However, the black arrows again demonstrated the uncorrelated regions where the increased 'signed Tγ' values produced on the high rails. Figure 5.20 illustrates the MRX-RSCM measurements on the left rail and shows a good match with higher levels of Tγ at several locations, identified by the increase in the number of blue highlighted arrows. Contrary to the observed defect data, the MRX-RSCM measurements demonstrate damage on low rails of the checked curved track sections which in turn provided a better correlation with the level of Tγ, such as at Ch.1+800 km and 7+000 km. In addition, even though the 'signed Tγ' successfully predicted the damage on most of the high rails of checked curves due to higher values generated at tread contact, it produced zero damage at Ch.4+500 km. Nonetheless, this provided a good correlation, as there were no cracks detected by the inspection tool.
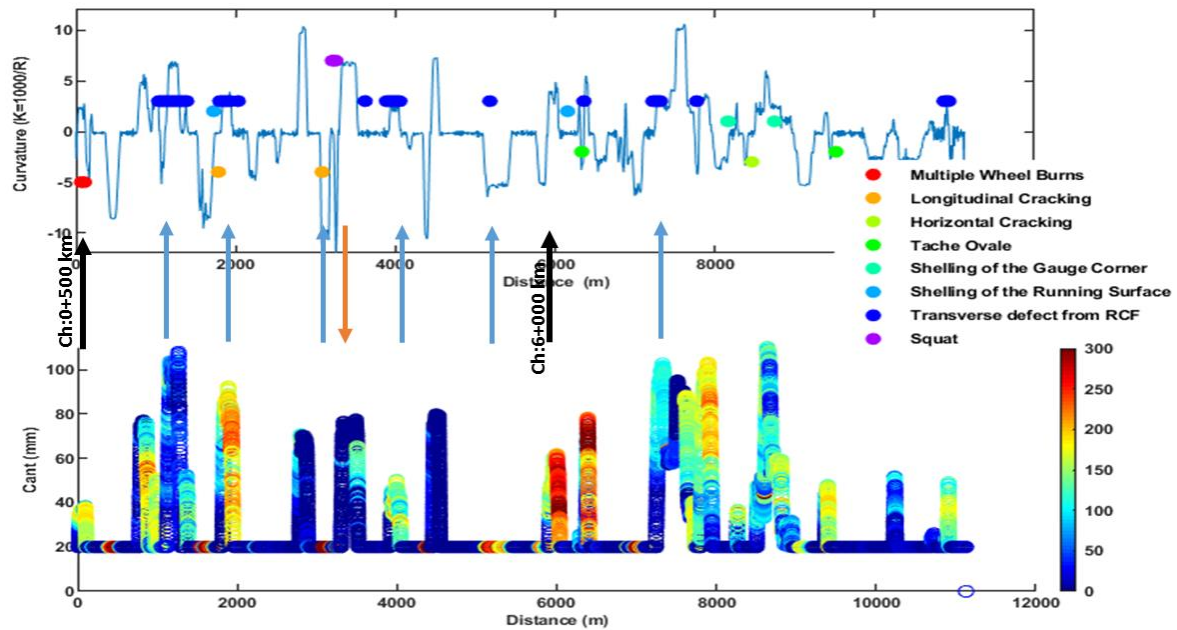
Figure 5.19: 'signed Tγ' predictions and reported defects on the left rail of the Bakerloo NB line
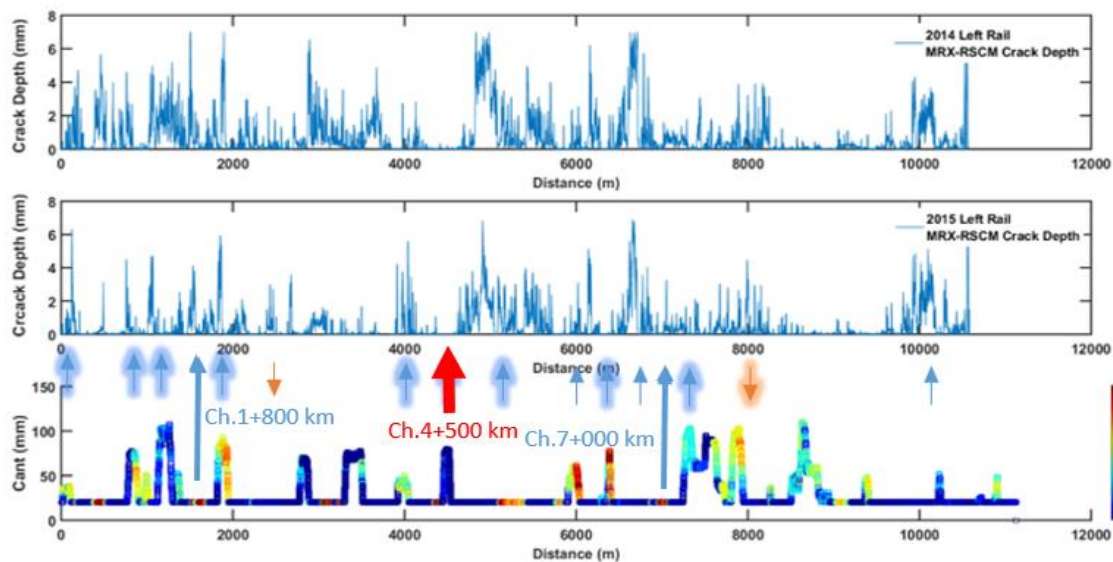


Figure 5.20: 'signed Tγ' predictions and MRX-RSCM measurements on the right rail of the Bakerloo NB line

In summary; the track characteristics and high levels of acceleration and braking associated with stations' locations were shown to have a significant influence on the energy levels of the Bakerloo line. The 'signed Tγ' predicted locations susceptible to damage on both high and low rails of checked curves due to greater energy generated at tread (high rail) and low rail contacts. In addition, it was also noted in some of the high rail checked curves that signing the Tγ based on the longitudinal creep force helped to differentiate between damaged and undamaged areas, since lower energy levels were indicated at sites where no RCF cracks were reported. However, the 'signed Tγ' approach provided several poor predictions on shallower unchecked curves (R>200). While the damage susceptibility on certain high rails was overestimated, it underestimated the number of locations on low rails and tangent track sections. The inclusion of the additional forces associated with

traction and braking and the speed variations stemming from the stop-start nature of the operation influenced the direction of creep forces and in some cases produced larger Tγ values in tangent platform sections compared to other tangent tracks on the line.

## 5.2.2 Jubilee (NB) line

The Jubilee (NB) line also has curvaceous track geometry but the minimum curve radius is 250 m and hence, no checks rail were required for this line.    Figure 5.21 demonstrates the 'signed Tγ' values generated on both left and right rails of the line. In addition, the tunnel entrance and exit and some of the stations' locations are presented in the plot. The other line characteristics are provided in the Chapter 3.1.2.
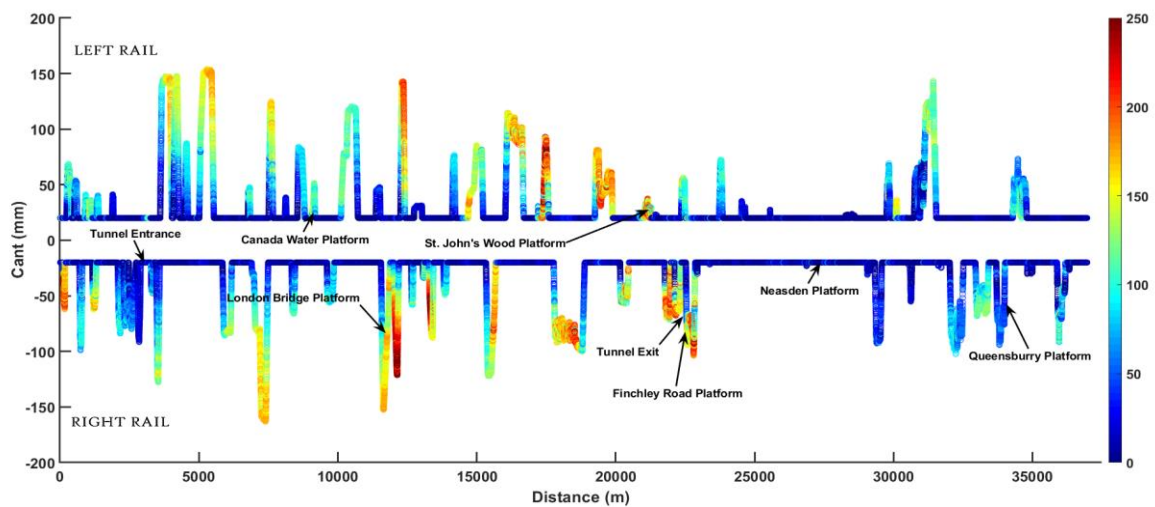


Figure 5.21: 'signed Tγ' results on the left and right rails of the Jubilee NB Line

Owing to larger curve radii and the increased number of tangent platforms, the maximum energy level was relatively smaller than seen in the Bakerloo line. The higher Tγ values can be seen on the high rail of the curve sections and particularly inside the tunnel due to higher friction coefficient compared to outside regions. In order to demonstrate the effect of lubrication, the track lubrication points are also presented in Figure 5.22.
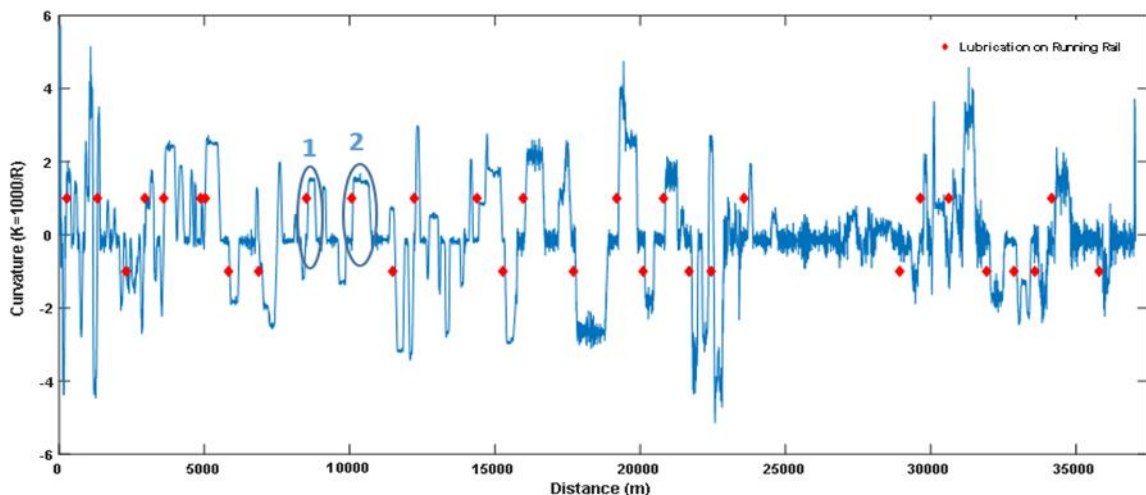


Figure 5.22: The track lubricator point positions in the Jubilee NB line

As it was expected, due to their proximity to traction zones, higher energy levels were occurred at curved platforms located at St. John's Wood and Swiss Cottage tube stations and tangent platform in the Neasden station. Although Canada Water was not located on curved tracks, it was noticed that the Tγ levels were substantially increased particularly on the curves which were located just after these stations due to the larger traction forces. However, this situation became more critical when there was no lubrication applied in tracks such as London Bridge platform. In addition to the traction effect, the large cant had a significant influence on Tγ levels such as the greater cant in 2$^{nd}$ curve highlighted in Figures, resulted in a lower cant deficiency and increased Tγ by approx. 50 N.

The reported defects on the left rail and the associated damage susceptibility predictions are presented in Figure 5.23. It demonstrates that "signed Tγ" was again successful in predicting the locations with observed high rail shelling type of defects especially between Ch.15+000-23+000 km. However, the location of low rail shelling and the squats which were largely reported in the Ch.23+000-35+000 km (outside section) could not be predicted. However, it was declared by LUL staff that some of the reported squats in these long tangent track sections could be stud type defects, which are associated with thermal damage rather than fatigue and therefore, it cannot be expected that Tγ would predict these defects. Even though no defects were reported in the JLE section between Ch.5+000-14+000 km, this resulted in poor agreement with the higher levels of Tγ on the high rail of curves in this section. Smaller crack depths can also be seen in the MRX-RSCM measurements in Figure 5.24 which might stem from aforementioned reasons in Chapter 3.3.4. The decrease in the successive crack depth measurements presented in Figure 5.24 were caused by grinding and/or rail replacement activitie such as the crack depth reduction at around Ch.16+000 km in the year 2015 caused by the rail replacement in 2014.
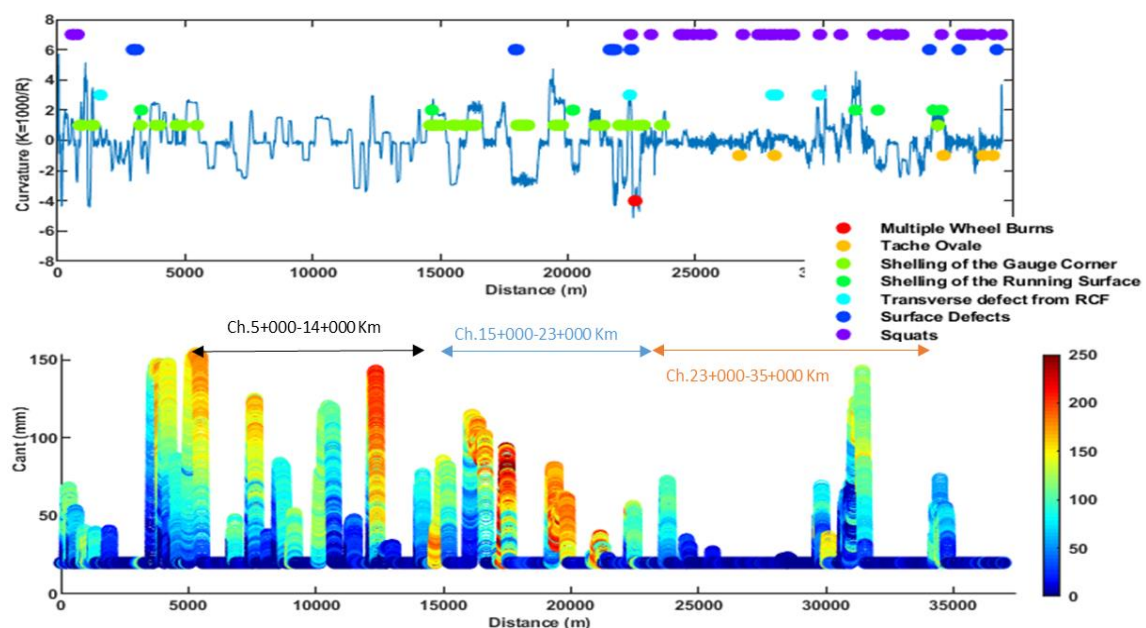


Figure 5.23: 'signed Tγ' predictions and reported defects on the left rail of the Jubilee NB line
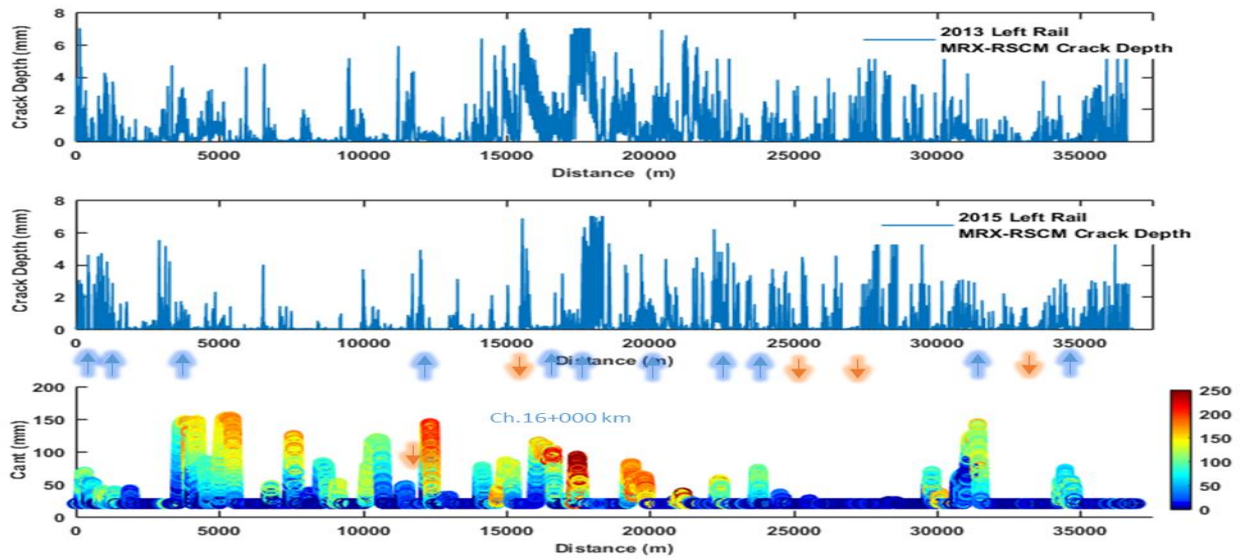
Figure 5.24: 'signed Tγ' predictions and MRX-RSCM measurements on the left rail of the Jubilee NB line

The right rail damage predictions given in Figures 5.25 and 5.26 show better correlation with the field data. With the help of additional traction forces, the energy values were increased and enabled to predict the defects after the tangential platforms between Ch.25+000-28+0000 km.
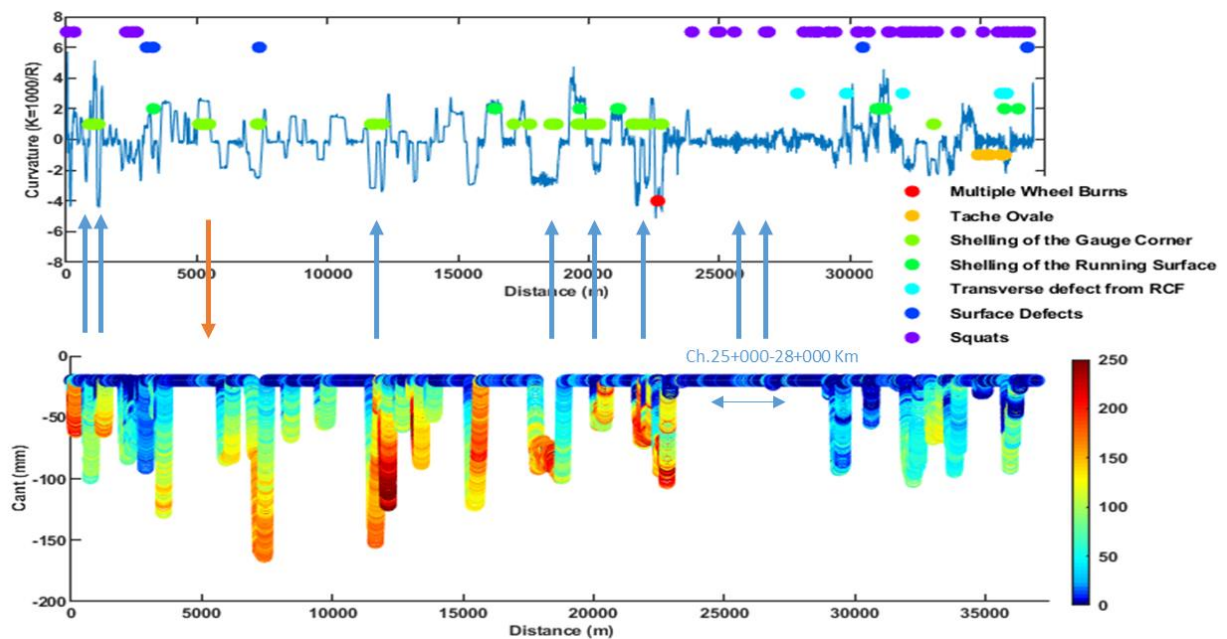


Figure 5.25: 'signed Tγ' predictions and reported defects on the right rail of the Jubilee NB line

In summary; the 'signed Tγ' succeeded to predict the locations susceptible to damage at several locations on the high rail and particularly traction areas following tangent platforms. However, although no defects were reported on high rails of JLE section, the model predicted a higher susceptibility to RCF damage in these areas. However, the model estimated a low susceptibility to damage on the remaining tangent tracks and low rails where defects were recorded.
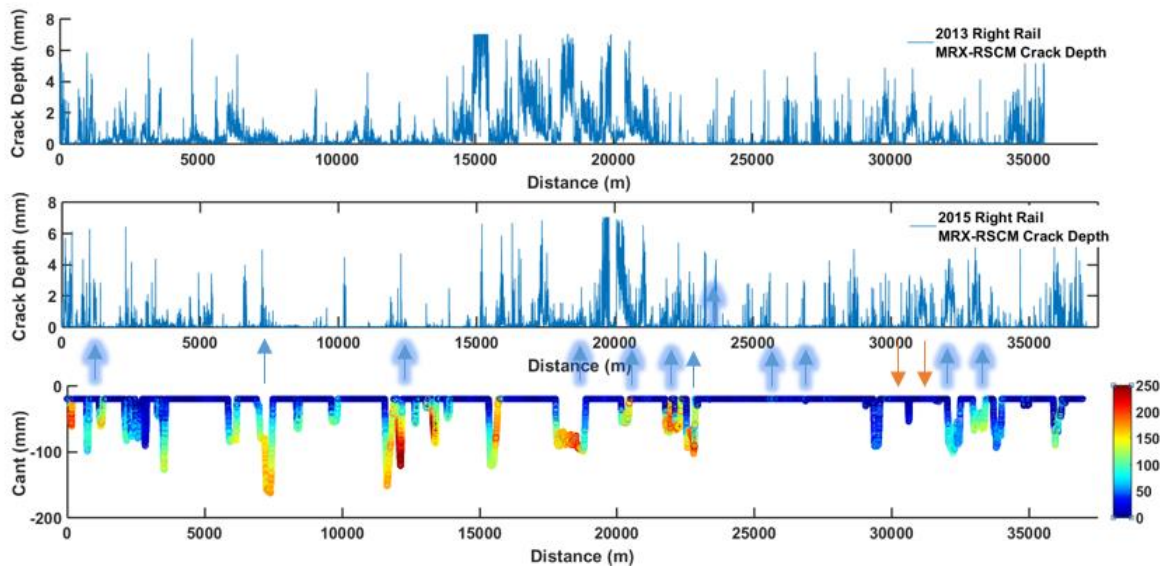
Figure 5.26: 'signed Tγ' predictions and MRX-RSCM measurements on the right rail of the Jubilee NB line

## 5.3 Conclusions and discussions

The effects of various route characteristics on 'signed Tγ' were evaluated to test the applicability of the WLRM for predicting the damage susceptibility of the studied LUL lines. In general, the 'signed Tγ' demonstrated the influence of a number of key factors as summarised below:

- Traction/braking forces; the inclusion of the additional forces associated with traction and braking resulted in an increase in Tγ at tread (high and low rails) contact whereas, at the flange contacts only a small increase on both longitudinal creep forces and Tγ was apparent, as the majority of the flange contact was in the slip condition. However, in order to better understand their influence on stick and slip conditions, local wheel-rail contact models (which calculate the distribution of the tangential forces) such as FASTSIM should be used.

- Curve radius; As the curve radius decreases on all the lines, the mean 'signed Tγ' values increased at all the contacts.
  - On the Bakerloo line, the presence of check rails as well as the other infrastructure characteristics influenced the level of Tγ, resulting in the tread and low rail contacts being more susceptible to damage. By contrast, the Tγ levels at flange contacts were considerably higher on unchecked curves (curve radius > 200m).
  - On the Jubilee line, the LT5 profile tended to produce lesser number of flange contacts and hence, the energy at the tread contacts were higher.
  - In contrast to previous WLRM studies, the metro-system tracks produced relatively larger values on high tread and low rail contacts which may be caused by the start-stop nature traffic with high traction/braking forces.

- Wheel-rail friction coefficient; Reducing the friction coefficient from μ=0.45 and lubrication implementation generally decreased the level of Tγ. Due to the interaction of wear and RCF in the current WLRM damage function, this reduced the risk of wear, but increased the RCF damage risk. It should be also noted that the friction coefficients and the presumed creepage-creep force relationship in VAMPIRE can be influenced by surface conditions. Therefore, in order to generate more accurate results, the calibrated models or more advanced models should be used to better represent actual conditions.

- Track irregularities; Even though the track irregularities did not significantly affect the Tγ results, they influenced the location of contacts on the railhead. In certain cases, creep force directions were changed, causing an increase in 'signed Tγ' and damage risk accordingly.

- Different wheel-rail profile shapes; The selected worn wheel and rail profiles had a key impact on 'signed Tγ' levels when compared to the new case.
    - Lightly worn wheel (WW1) profiles generated a lower conicity, reducing the Tγ at tread contacts but, increasing the levels at flange contacts.
    - Conversely, the moderately and severely worn profiles particularly the hollow worn wheels led to higher conicity. Thus, the energy at tread contacts did not show a significant difference but, the values at flange contact were raised considerably. Also, the worn cases influenced the creep force direction at low rail contacts and in turn raised the 'signed Tγ'.

As a result of the observations above, it can be concluded that whereas the track characteristics, such as curve radius and friction coefficient, had a key impact on Tγ levels, the effect of both variations in track irregularities and worn wheel-rail profile shapes can significantly influence the contact conditions and therefore wheel-rail forces and damage locations on the railhead. This suggested that to accurately predict susceptibility of a rail to damage, all of these factors need to be taken into account. For example, whilst some combinations might give rise to wear and/or RCF risk, the others might have no impact on the current condition. In order to increase the accuracy of damage predictions and to reflect these variations in the model, the total number of passages should be accumulated considering the range of duty conditions observed by the rail. Different wheel and rail profiles, applied lubrication, track irregularities and traction/braking forces should be included and the predicted damage should be accumulated.

Due to uncertainties of the breaking points of the WLRM for use on metro system, the location of high values of 'signed Tγ' was used as an indicator of high susceptibility to damage and compared with the field defect locations (longitudinally). Even though the method of signing Tγ eliminated substantial number of contacts in the route simulations, the 'signed Tγ' was found to successfully predict the locations of several damage regions

reported in the defect data sheet and MRX-RSCM data. This is particularly evident on checked curves where the magnitude of forces at high and low rail tread contacts corresponding to locations of observed damage. However, similar to previous WLRM results (Evans et al., 2008),  the use of 'signed Tγ' was shown to overestimate the number of locations with observed damage on the high rails as indicated by black arrows in Figures, but underestimate the number of locations on the low rails of the relatively shallower curves (R > 200m). However, it should be noted that although the defects were recorded as RCF related, some of them may be initiated by other factors such as studs (thermal damages) especially on the Jubilee line. Since, the WLRM was developed based on plastic deformation accumulations, it cannot estimate these type of damages. In addition, some of the inaccurate predictions can also be associated with differences in rail ages throughout the lines and grinding activities. Most importantly, the high values can give rise to increased wear rate which in turn may remove the initiated cracks.

In summary; the results presented in this chapter illustrated that although the signed Tγ successfully showed the effect of different route characteristics, it was sometimes unable to predict all locations which were observed to be susceptible to damage along the entire metro lines. When planning maintenance, both over- and under- estimations of damage can be very critical, whereas the underestimation may lead to unplanned maintenance, renewals and hence, increased maintenance costs, the overestimation might cause to premature rail replacements and lack of confidence in the modelling.

In order to develop a more accurate model, the key areas which contribute to inaccurate predictions were identified in the research. Figure 5.27 highlights these key areas (in red) which are described in more detail below.
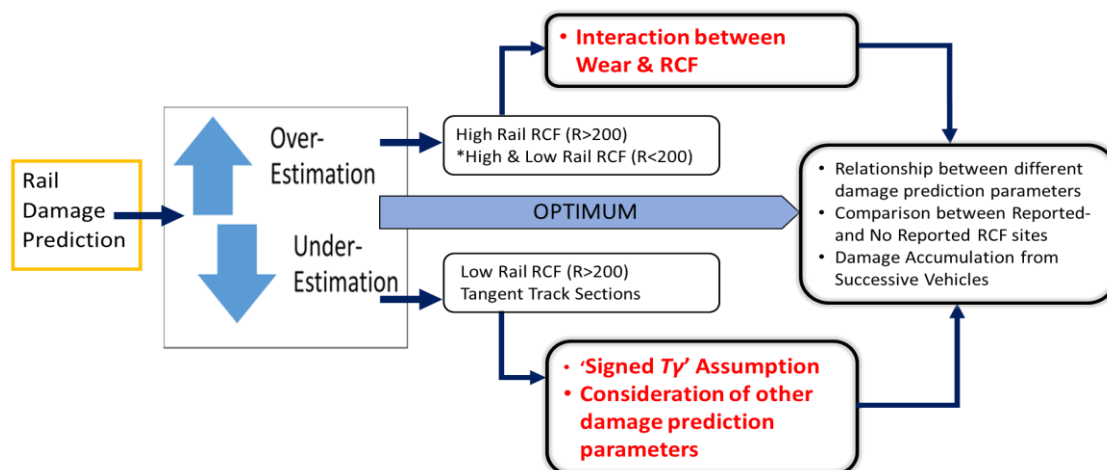


Figure 5.27: Key areas leading to over- and under-estimations of rail damage in WLRM

Interaction between Wear and RCF Damage:

Even though wear is caused by several different mechanisms which were explained in Chapter 2.2.1, it has been also mentioned that the accumulation of plastic deformation in

rails lead to both wear and RCF damage. However, there are still uncertainties as to when wear or RCF dominates and how these two phenomena interact with each other. Since the WLRM damage function was developed empirically from the comparisons between predictions and site observations (including wear and RCF), the influence of a mild wear regime was incorporated into the model when the energy at the wheel-rail contact reaches the peak damage ('signed Tγ'=65 N) limit. After this limit, wear damage starts to increase, but it is not sufficient to remove the initiated cracks. The model assumes that the wear rate (severe-catastrophic regime) dominates the crack growth after the wear-RCF balance ('signed Tγ'=175 N) limit is exceeded. However, these assumptions can lead to an overestimation of RCF on the high rails of metro lines, the poor correlation of larger predictions with no reported defects might be resulting from an exceedance of the wear rate over the crack propagation rate.

In order to investigate this problem and to better understand the interaction between wear and RCF, it was proposed that the observed worn area should be compared to the crack area/depth for selected sites. Due to successes in previous studies, the BRR wear function was suggested to be considered in rail wear rates' predictions. One of the advantage of the BRR model is that wear can take at all values of 'raw Tγ' and applicable to all contacts by showing the changing wear regimes while, the WLRM considered only the 'signed Tγ' regions and the wear was generally described by its interaction with RCF damage.

'Signed Tγ' Assumption:

Similar to the finding of the previous WLRM studies, this study also confirmed that although it gave relatively good validation of locations susceptible to classic high rail RCF, it resulted in an over-or under-estimation of the damage locations in certain circumstances. The previous studies suggested that different creep force angles may generate different types of damage and the subsequent studies have proposed a relationship between the resultant creep force angle and damage risk (Evans et al. 2008; Bevan, 2011). For this reason, the 'raw Tγ' and the creep force angle were proposed to take into account in the research to improve the accuracy of damage predictions.

Consideration of other damage prediction parameters:

Although some inaccurate predictions can be associated with the assumed method of signing Tγ, there might be other reasons causing the poor validation. The 'raw Tγ' and different creep force angles will certainly provide an improvement in the damage estimations compared to current WLRM but, it was also apparent that the creepages and creep forces might not be sufficient to describe the overall changes at the wheel-rail contact. For instance, the contact load, which is one of the crucial parameter showing the severity level of the resulting wheel-rail contact, was not taken into account in the model

inputs. In order to identify changes between the sections experiencing high susceptibility to defects or having no reported defects, it was proposed that comparison of different damage prediction parameters should be evaluated in the research.

As introduced in the literature review; the Shakedown Map is another method for estimating rail damage susceptibility based on vehicle dynamics simulation outputs and has provided relatively good predictions in several previous studies. In addition, the consideration of the load factor and traction coefficient will give an opportunity to take into account the changes in aforementioned contact parameters.

# Chapter 6    Interaction of Damage Prediction Parameters

The previous chapter demonstrated that, although the 'signed Tγ' used in the WLRM succeeded in showing the influence of key vehicle-track characteristics on rail damage susceptibility, it provided certain inaccurate damage predictions when its results were compared with field defect locations (longitudinally) along the studied lines.

In order to increase the accuracy of the predicted damage, the consideration of 'raw Tγ' and different creep force angles were some of the approaches that were investigated in the previous studies to scale the damage. Although these studies demonstrated the relationship between the resultant creep force angle and damage risk in several sites, this research argued that the creepages and creep forces might not be sufficient to describe the changes at the contact conditions and hence, it proposed to also use the Shakedown Map due its successes in previous studies and the potential for integration with vehicle dynamics simulations.

To understand the interaction between a range of different damage prediction parameters, including: Tγ, load factor and traction coefficient and creep force angle, the outputs from the vehicle dynamic route simulations were compared in the first section of this chapter. In addition, the parameters were also compared to the location and severity of damage at selected sites, which includes sites with and without reported RCF defects. As a result of this study, a combination of both the Shakedown Map and Tγ was proposed to help to increase the accuracy in the prediction of the susceptibility of the rail to wear and RCF damage. The subsequent sections explain the proposed models developed in this research.

## *6.1 Relationship between damage prediction parameters*

The relationship between the raw Tγ (e.g un-signed), creep force angle and the Shakedown Map parameters of load factor (LF) and traction coefficient (T/N) were examined. As detailed in Section 2.6, LF and T/N are defined as follows;

$$LF = {P_0}\big/{k} = \frac{3F_N}{2\pi abk} \qquad (6.1) \qquad\qquad T/N = {\sqrt{F_{lat} + F_{long}}}\big/{F_N} \qquad (6.2)$$

where $P_0$ is the maximum contact stress (N/mm$^2$), $k$ is the shear yield strength of the material (N/mm$^2$), $F_{lat}$ is the lateral creep force (N), $F_{long}$ is the longitudinal creep force (N), $F_N$ is the normal load (N) and a, b are the semi-axes of the wheel-rail contact patch. Since this chapter concentrates on the changes of the wheel-rail contact parameters and

k limit is related with the material properties, the maximum contact stress was used instead of load factor in this part of the study.

To obtain the 'signed Tγ' in the WLRM in the previous Chapter 5, the raw Tγ values were filtered by the creep force angle 0°-90° and 270°-360° (positive longitudinal creep force in the wheel) that corresponds to traction (negative) direction on the rail. The creep force angle is the resultant creep force angle $'\theta'$ between longitudinal and lateral creep forces:

$$\theta = \arctan\left(\frac{F_{lat}}{F_{long}}\right) \tag{6.3}$$

For the ease of demonstration in the following section, the creep force angles $\theta$ are shown according to their regions. The angle $\theta$ could be located in one of the 4 quadrants/regions which is shown in Figure 6.1. According to this demonstration, the regions I and IV display the traction direction while, the regions II and III show the braking direction.
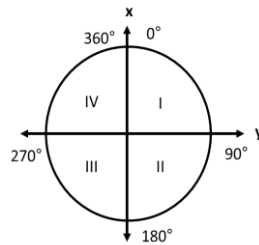


Figure 6.1: Creep force angles shown in the 4 regions between 0° and 360°

Due to several number of route simulations containing a significant volume of data, the most dominant type of wheel-rail profile combination (given in Section 4.2.2) was selected: worn rail profiles with the lightly worn wheel profiles (WW1) to show the differences between the damage parameters. As it can be expected from the comparison of wheel-rail profile shapes in Chapter 5.1.5, the results might alter when different profiles are taken into account in the simulations but, this case gives certainly the most common condition occurred on the studied lines.

### 6.1.1 Tγ and traction coefficient (T/N)

The relationship between Tγ and traction coefficient (T/N) has been compared with variations in creep force angle and curve radius. Figures 6.2 and 6.3 show the Tγ and T/N at the right tread contacts of the Bakerloo and Jubilee Northbound (NB) lines respectively, where each point represents a single contact point through the route simulation. As it can be seen there was generally a linear relationship between both of the parameters at low levels of T/N. However, as T/N increased (after approximately 0.31 level), the contacts saturated and Tγ values substantially raised. Regarding the Jubilee line, this deviation was observed at both of 0.25 and 0.31 T/N levels due to different friction coefficients used in the (dry) tread regions for over-and-underground sections. While μ=0.25 was taken as at overground section, it was selected as 0.36 for underground (as detailed in Section 4.2.3).

But, these limits were noted in the research as the previous studies pointed out that they are the transfer region from subsurface to surface damage in the Shakedown Map (Johnson, 2000). While 0.25 was demonstrated as the starting point of surface damage in the line contact, the 0.30-0.32 was given for the Shakedown map for point contacts.
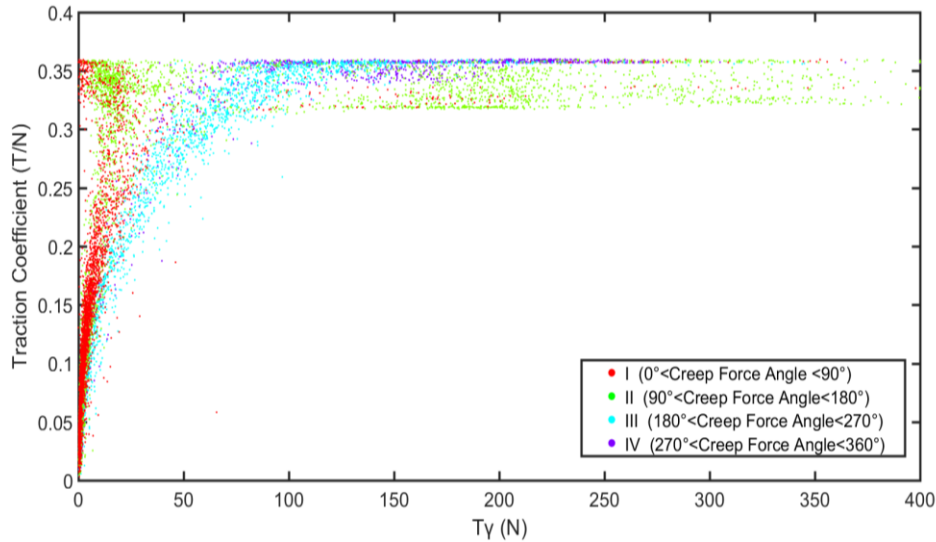


Figure 6.2: T/N against Tγ at the right tread contacts of Bakerloo NB line under different creep force angle regions

Variations in Tγ and T/N can be seen with the creep force angles which is influenced by the start-stop nature of traffic and the position of the tread contacts, e.g. whether it is located on the high/outer side or low/inner side of the curved tracks. On the Bakerloo line, the presence of the check rail also influenced the direction of the creep force and therefore, the resulting creep force angle. The results suggested that contacts in the braking regions (II:90°-180° and III:180°–270°) also had high susceptibility to generate rail damage. Similarly, the braking region (III:180°–270°) in the Jubilee line had high energy values in both of μ=0.25 (overground) and μ=0.36 (underground) regions.
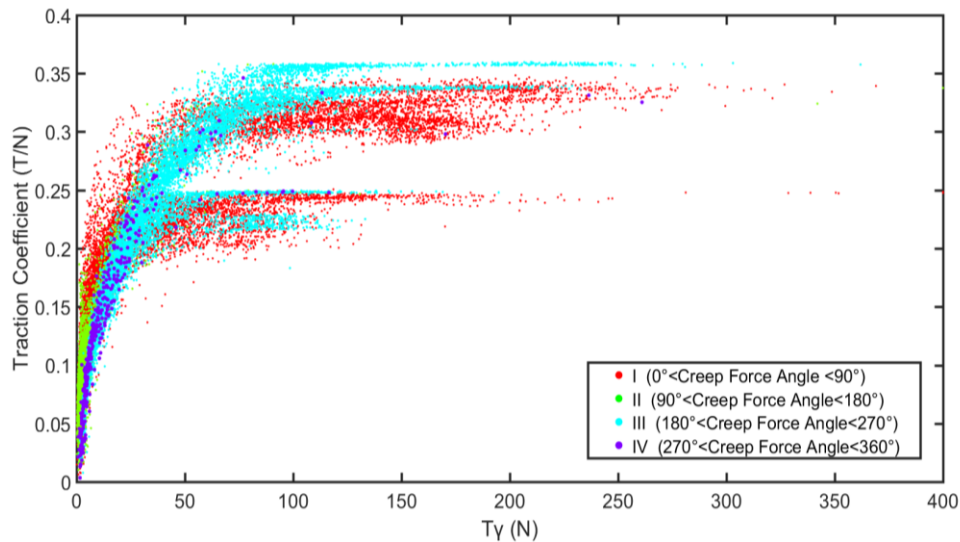


Figure 6.3: T/N against Tγ at the right tread contacts of Jubilee NB line under different creep force angle regions

As it is expected, the right flange contact results presented in Figures 6.4 and 6.5 display that they were mainly in traction direction with considerably high Tγ and T/N values compared to tread contacts. But, their severity on the Jubilee line was lower than the Bakerloo line due to LT5 wheel profile. It can be seen that the majority of them were saturated (T/N >0.15), as the minimum coefficient of friction was taken as 0.15.
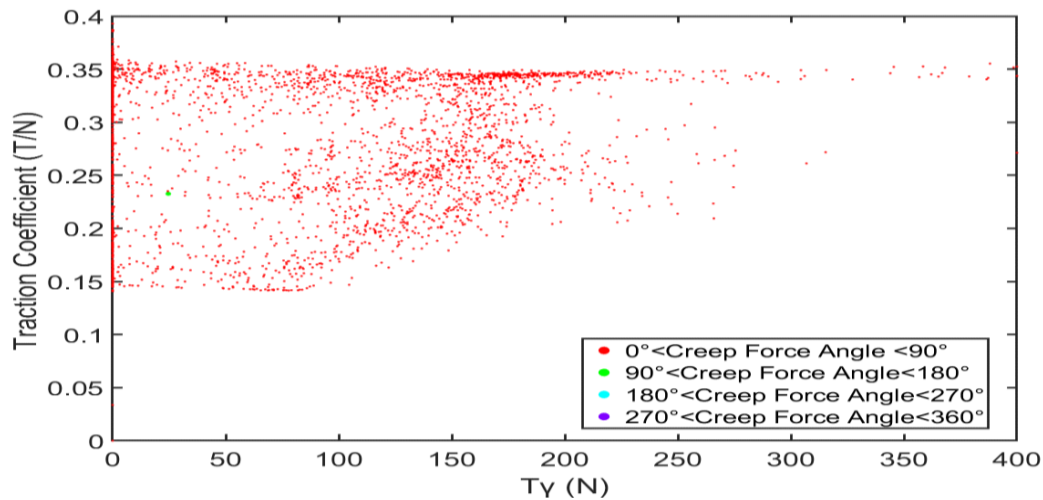


Figure 6.4: T/N against Tγ values at the right flange contacts of Bakerloo NB line under different creep force angle regions
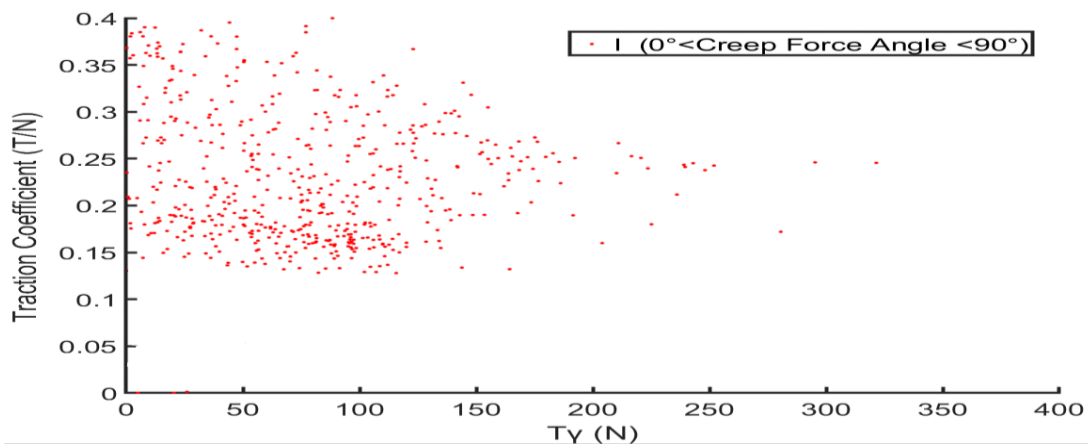


Figure 6.5: T/N against Tγ at the right flange contacts of Jubilee NB line under different creep force angle regions

The relationship between T/N and Tγ and variation in curve radius on the Bakerloo line is illustrated in Figure 6.6. The results showed that as the curve radius decreased, both the T/N and Tγ increased and the largest values were observed on high rails (left hand curve R<200 m) and low rails (right hand curve R<200 m) of checked curves. When they were compared with creep force angles, it can be seen that while the angles on the high side were often in braking (II :90°-180°), they were usually in traction (IV:270°-360°) region on the low side. This was mainly resulting from the presence of check rail contact on these curves. On the contrary to checked curves, low rails seemed to have larger energy values compared to tread contacts on high side even with similar T/N values. It should be noted

that the most of the high rail contacts are in two-point tread and flange contacts and hence, the total energy of high rail may have been potentially shared between the tread and flange contacts.
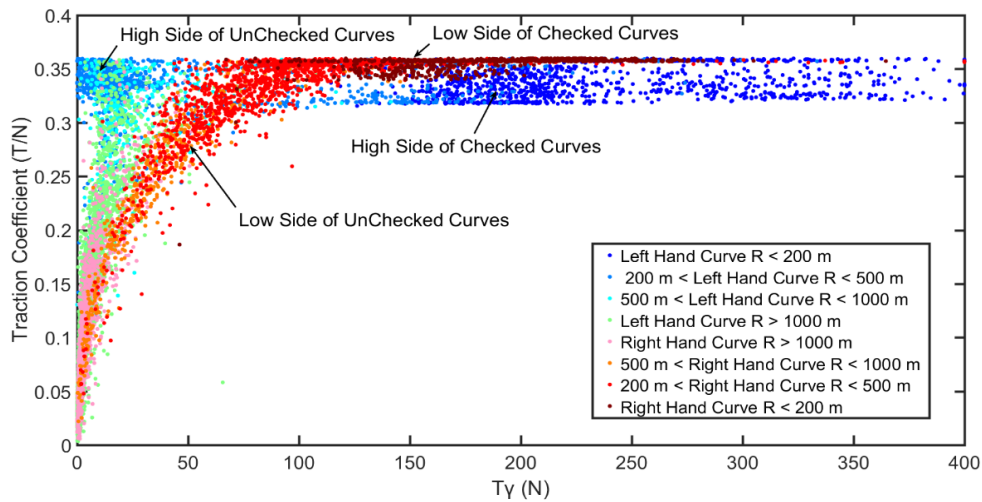


Figure 6.6: T/N against Tγ at the right tread contacts of Bakerloo NB line under different curvature ranges

Figure 6.7 provides the relationship on the Jubilee line and shows that low rails had relatively larger T/N values when compared to high rails, but lower levels of Tγ. However, it was also revealed that although some of the contacts having similar track conditions exceeded the 0.25 limit, the others were below this limit due to the different friction coefficient used for the dry conditions (over-and-underground) in the simulations. When the results were compared with creep force angles, it was apparent that the dominant angle region was braking (III:180°-270°) on low rails and traction (I:0°-90°) on high rails. This was also noticed for the similar curvature ranges on the Bakerloo line.
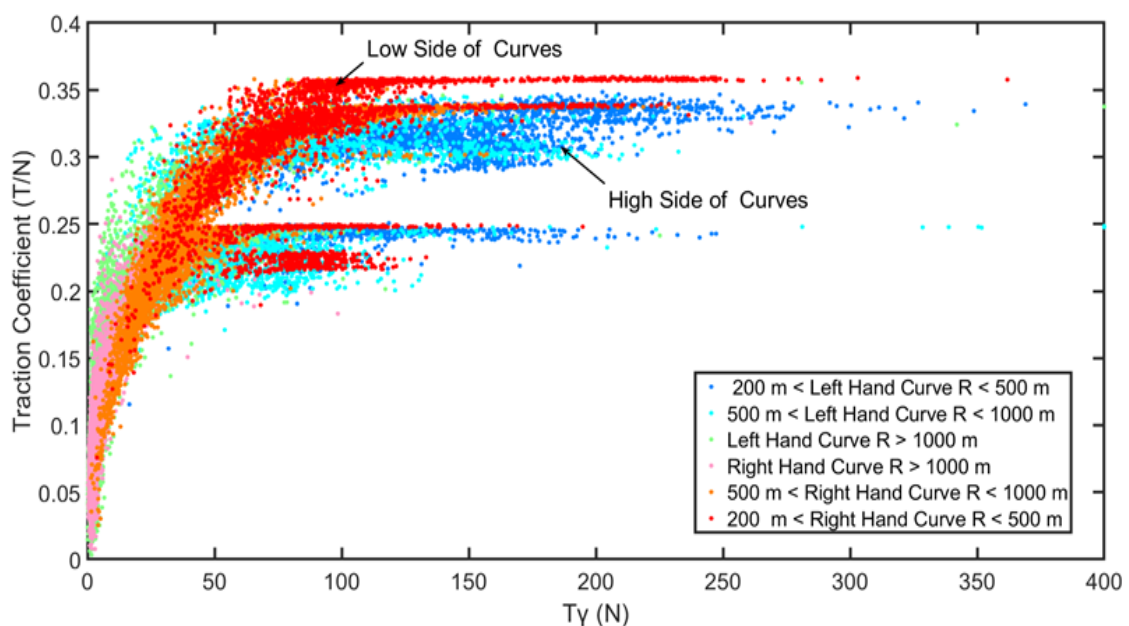


Figure 6.7: T/N against Tγ at the right tread contacts of Jubilee NB line under different curvature ranges

135

The flange contact results are given in Figure 6.8 and 6.9. Regarding the Bakerloo line, the T/N values were similar for most of the flange contacts whereas the energy levels on tight curves were generally higher than the shallower curves. Therefore, the Tγ was again found to be successful in showing the effect of curve radius and vehicle curving performance on damage susceptibility. It can be also seen, the worn wheel-rail profile combination (WW1) produced limited number of flange contacts on checked curves, as the check rail acts to restricts the movement of the wheelset towards the high rail. Similar to the Bakerloo line, the narrower curves of the Jubilee line in Figure 6.9 generated higher Tγ results with the exception of lesser number of flange contacts particularly occurred on the 200 m < Left Hand Curve < 500 m range.
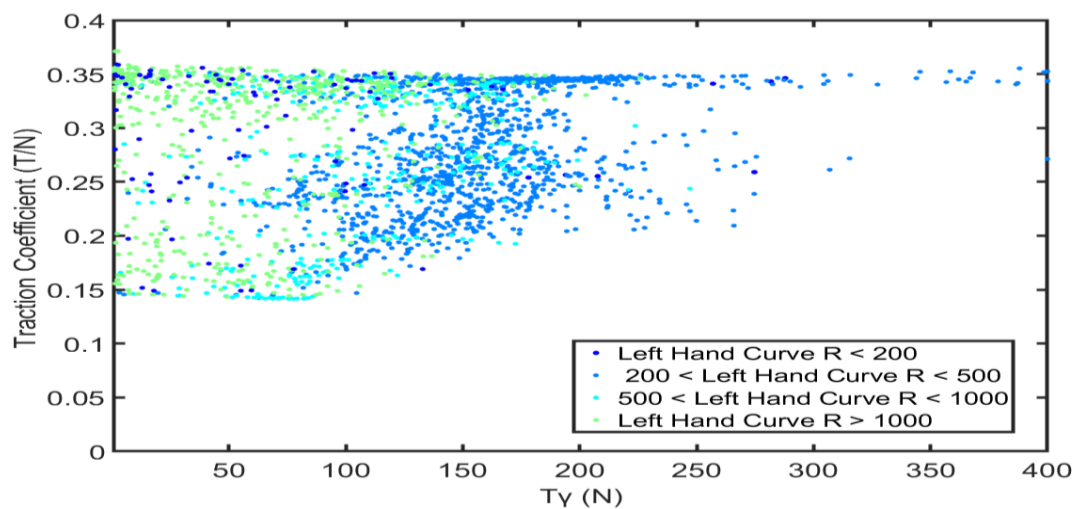


Figure 6.8: T/N against Tγ at the right flange contacts of Bakerloo NB line under different curvature ranges
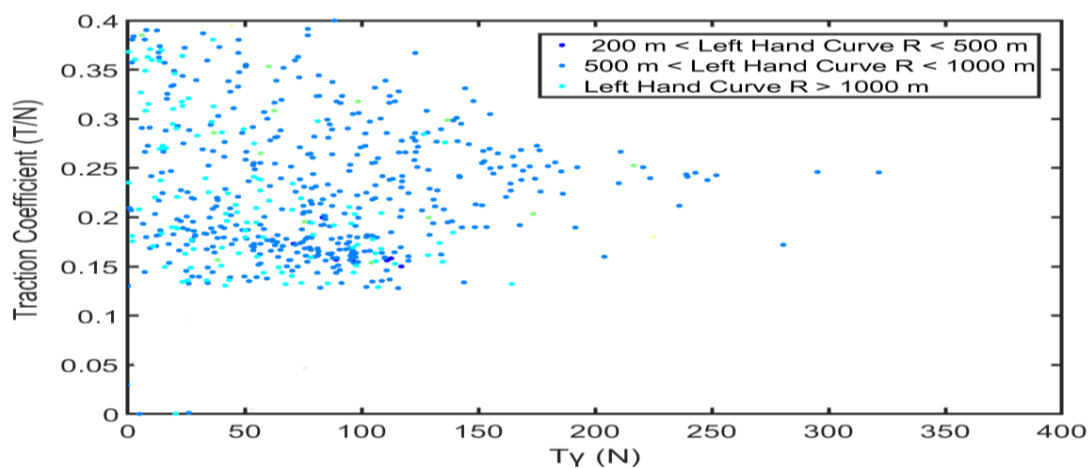


Figure 6.9: T/N against Tγ at the right flange contacts of Jubilee NB line under different curvature ranges

## 6.1.2 Tγ and contact stress (P₀)

The relationship between Tγ and maximum contact stress ($P_0$) was compared for the Bakerloo and Jubilee lines. Figure 6.10 below displays the values at the right tread contact

under different creep force angle regions. The $P_0$ ranges between 1000 – 3000 N/mm$^2$ regardless of the level of T$\gamma$. However, it was also noticed that the contacts on the traction regions particularly, the region (I:0°-90°) produced significantly lower values of T$\gamma$ compared to those generated in the braking regions (II:90°-180° and III:180°-270°).
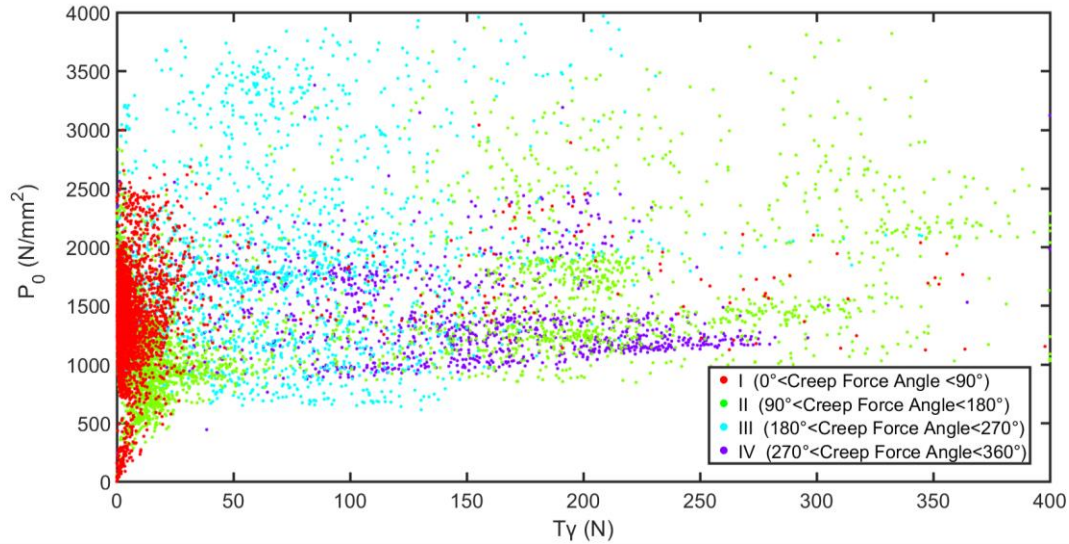


Figure 6.10: $P_0$ against T$\gamma$ at the right tread contacts of Bakerloo NB line under different creep force angle regions

Figure 6.11 presents the $P_0$ on the Jubilee line. Although the axle loads are higher on this line, the lesser number of flange contacts might give rise to larger single-point tread contact patch areas on the high rail and hence, a lower $P_0$ values. When the creep force angle regions are compared, a greater proportion of values are in the traction region (I:0°-90°) had larger T$\gamma$ than the braking region (III:180°-270°).
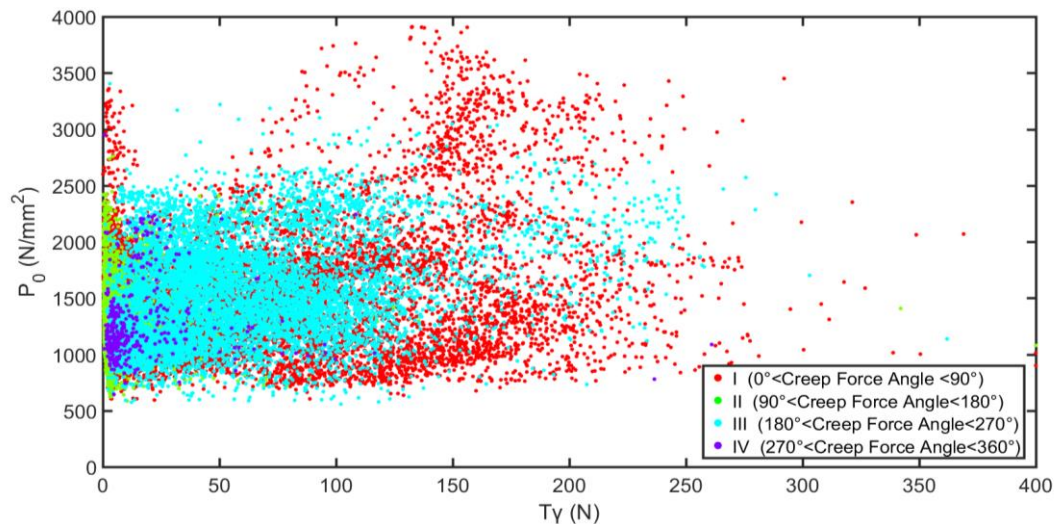


Figure 6.11: $P_0$ against T$\gamma$ at the right tread contacts of Jubilee NB line under different creep force angle regions

Flange contact results for both of the lines are provided in Figures 6.12 and 6.13. As it can be seen, the Po values were considerably larger on the Bakerloo line due to wheel-rail profile combination and the higher proportion of narrower curves. While the maximum

values reached 6000 N/mm$^2$ levels, the highest results were 2500 N/mm$^2$ on the Jubilee line. Additionally, they display that there was a relatively good correlation between Po and Tγ which might be resulting from the larger energy levels produced at sharper curves with higher contact stress values than the shallower curves on the lines.
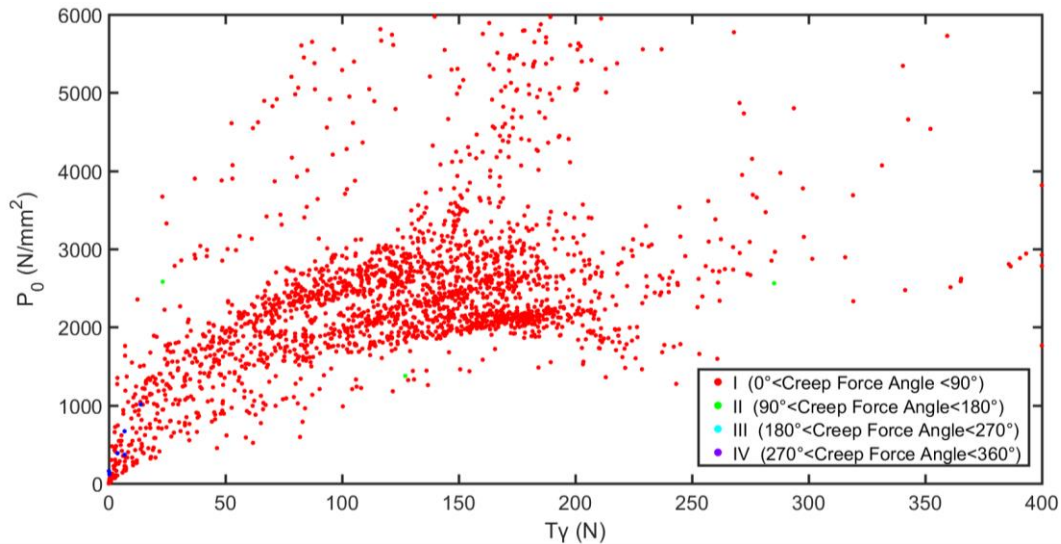


Figure 6.12: P$_0$ against Tγ at the right flange contacts of Bakerloo NB line under different creep force angle regions
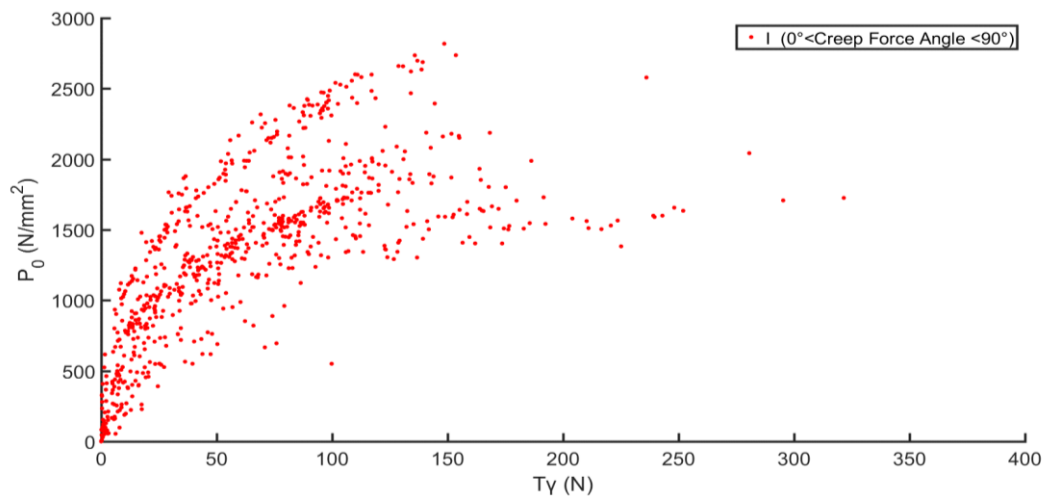


Figure 6.13: P$_0$ against Tγ at the right flange contacts of Jubilee NB line under different creep force angle regions

Under different curvature ranges, Figure 6.14 demonstrated that the contact stresses were larger on high side of checked curves than their low side. By contrast, unchecked curves led to different results as the contacts on low rails had relatively greater values than high rails. When there is a two-point contact, the total normal load is mainly apportioned between tread and flange contacts on high rails and this may give rise to one of the contact. Additionally, the larger contact patch area which is usually generated at single tread contacts might reduce P$_0$ values at these contacts. The low rails particularly the BH profiles also produced two-point contacts on low rails. This may be also responsible for the changes at contact pressures on these rails.
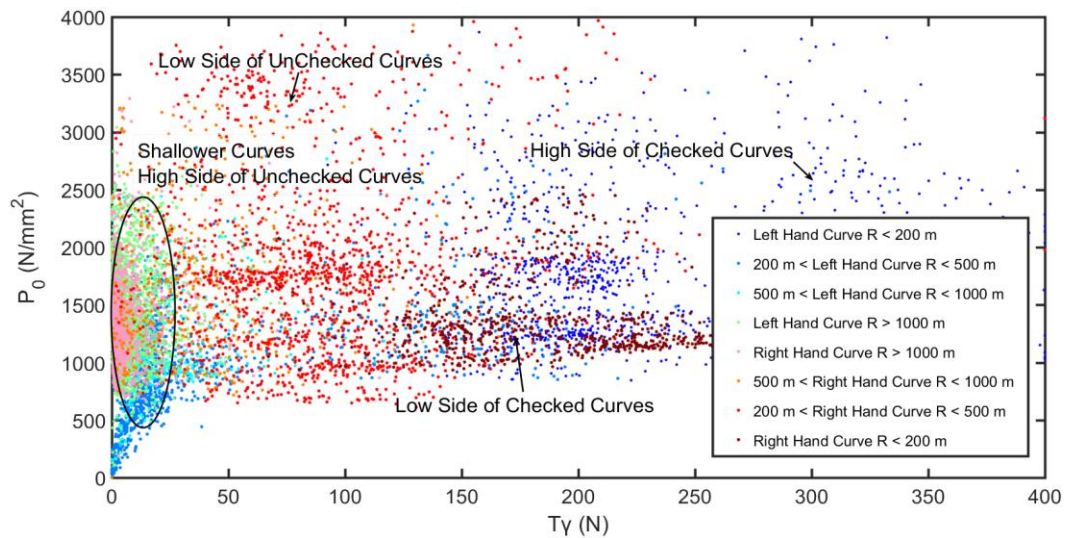
Figure 6.14: $P_0$ against Tγ at the right tread contacts of Bakerloo NB line under different curvature ranges

In contrast to Bakerloo line, tread contacts had larger stresses on high rails than low rails of Jubilee line which are illustrated in Figure 6.15. Again, owing to limited number of flange contacts, the load is mainly carried by the single tread contacts on high rails. However, the shallower curves produced similar results on both of the rails.
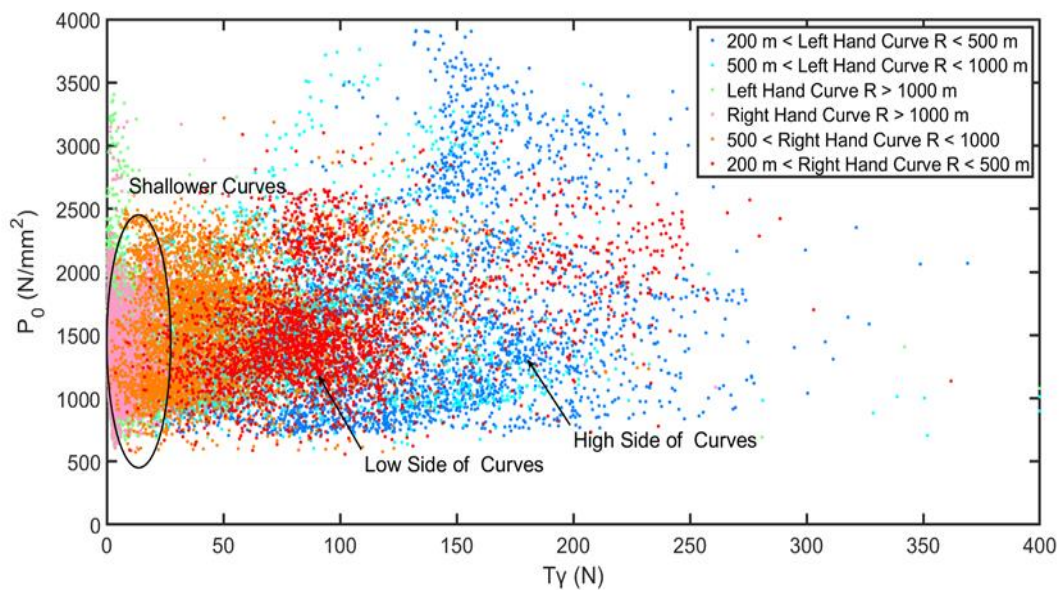


Figure 6.15: $P_0$ against Tγ at the right tread contacts of Jubilee NB line under different curvature ranges

As it was previously mentioned in this section, Tγ and $P_0$ had a better correlation at flange contacts which are also demonstrated in Figures 6.16 and 6.17. Both of the values showed an increment when the curve radius was reduced on the lines.
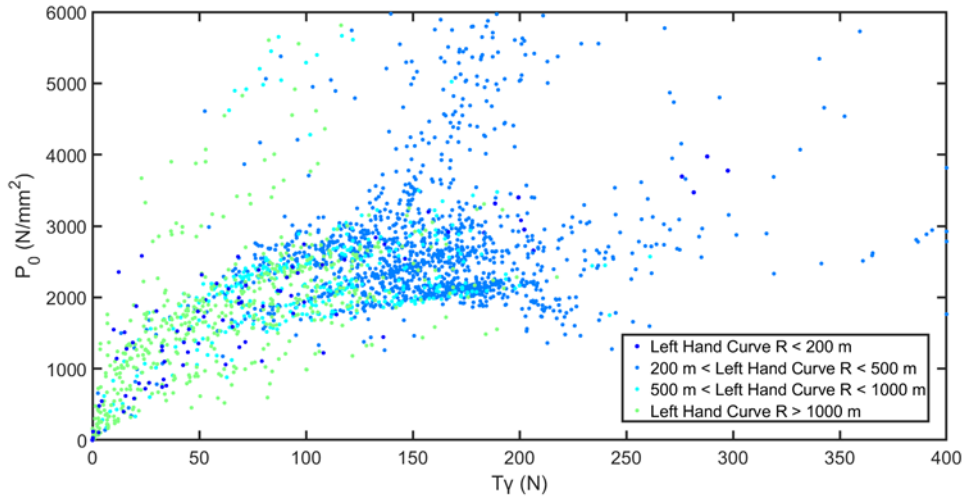
Figure 6.16: $P_0$ against $T\gamma$ at the right flange contacts of Bakerloo NB line under different curvature ranges
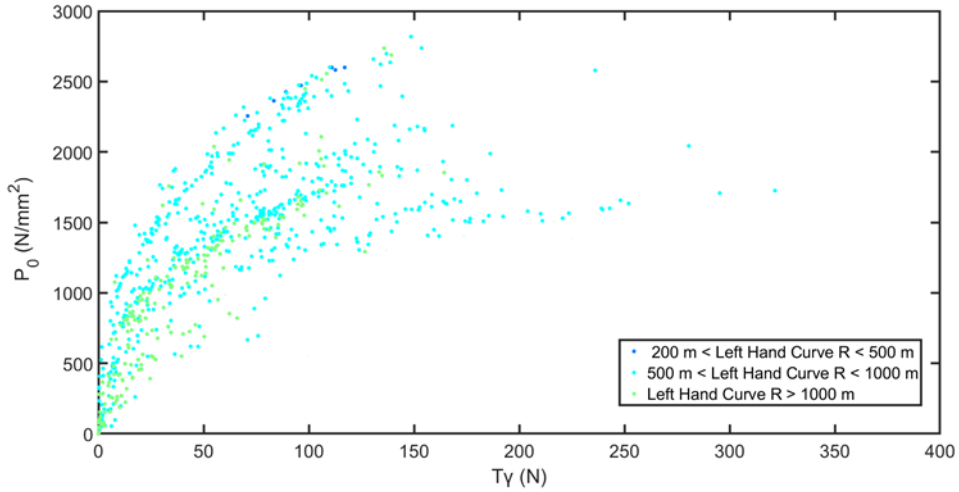


Figure 6.17: $P_0$ against $T\gamma$ at the right flange contacts of Jubilee line under different curvature ranges

### 6.1.3  Summary of the section results and discussions

The results presented in the previous sections illustrate the relationship between a range of damage prediction parameters at the different wheel-rail contacts. The aim was to understand the changes in the wheel-rail contact conditions along the lines, which can influence the selected parameters under different creep force angles and curvature ranges.

The main observations include:

- Since the T/N levels are limited by the selected friction coefficients, the linear relationship between $T\gamma$ and T/N was modified close to these values. After reaching the saturated condition, the contacts show substantial increases in $T\gamma$ while, the T/N values become constant. As the friction coefficients for the dry tread region were chosen as μ=0.25 (overground) and μ=0.36 (underground), the deviations were observed in this region. Therefore, whereas some of the tread contacts with similar track conditions and $T\gamma$ levels exceeded the 0.25 and 0.31 limits (Jubilee and Bakerloo, respectively), the

140

others were lower than these limits. It should be also noted that since these limits were indicative of the transfer points from subsurface to surface damage regions in the Shakedown Map, it was suggested to be further investigated during this research.

- It was observed that the most of the flange contacts were saturated, min. T/N > 0.15 levels equal to min. coefficient of friction.

- The Tγ and $P_0$ values at flange contacts provided better correlation than tread contacts. The two-point contact conditions, especially on the high rail affected the contact patch area and stress levels at the tread contacts accordingly.

- Although the T/N values were slightly influenced by the different curvature ranges due to the above reason, the Tγ values were again found to be more successful in showing the effect of changes in curve radius.

- Moreover, Figures helped to find the dominant creep force angle regions in each curvature range. Although the angle regions were provided for the right rails, it was noticed that the left rails produced the opposite regions which are given in

- Table 6.1. The similar curvature ranges resulted in similar angle regions on both of the lines. This showed that the creep force directions at the contacts were primarily dependent on the position of the rails on the lines. Whereas both flange and tread contacts on high/outer side of the curved tracks generated traction direction (region I:0°-90° and IV:270°-360°), the braking directions (region II:90°-180° and III:180°-270°) were occurred on the low/inner side of the curved tracks. The influence of check rails can be seen, which modified the force directions on the Bakerloo line resulting in the low rails being in traction direction and high rails in braking direction.

Table 6.1: The dominant creep force angle regions on the selected curvature ranges of studied lines

| | High Side of Checked Curves R<200 m | Low Side of Checked Curves R<200 m | High Side of UnChecked Curves 200 m <R<500 m | Low Side of UnChecked Curves 200 m <R< 500 m | Lines |
|---|---|---|---|---|---|
| Right Rail Tread Contact | II | IV | I | III | BAK |
| | | | I | III | JUB |
| Left Rail Tread Contact | III | I | IV | II | BAK |
| | | | IV | II | JUB |
| Right Rail Flange Contact | | | I | | BAK |
| | | | I | | JUB |
| Left Rail Flange Contact | | | IV | | BAK |
| | | | IV | | JUB |

## 6.2 Comparison of damage prediction parameters between reported and no reported RCF sites

To find the optimum solution between over- and under-estimations in modelling results, it is very significant to observe the changes at contact parameters between the reported and

no reported RCF sites. In this study, the critical sites which were reported in the defect data sheets given in the Chapter 3 were compared with the sites having no recorded defects in this data. In order to cover the changes on the sections with different characteristics, the selected sites were divided into three main categories:

1) Curved tracks (R> 200 m; BAK and JUB lines)
2) Checked curved tracks (R<200 m; BAK)
3) Tangent tracks (BAK and JUB lines)

Each site was 50 m long and the WW1 profile simulation cases was again considered in this analysis to demonstrate the dominant contact conditions on the lines.

## 6.2.1 Selected sites on the curved tracks

Since check rails were excluded in this section, the comparison was made on both of the lines. Figures 6.18 and 6.19 illustrate the selected sites on Bakerloo and Jubilee NB lines, respectively. In order to compare the changes in damage parameters between underground (tunnel) and overground (surface) sections, the red circled regions in Jubilee line were selected in the study.
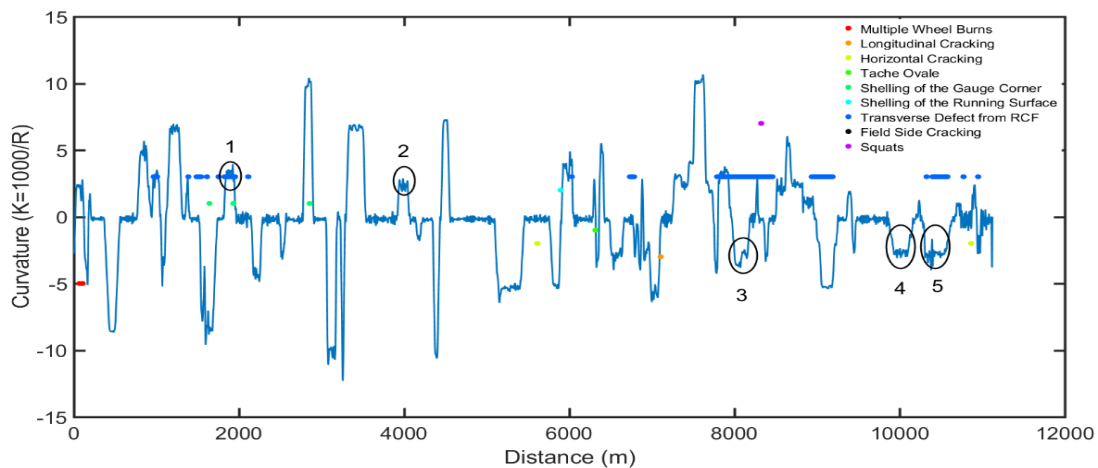


Figure 6.18: The selected reported and no reported sites on the right rails of Bakerloo NB line
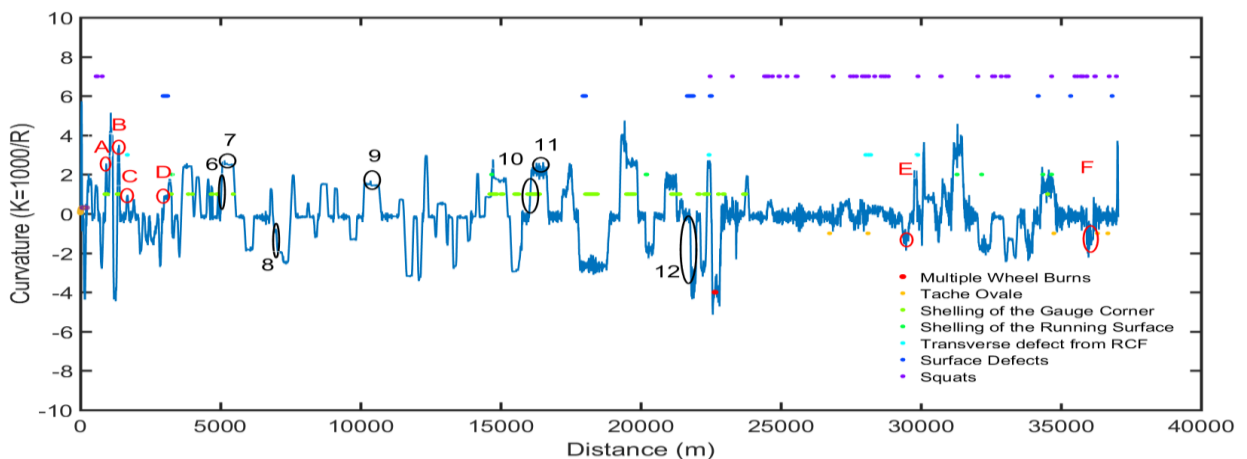


Figure 6.19: The selected reported and no reported sites on the lefts rails of Jubilee NB line

142

The track characteristics of the selected sites are presented in Table 6.2. The chainages, rail position and profile, curve radius, applied cant, cant deficiency and section type were provided for all sites. While the orange highlighted rows show the information for Bakerloo line, the grey rows for Jubilee line including the overground sections written in red colour. As it was mentioned in the Chapter 3.1, the cant deficiency values were significantly small and cant excess sometimes was occurred on the Bakerloo line. Since the selected sites were located in the old tunnel section of Jubilee lines, the cant deficiency values also low compared to other sections on this line. Similarly, the overground sections had small cant deficiency with the zero applied cant in Canning Town station (Site D). To identify the changes on different track positions, both high and low rail sections were selected in the study. In addition, to show the effect of unlubricated curved track, transition and different rail profiles (BH and FB) on rail damage prediction parameters, the analysis included the specific sites which were given in Table 6.2.

Table 6.2: The track characteristics of the selected sites for the curved tracks

| Site | Chainage (KM) | Rail Position | RCF Damage Condition | Curve Radius (m) | Applied Cant (mm) | Cant Deficiency (mm) | Rail Profile | Section Type |
|------|---------------|---------------|----------------------|------------------|-------------------|----------------------|--------------|--------------|
| 1 | 1+850-1+900 | Low Rail | Reported RCF (Squat with T/O) | 286 | 80 | 4 | FB | Underground (Tunnel) |
| 2 | 3+950-4+000 | Low Rail | No reported RCF | 400 | 40 | 20 | BH | Underground (Tunnel) |
| 3 | 8+000-8+050 | High Rail | Reported RCF (Squat with T/O) | 286 | 100 | 5 | FB | Underground (Tunnel) |
| 4 | 9+900-9+950 | High Rail | No reported RCF | 385 | 80 | -9 | BH | Underground (Tunnel) |
| 5 | 10+450-10+500 | High Rail *Unlubricated | Reported RCF (Squat with T/O) | 364 | 70 | -7 | FB | Underground (Tunnel) |
| 6 | 4+970-5+020 | High Rail Transition | No reported RCF | 1000 | 70 | -36 | FB | Underground (Tunnel) |
| 7 | 5+250-5+300 | High Rail | No reported RCF | 400 | 150 | 39 | FB | Underground (Tunnel) |
| 8 | 6+900-6+950 | Low Rail Transition | No reported RCF | 1000 | 60 | 11 | FB | Underground (Tunnel) |
| 9 | 10+300-10+350 | High Rail | No reported RCF | 667 | 110 | -10 | FB | Underground (Tunnel) |
| 10 | 16+050-16+100 | High Rail Transition | Reported RCF (Shelling on the Gauge Corner) | 667 | 75 | -9 | FB | Underground (Tunnel) |
| 11 | 16+200-16+250 | High Rail | Reported RCF (Shelling on the Gauge Corner) | 476 | 100 | 29 | FB | Underground (Tunnel) |
| 12 | 21+740-21+790 | Low Rail Transition | Reported RCF (Shelling on the Running Surface) | 435 | 40 | 45 | FB | Underground (Tunnel) |
| A | 0+910-0+960 | High Rail | Reported RCF (Shelling on the Gauge Corner) | 445 | 35 | 45 | FB | Overground (Ballasted) |
| B | 1+340-1+390 | High Rail | Reported RCF (Shelling on the Gauge Corner) | 325 | 35 | 45 | FB | Overground (Ballasted) |
| C | 1+655-1+705 | High Rail | No reported RCF | 1125 | 15 | 15 | FB | Overground (Ballasted) |
| D | 3+090-3+140 | High Rail | Reported RCF (Squat with T/O) | 1125 | 0 | 0 | FB | Overground (Ballasted) *Canning Town Station |
| E | 32+050-32+100 | Low Rail | No reported RCF | 575 | 85 | 45 | FB | Overground (Ballasted) |
| F | 36+000-36+050 | Low Rail | Reported RCF (Squat) | 775 | 65 | 0 | FB | Overground (Ballasted) |

Figure 6.20 displays the comparison of Tγ and T/N results on the selected sites of the curved tracks. Whilst the green and magenta colour show the reported RCF sites, the blue and red colour indicate the no reported RCF sites on the Bakerloo and Jubilee lines, respectively. Additionally, each marker represents different contacts on the rails. As shown, most of the contacts on the reported and no reported RCF sites were clustered in two different areas as indicated by grey dashed colour boundaries. When the values were below this limit, the contacts might seem to have less effect on damage risk. Similar to the results of the previous section, the traction coefficients were limited by the selected friction coefficients. For instance, the T/N values in the reported sites of overground section cannot exceed the μ=0.25 limit. But, it is apparent that they had greater energy values than the no reported sites. Also, the 0.31-0.32 T/N played a crucial role in the underground section. In spite of the low Tγ values in this region, the RCF damage was observed for the contacts which had larger T/N values than 0.31-0.32 levels. When the contacts were particularly analysed, it was noticed that the highest results were produced on the unlubricated curve due to larger friction coefficients. Additionally, even though no cracks were recorded on the BH type of low rails, the contacts showed excessive values which mainly resulting from the higher conicity in this rail-wheel profile combination. Moreover, some reported RCF sites on the Jubilee line (magenta colour) were below the limit. This was mainly caused by the changing track geometry on the selected transition sites. Although some contacts of this site had high values, the smaller results could not pass this limit. Furthermore, when the results were compared with different defect types such as (shelling and squat), no clear response was obtained in this analysis.
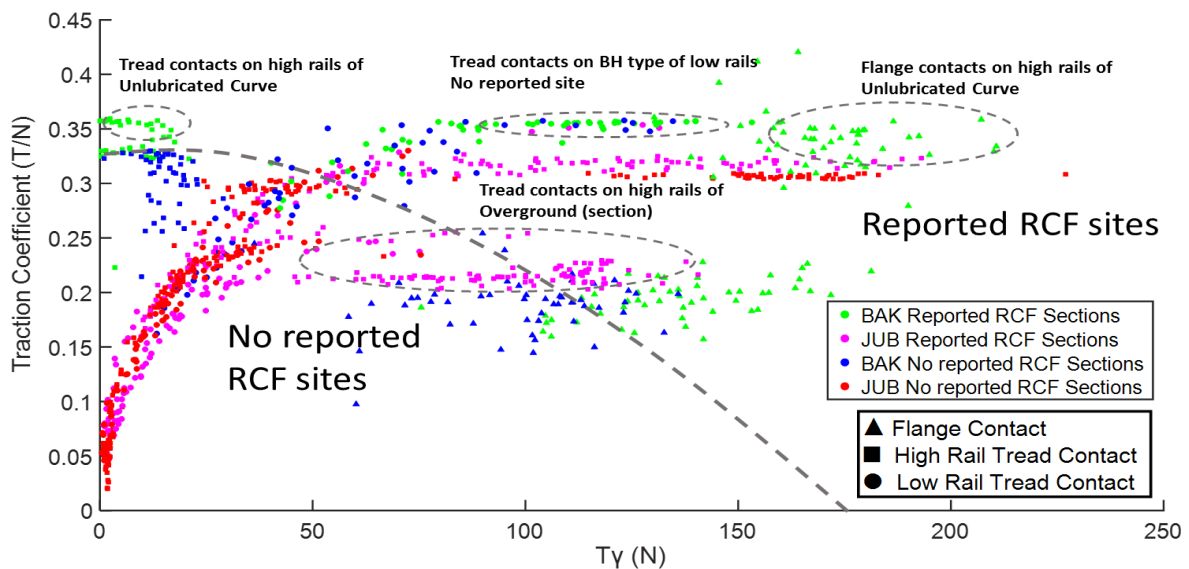


Figure 6.20: The comparison of Tγ and T/N on the selected sites of curved tracks

Figure 6.21 illustrates the comparison of the creep force angle regions with reported and no reported RCF damage on the Jubilee line. As expected, the majority of high (left) rail and low rail tread contacts were on the traction region (IV:270-360) and braking regions

(II:90°-180° and III:180°-270°), respectively. This again confirmed that the creep force direction did not seem to have an influence on damage risk since, the values primarily depended on the position of rails and route characteristics
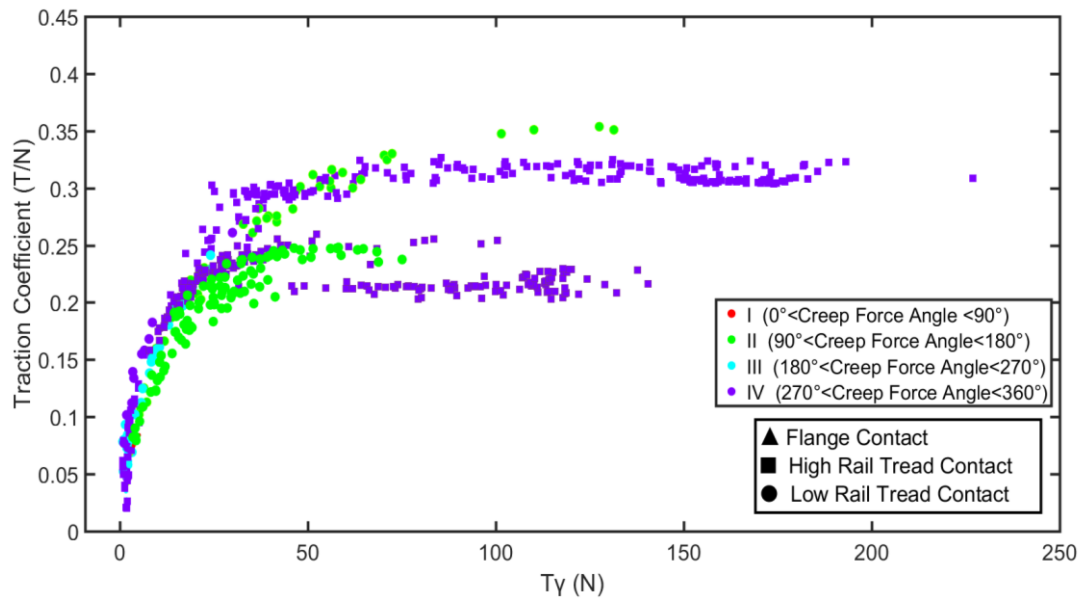


Figure 6.21: The comparison of different creep force angle regions on the selected sites of Jubilee NB line

In the case of the Bakerloo line given in Figure 6.22, the majority of flange and high rail tread contacts were in the traction direction (I:0°-90°) and the low rails were in the braking direction (III:180°-270°). Due to difference in rails (left or right) between the selected sites, the traction region (I) generated on the right rail of the Bakerloo line, and region (IV) was generated on the left rail of the Jubilee line.
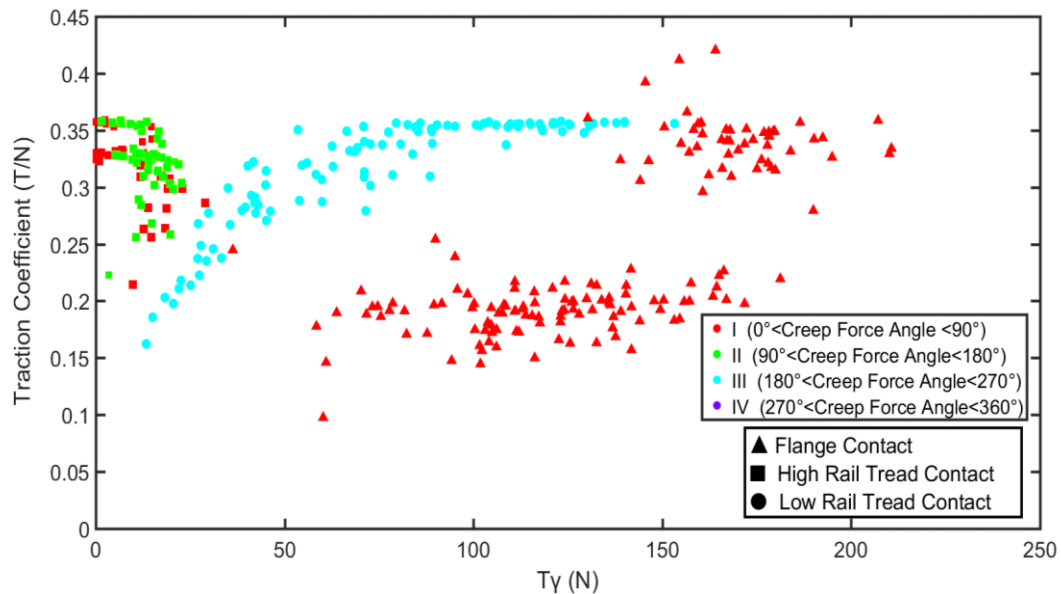


Figure 6.22: The comparison of different creep force angle regions on the selected sites of Bakerloo NB line

However, in contrast to creep force angles, the maximum contact stress results which are presented in Figure 6.23 potentially provide the opportunity to predict different damage

mechanisms. The high values which were particularly occurred on the no reported RCF sections suggested that the high wear rate on these sites might remove the initiated cracks. Hence, no RCF defects were observed on these sites. For example, it was noticed that although the BH type of low rails exceeded the critical T/N limit, the contact stresses on this site were also high. Thus, this might give rise to wear rather than RCF damage on this site. But, the contacts both on the over-and-underground sections led to RCF cracking when they were mainly located between the two boundaries shown in Figure 6.23. The lower limit was found to be 600 $N/mm^2$ and upper limit was 2100 $N/mm^2$. In addition, the larger Tγ values inside these upper and lower limits were seen to be more prone to RCF cracking. When the Tγ levels are less than the specified region, the contacts were less susceptible to damage.
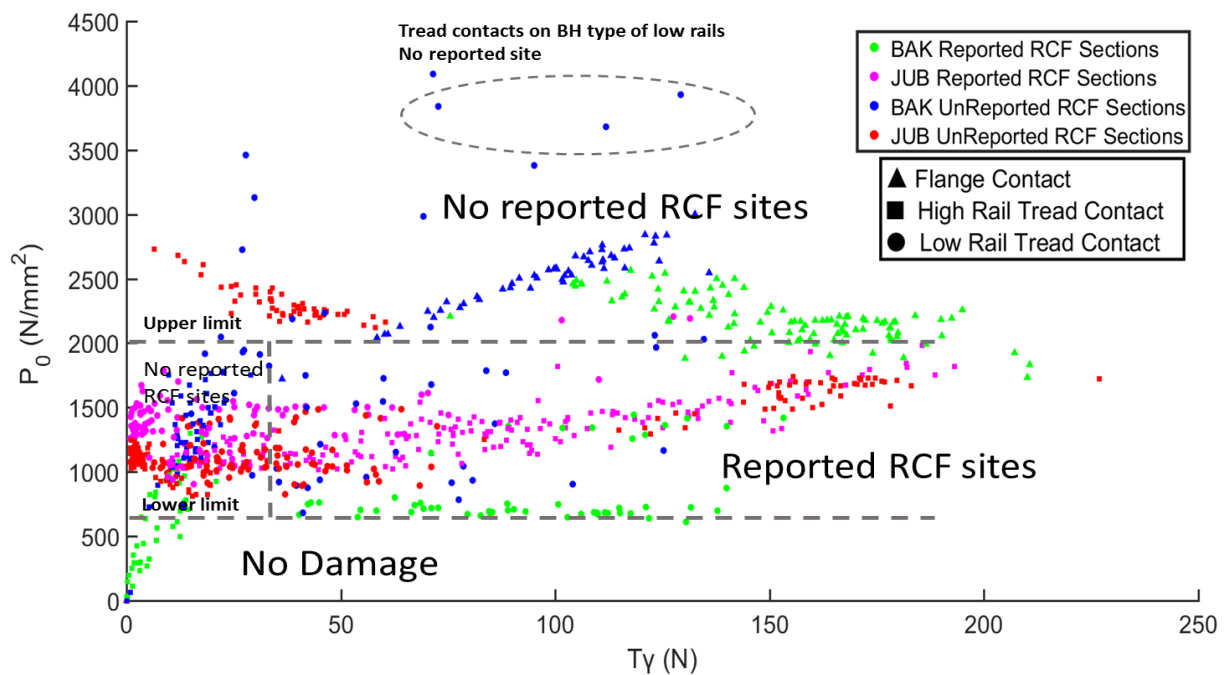


Figure 6.23: The comparison of Tγ and $P_0$ on the selected sites of curved tracks

## 6.2.2 Selected sites on the checked curved tracks

The high and low rails of checked curved sites were selected on the Bakerloo Southbound (SB) line. Figures 6.24 and 6.25 presented the selected sites on the lines respectively and Table 6.3 provides the track characteristics. Both the high and low rail sites were located on the relatively low cant deficiency regions.
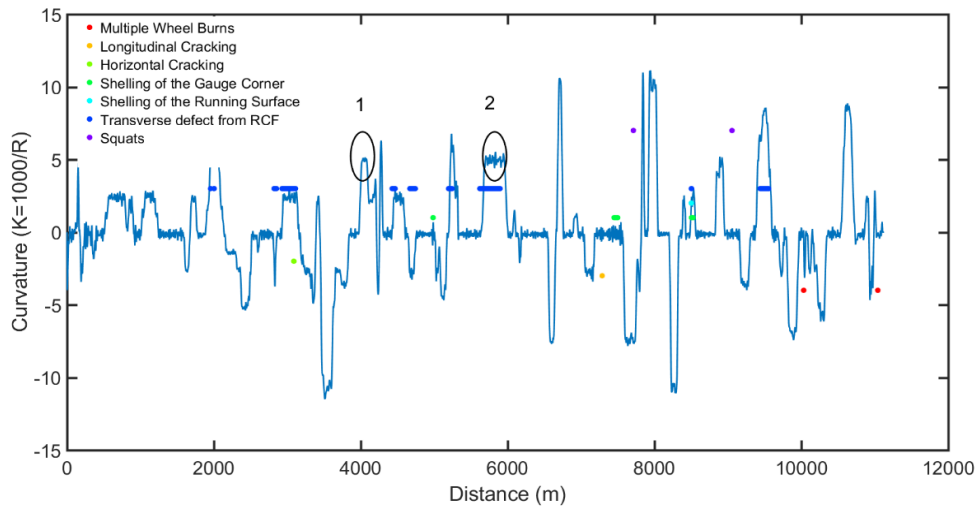
Figure 6.24: The selected reported and no reported sites on the lefts rails of Bakerloo SB Line
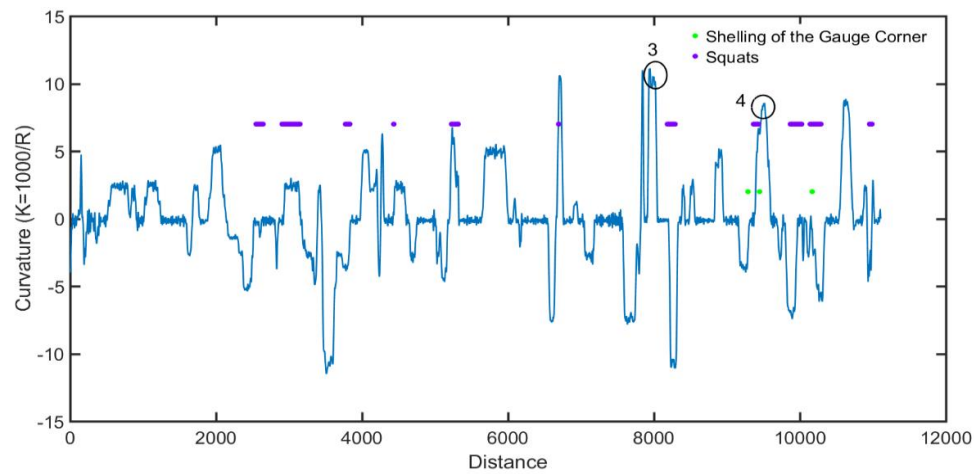


Figure 6.25: The selected reported and no reported sites on the right rails of Bakerloo SB Line

Table 6.3: The track characteristics of the selected sites for the checked curved tracks

| Site | Chainage (KM) | Rail Position | RCF Damage Condition | Radius (m) | Applied Cant (mm) | Cant Deficiency (mm) | Rail Profile | Section Type |
|---|---|---|---|---|---|---|---|---|
| 1 | 4+000-4+050 | High Rail | No reported RCF | 200 | 85 | 51 | FB | Underground (Tunnel) |
| 2 | 5+750-6+000 | High Rail | Reported RCF (Squat with T/O) | 200 | 85 | 51 | FB | Underground (Tunnel) |
| 3 | 7+950-8+000 | Low Rail | No reported RCF | 100 | 125 | 28 | FB | Underground (Tunnel) |
| 4 | 9+490-9+540 | Low Rail | Reported RCF (Squats) | 125 | 110 | 13 | FB | Underground (Tunnel) |

Figure 6.26 displays the comparison of Tγ and T/N results on the selected checked curved tracks. As the selected sites were located on the underground section, the T/N of 0.31 was again indicated as the boundary limit between no reported and reported defect sites. All the high and low rail contacts (green colour) occurred above this limit. However, due to the selection length/distance of the sites (50 m), some of the contacts' results of the no reported RCF sites exceeded the specified limit.
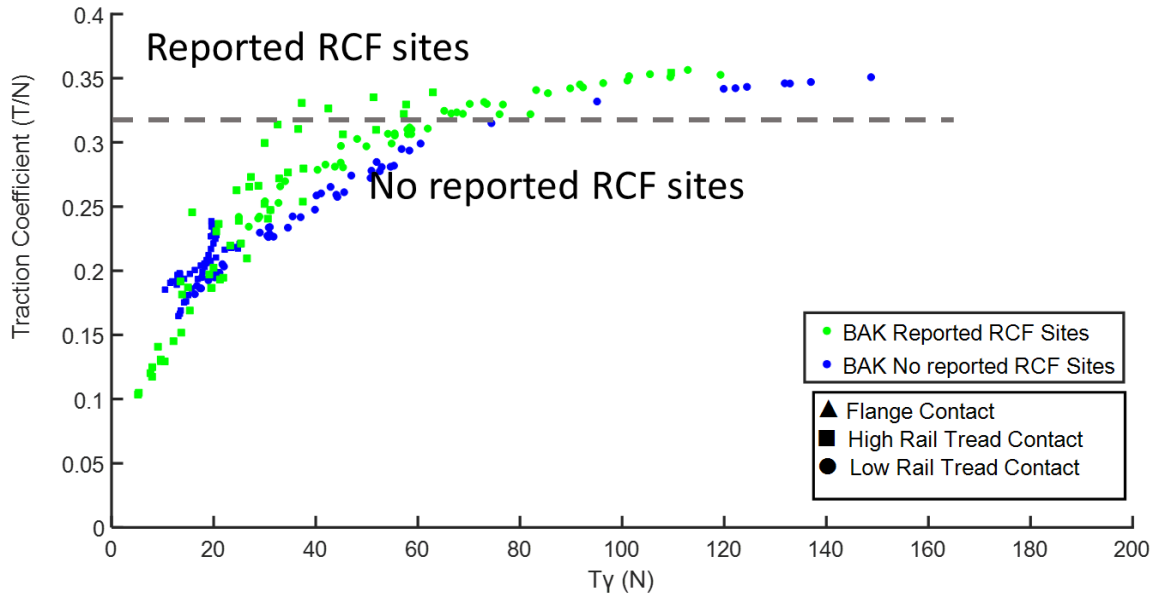
Figure 6.26: The comparison of Tγ and T/N on the selected sites of checked curved tracks

Regarding the creep force angles presented in Figure 6.27, they again did not show a major difference between the reported and no reported sites. While the contacts on the low rails occurred in the traction direction (IV:270°-360°), the high rails were in the braking direction (III:180°-270°).
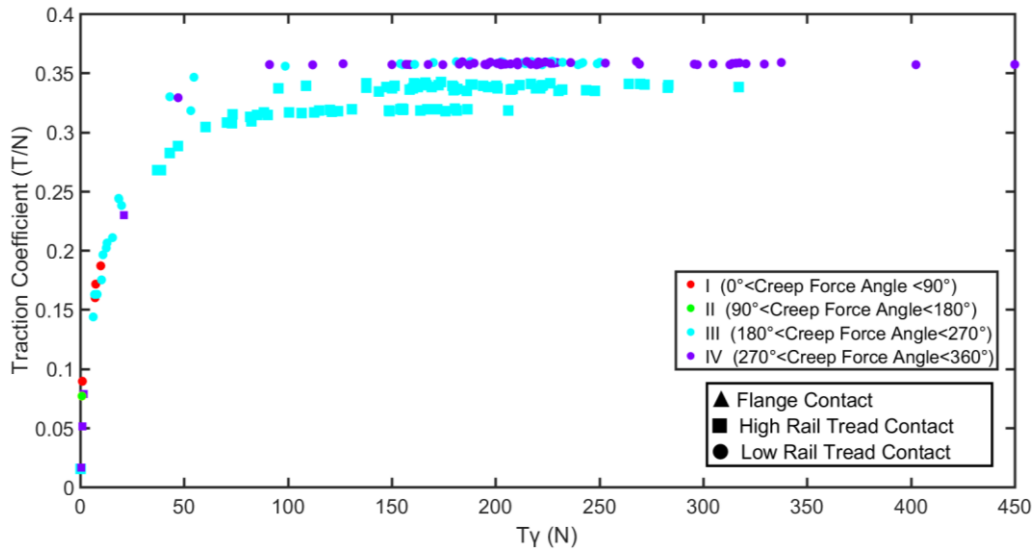


Figure 6.27: The comparison of different creep force angle regions on the selected sites of Bakerloo SB line

The $P_0$ values which are demonstrated in Figure 6.28 again put forward the possibility of interaction of wear on RCF damage. Several contacts particularly on the low rails of no reported sites potentially suggested the exceedance of wear rate over crack growth rate. However, due to larger areas on single tread contacts generated on both high and low rails, the $P_0$ mainly decreased at checked curve sites and they clustered between the specified limits. Nevertheless, it was apparent that the energy levels on the majority of contacts of the reported sites were considerably higher than the no reported sites.
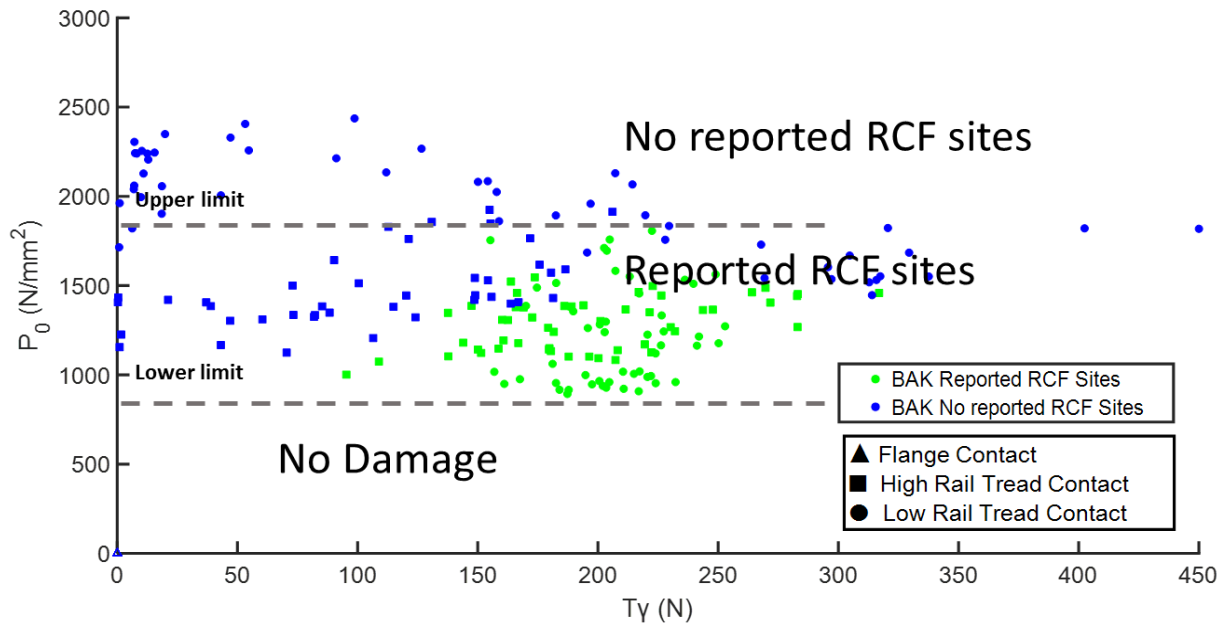
Figure 6.28: The comparison of Tγ and P₀ on the selected sites of checked curved tracks

## 6.2.3 Selected sites on tangent tracks

The tangent track sites were selected from both Bakerloo and Jubilee lines. Table 6.4 lists the reported defect and rail profile types. As the sites were located on a mixture of different directions and rails of the lines, the line plots were not prepared in this section.

Table 6.4: The track characteristics of the selected sites for the tangent tracks

| Site | Chainage (KM) | Rail Position | RCF Damage Condition | Rail Profile | Section Type |
|------|---------------|---------------|----------------------|--------------|--------------|
| 1 | 9+970-10+020 | Tangent Track | Reported RCF (Squats) | BH | Underground (Tunnel) |
| 2 | 8+420-8+470 | Tangent Track | Reported RCF (Squat with T/O) | BH | Underground (Tunnel) |
| 3 | 1+760-1+810 | Tangent Track | Reported RCF (Squat with T/O) | FB | Underground (Tunnel) |
| 4 | 4+700-4+750 | Tangent Track | No reported RCF | FB | Underground (Tunnel) |
| 5 | 15+970-16+020 | Tangent Track | Reported RCF (Shelling of the Gauge Corner) | FB | Underground (Tunnel) |
| 6 | 11+000-11+050 | Tangent Track | No reported RCF | FB | Underground (Tunnel) |
| A | 1+500-1+550 | Tangent Track | No reported RCF | FB | Overground (Ballasted) |
| B | 28+000-28+050 | Tangent Track | Reported RCF (Squats) | FB | Overground (Ballasted) |
| C | 35+700-35+750 | Tangent Track | Reported RCF (Squats) | FB | Overground (Ballasted) |

On the contrary to curved track results, the Tγ and T/N values on the selected tangent tracks which are illustrated in Figure 6.29 did not produce high values. Only some of the contacts on BH type of rails were greater than the 0.31 limit. The unsaturated contacts

149

both on the over-and-underground sections could not exceed the 0.25 limit. However, the majority of the reported sites (green and magenta colour) had larger Tγ and T/N values compared to no reported sites. When the results were compared between shelling and squat areas on the Jubilee line, it was observed that both of their values were similar.
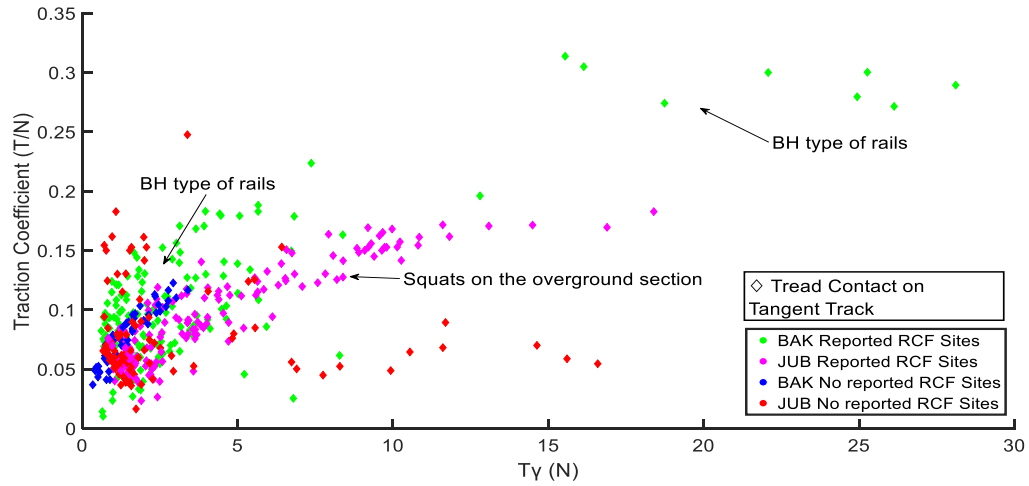


Figure 6.29: The comparison of Tγ and T/N on the selected sites of tangent tracks

Owing to effect of different rails (left or right) and the changing route characteristics of both of the lines, the creep force angle directions varied as shown in Figure 6.30. While some of the sites generated forces in the traction direction, the others occurred in the braking direction. However, the BH type of rails led to similar direction region (I:0°-90°) on both of the reported sites.
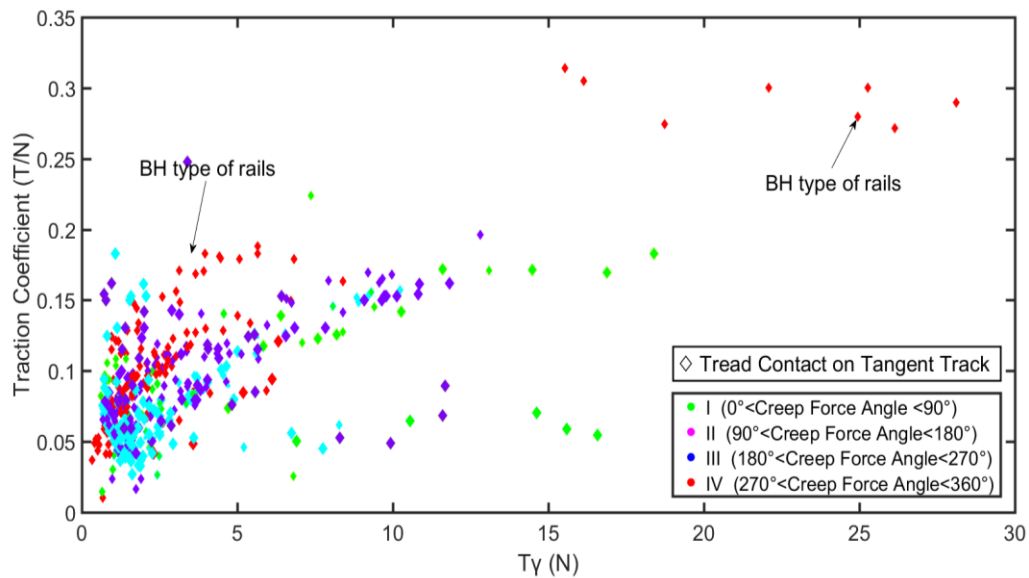


Figure 6.30: The comparison of different creep force angle regions on the selected tangent sites

Figure 6.31 shows the comparison of Tγ and $P_0$ results on the selected sites of the tangent tracks. As it can be noticed on the contact stress values, the upper limit which was proposed in the curve track site analysis was not reached by these contacts. The highest levels were observed on some of the BH type of rails. However, the Tγ was again found to

be effective at predicting the site which are more susceptible to RCF cracking. Moreover, it was also noticed that a higher contact stress was on sites with reported squat damage than shelling damage.
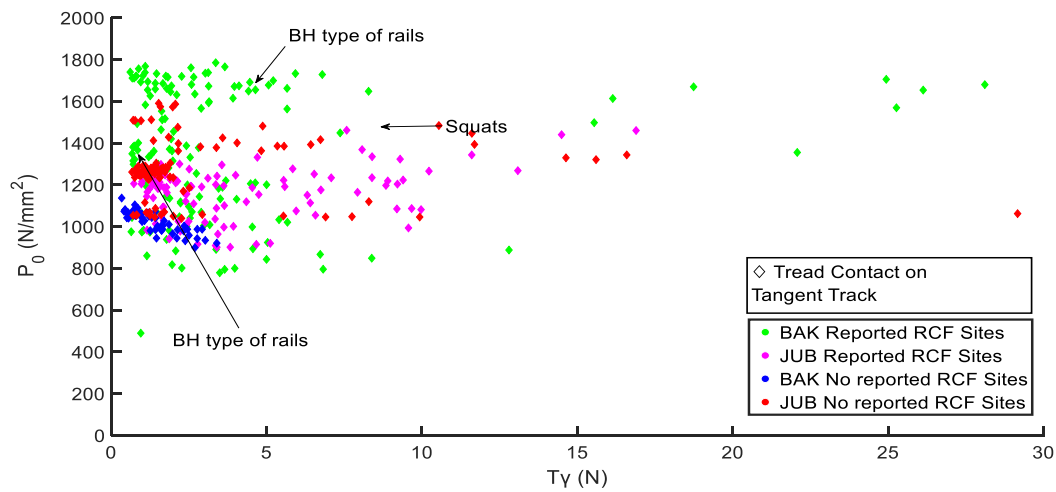


Figure 6.31: The comparison of Tγ and $P_0$ on the selected sites of tangent tracks

## 6.2.4   Summary of the section results and discussions

In this study, a range of damage prediction parameters were compared for sites with reported and no reported defects to identify which of them better describe the susceptibility of these sites to damage. In order to observe the changes in various conditions, the sites were selected from three main groups: curved track sections (R>200 m), checked curves track sections (R<200 m) and tangent track sections. The study concluded the following results regarding the 4 key parameters considered in the analysis:

Traction Coefficient (T/N):

- The shakedown theory stated that T/N values in the range 0.25 and 0.30 were the critical limits for rail surface damage for line and point contacts, respectively. The contacts generate plastic flow beneath the surface of the rail which can lead to subsurface damage when the T/N is below 0.30 limit whereas, plastic flow occurs on the running surface if this limit is exceeded. It should be noted that although several studies identified the limit as T/N=0.30, there were studies indicating that a limit of T/N=0.32 (Beagley, 1976). But, it is clear in the Shakedown Map that the limit is definitely higher than 0.30.

- Although the maximum friction coefficients had a significant impact on traction coefficients (μ=0.25 and μ=0.36 on over-and-underground sections), a T/N of 0.31 seemed to be the critical limit particularly for underground sections. Wheel-rail contacts which exceeded this limit were typically more prone to RCF cracking regardless of the Tγ values. This was observed on both high and low rails of checked (R<200 m) and unchecked curved (R>200 m) sites.

- Where the T/N limit was not exceeded especially in overground curved and tangent track sites, the level of $T\gamma$ became crucial as the higher values coincided with sites with reported RCF damage.

Creep Force Angle

- The creep force angles did not generally vary between reported and no reported RCF sites.

Maximum Contact Stress ($P_0$)

- Similar to T/N results, the maximum contact stress values differed between the selected sites. Higher stresses were particularly evident on the no reported sites. Thus, this potentially suggested that the wear rate on these sites might exceed the crack growth rate and hence, the initiated cracks are removed by wear.
- The reported sites mostly occurred between the defined upper and lower limits. However, it was also noticed that the RCF susceptibility between these limits was raised by the increase in $T\gamma$ levels. While the smaller energy values demonstrated no recorded defects, the higher values showed observed damage.

Energy Parameter ($T\gamma$)

- Even though the $T\gamma$ values seemed to be not as distinctive as Shakedown Map parameters of T/N and $P_0$ in differentiating the sites susceptible to damage, it was certain that higher $T\gamma$ values were in site with reported RCF.

As a result, the importance of both $P_0$ and T/N levels on observed damage put forward the use of Shakedown Map in the research. Therefore, Figure 6.32 was plotted to show the specified critical limits for all contacts on the selected sites. The majority of the contacts on the reported sites were located between the upper and lower limit of contact stress values. However, these indicated limits do not correspond to the boundaries in the Shakedown Map. The contact stresses should be divided by the shear yield limit to obtain load factors in the y-axis of the Shakedown Map. It was noticed particularly on the high rail sites that although the tread contacts were inside the limits, the flange contacts had higher $P_0$ values which showed that while the tread contact may lead to RCF damage on rails, the flange contacts may result in wear damage.

It should be noted that the sites which were reported in the defect data sheets as presented in the Chapter 3 were taken into account in this part of the research. Even though this data consisted of both ultrasonic and visual inspection results, it may contain some detection errors. For instance, the thermal damages (e.g:studs) could be reported as squat or shelling defects. In addition, due to rail age (recent rail replacements and/or grinding activities), no RCF could be detected on these no reported sites. In order not to

mislead the research, several sites with different characteristics and 50 m reported distance were taken into account. However, as it can be seen, this selection distance caused some of the contacts to occur inside the limits while, the others were outside the limits. Although the total affected distances were recorded in the defect data sheets, there were sometimes misinformation in which it was not clear whether the cracking was observed continuous or intermittently at these sites.
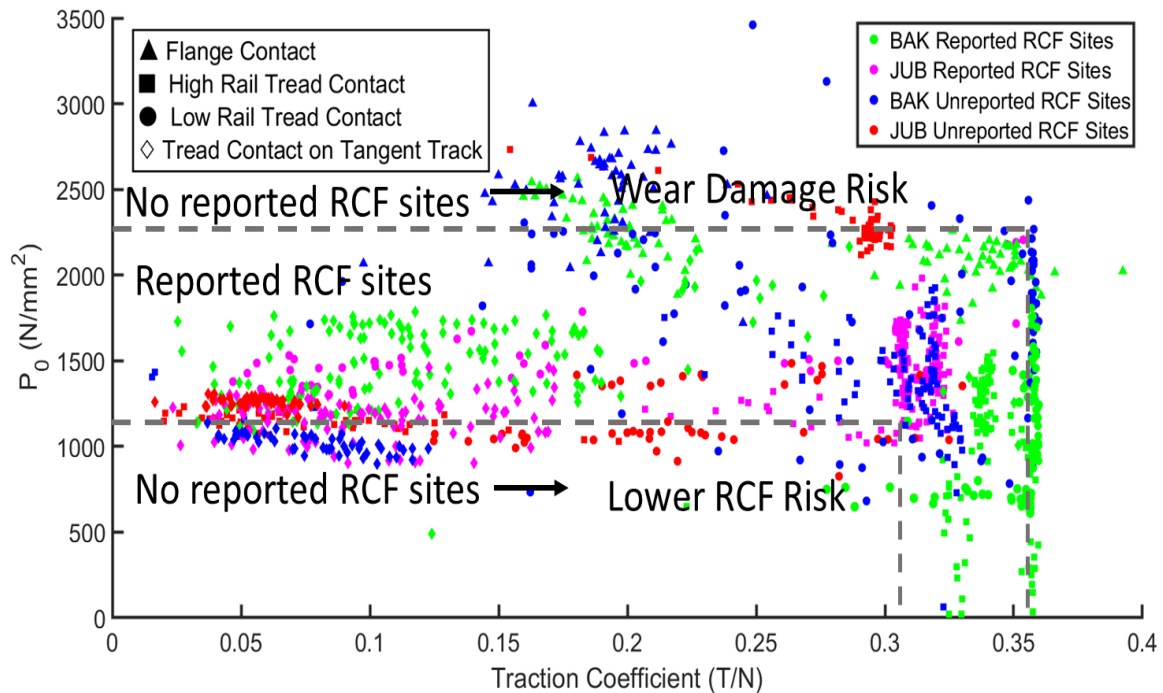


Figure 6.32: The comparison of reported and no reported RCF sites on the Shakedown Map

Furthermore, even though the study potentially provided opportunity to predict different damage mechanisms such as wear and RCF, they failed to identify different defect types. Nevertheless, it was noticed that the reported squat defects on the tangent track site produced greater contact stresses than the shelling sites on the Jubilee line.

## 6.3 The use of Tγ with Shakedown map in rail damage prediction

To observe the changes in Tγ levels on the Shakedown Map, Figure 6.33 was prepared. Whereas the colour of the points represents the different risk levels of the WLRM (Tγ ranges), the shape of the marker indicates different contacts on the selected reported and no reported sites. As it can be seen, while the predicted risk levels were raised by the increase in T/N values, the $P_0$ did not show a good correlation as the values varied for different contacts. For instance, the flange contacts which had significantly high contact stresses produced lower energy results. Even though the comparison study suggested that these contacts might give rise to larger wear rates in rails, it was noticed that they had relatively small energy values such as 15 N < Tγ ≤ 65 N (RCF Only) and 65 N < Tγ ≤ 175 N (RCF and Wear). Nonetheless, this finding supported the argument that the lower energy

values might also contribute to wear. In order to take into account these lower values, it was proposed to use the BRR model function in the research. The total worn area/depth predicted by this model was accounted for the crack depth estimations to find the dominant damage in rails.
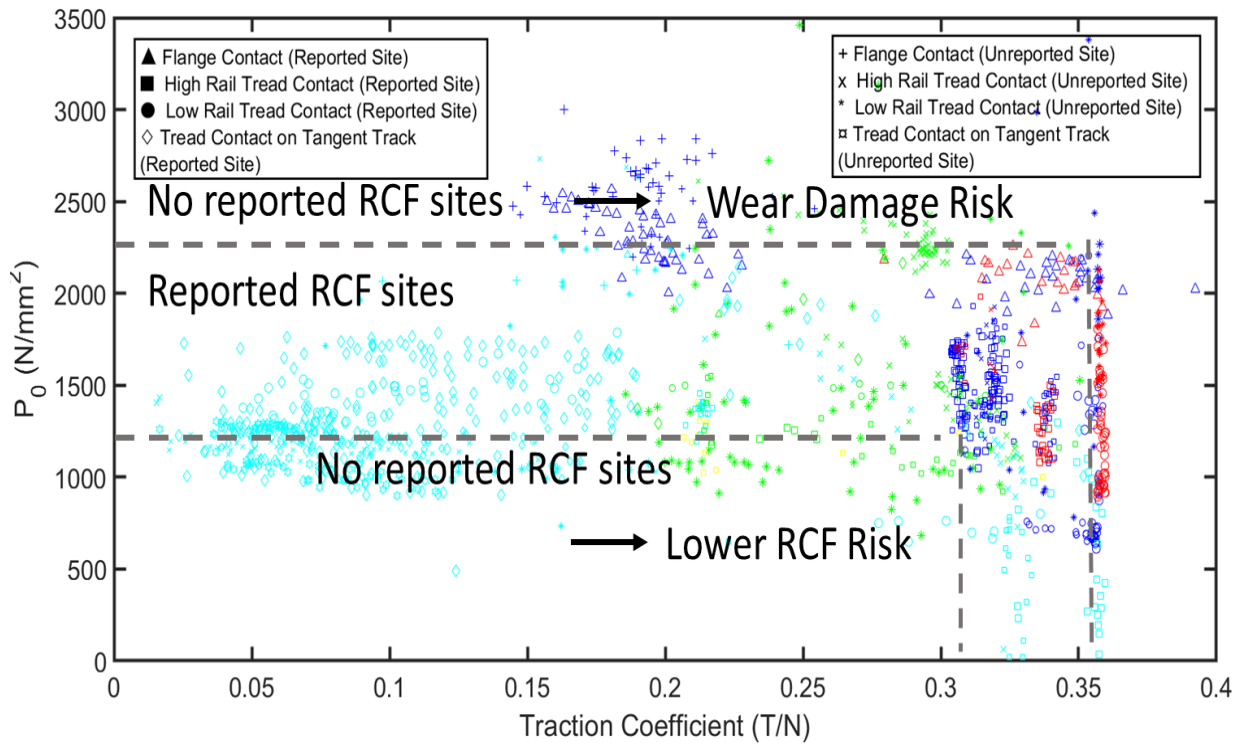


Figure 6.33: The comparison of WLRM different risk levels between the reported and no reported RCF sites on the Shakedown Map

In the RCF damage prediction, the results from the reported sites were considered and it was found that the all three parameters played a key role in observed damage. Whereas the contacts were mainly generated between the specified upper and lower limits on the Shakedown Map, Tγ was also seen to give rise to RCF risk.

As a consequence, the simulation results and the comparisons presented in the previous sections demonstrated that improvements in the modelling of rail damage susceptibility can be achieved with a combination of wheel-rail contact energy and parameters associated with shakedown theory. The previous study stated that the Shakedown Map was less satisfactory for predicting the cumulative plastic deformation which took place with repeated rolling cycles (Zhao, 2012). Thereby, it was only used to differentiate the damage type; wear and RCF. Instead, the Tγ was utilised to quantify the severity of each damage type and several calibrations based on measured crack depths were applied to the new RCF crack depth prediction model.

To define the wear and RCF associated regions in the Shakedown Map, the iterative process displayed in Figure 6.34 was implemented. In relation to wear predictions, various (upper) $P_0/k$ and T/N values were assigned. If the contact parameters were inside this

selected region, the BRR function was applied and the results compared with MiniProf measurements. Subsequently, the outside region were assigned for the RCF predictions. The significance of a T/N = 0.31 as well as the lower and upper limits; 0.25 < T/N < 0.36 in the previous comparison plots played a key role. The corresponding Tγ values were taken to define the new breaking points of the model. After filtering the contacts with the related RCF region in the Shakedown Map, the new breaking Tγ points were associated with the MRX-RSCM crack depth measurements. When the differences between predictions and measurements in terms of both RCF and wear were acceptable meaning that the optimum solutions were obtained considering the changes in site measurements on sites with various track characteristics, then the iterative process was ended. The next section explains the reasons for the selected regions in the model in more detailed and included the support from literature review.
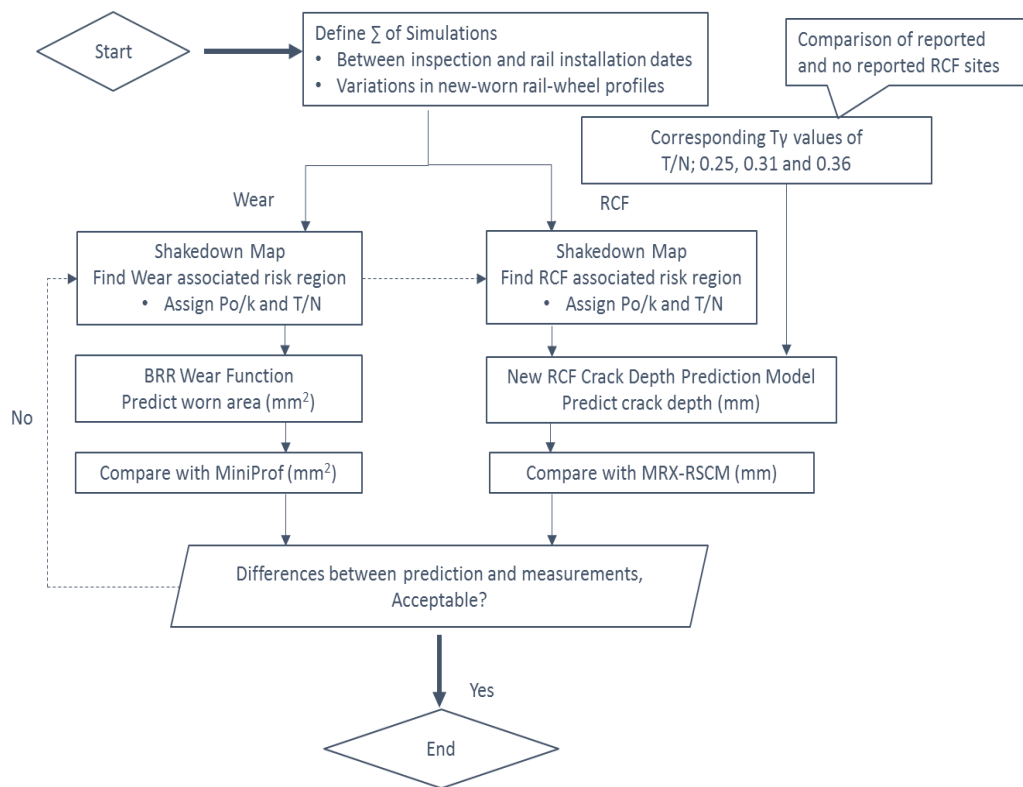


Figure 6.34: Iterative process in the development of new rail damage prediction method

## 6.3.1 Wear damage prediction

The damage propensity levels of the contacts were first evaluated by using the Shakedown Map and then the BRR function was implemented accordingly. Whilst several different mechanisms lead to wear in rails such as adhesion, abrasion and oxidation, the high plastic flow accumulation also causes wear and RCF cracking. It was often stated in previous literature that the ratchetting process in which the material accumulated net unidirectional strain during each cycle led to either removal of material from the surface or initiated RCF

cracks (Hyde, 2011). To find the dominant failure mechanism under the test conditions, several experiments were conducted with rolling direction reversals. It was revealed that while there was high wear rate in unidirectional strain accumulation, the wear rate reduced after the reversal. But, although RCF cracks were also initiated under unidirectional rolling-sliding, their propagation did not cease upon reversal. Therefore, it was concluded that while wear was mainly driven by ratchetting, this process as well as other failure mechanisms such as HCF and/or LCF contributed to crack propagation (Franklin, Chung, & Kapoor, 2003). Additionally, as it was aforementioned in Chapter 2.6, while the crack initiation was experienced for the higher $FI_{surf}$ values (associated with ratchetting limit), the occurrence of wear in the subsequent cycles removed the initiated cracks (Ekberg et al., 2014). Similarly, the $FI_{surf}$ values had highest values when the Damage Index (Tγ > 175 N) was negative (Stichel et al., 2008).

Even though the ratchetting was stated to be responsible for both of damage types, there were still uncertainties which factors or loading give rise to wear or RCF initiation. One of the previous studies found that while normal loads which mainly resulted from axle loads gave rise to thicker plastically deformed layers, shear loads causing from traction and braking forces led to thinner deformations in the material (Schilke, 2013). Similarly, another study which carried out experiments to understand the damage mechanisms in heavy-haul and high speed lines found that the plastic deformation was relatively thicker under heavy axle loads and wear was mainly observed in these conditions. However, the higher speeds caused deformations with thin layers and the cracks were often experienced in these cases (Zhong et al., 2011). This result was also declared in an earlier study by mentioning that the wear degree of material could be represented by the thickness of flow layer. The thicker the flow layers, the severe wear will be observed in rails (Qiu, Pei, & Jin, 1996).

Moreover, the previous wear prediction studies which were mentioned in the Chapter 2.4.2 also highlighted the importance of using contact pressure in the wear damage predictions. For instance, the earlier study stated that the mild wear regime was observed to be mainly dependent on the applied contact stress but independent of creepage (Bolton et al., 1982). Likewise, the subsequent studies stated that while using Tγ/A approach enabled to present wear regime transitions, it did not demonstrate how other parameters such as contact pressure and slip velocity individually affected wear rate (Lewis & Olofsson, 2004).

Similar to the findings in the literature review, the larger contact stresses of the no reported RCF sites in this study potentially suggested the higher wear rate over crack growth rates. As a result, to consider the high contact stress values in the wear predictions, the wear risk was associated with ratchetting mechanism on the Shakedown Map. Additionally, the LCF failure which is the plastic shakedown was also considered in the

research. Since the LCF would initiate damage in the sub-surface, it was suggested that this might also contribute to thicker plastic deformations.

As the ratchetting limit was calculated based on the non-linear kinematic hardening law that was applied to elastic-perfectly plastic material on the Shakedown limit, the following formula was used to calculate shear yield limit 'k' (Burstow et al., 2008). The tensile strength value of the R260 steel was obtained from the standard EN 13674-1. Previous experiments found that although work hardening increased the shear yield limit on the surface due to wheel passages, it reduced linearly and became constant after reaching certain depth (Jones, Tyfour, Beynon, & Kapoor, 1997). However, this was also affected from the surface friction conditions, whereas the maximum levels occurred at a 0.45a depth, increased the shakedown limits under μ=0.1, the maximum generated at the surface, with a lower effect in shakedown limit under μ=0.5 (dry case). Since the research considered the route simulations with changing contact conditions, a constant value of 400MPa was selected.

$$k = \frac{\sigma_{yield} + \sigma_{UTS}}{2\sqrt{3}} = \frac{508 + 880}{2\sqrt{3}} = 400 \text{ MPa} \tag{6.4}$$

Figure 6.35 shows the proposed wear risk on the Shakedown Map. When the parameters: load factor ($P_0$/k) and traction coefficient (T/N) of the contact lay inside the specified regions, it was suggested that these contacts led to wear damage. In order to understand its severity, the energy (Tγ) of the contacts was considered and the total worn area from the successive wheel passes was calculated by using the BRR function. The recent wear curves with third body layers was not applied since, their wear coefficients were related with weight loss per area (μg/m/mm$^2$) (Hardwick et al., 2014).
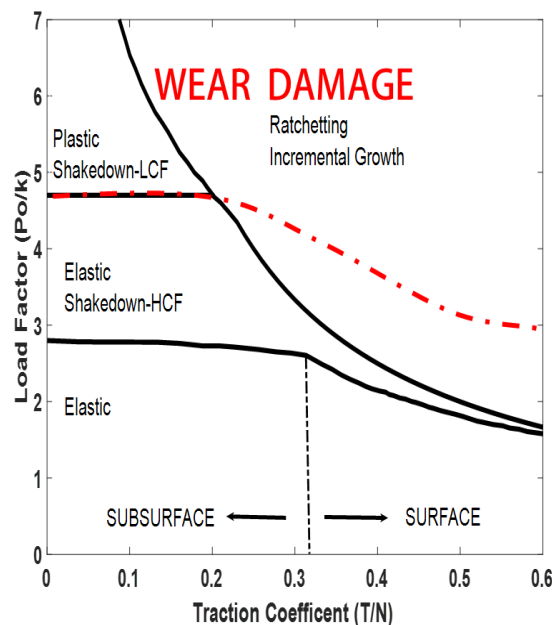


Figure 6.35: The proposed wear risk (region) on the Shakedown Map

## 6.3.2 RCF damage prediction

Since the previous studies highlighted the importance of large shear stresses in RCF damage, it was initially suggested to use 0.31 T/N limit, as it was also indicated as the surface damage limit in the Shakedown Map for point contacts. However, while 0.31 T/N limit was exceeded by the contacts on reported track sites in the tunnel section, it could not be exceeded by them on the overground and tangent track sites. To predict the damage in these areas and develop a model which is applicable to track with various conditions, the 0.25 limit was also taken into account in the research. In addition, this limit was also declared as the critical between surface and subsurface damage for line contacts. Therefore, the T/N of 0.25, 0.31 and 0.35 were selected to define the new breaking points of the model. To accumulate the damage predictions, the corresponding Tγ values were found for high and low rails which is presented in Table 6.5.

Table 6.5: The proposed Tγ breaking points of the new model

| T/N | Selected Corresponding Curve Radius on High Rails (m) | Selected Corresponding Curve Radius on Low Rails (m) | Selected Corresponding Tγ on High Rails (N) | Selected Corresponding Tγ on Low Rails (N) | Proposed Tγ for all contacts (N) |
|---|---|---|---|---|---|
| 0.25 | 1200 | 700 | 15 | 30 | 15 |
| 0.31 | 650 | 500 | 60 | 60 | 65 |
| 0.35 | 250 | 250 | 175 | 125 | 175 |

As it can be seen on the last column of Table 6.5, the selected breaking points in this research were identical to the WLRM. The thresholds adopted in the WLRM were proposed based on the large number of field observations and experimental results. Even though the studied metro lines consist of different vehicle-track characteristics which result in different trends in the energy levels at the wheel-rail interface, these selected values cover a significant range of contact on both the high and low rails. For instance, while the smaller curve radius increased the Tγ substantially, the use of lower friction coefficients due to lubrication application decreased the energy values compared to using a relatively high friction coefficient of μ=0.45 in the original WLRM. Therefore, the magnitude of the energy remained similar in this model.

However, in contrast to the original WLRM, the energy values in this model are the 'raw Tγ' outputs and therefore, they are not scaled by the direction of the creep forces. But, damage is only calculated for contacts where their shakedown parameters lay inside the given region defined in Figure 6.36. As the previous comparison study potentially suggested the 0.25 T/N limit to be the lowest risk levels between reported and no reported sites, the results higher than this limit were only considered in this method. Additionally, while the WLRM predicted wear risk for Tγ values higher than 175 N, the new model suggested to cause an increased RCF risk as displayed in Figure 6.37 under the defined

contact stresses and traction coefficients. This also supported the previous wear study stating that the further increase in Tγ/A values led to the development of RCF cracks on the worn surfaces (Lewis et al., 2010). Even though all the failure mechanisms in the Shakedown Map may contribute to RCF damage, the contacts which were in the ratchetting region were suggested to be primarily responsible in this research. Since one of the objectives of this research is to investigate the interaction between wear in RCF, the ratchetting failure mechanism was only considered and due to this certain reduction in the total number of wheel passes were made which is further explained in Chapter 7. It should be also noted that site observations demonstrated that the HCF produced less visible damage (Ringsberg, 2001).
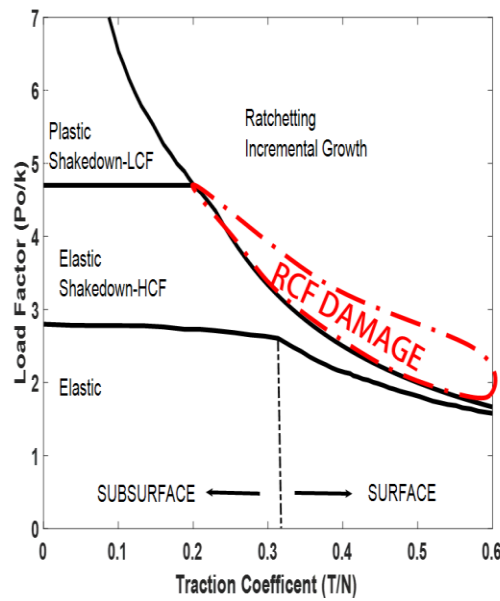


Figure 6.36: The proposed RCF damage risk on the Shakedown Map
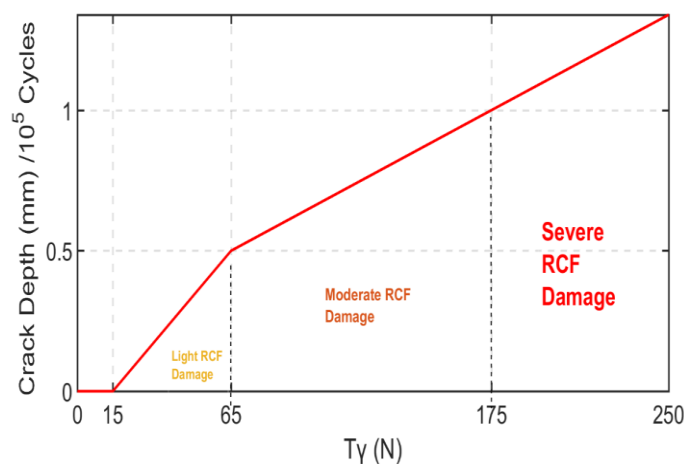


Figure 6.37: The proposed new RCF prediction model

In the previous studies, it was stated that both WLRM and Shakedown Map demonstrated good correlation with plastic flow accumulation which was mainly occurred in the first crack propagation phases (Phase 1). However, the increase in further crack depth was mainly

dependent on other factors such as fluid mechanism, thermal and residual stresses as aforementioned in Chapter 2. In this research, the new RCF crack depth prediction model was developed/validated using the consecutive MRX-RSCM measurements conducted during the initial two-year period after rails were installed. Therefore, the model input Tγ became applicable to predict the damage in these initial measurements. Nonetheless, the research argued its uses in further crack propagation phases since, the parameter can be used to accumulate damage predictions and hence, to estimate the rate of crack development between successive monitoring inspections

## *6.4 Conclusions and discussions*

As a result of the relationship between the selected damage prediction parameters and their comparison between the reported and no reported RCF sites, a combination of both the Shakedown Map and Tγ was proposed to help the increase the accuracy in the prediction of susceptibility of the rail to wear and RCF damage. Due to a limitation of the Shakedown Map in damage accumulation predictions, it was only used to classify the dominant rail damage mechanism in relation to wear and RCF. But, the Tγ was used in summing the damage predictions. While the BRR function was used in the wear prediction, a new RCF crack depth prediction model was developed from the critical T/N limits (0.25, 0.31 and 0.35) noted during the investigation. Their corresponding Tγ values were linked to MRX-RSCM measured crack depths as a consequence of large number of iterations conducted in the research.

As it was aforementioned in the Chapter 2.7, the previous studies highlighted that although the Shakedown Map underestimated the RCF damage owing to limitation of T/N by friction coefficient, the WLRM overestimated it, as the high creepages (>5%) demonstrated that it did not lead to increased crack propagation. In the research, these constraints were also taken into account and hence, the Shakedown Map was suggested to only be used in damage classification. But, due to lower creepages in the simulation results than the specified limit, the raise in Tγ was again suggested to result in increased RCF risk.

It was previously observed in the experiments that both LCF, HCF and ratchetting failure mechanisms in the Shakedown Map were responsible for RCF cracking. However, the results of the comparison study demonstrated that the T/N of 0.25 and 0.31 in the reported RCF sites are very significant and made the ratchetting failure essential in the RCF crack initiation. According to previous studies on the literature, the wear was observed when only the ratchetting limit was exceeded during the experiments. It should be also noted that the Shakedown Map was developed based on certain assumptions. Whereas the effect of partial slip which was particularly observed at tread contacts may decrease the ratchetting limit, the contacts with smaller lateral widths (b≤a) may increase it. Since it is

still uncertain how both of the parameters affect the shakedown limit at the same time, the existing diagram was continued to be used in the research.

Furthermore, the previous studies stated that even though the Shakedown Map and Tγ showed good correlation with plastic flow accumulation in the initial phase of crack development, further phases were highly dependent on other factors such as fluid mechanism, thermal and residual stresses. For this reason, the crack depth measurements conducted during the first two-years of rail life were used both in the development and validation of the new model. Nevertheless, the research argued that the applicability of the model in further crack propagation phases as, the Tγ parameter provides opportunity to accumulate damage predictions in order to find estimate the rate of crack development between successive monitoring inspections.

# Chapter 7  Prediction of Wear Damage

In this chapter, the proposed new wear prediction methodology was applied to the selected critical sites provided by LUL. Whilst the first section describes these sites, the second section explains the determination of number of simulation cases taken into account to describe the duty conditions experienced by the rails at these sites. In the last section of the chapter, the predicted rail wear in terms of worn area loss is compared with worn area loss from measured rail profiles under various track conditions.

## 7.1  Site selection

On LUL, a number of sites recently re-railed due to severe RCF cracking were selected for detailed monitoring under the 'RCF Monitoring Sites' study. The aim of this monitoring was to observe the crack development (e.g. initiation and propagation) at critical sites where RCF was frequently reported in the past. As it was aforementioned in the Bottom-Up approach used in the field crack data analysis (Chapter 3.3), this provides a useful opportunity to better understand the factors causing damage in the critical sites and help to develop more efficient maintenance strategies. During this study, the rail condition at these sites was monitored at certain intervals using several measurement techniques, including MRX-RSCM and MiniProf measurements to detect the severity of any defects and level of rail wear, respectively.

Table 7.1 lists the selected sites on the Bakerloo and Jubilee lines that were further studied in this research. It provides the sites' LCS numbers, location and the start and end chainages in each LCS section. Additionally, it illustrates when the rails were re-railed and the MiniProf and MRX-RSCM measurement dates.

Table 7.1: The properties of the selected RCF Monitoring sites

| Site | Line | LCS Code | LCS Location | Side R/L | LCS Start (m) | LCS End (m) | Distance (m) | Re-Rail Date | MiniProf Date | MRX-RSCM 1 Date | MRX-RSCM 2 Date |
|---|---|---|---|---|---|---|---|---|---|---|---|
| RCF-BAK-1 | BAK | B068/BNBLO | PADDINGTON TO WARWICK AVENUE | R | 223 | 762 | 539 | 04/05/2015 | 11/02/2016 | 14/11/2015 | 30/09/2016 |
| RCF-BAK-2 | BAK | B122/BSBLO | BAKER STREET TO REGENTS PARK | L | 443 | 718 | 275 | 20/03/2015 | 09/02/2016 | 17/11/2015 | 03/10/2016 |
| RCF-BAK-3 | BAK | B066/BNBLO | WARWICK AVENUE TO MAIDA VALE | R | 347 | 598 | 251 | 04/06/2015 | 11/02/2016 | 11/11/2015 | 10/10/2016 |
| RCF-BAK-4 | BAK | B068/BSBLO | WARWICK AVENUE TO PADDINGTON | L | 326 | 508 | 182 | 20/04/2015 | 11/02/2016 | 14/11/2015 | 30/09/2016 |
| RCF-BAK-5 | BAK | B068/BSBLO | WARWICK AVENUE TO PADDINGTON | R | 302 | 546 | 244 | 16/04/2015 | 11/02/2016 | 14/11/2015 | 30/09/2016 |
| RCF-BAK-6 | BAK | B062/BNBLO | KILBURN PARK TO QUEENS PARK | R | 129 | 309 | 180 | 17/06/2015 | 29/02/2016 | 11/11/2015 | 10/10/2016 |
| RCF-BAK-7 | BAK | B134/BNBLO | WATERLOO TO EMBANKMENT | R | 225 | 350 | 125 | 20/12/2014 | 08/03/2016 | 13/11/2015 | 14/11/2016 |
| RCF-BAK-8 | BAK | B134/BNBLO | WATERLOO TO EMBANKMENT | L | 200 | 340 | 140 | 20/12/2014 | 08/03/2016 | 13/11/2015 | 14/11/2016 |
| RCF-BAK-9 | BAK | B068/BNBLO | PADDINGTON TO WARWICK AVENUE | R | 92 | 197 | 105 | 29/04/2015 | 11/02/2016 | 14/11/2015 | 30/09/2016 |
| RCF-BAK-10 | BAK | N115/BSBLO | WATERLOO SOUTHBOUND STATION | R | 0 | 113 | 113 | 31/07/2015 | 06/10/2016 | 13/11/2015 | 13/10/2016 |
| RCF-JUB-1 | JUB | F044/JNBLO | GREEN PARK TO BOND STREET | L | 66 | 490 | 424 | 10/12/2014 | 31/08/2016 | 28/04/2016 | |
| RCF-JUB-2 | JUB | B114/JNBLO | BAKER STREET TO ST. JOHNS WOOD | R | 397 | 515 | 118 | 20/04/2014 | 25/08/2016 | 22/03/2016 | |
| RCF-JUB-3 | JUB | B112/JNBLO | ST. JOHNS WOOD TO SWISS COTTAGE | L | 634 | 735 | 101 | 20/08/2014 | 02/09/2016 | 22/03/2016 | |

## 7.2 Scaling of number of simulations

The changes in the Tγ levels due to different vehicle-track characteristics (as detailed in Chapter 5.1) highlight the importance of representative damage accumulation in prediction studies. It was concluded that to increase the accuracy of damage predictions, the duty conditions that are observed by the rail and the variation in contact conditions resulting from successive wheel passes should be taken into account in the modelling.

Therefore, the total tonnage and the number of axle passes for different inspection intervals was calculated considering the number of train passes in each day (as provided by LUL). To demonstrate the influence of variety of wheel profiles, different wheel-rail profile combinations were used as detailed in Chapter 4.2.2. In the wear damage predictions, different combinations were selected considering the duration of time between the rail-installation and MiniProf inspection dates. The wheel profiles were varied based on the computed wear distributions given in the similar section.

Figure 7.1 demonstrates the time duration (no. of days) which took place between the rail installation and different rail inspection activities. Considering the given number of train passes in each day, the total number of axle passes were computed. Figure 7.1 shows the values only for RCF-BAK-3 site. In this site, the MiniProf measurements were carried out between two consecutive MRX-RSCM inspections. However, this condition was different for other monitoring sites.
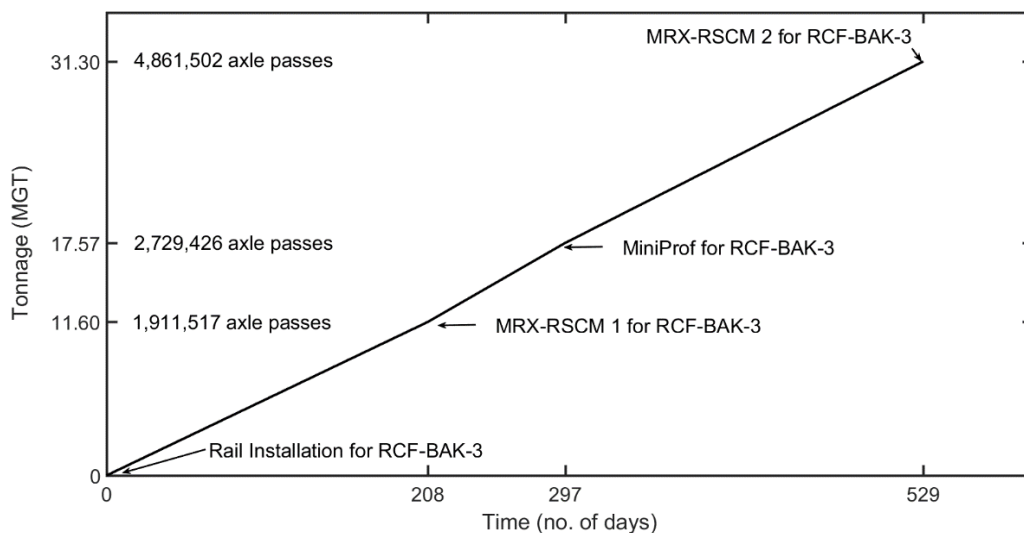


Figure 7.1: Time difference between rail installation and different rail inspection activities for RCF-BAK-3 site and their corresponding tonnage/no. of total axle passes

It was noted that when the proposed wear prediction methodology was applied to all simulated wheel-rail contacts, the calculated total worn areas were significantly higher than the field measurements. As it can be expected that from the differences in wear curves with third body layers, the (dry) BRR function resulted in greater predictions on real-track conditions. In addition to this, various types of shakedown responses take place

under repetitive wheel passages; while some passages will exceed the shakedown limit and cause plastic deformation to accumulate, the other passages as well as the surface displacement resulting from this previous exceedance might affect the shakedown limit and hence, lead material to a reversion to a shakedown state or continue to increase ratchetting. Previously, it was observed in the experiments that when the material was removed from the surface by wear, a new layer with different accumulated strain history was subjected to contact forces. This condition may either reduce the ratchetting per cycle or postpone it when the subsequent loads were below the shakedown limit. Therefore, the wear rate may drop in the subsequent cycles (Franklin et al., 2003). Although the new method only considered the associated wear risk region on the Shakedown Map to decrease the overestimations of the previous models, a further scaling factor had to be applied to the total no. of axle passes. This also showed that most of the energy produced at the wheel-rail contact including the large Tγ levels were not transformed in to wear or RCF damage.

As a result of the number of iterations, a scaling factor of 1% was implemented for the tonnage levels≤30 MGT and a relatively smaller factor of 0.5% was used after this tonnage limit due to drop in wear rates after certain time. Figure 7.2 displays the usage of a scaling factor and different rail-wheel profile combinations in damage prediction accumulations for each inspection. Since the MiniProf measurements were generally conducted at approximately at 17 MGT, new rail profile combinations initially were used up to 15 MGT. After this limit, the worn rail profile combinations were utilised in the analysis. In each of the new and worn rail cases, different wheel profiles were also used with new, light, moderate and severely worn cases selected to match the wheel wear distribution for the specific fleet as previously mentioned in Chapter 4.2.2. The formulas which help to calculate the number of simulations considered in the predictions on both Bakerloo and Jubilee lines are given in the Appendix A.
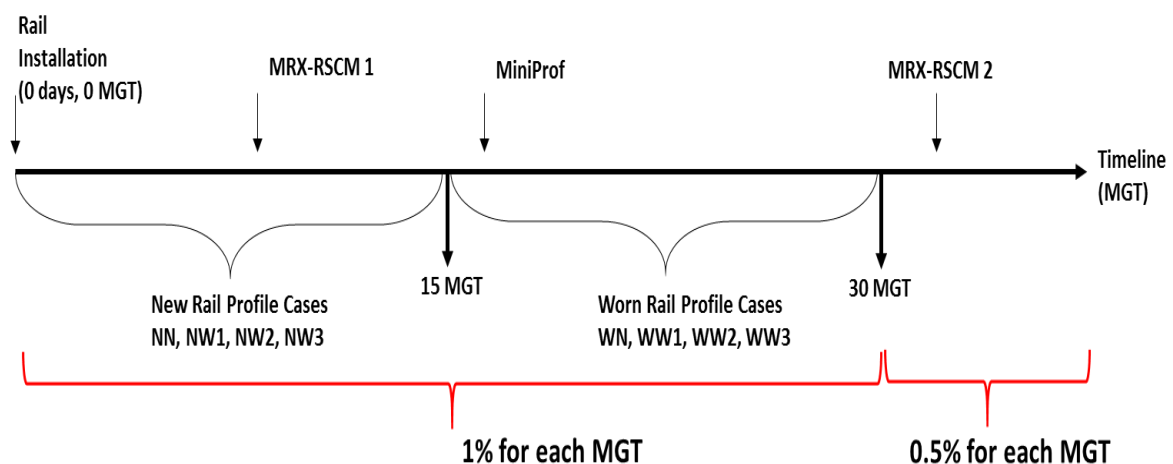


Figure 7.2: Usage of scaling factor and different rail-wheel profile combinations in damage prediction accumulations for each inspection

## 7.3 Wear damage prediction results

Based on the tonnage when the MiniProf measurements were conducted in each site, different wheel-rail profile combinations were selected and related scaling factor were applied to the total number of simulations. The contacts which were more prone to generate wear risk were filtered using the associated wear risk region on the Shakedown Map. Then, the BRR function was applied to predict the total worn area in rails. Figure 7.3 displays the steps in the proposed wear prediction methodology.
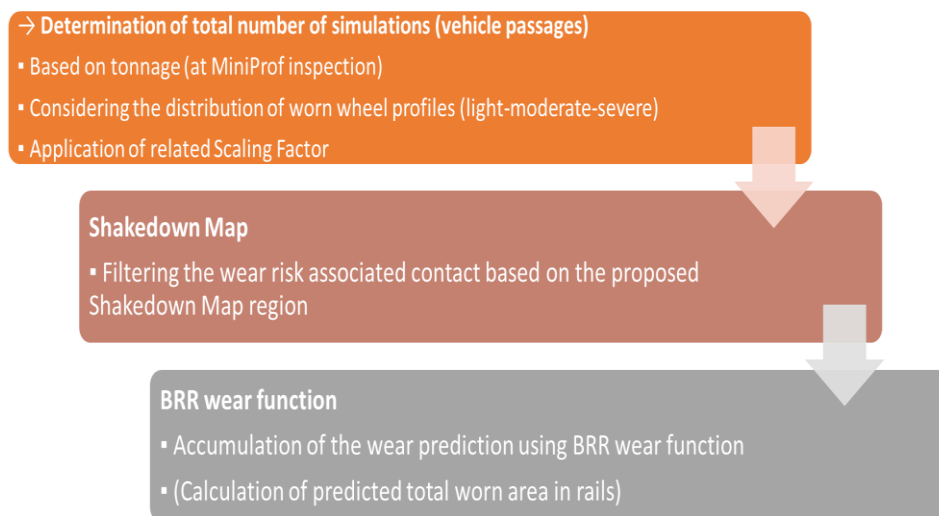


Figure 7.3: Steps in rail wear prediction methodology

In this study, the predicted loss in worn area in each selected rail profile were compared to the values determined from rail profiles measured during the monitoring study. The MiniProf software was used to determine the wear magnitude of each worn profile, defined as the loss of profile area (mm$^2$) when compared to a reference (new) profile. Figure 7.4 shows an example of worn (hatched) area between the reference and measured CEN 56E1 profiles.
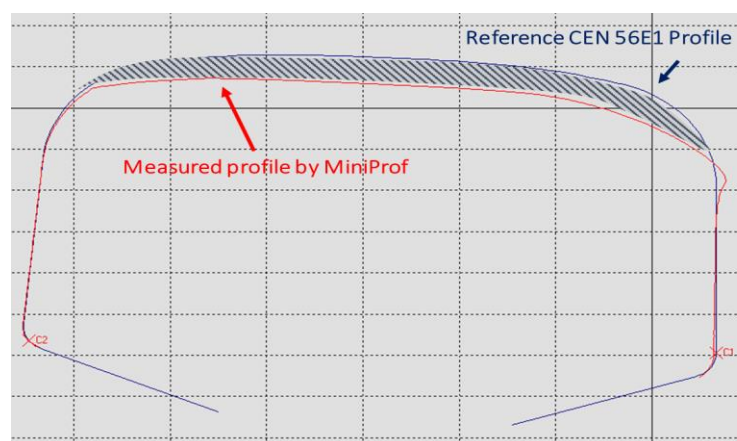


Figure 7.4: Calculation of worn area between reference and measured CEN56E1 profiles in MiniProf

However, it should be noted that some of the measured rail wear values might contain some discrepancies stemming from several factors. Firstly, the MiniProf software used to determine the change in profile shape by employing a reference (design) profile as a datum. It was assumed that although the rails were recently installed, the rails are manufactured to the same profile shape, by neglecting the manufacturing tolerances. When the manufacturing tolerances in the standard EN 13674-1 are considered, this could be either positive (more material) or negative (less material) on the railhead. Secondly, inspection errors which were often caused from contaminants on the rail surface might result in spurious spikes in the measurements. Thirdly, the failures generated when aligning the measured profiles with the reference profile in the software could give rise to total discrepancies and make the perceived worn area differ from the actual conditions.

In order to test the new wear damage prediction method in various track characteristics, the given rail profiles in the RCF monitoring sites were grouped into five different track categories as follows:

1) High rails (outer side) on un-checked curved track with a radius R>200 m
2) Low rails (inner side) on un-checked curved track with a radius R>200 m
3) High rails (outer side) on checked-curved track with a radius R<200 m
4) Low rails (inner side) on checked-curved track with a radius R<200 m
5) Rails on tangent tracks

## 7.3.1  High rails on R>200 m curved tracks

The characteristics of the selected high rail profiles (outer side) of R>200 m curved tracks are provided in Table 7.2. As it can be seen, the rails were located in different lines with various radii. While some of them were positioned in transitions, the majority of them placed in the curved sections. Instead of the exact time, the time (duration days) between the rail installation dates were shown for each 50-day range. For this reason, the MGT levels changed for the similar time ranges. Moreover, in order to compare the wear predictions in lubricated and unlubricated curves, the case 9 was included which was an unlubricated curve.

Table 7.2: The characteristics of the selected high rail profiles on R>200 m curved tracks

| Case No. | Line | RCF Monitoring Sites | LCS Code | Time (no. of days) Range | MGT | Chainage (KM) (Total distance in each line) | Radius (m) | Note | Rail Profile |
|---|---|---|---|---|---|---|---|---|---|
| 1 | BAK | RCF-BAK-1 | B068BNBLO | 300 | 16.6 | 8+048 | 269 | Curve | FB |
| 2 | BAK | RCF-BAK-1 | B068BNBLO | 300 | 16.6 | 8+128 | 351 | Transition | FB |
| 3 | BAK | RCF-BAK-4 | B068BSBLO | 300 | 17.6 | 2+953 | 446 | Curve | FB |
| 4 | BAK | RCF-BAK-4 | B068BSBLO | 300 | 17.6 | 3+053 | 410 | Curve | FB |
| 5 | BAK | RCF-BAK-8 | B134BNBLO | 450 | 26.2 | 1+862 | 315 | Curve | FB |
| 6 | BAK | RCF-BAK-8 | B134BNBLO | 450 | 26.2 | 1+942 | 340 | Transition | FB |
| 7 | JUB | RCF-JUB-1 | F044JNBLO | 650 | 55.5 | 16+098 | 476 | Curve | FB |
| 8 | JUB | RCF-JUB-1 | F044JNBLO | 650 | 55.5 | 16+298 | 472 | Curve | FB |
| 9* | BAK | RCF-BAK-6 | B062BNBLO | 250 | 14.9 | 10+545 | 388 | Curve | FB |

*unlubricated curve

Table 7.3: Comparison of predicted and measured worn areas on high rail profiles of R>200 m curved tracks



| | |
|---|---|
| **1** — Total Predicted Worn Area=8.3 mm² / Total Measured Worn Area=7.8 mm² | **2** — Total Predicted Worn Area=7.1 mm² / Total Predicted Worn Area=6.5 mm² |
| **3** — Total Predicted Worn Area=8.9 mm² / Total Measured Worn Area=8.5 mm² | **4** — Total Predicted Worn Area=11.6 mm² / Total Measured Worn Area=9.8 mm² |
| **5** — Total Predicted Worn Area=16 mm² / Total Measured Worn Area=13 mm² | **6** — Total Predicted Worn Area=14.1 mm² / Total Measured Worn Area=12.5 mm² |
| **7** — Total Predicted Worn Area=38.1 mm² / Total Measured Worn Area=27.5 mm² | **8** — Total Predicted Worn Area=25.3 mm² / Total Measured Worn Area=18.6 mm² |

Table 7.3 provides the comparison of predicted and measured worn areas on high rail profiles of curved track with a radius R>200 m. In the study, the maximum (peak) results in these plots were compared with the measured values. When there was more than one peak, the values were summed to find the total worn area. These plots also illustrate the relationship between predictions and measurements in terms of both magnitude and location. As it can be seen, there was a good agreement between the predicted and measured rail wear especially in newer rails; with the worn area and the location (lateral) of worn region on railhead were predicted with a reasonable level of accuracy using the new method. This showed that the higher contact stresses which were mainly produced at flange contacts in new rail profile combinations were responsible for the wear in rails. However, the over-estimation was observed on relatively older rails. Although the worn rail profile combinations helped to demonstrate the spread of wear over railhead such as cases 6 and 7, the values became considerably higher than the field measurements. There might be several reasons causing these problems. Due to differences in the plastic flow accumulation history in the deeper layers and the changes in the ratchetting rates, the wear rate can reduce after certain time (>300 days) and reach steady-state regime. But, it was still uncertain when the steady state wear was generated in reality whereas the cases 7 and 8 were located on the similar curve radii, there was a large difference in the actual worn areas. Therefore, the rail profiles should be measured more frequently to define these changes in wear rates and more worn wheel profiles should also be considered to describe the changes in contact conditions. The (dry) BRR function inevitably provided a better agreement with the unlubricated case 9 presented in Table 7.4.

Table 7.4: Comparison of predicted and measured worn areas on high rail profiles of R>200 m curved tracks (unlubricated case)
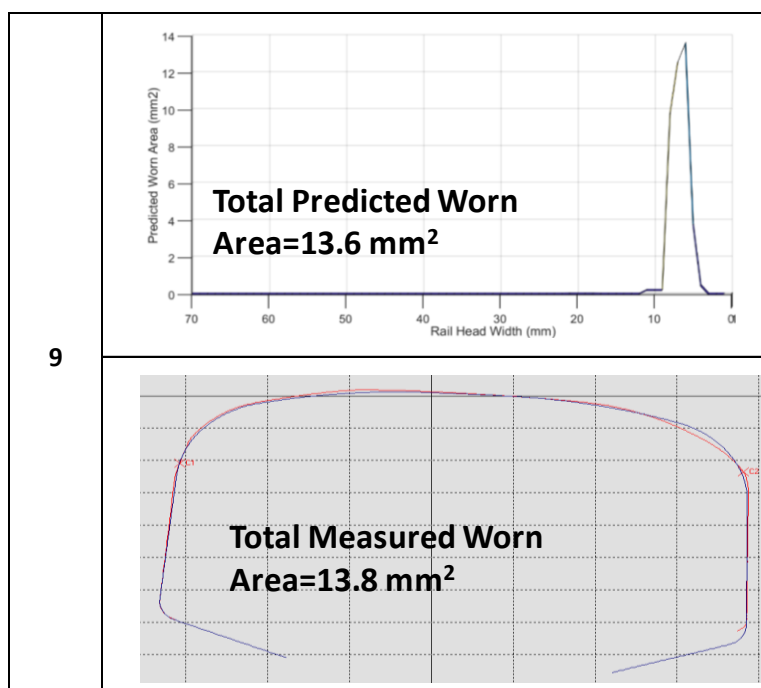
## 7.3.2  Low rails of R>200 m curved tracks

The low rail profiles (inner side) of R>200 m curved tracks that were selected in the research are listed in Table 7.5

Table 7.5: The characteristics of the given low rail profiles of R>200 m curved tracks

| Case No. | Line | RCF Monitoring Sites | LCS Code | Time (no. of days) Range | MGT | Chainage (KM) (Total distance in each line) | Radius (m) | Note | Rail Profile |
|---|---|---|---|---|---|---|---|---|---|
| 1 | BAK | RCF-BAK-1 | B068BNBLO | 300 | 16.6 | 7+848 | 321 | Curve | BH |
| 2 | BAK | RCF-BAK-1 | B068BNBLO | 300 | 16.6 | 7+948 | 1333 | Transition | FB |
| 3 | BAK | RCF-BAK-5 | B068BSBLO | 300 | 17.8 | 2+953 | 446 | Curve | FB |
| 4 | BAK | RCF-BAK-5 | B068BSBLO | 300 | 17.8 | 3+053 | 410 | Curve | FB |
| 5 | BAK | RCF-BAK-5 | B068BSBLO | 300 | 17.8 | 3+143 | 1064 | Transition | BH |
| 6 | BAK | RCF-BAK-7 | B134BNBLO | 450 | 26.2 | 1+862 | 315 | Curve | FB |
| 7 | BAK | RCF-BAK-7 | B134BNBLO | 450 | 26.2 | 1+942 | 340 | Transition | FB |
| 8 | JUB | RCF-JUB-2 | B114JNBLO | 850 | 72.7 | 19+496 | 417 | Curve | FB |
| 9 | JUB | RCF-JUB-3 | B112JNBLO | 750 | 62.7 | 21+805 | 315 | Curve | FB |

The proposed rail wear prediction methodology was found to be reasonably successful on low rails on curved tracks with a radius R>200 m which are displayed in Table 7.6. For example; while the cases 3 and 4 were located on the similar curve radii, the worn areas were considerably different and the new method succeeded to demonstrate this change in its results. In addition, contrary to high rails, it provided relatively good predictions on older rails particularly, low rail profile on RCF-JUB-2 site (case 8). However, although the predicted total worn area was seem to be acceptable for a curve radius of 315 m on RCF-JUB-3 site (case 9), the smaller actual worn area caused an inaccurate prediction in this case.

It was also noted in the low rail results that there was a large step change in the predicted locations. Similar to modification on the running band in these rails, the wear region was moved from gauge corner to the crown of the rail. But, while this was particularly evident on curved tracks, such as cases 3 and 6, the wear was predicted close to the gauge corner on transitions and BH type rails. In certain conditions, this led to an underestimation of damage particularly in BH rail cases 1 and 5.  Even though sharp gauge corner radius in these rails produced higher conicites and resulted in larger Tγ values, it limited the predictions occurring close to the gauge region and in turn decreased the severity as the wear was spread over the railhead in the actual condition. However, it should be also noted that although BH and FB type of rails have similar hardnesses and manufactured under similar processes, the amount of removed material was considerably greater in BH rails.

Table 7.6: Comparison of predicted and measured worn areas on low rail profiles of R>200 m curved tracks
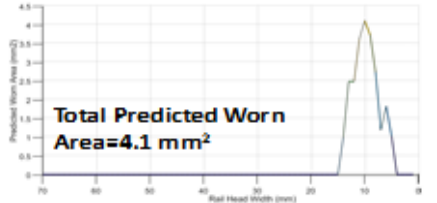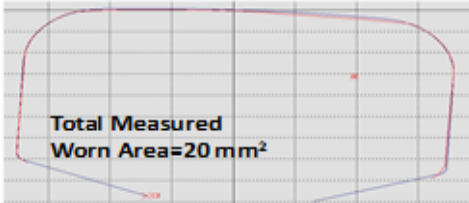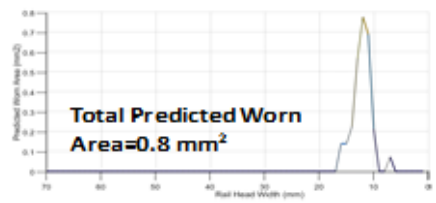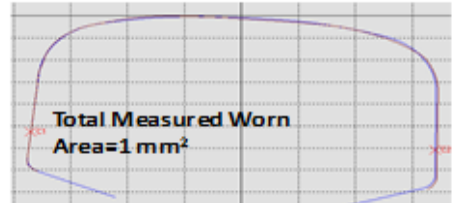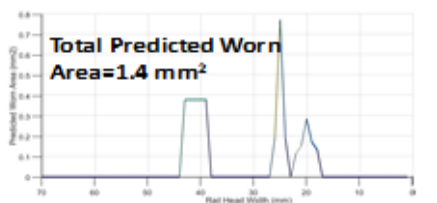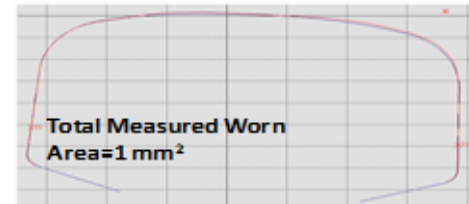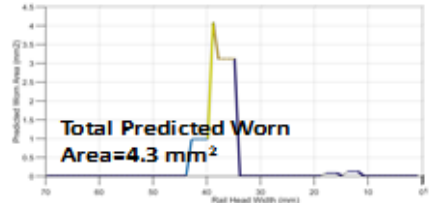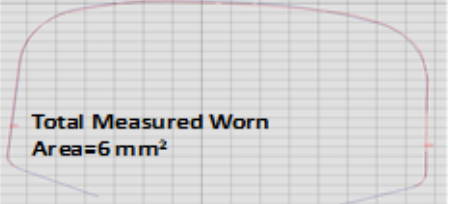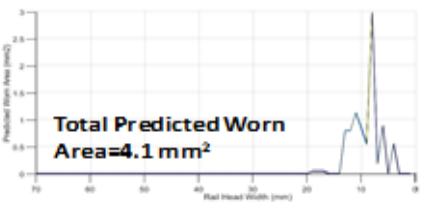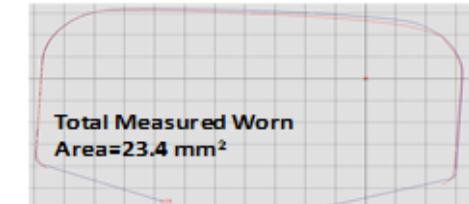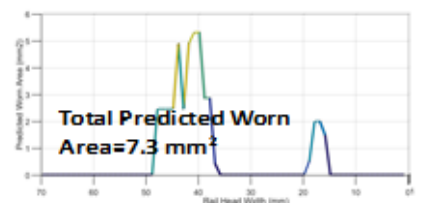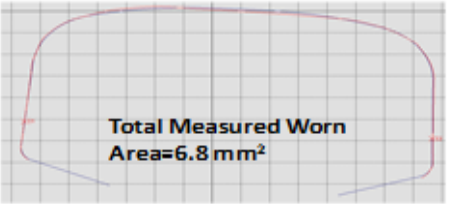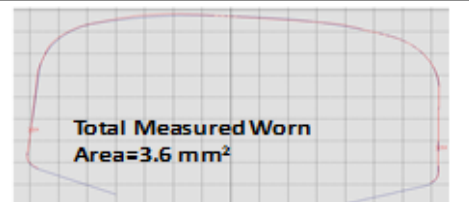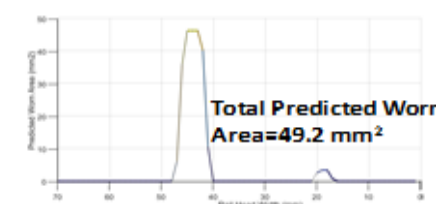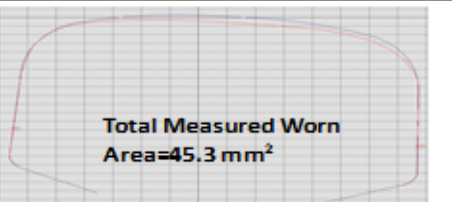


| | | | |
|---|---|---|---|
| **1** | Total Predicted Worn Area=4.1 mm² / Total Measured Worn Area=20 mm² | **2** | Total Predicted Worn Area=0.8 mm² / Total Measured Worn Area=1 mm² |
| **3** | Total Predicted Worn Area=1.4 mm² / Total Measured Worn Area=1 mm² | **4** | Total Predicted Worn Area=4.3 mm² / Total Measured Worn Area=6 mm² |
| **5** | Total Predicted Worn Area=4.1 mm² / Total Measured Worn Area=23.4 mm² | | Total Predicted Worn Area=7.3 mm² / Total Measured Worn Area=6.8 mm² |
| **6** | Total Predicted Worn Area=3.7 mm² / Total Measured Worn Area=3.6 mm² | **7** | Total Predicted Worn Area=49.2 mm² / Total Measured Worn Area=45.3 mm² |

Table 7.7: Comparison of predicted and measured worn areas on low rail profiles of R>200 m curved tracks (cont'd)
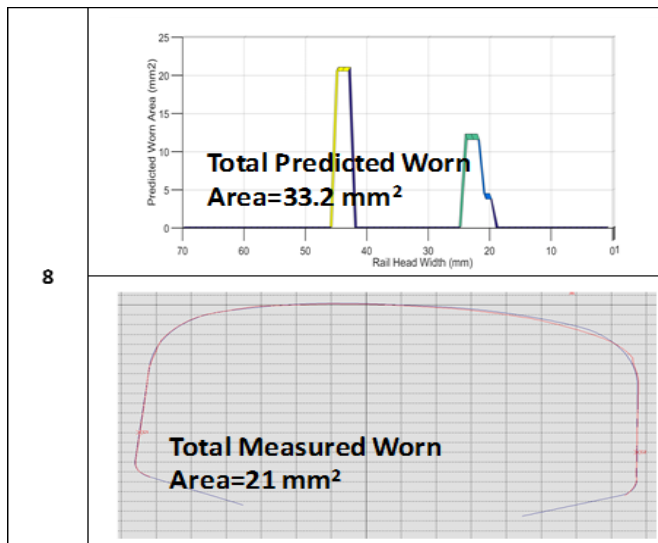


## 7.3.3 High rails on R<200 m checked-curved tracks

In order to predict the wear damage on checked curved tracks, additional effort was required to ensure the actual track conditions were modelled. The check rail position was shifted laterally to account for a change in flangeway clearances over time as might be expected in practice. Therefore, a large number of simulations cases were considered to reflect this alteration on the field. Although some simulations considered the check rail contact occurrence, certain simulations were set-up to neglect check rail contact and hence, severe flange contact was predicted in these cases. Table 7.8 shows the properties of the high rails (outer side) in the selected cases.

Table 7.8: The characteristics of the given high rail profiles of R<200 m checked-curved tracks

| Case No. | Line | RCF Monitoring Sites | LCS Code | Time (no. of days) Range | MGT | Chainage (KM) (Total distance in each line) | Radius (m) | Note | Rail Profile |
|---|---|---|---|---|---|---|---|---|---|
| 1 | BAK | RCF-BAK-2 | B122BSBLO | 350 | 20.6 | 5+779 | 200 | Curve | FB |
| 2 | BAK | RCF-BAK-2 | B122BSBLO | 350 | 20.6 | 5+879 | 200 | Curve | FB |
| 3 | BAK | RCF-BAK-3 | B066BNBLO | 250 | 14.7 | 9+040 | 175 | Curve | FB |
| 4 | BAK | RCF-BAK-3 | B066BNBLO | 250 | 14.7 | 9+165 | 175 | Curve | FB |

When the MiniProf files for the high rails were examined, it was noted that the wear was generated mostly on the gauge corner rather than on the crown of railhead. This showed that the check rail contact in these regions (and/or during this time period) had a lesser occurrence or the greater contact stresses at flange contact increased the worn area on the gauge corner.

As check rail contacts caused a single contact on the high rails and therefore, the larger contact patch areas lowered the contact stresses and in turn wear risk on the top of rail head was reduced. As it can be seen on Table 7.9, the location of the worn area over the railhead was effectively predicted but, the proposed new method produced significantly

greater values due to the higher time period on RCF-BAK-2 site (case 1 and 2). When the measured areas were considered particularly on the RCF-BAK-3 site (case 3 and 4), it can be also seen that the checked curves resulted in larger wear than the unchecked curves (R>200 m) for similar tonnage levels. Nevertheless, the values were still smaller than the unlubricated curve in the case 9 presented in Table 7.4.

Table 7.9: Comparison of predicted and measured worn areas on high rail profiles of R<200 m checked-curved tracks
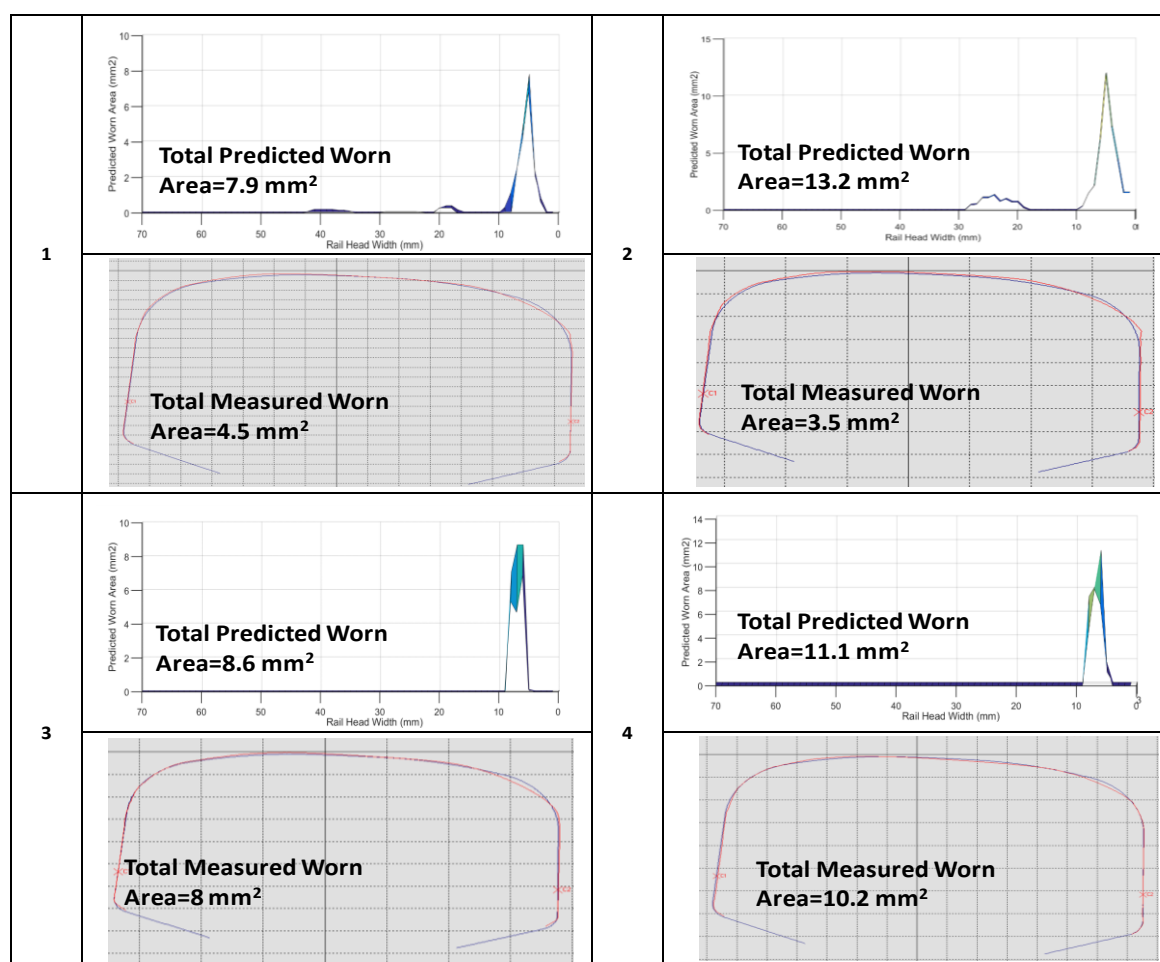


## 7.3.4  Low rails on R<200 m checked-curved tracks

In the low rails (inner side) of checked-curved tracks, the given RCF-BAK-10 site was located in the Waterloo Station. The MiniProf measurements were conducted on the three different points along this site and the characteristics of these cases are provided in Table 7.10.

Table 7.10: The characteristics of the given low rail profiles of R<200 m checked-curved tracks

| Case No. | Line | RCF Monitoring Sites | LCS Code | Time (no. of days) Range | MGT | Chainage (KM) (Total distance in each line) | Radius (m) | Note | Rail Profile |
|---|---|---|---|---|---|---|---|---|---|
| 1 | BAK | RCF-BAK-10 | N115BSBLO | 450 | 25.9 | 9+451 | 159 | Transition | FB |
| 2 | BAK | RCF-BAK-10 | N115BSBLO | 450 | 25.9 | 9+501 | 118 | Curve | FB |
| 3 | BAK | RCF-BAK-10 | N115BSBLO | 450 | 25.9 | 9+541 | 139 | Transition | FB |

Due to high level of traction and braking forces at the station locations, high rates of wear were expected in this site. Table 7.11 demonstrates these high predictions generated on these cases. Even though the predicted total worn area had a good correlation on the case 2 (where the curve radius is the smallest), the high values on the cases 1 and 3 (curve transitions) provide a poor agreement with the field measurements. The worn areas on the transitions were significantly lower compared to curved section. The differences in the flangeway clearances particularly, the temporary changes in the lateral shifts along the platform gave rise to either check-rail contact or flange contact occurrence on these tracks.

Table 7.11: Comparison of predicted and measured worn areas in low rail profiles of R<200 m checked-curved tracks
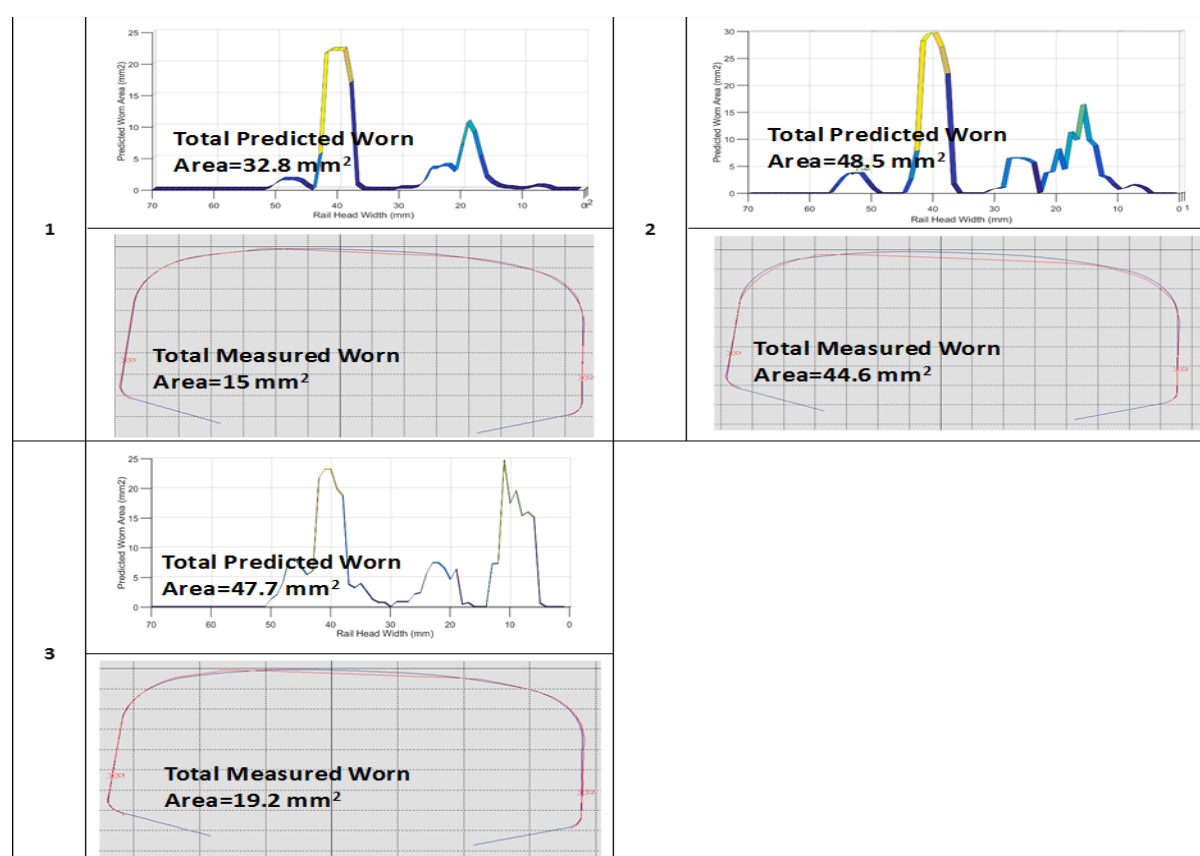


## 7.3.5  Rails on tangent tracks

The rail profiles on tangent tracks were gathered from different sites which are demonstrated in Table 7.12.

Table 7.12: The characteristics of the given rail profiles on tangent tracks

| Case No. | Line | RCF Monitoring Sites | LCS Code | Time (no. of days) Range | MGT | Chainage (KM) (Total distance in each line) | Radius (m) | Note | Rail Profile |
|---|---|---|---|---|---|---|---|---|---|
| 1 | BAK | RCF-BAK-1 | B068BNBLO | 300 | 16.6 | 8+438 | - | - | BH |
| 2 | BAK | RCF-BAK-3 | B066BNBLO | 250 | 14.7 | 8+960 | - | - | FB |
| 3 | BAK | RCF-BAK-8 | B134BNBLO | 450 | 26.2 | 1+802 | - | - | FB |

The proposed new wear method succeeded to predict wear on tangent tracks. But, the predicted areas were smaller than the actual measurements owing to smaller shakedown parameters and Tγ values as shown in Table 7.13. The largest prediction of 3.1 mm² that occurred on BH type of rails could not match with the considerably high value of 23.2 mm² obtained from the measured rail profiles. Similarly, the relatively lower worn area on FB type of rails again could not show a good correlation with the predictions since the results were significantly small.

Table 7.13: The comparison of predicted and measured worn areas in rail profiles on tangent tracks
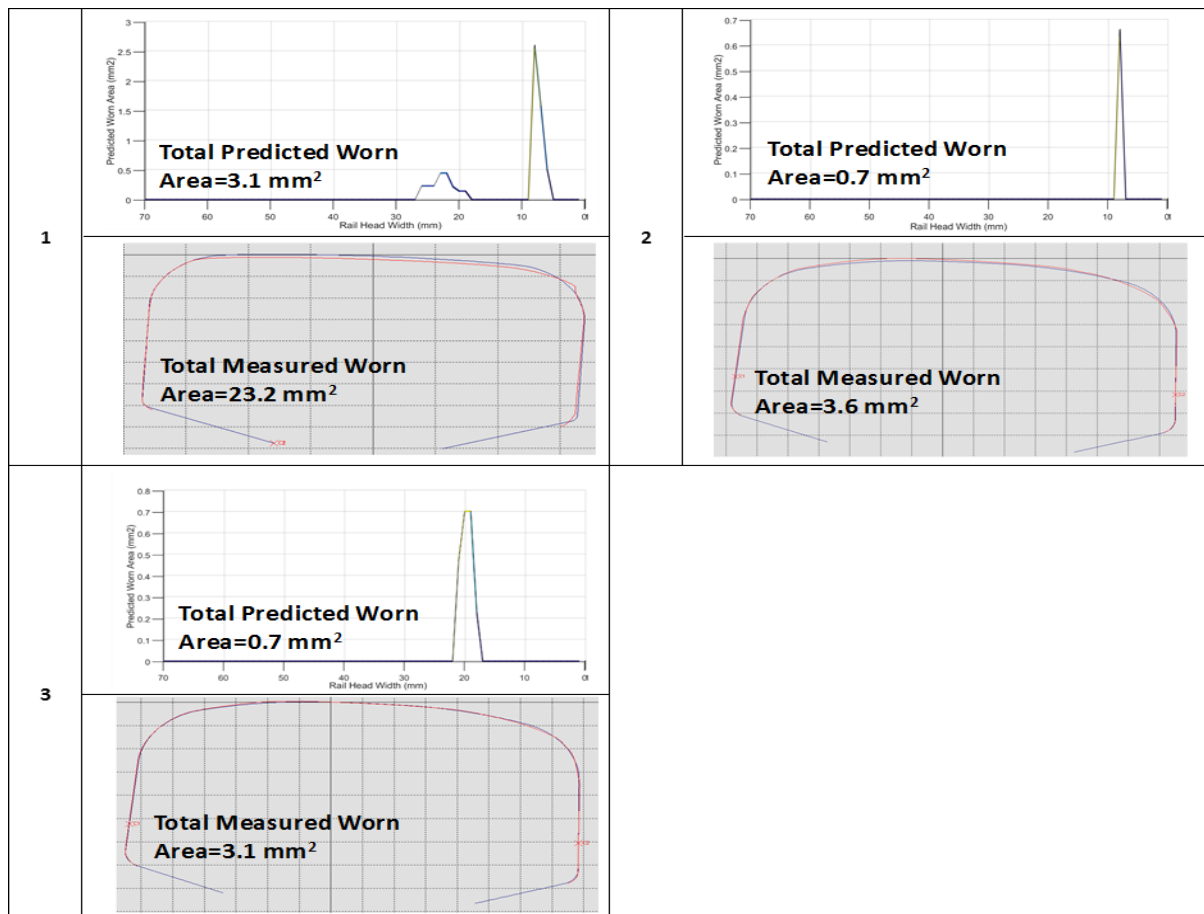


## 7.4 Conversion of worn area to depth

In order to consider the interaction of wear in the RCF crack depth predictions in Chapter 8. The predicted wear depth from the worn area was required to decrease the estimated total crack depth for a similar time interval and the final output was then compared with the MRX-RSCM crack depth measurements.

As previously mentioned, the MiniProf software was used to measure the wear depth in actual rails from the differences to the reference profile. Due to the different shape of worn high and low rail profiles, the wear (loss of area and vertical wear depth) was measured in the rail gauge corner and rail crown (top/head) regions.

The calculated area loss and vertical wear depths are plotted in Figures 7.5 and 7.6 for high and low rail profiles, respectively. Trend lines were overlaid for both rail gauge and crown data to allow conversion from area loss to depth. Even though the check rail tracks were included in both high and low rail cases, the linear trend line gave an acceptable fit distribution through the data. The coefficient of determination ($R^2$) which quantifies the goodness of fit of the trend line to the dataset was found be higher than 0.70 and reached 0.82 for the rail crown depth conversion on low rails.

The equations for the lines provided in the figures was then used to convert the predicted worn area loss to wear depth in each case. These values were utilised in Chapter 8 to predict the net crack depth due to the interaction of wear by removing the predicted wear depth.
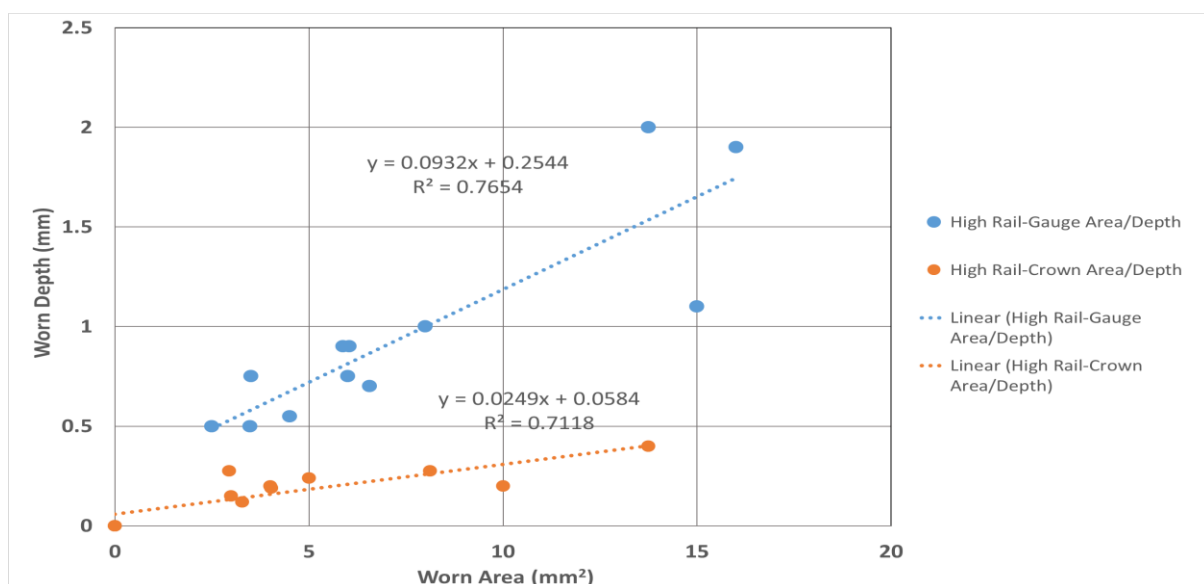


Figure 7.5: Worn area/depth conversion for high rail cases
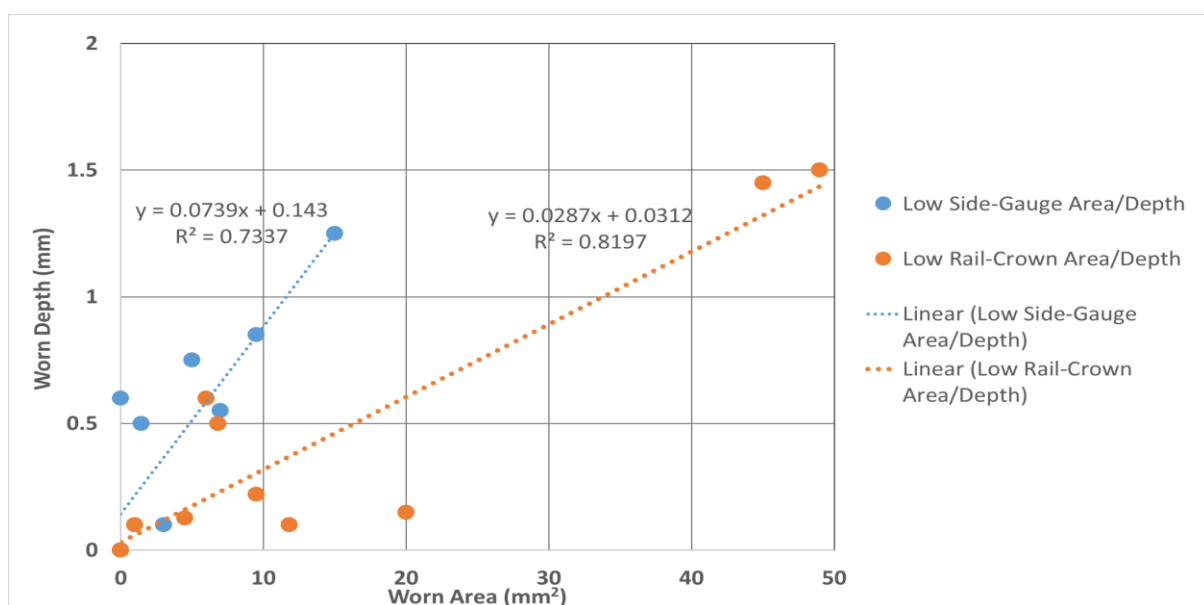


Figure 7.6: Worn area/depth conversion for low rail cases

## 7.5 Conclusions and discussions

The proposed new wear damage prediction method was validated on the selected RCF sites monitored by LUL. As the site data included detailed information on the rail installation dates and any subsequent maintenance activities, it provided the opportunity to accurately accumulate the damage predictions.

The initial results led to wear predictions that were significantly higher than the actual levels of wear seen on-track. As it can be expected from the differences in wear curves with third body layers, the use of dry BRR wear function resulted in greater predictions. But, these recent curves were not implemented in the research as the wear coefficients related with mass loss per area ($\mu g/m/mm^2$). Additionally, it was demonstrated that the wear rate reached steady–state regime after certain time and based on the iterative process, scaling factors : 1% for each tonnage level up to 30 MGT and 0.5% after this limit were defined. This clearly showed that the most of the energy produced at the wheel rail contact did not transform to any RCF and wear damage.

In order to evaluate the efficiency of this new method on sites with various track characteristics, the measured MiniProf rail profiles were grouped into five different track categories, as illustrated in the legend of Figure 7.7.
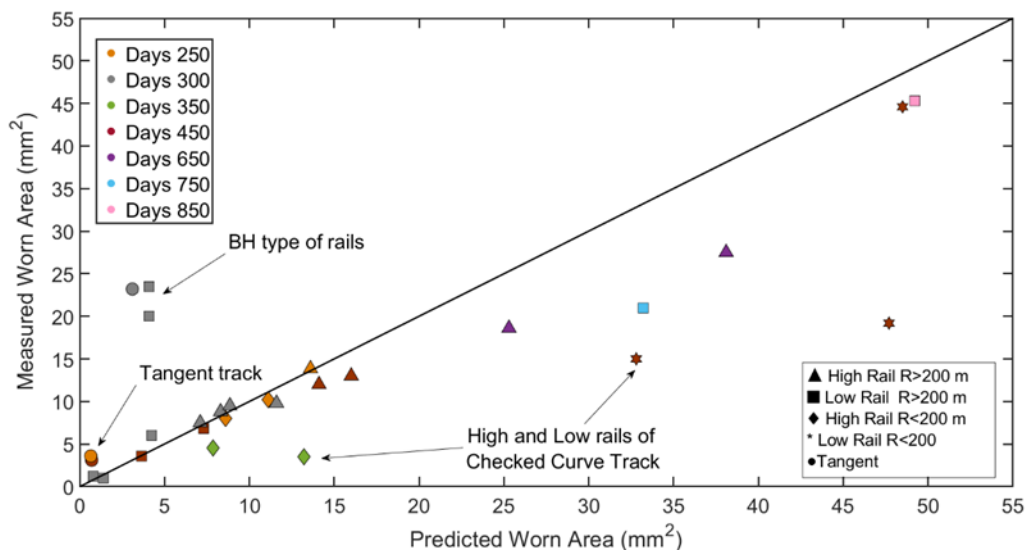


Figure 7.7: The comparison of predicted and measured worn areas for all cases

Figure 7.7 shows the comparison between the predicted and measured area loss for all cases including a linear trend line (with values closer to the trend line indicating a more accurate prediction of the measured wear). Even though there could be certain measurements errors stemming from the reasons previously explained in Chapter 7.3, the majority of the cases showed a good match and the predictions were found to be acceptable especially on high and low rails of R>200 m (unchecked) curved tracks. Even

though the dry condition BRR function was used on lubricated high rail cases, the estimations provided better agreement than the lubricated wear coefficients.

In addition, the lateral locations of the wear across the rail head were also successfully predicted in several locations which agrees with previous research which concluded that the propagation of wear was confined within the plastically deformed layer, whereas the RCF cracks were observed to grow beyond this layer (Tyfour, 1995). However, the new method produced under-and over-estimations in certain cases that are discussed further below:

Under-estimation: Although the wear predictions were relatively larger on BH type of rails due to a higher initial conicity, the results were still insufficient to reach the actual measurements, as the sharp gauge corner radius limited the predicted wear on the gauge region.

Additionally, the method showed considerably lower results on the tangent tracks owing to smaller shakedown parameters and Tγ values. There might be several factors causing these inaccuracies. In reality, track geometry changes over time, altering track irregularities and affecting the dynamic behaviour of vehicles. This may sometimes lead to higher material removal in rails. Moreover, the worn areas might also be influenced by the changes in wheel profile shapes. Although the research considered the effect of track irregularities and three representative worn wheel profiles (light, moderate, severe) and their effect on contact energy under different curvature ranges as previously demonstrated in Chapter 5.1.3 and 5.1.5, they may have higher influences on contact conditions particularly on the tangent tracks.

Over-estimation: The uncertainty in flangeway clearance between the check and running rails information gave rise to greater results. Although both with and without check rails' simulations were considered in the simulations, the change in the lateral shifts along the similar sites resulted in poor agreement on some cases. Nevertheless, the actual worn areas were successfully predicted in certain cases such as cases 3 and 4 on high rails and case 2 on low rails.

Furthermore, the method caused higher predictions for older rails. For example, whereas the total worn area was predicted as 33.2 $mm^2$ on case 9 (low rails on R>200 m curved tracks), the measured area was 21 $mm^2$. Even though a further scaling factor of 0.05% was used after 30 MGT in the damage accumulation in order to reflect the steady-state wear regime and decrease in ratchetting rate, the predictions became higher compared to measured values and there are still uncertainties when rails reach steady state wear regime as while, the cases 7 and 8 were located on the similar curve radii, there was a large difference in the actual worn areas.

Furthermore, the changes in rail profile measurements should be monitored by conducting MiniProf measurements in certain intervals (every ~10-15 MGT). With respect to this, changes in wear rate over time can be better observed and in turn, it may provide an opportunity to decrease the overestimation in relatively older rails.

It should be finally noted that more detailed contact modelling is also required to further increase the accuracy in predictions. As the wear generates in the slip region of the contact, the adhesion and slip areas as well the distributions of the contact stress and creep forces should be given. This will certainly help to understand the changing conditions over the contact patch and to obtain better correlations with the measurements in terms of both magnitude and location.

# Chapter 8    Prediction of RCF Damage

This chapter presents the results of the proposed new RCF crack depth prediction method. This method has been applied to selected RCF monitoring sites on LUL with different track characteristics. The damage predictions were compared to the surface damage map and crack depth data obtained from measurements using the MRX-RSCM. Additionally, a further study was conducted using different worn and new with higher hardness and different rail profile shapes to provide guidance on LUL's maintenance strategy.

## 8.1  Site selection and MRX-RSCM crack measurements

A number of sites were selected from the LUL RCF Monitoring sites. As previously mentioned in Chapter 7.1, field data collated during this monitoring programme provided valuable information to support the definition of the model inputs and validation of the predictions. This included rail profile shape, measured using a MiniProf rail device and surface crack and damage depth data, measured using the MRX-RSCM. The sites were monitored following rail replacement, with two MRX-RSCM consecutive inspections were carried out on the Bakerloo line sites, but only one measurement was conducted on the Jubilee line sites. The list showing the location of all these sites and the rail inspection dates are given in Table 7.1. In addition, further details of each of the selected sites in this study are provided in Table 8.1-8.5.

The MRX-RSCM has been mainly used on LUL in order to support rail maintenance decisions. Although it provides valuable information in rail inspections, some discrepancies were noted when the outputs were analysed in detail in Chapter 3.3.3. Therefore, in order to increase the reliability of its outputs for use in the model validations, the data was further post-processed in this step of the research.

Previous validation studies demonstrated differences between the measured and actual crack depths, resulting in an over-estimation of the crack depth as aforementioned in Chapter 2.2.1. Following discussions with MRX, it was stated that the overestimation may be caused by the differences between the length of the rail samples and the MRX-RSCM measurement interval. Since the detector outputs the maximum crack depths in 1-m intervals, the crack depths in relatively shorter rail samples might become smaller than the measurements. Therefore, the output interval was reduced to 250 mm by further post-processing the measurements in order to increase the accuracy for each reported crack on the surface damage map.

Due to changes in railhead profile shape and slippage in the distance measurement wheel, the MRX-RSCM system produced different distance outputs for the same LCS section. To

solve this data aligning problem, especially in consecutive measurements, the weld locations of these recently re-railed sites were carefully identified and when the distances between two welds were close to 18 m (rail length manufactured in plain track), these sites were selected for further analysis in the research.

## 8.2 RCF damage prediction results

During the development of RCF cracks (both initiation and propagation), wear is also present, removing material from surface of the rail. Whereas this can sometimes result in the complete removal of the initiated cracks, it may shorten the depths of deeper cracks. Therefore, the measured crack depths become the net values which are also reduced by wear. Based on the tonnage elapsed following each MRX-RSCM inspection, the number of total simulations were firstly determined by applying the related scaling factor and the distribution of different rail-wheel profile combinations were defined as aforementioned in Chapter 7.2. Since the crack growth rate changes during the different phases as previously presented in Figure 2.10, it became inevitable to apply different scaling factors over time. When the contact parameters lay inside the specified RCF region on the Shakedown Map, it was suggested that these contacts were more susceptible to RCF cracking. To estimate (total) crack depths, the new RCF prediction model was used. To consider the interaction of wear in the RCF predictions, the wear was also estimated using the proposed wear methodology for the same duration/tonnage with MRX-RSCM. The predicted total worn areas were converted to depths in the rail gauge corner and rail crown (top/head) regions using the Equations defined in Chapter 7.4.  To find the net RCF crack depth, the predicted wear depths were subtracted from the total RCF crack depths. Figure 8.1 shows the steps which were undertaken in the RCF crack depth predictions.

The following sections present the comparisons of the measured and predicted net crack depths in the selected sites. Additionally, the figures provided in Appendix B were prepared to demonstrate the correlations in terms of crack location and severity. In the first plot, the measured surface damage maps were overlaid with the model predictions over railhead and second plot provides a comparison of the predicted and measured crack depths. The colour scales presented in the crack location comparison plots (sub-plot 1) demonstrate the predicted net crack depth values, with the white areas (grey in the MRX-RSCM surface damage map) indicating regions where the estimated RCF damage was zero which means that the damage was either removed through wear or no damaging contacts were predicted in this region. Similar to the MRX-RSCM data, a dark blue colour represents a relatively small estimated crack depth, whereas a red colour indicates a much larger depth. On these figures, certain regions are highlighted to indicate the correlations between the simulation and measurement results, with black rectangles highlighting the predictions

that correlate well with the measured damage and red circles show the uncorrelated regions.



Figure 8.1: Steps in RCF crack depth prediction methodology

## 8.2.1 High rails on R>200 m curved tracks

The RCF crack depths were firstly predicted on the selected high rail sections of the RCF monitoring sites. Considering the weld locations and the 18 m rail lengths, the location of the site within the MRX-RSCM measurement data was determined. Table 8.1 shows these selected distances and the other characteristics of these sections. RCF-BAK-6 site was located in an unlubricated curve and therefore, cases 8 and 9 were included in order to provide a comparison with the lubricated cases.

Table 8.1: Characteristics of the high rails on selected R>200 m curved tracks

| Case No. | Line | RCF Monitoring Sites | LCS Code | MRX_RSCM Measurement | MGT | Starting Chainage (KM) at total Simulation Distance | End Chainage (KM) at total Simulation Distance | Average Radius (m) | Note | Rail Proflie |
|---|---|---|---|---|---|---|---|---|---|---|
| 1 | BAK | RCF-BAK-1 | B068BNBLO | MRX-RSCM-1 | 11.4 | 8+011 | 8+065 | 305 | Curve | FB |
| 2 | | | | MRX-RSCM-2 | 30.3 | | | | | |
| 3 | BAK | RCF-BAK-4 | B068BSBLO | MRX-RSCM-1 | 12.3 | 2+965 | 3+020 | 440 | Curve | FB |
| 4 | | | | MRX-RSCM-2 | 31.3 | | | | | |
| 5 | BAK | RCF-BAK-8 | B134BNBLO | MRX-RSCM-1 | 22.5 | 1+892 | 1+928 | 285 | Curve | FB |
| 6 | | | | MRX-RSCM-2 | 44.2 | | | | | |
| 7 | JUB | RCF-JUB-1 | F044JNBLO | MRX-RSCM-1 | 44.5 | 16+144 | 16+180 | 430 | Curve | FB |
| 8* | BAK | RCF-BAK-6 | B062BNBLO | MRX-RSCM-1 | 8.6 | 10+399 | 10+459 | 362 | Curve | FB |
| 9* | | | | MRX-RSCM-2 | 28.3 | | | | | |

*: Cases 8 and 9 were located on an unlubricated curve.

Some of the comparison of RCF crack depth predictions with MRX-RSCM measurements for the selected high rail cases are provided in Figures 8.2 and 8.3. As it can be seen, the

new model produced reasonable predictions particularly at first inspections as the majority of values are lower than 0.5 mm. However, there are certain differences occurred in the second inspections such as the relatively higher predictions can be noted in case 7. Although the aforementioned reasons in Chapter 7 such as the decay in ratchetting rates had an influence, the RCF mechanism is highly complex and many factors play a key role in further propagation as clarified in Chapter 2. The research conducted several calibrations to predict the changes in consecutive measurements but, the effects of all above factors made it harder to predict the further position and orientation of crack.

Nonetheless, Figures 1-4 in Appendix B helped to visualize comparisons over railhead and to identify the contact conditions that were more responsible for RCF. For instance, while the lightly worn wheels with new rail profile (NW1) generated larger flange contact stresses and hence, increased wear in this region, the moderately-severely worn wheels (NW2 and NW3) generated single tread contacts which in turn gave rise to RCF risk on these regions which can be observed in the cases 1 and 3 (RCF-BAK-1 and RCF-BAK-4). But, when the MRX-2 inspections (cases 2 and 4) were considered at these sites, it was noticed that while the some of the cracks on the crown of railhead seemed to be removed by wear, the other cracks continued to propagate and new cracks initiated close to gauge corner. The higher conicities particularly generated by moderately-severely worn wheels in worn rail profile cases (WW2 and WW3) gave rise to wear risk but, the dominant lightly worn wheel (WW1) was primarily responsible for RCF cracking on both tread and flange contacts. The estimations were also conducted for the unlubricated curve track site: RCF-BAK-6 (cases 8 and 9). Due to higher friction coefficients, the larger Tγ values resulted in increased depth predictions. But, the measured crack depths were relatively smaller and hence it provided a poor agreement with the predictions. To increase the prediction accuracy on these sites, it was suggested to raise the computed wear depth conversion factor since, it might be insufficient to reflect the real case in unlubricated curves as it was also observed in the MiniProf files. Furthermore, site visits were conducted to inspect the surface condition of the rails at the selected sites. It was revealed that this condition provided a better correlation with the estimations since, there were no severe defects observed on the sites, especially in the field side region of the rail. For instance, the shelling at Ch. 8+030-8+035 km on case 2 might be resulted from the accumulated damage close to gauge corner. After a certain time, the crack might turn upwards and form a shelling type of defect. In addition, the head checks which were recorded at around Ch.2+973-2+978 km on case 4 may be caused by the predicted damage close to again gauge corner. Similarly, the predicted accumulated damage around Ch.1+915 km on case 6 might be responsible for the gauge lipping. However, it should be also noted that the MRX-RSCM can also detect the sub-surface defects. Thus, whereas no major defects were observed

during site visits, there could be damage initiated under the rail surface. Also, the grinding which took place after MRX-RSCM inspections can also remove the measured cracks.

Figure 8.2: Comparison of RCF predictions with MRX-RSCM measurements on high rail case of RCF-BAK-1 site (Cases 1 and 2)

Figure 8.3: Comparison of RCF predictions with MRX-RSCM measurements on high rail case of RCF-BAK-4 site (Cases 3 and 4)

## 8.2.2 Low rails in R>200 m curved tracks

The selected low rail cases are given in Table 8.2 and the RCF-BAK-9 site was BH rail.

Table 8.2: The characteristics of the low rails on R>200 m curved tracks

| Case No. | Line | RCF Monitoring Sites | LCS Code | MRX_RSCM Measurement | MGT | Starting Chainage (KM) at total Simulation Distance | End Chainage (KM) at total Simulation Distance | Average Radius (m) | Note | Rail Profile |
|---|---|---|---|---|---|---|---|---|---|---|
| 1 | BAK | RCF-BAK-5 | B068BSBLO | MRX-RSCM-1 | 12.5 | 2+923 | 2+959 | 440 | Curve | FB |
| 2 | | | | MRX-RSCM-2 | 31.5 | | | | | |
| 3 | BAK | RCF-BAK-9 | B068BNBLO | MRX-RSCM-1 | 11.7 | 7+798 | 7+852 | 285 | Curve | BH |
| 4 | | | | MRX-RSCM-2 | 30.6 | | | | | |
| 5 | BAK | RCF-BAK-7 | B134NBNLO | MRX-RSCM-1 | 22.5 | 1+827 | 1+881 | 285 | Curve | FB |
| 6 | | | | MRX-RSCM-2 | 44.2 | | | | | |
| 7 | JUB | RCF-JUB-2 | B114JNBLO | MRX-RSCM-1 | 59.5 | 19+430 | 19+448 | 265 | Transition | FB |

Some of the results of low rail cases on R>200 m curved tracks are presented in Figures 8.4 and 8.5. Compared to high rail cases, it seemed that the new model produced better agreement and the differences between measurements were relatively small in both of the inspections (cases 1-5). Also, the larger wear rates in BH rails caused a reduction in crack depths which again showed better correlation than the wear predictions. However, major differences were observed and the predictions were substantially smaller in case 6 but, the site observations demonstrated that there were no defects on this site. The surface damage map correlations in Appendix B (Figures 6-9) suggested that the single tread contacts with lower stress levels mostly resulted in higher RCF predictions than wear risk. While the cracks were first occurred on the top of railhead in the first inspections, the increase in tonnage (rail age) gave rise to severe field cracking.
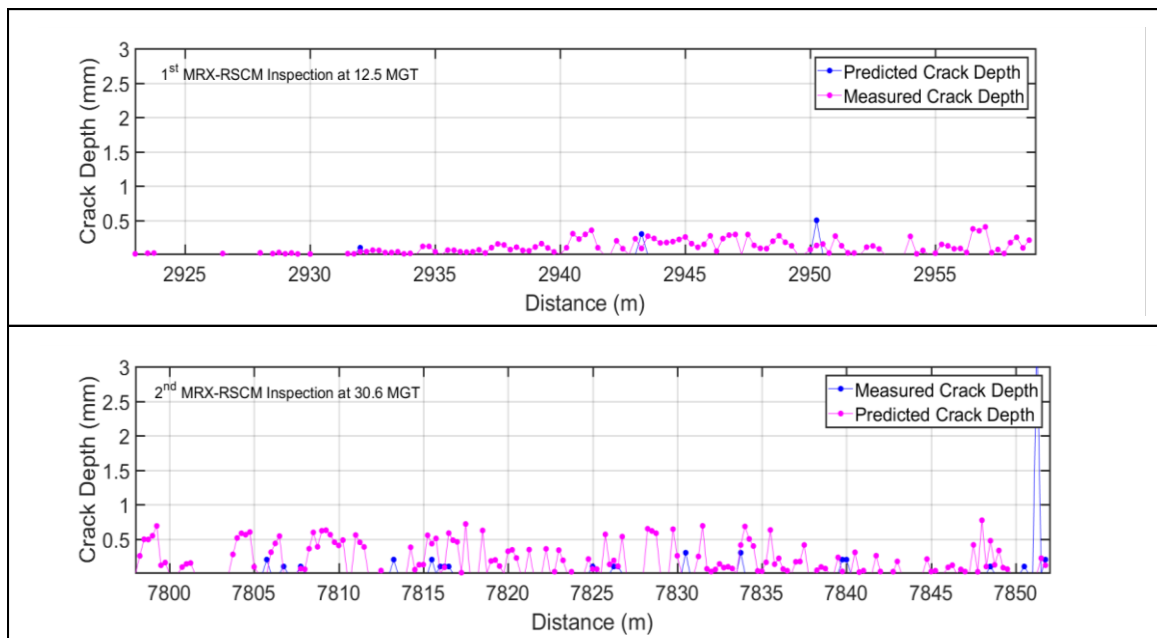


Figure 8.4: Comparison of RCF predictions with MRX-RSCM measurements on low rail cases of RCF-BAK-5 site (Cases 1 and 2)
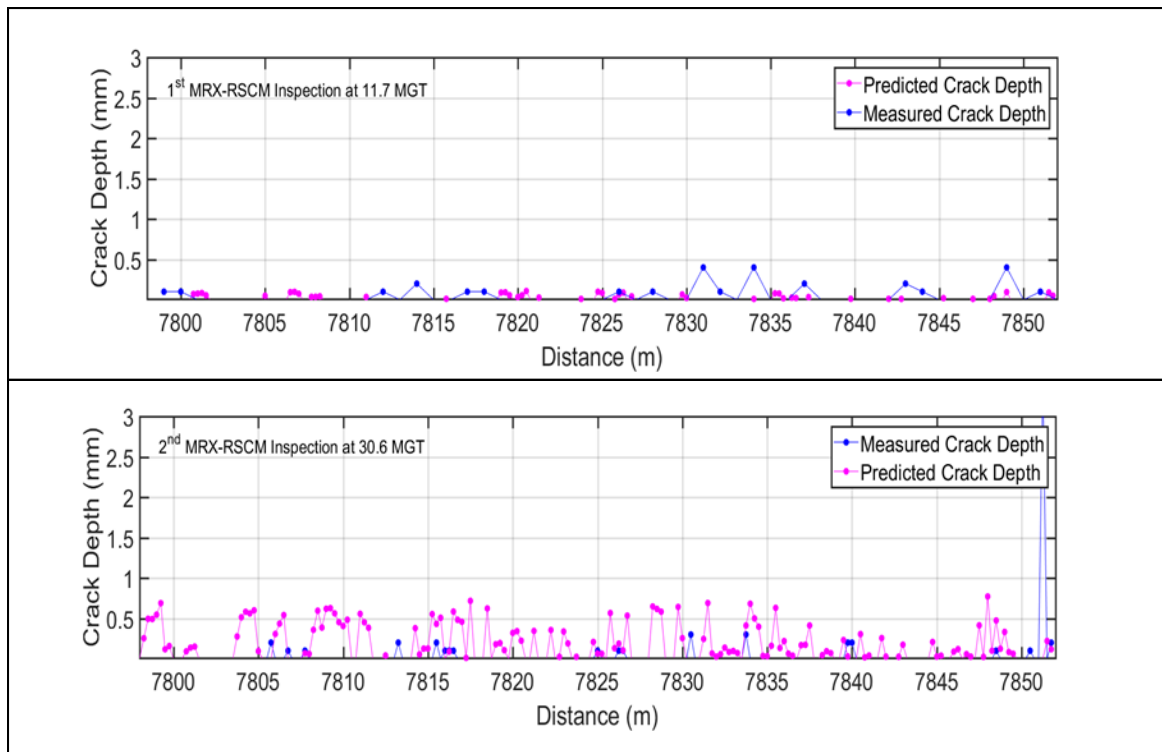
Figure 8.5: Comparison of RCF predictions with MRX-RSCM measurements on low rail cases of RCF-BAK-9 site (cases 3 and 4)

## 8.2.3  High rails on R<200 m checked curved tracks

The new RCF damage prediction method was also tested on the checked curved tracks. Table 8.3 shows the properties of these selected high rail sections in this study.

Table 8.3: The characteristics of the high rails on R<200 m checked-curved tracks

| Case No. | Line | RCF Monitoring Sites | LCS Code | MRX_RSCM Measurement | MGT | Starting Chainage (KM) at total Simulation Distance | End Chainage (KM) at total Simulation Distance | Average Radius (m) | Note | Rail Proflie |
|---|---|---|---|---|---|---|---|---|---|---|
| 1 | BAK | RCF-BAK-2 | B122BSBLO | MRX-RSCM-1 | 14.3 | 5+689 | 5+743 | 200 | Curve | FB |
| 2 | | | | MRX-RSCM-2 | 33.3 | | | | | |
| 3 | BAK | RCF-BAK-3 | B066BNBLO | MRX-RSCM-1 | 9.5 | 9+058 | 9+112 | 190 | Curve | FB |
| 4 | | | | MRX-RSCM-2 | 29.2 | | | | | |

Due to a lack of information on the distribution of actual flangeway clearances with MGT (or time), both simulations with and without check rails were considered in this analysis. However, this condition led to overestimation which was particularly noticed in cases 2 and 4 illustrated in the Figures 8.6 and 8.7. As it can be also seen in Figures 10-11 in Appendix B, the two damage bands were predicted between 20 and 40 mm of railhead owing to consideration of check and uncheck contact simulations. But, the MRX-RSCM detected isolated cracks in these sites.

Nevertheless, head checks close to gauge corner and cracking on the crown of railhead were observed during site visits which again provided a better correlation with the predictions than the NDT measurements.
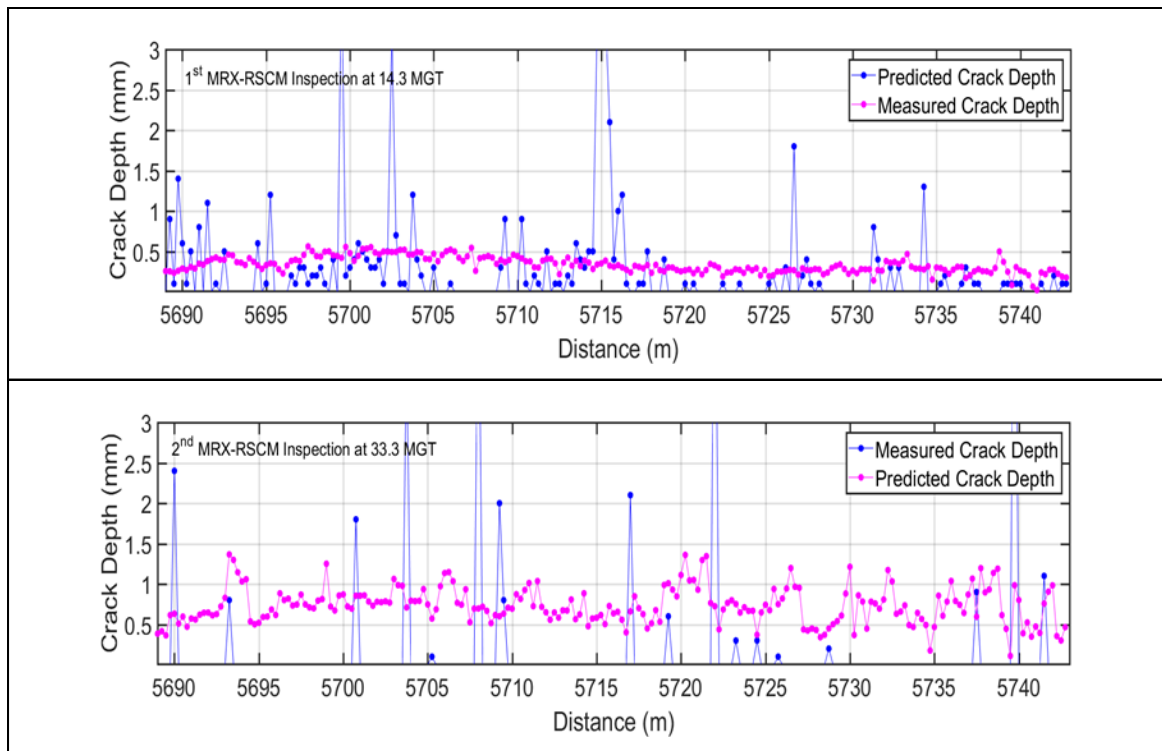


Figure 8.6: Comparison of RCF predictions with MRX-RSCM measurements on high rail cases of RCF-BAK-2 (Cases 1 and 2)
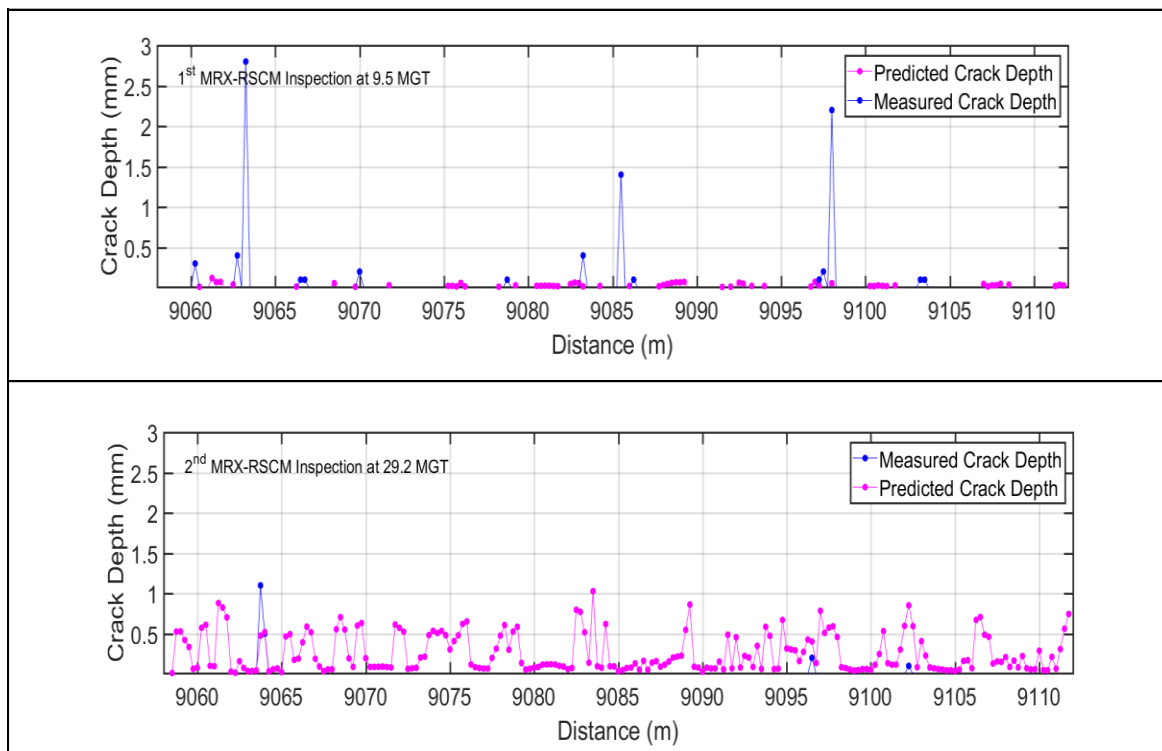


Figure 8.7: Comparison of RCF predictions with MRX-RSCM measurements on high rail cases of RCF-BAK-3 (Cases 3 and 4)

## 8.2.4 Low rails on R<200 m checked curved tracks

Regarding the low rails on checked curved tracks, the cracks which were measured on the Waterloo station again were estimated in the study. The properties of these cases are given in Table 8.4.

Table 8.4: The characteristics of the low rails on R<200 m checked-curved tracks

| Case No. | Line | RCF Monitoring Sites | LCS Code | MRX_RSCM Measurement | MGT | Starting Chainage (KM) at total Simulation Distance | End Chainage (KM) at total Simulation Distance | Average Radius (m) | Note | Rail Profile |
|---|---|---|---|---|---|---|---|---|---|---|
| 1 | BAK | RCF-BAK-10 | N115BSBLO | MRX-RSCM-1 | 6.2 | 9+469 | 9+505 | 125 | Curve | FB |
| 2 | | | | MRX-RSCM-2 | 27.8 | | | | | |

As it can be seen in Figure 8.8, the low tonnage resulted in smaller crack depth predictions. Although the consideration of check and unchecked simulations enabled to increase the RCF damage predictions, the estimated depths were considerably lower than the measurements. Again, the Figure 12 in Appendix B and the site visit revealed that that there was no major cracking particularly on the field side of the rails. However, this condition might be resulting from the larger wear rates occurred between the second inspection and site visit.
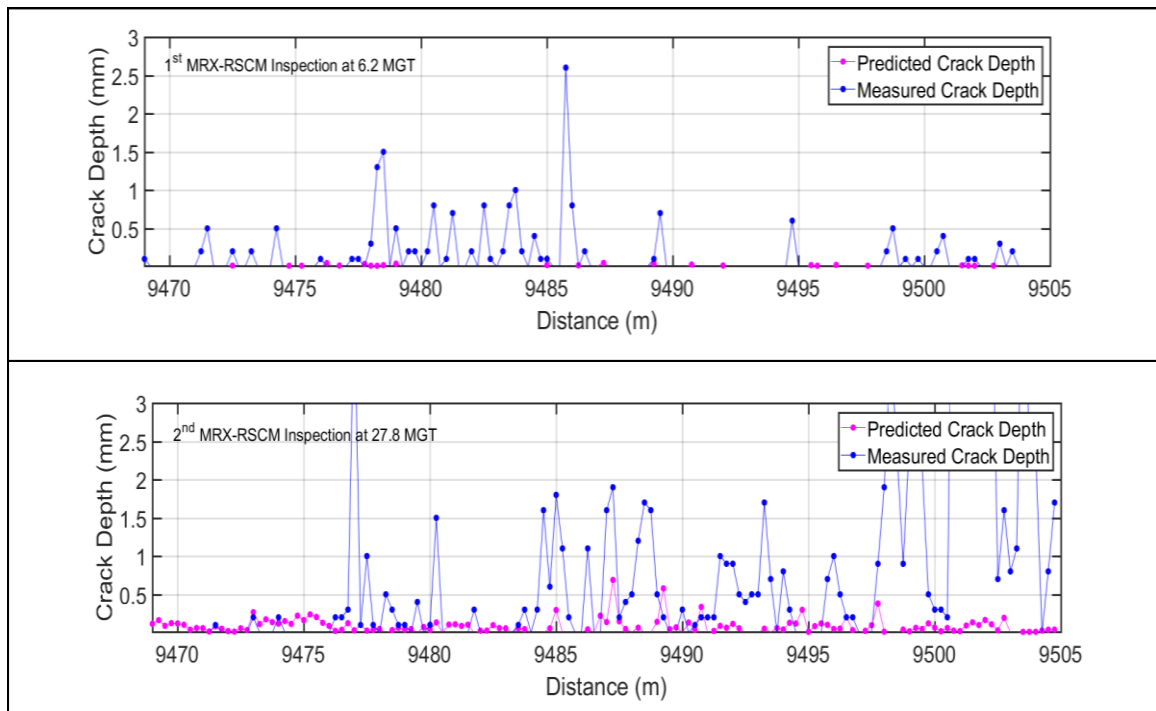


Figure 8.8: Comparison of RCF predictions with MRX-RSCM measurements on low rail cases of RCF-BAK-10 (Cases 1and 2)

## 8.2.5 Rails on tangent tracks

The cases in tangent tracks were again gathered from different sites which are listed in Figure 8.5.

Table 8.5: The characteristics of the rails on tangent tracks

| Case No. | Line | RCF Monitoring Sites | LCS Code | MRX_RSCM Measurement | MGT | Starting Chainage (KM) at total Simulation Distance | End Chainage (KM) at total Simulation Distance | Average Radius (m) | Note | Rail Profile |
|---|---|---|---|---|---|---|---|---|---|---|
| 1 | BAK | RCF-BAK-8 | B134BNBLO | MRX-RSCM-1 | 22.5 | 1+802 | 1+820 | | Tangent | FB |
| 2 | | | | MRX-RSCM-2 | 44.2 | | | | | |
| 3 | JUB | RCF-JUB-1 | F044JNBLO | MRX-RSCM-1 | 44.5 | 15+964 | 16+018 | | Tangent | BH |
| 4 | JUB | RCF-JUB-3 | B112JNBLO | MRX-RSCM-1 | 48.9 | 21+738 | 21+756 | | Tangent | FB |

The tangent track comparisons are displayed in Figures 8.14 to 8.16. Similar to wear estimations, the RCF predictions were considerably lower than the sites in other track categories. For example, the maximum estimated depth of 0.2 mm was calculated where the tonnage was approximately 44 MGT in case 2. Although some sites had higher crack depth measurements, the predictions again provided more reasonable results, as no defects were observed during the site visits as can be seen on Figures 13-15 in Appendix B. When the longitudinal crack correlations were considered in case 4, it can be clearly seen that the proposed method provided good agreement.
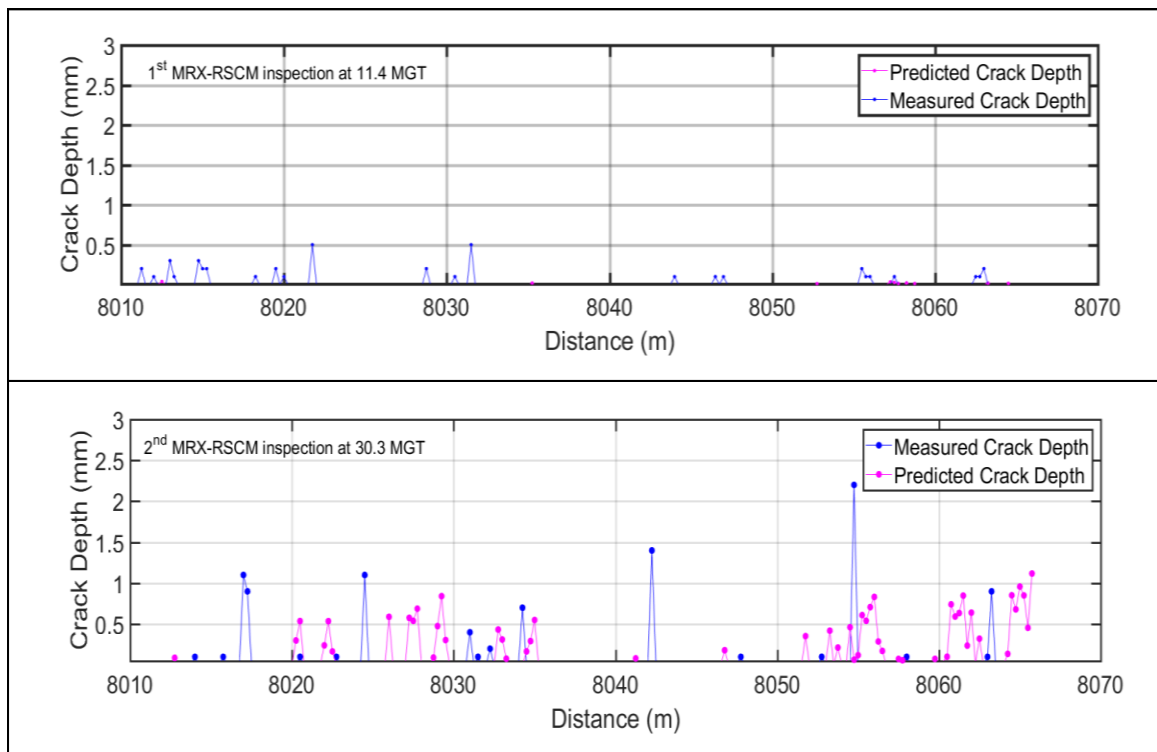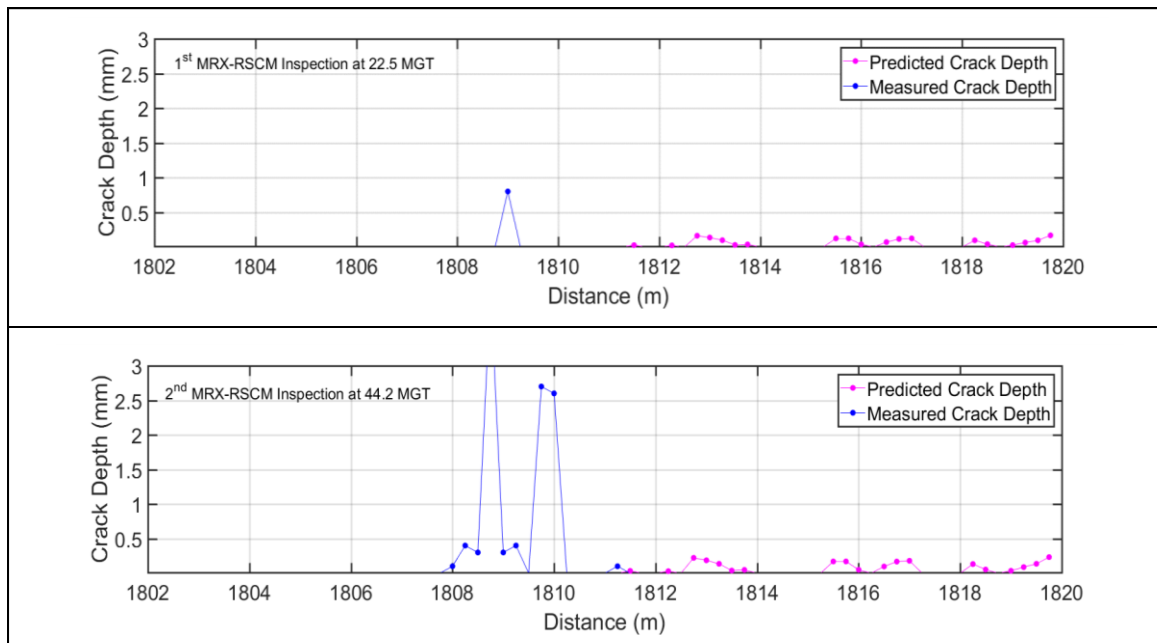


Figure 8.9: Comparison of RCF predictions with MRX-RSCM measurements on rail cases of RCF-BAK-8 (Cases 1 and 2)



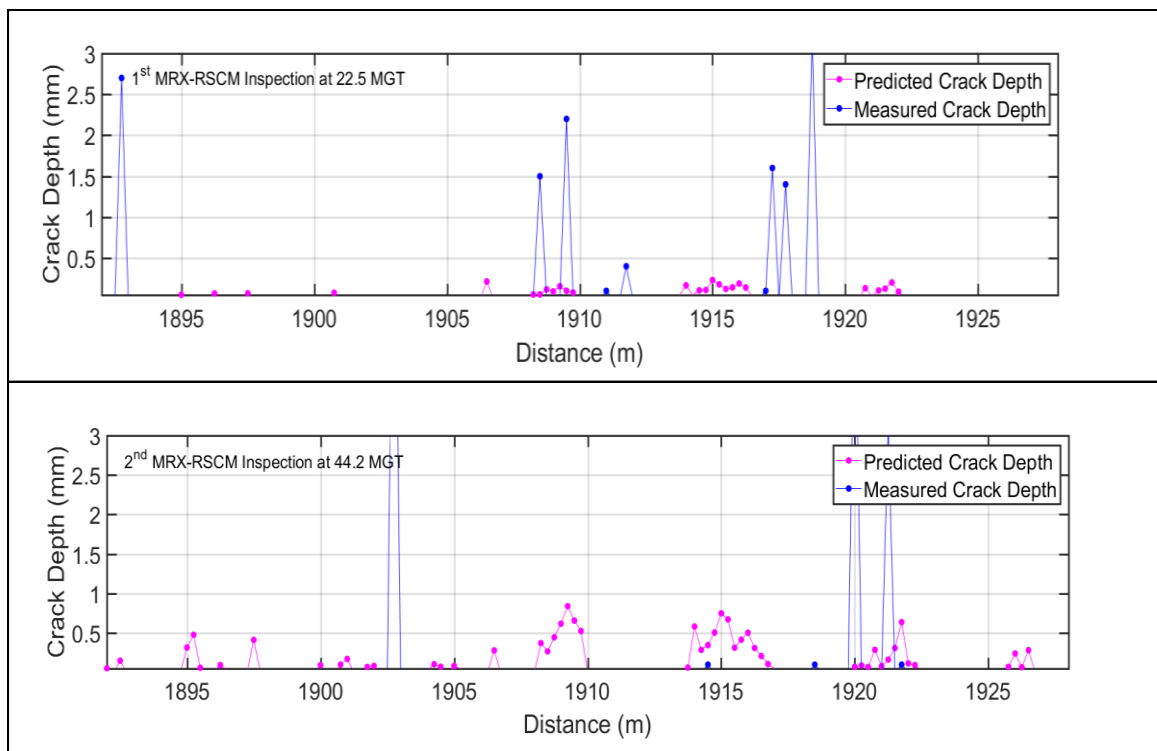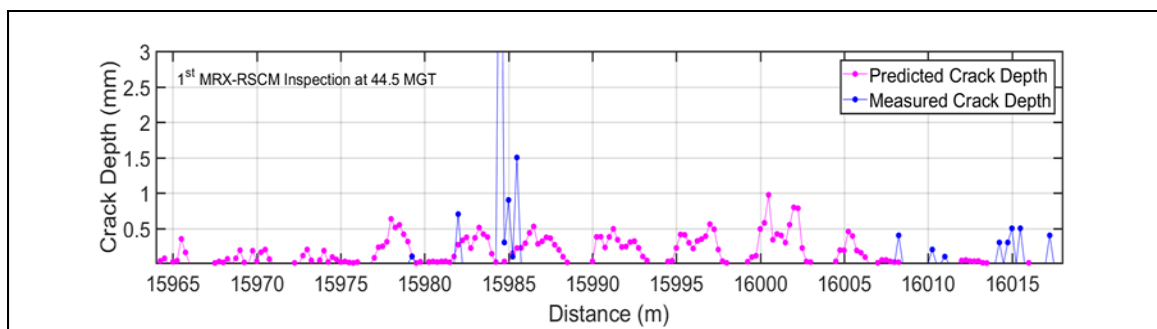Figure 8.10: Comparison of RCF predictions with MRX-RSCM measurements on rail cases of RCF-JUB-2 (Case 3)
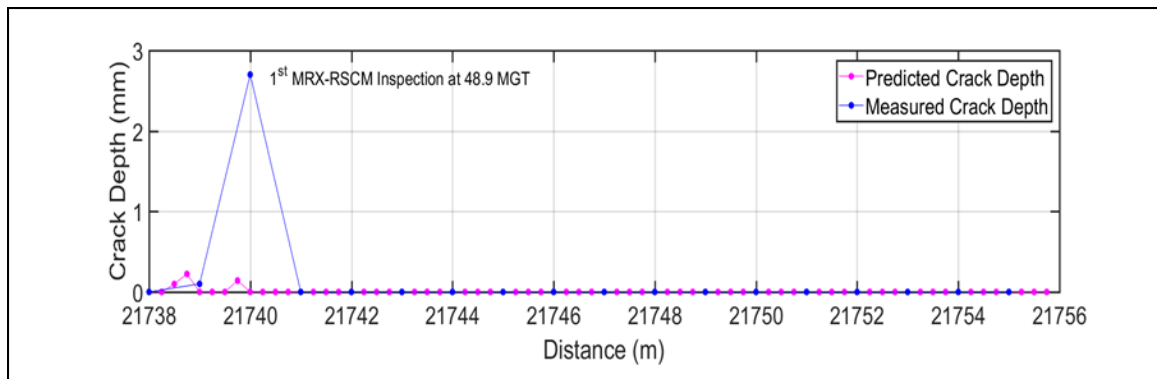
Figure 8.11: Comparison of RCF predictions with MRX-RSCM measurements on rail cases of RCF-JUB-3 (Case 4)

## 8.3 Recommendations on rail maintenance

As the research is also aimed to provide guidance on LUL's maintenance strategy, the RCF crack depth and wear prediction methods were further applied on the certain sites. To mitigate these RCF cracks, the maintenance particularly the grinding in railways is generally carried out as a preventive maintenance regime which divided into fixed-interval maintenance (cyclic) and condition-based maintenance (Kumar, Espling, & Kumar, 2008). Due to aforementioned limitations, LUL often conducts fixed-interval maintenance based on the 'track loading factor' calculated from the tonnage and running speed of each of the line sections as aforementioned in Chapter 3.1. However, one of the previous studies noted the negative consequences of frequent grinding by stating that while one-third of the removed material was related to wear, grinding removed the two-thirds of the material in rails (Chattopadhyay, Reddy, & Larsson-Kråik, 2005). Thereby, the optimum solution is to apply a condition based regime which should be based on the result of the accurate RCF and wear (including their interaction) predictions.

In this research, it was suggested that the proposed methods can also provide opportunity to predict the condition of rails prior to next inspection and conduct the necessary grinding effectively. Future RCF and wear severity levels might then be estimated by reviewing previous inspection results and define how the rails should be maintained in the next activity. The estimated net RCF crack depths which are reduced by the predicted wear depths will help to find the necessary depth of material that need to be removed by grinding. As it was noted particularly in the RCF damage prediction study that the majority of the estimated and measured cracks from the first inspection using the MRX-RSCM system were disappeared and new cracks were starting to initiate in the second inspection. However, this condition may alter in the following time periods due to changes in railhead profile shape and the impact on the contact conditions with variation in worn wheel profile shapes. To demonstrate the effect of changing railhead profile shapes on damage predictions (meaning that the variations in estimations throughout the rail life), the wear and RCF crack depths were estimated for new and two different worn rail profiles

measured from the similar locations. The damages were accumulated on both high rail (RCF-BAK-8) and low rail (RCF-BAK-7) for the similar 10 MGT.

Figures 8.12 and 8.13 display high and low rail results, respectively. While the new high rail profiles generated the maximum level of wear depth, the severely worn rail profile caused higher predictions with considerably larger RCF damage region. On the low rail site, the RCF damage seemed to be more critical than wear. But, as the rail wears over time (severe worn profile), the wear predictions increased which led to reduction in RCF predictions. It should be also noted that the higher RCF estimations may also give rise to lipping and/or rail flattening observed in the field observations/measurements.
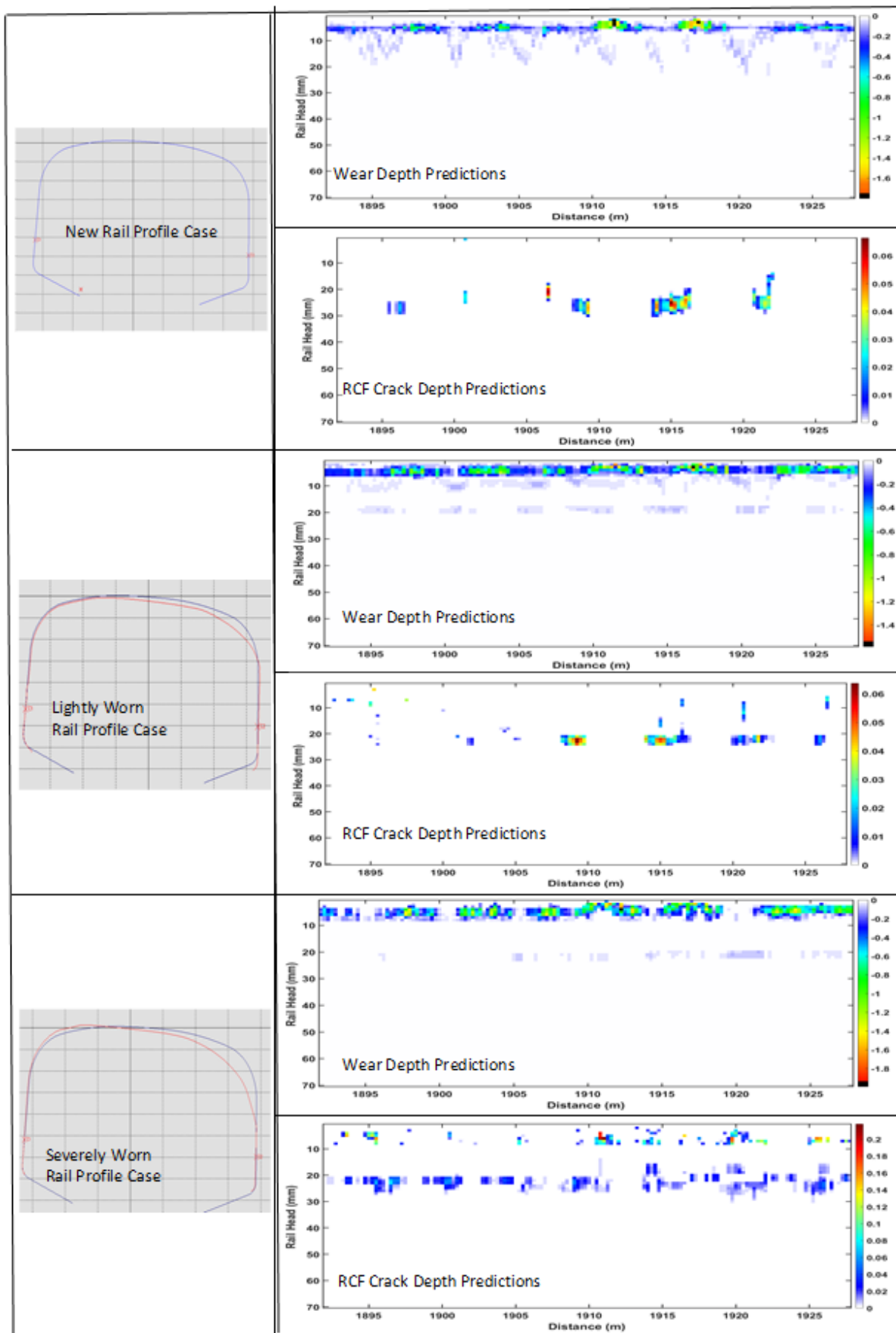
Figure 8.12: Changes in predicted RCF and wear depths under the new and different worn high rail profile shapes on RCF-BAK-8
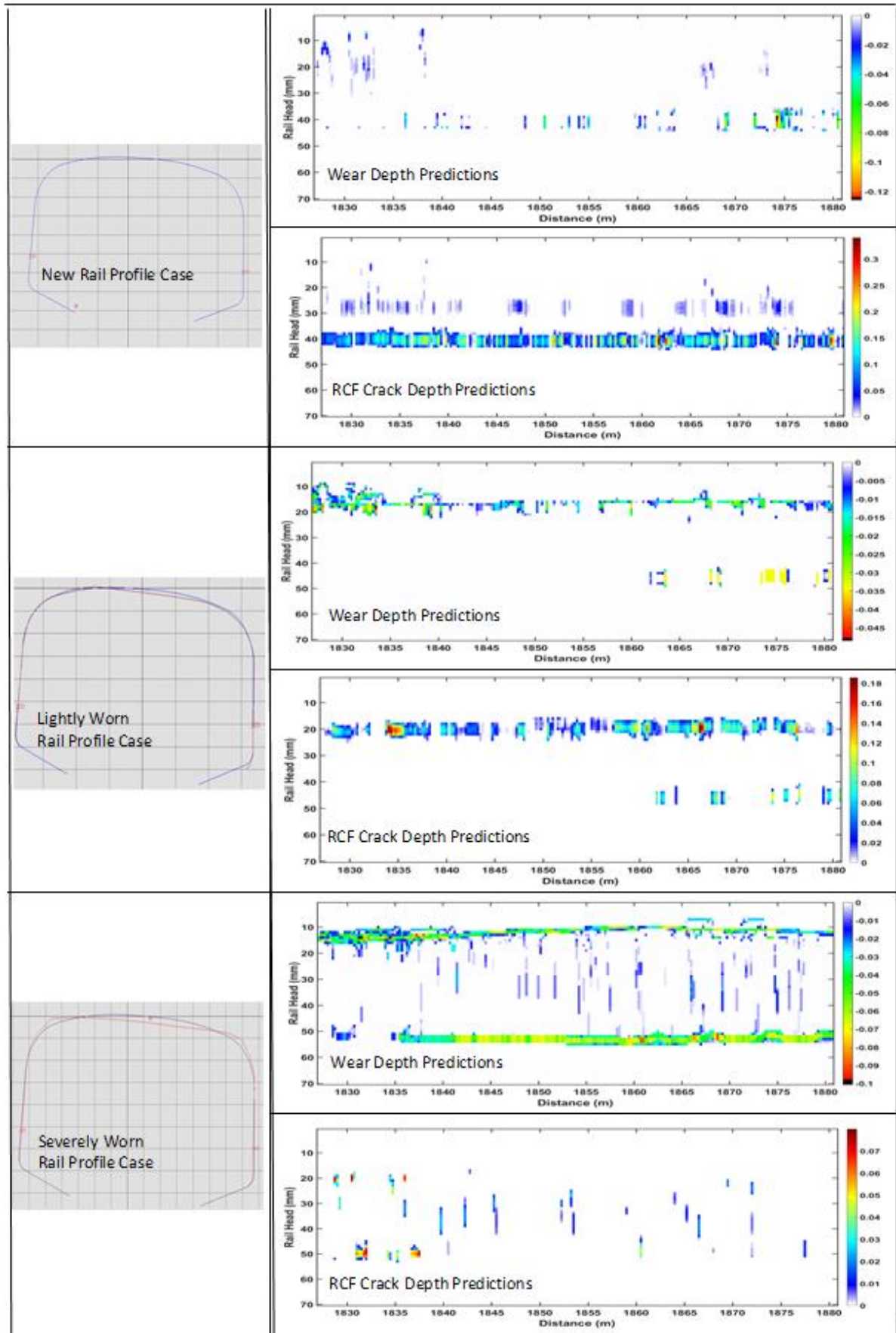
Figure 8.13: Changes in predicted RCF and wear depths under the new and different worn low rail profile shapes on RCF-BAK-7

Since the new prediction method used the Shakedown Map to classify the dominant damage type in rails, the maintenance recommendations can be also given considering this theory. In order to move contacts from the ratchetting failure region, the following suggestions can be given:

- Using harder steel which will increase shear yield limit (k) of the material can cause a reduction in the load factor
- Using different wheel-rail profiles may influence the contact dimensions and result in larger patch areas. This will help to decrease the maximum contact pressures

In order to understand their influences on predicted damage, the R350HT steel (k=535 MPa) and CEN 60E2 (k=400 MPa for R260) anti-head check rail profiles were used as an example in this analysis. Figures 8.14 and 8.15 provide their accumulated depth estimations. In contrast to new rail profile with R260 steel in Figure 8.17, the wear depth predictions are slightly lower (including the affected regions over railhead) in the R350HT and CEN 60E2 high rails. However, whereas the former produced relatively higher RCF predictions than R260 steel, the latter condition generated considerably smaller RCF predictions. On the low rail site, it can be clearly seen that the both rails produced lower crack and wear depth predictions than the R260 rail. But, the R350 HT steel seemed to be more advantageous than CEN 60E2 profile.
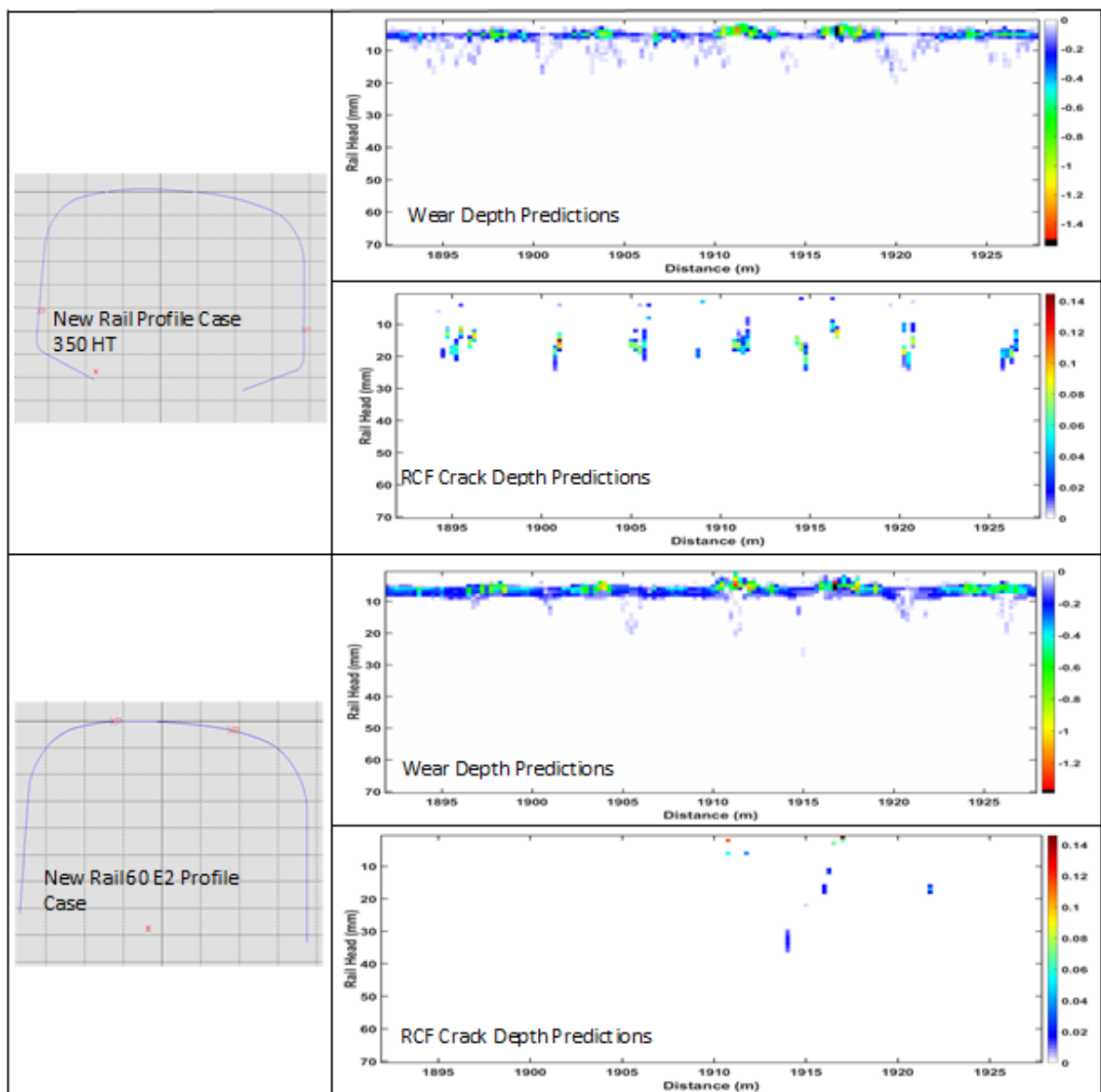
Figure 8.14: Effect of using harder steels and anti-head check profile on the RCF and wear depths' predictions of high rail (RCF-BAK-8)
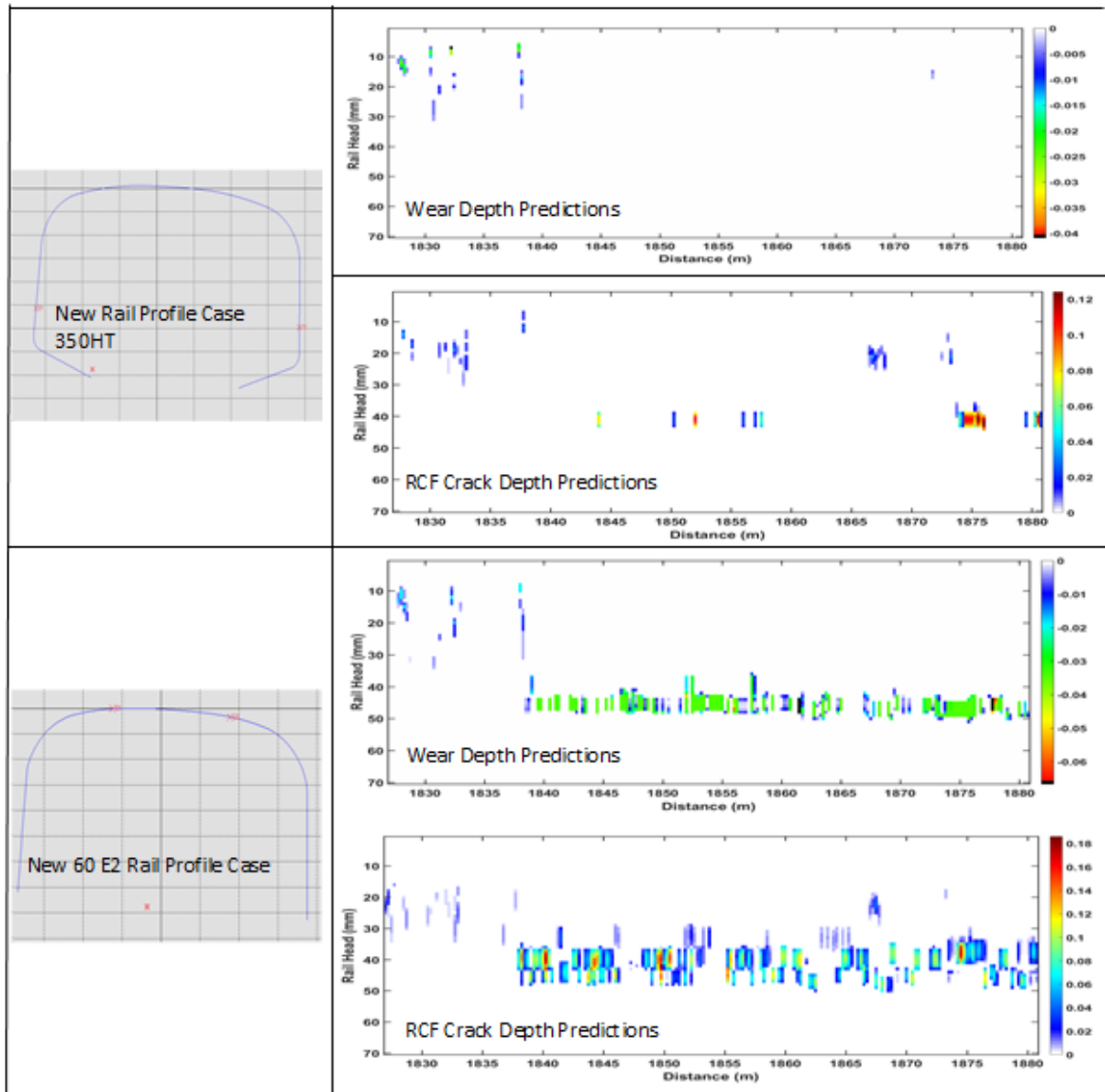
Figure 8.15: Effect of using harder steels and anti-head check profile on the RCF and wear depths' predictions of low rail (RCF-BAK-7)

## 8.4 Conclusions and discussions

Based on the findings in the previous studies and results in this research, it was proposed that the contacts having higher shear forces with moderate contact stresses were more prone to RCF cracking. Depending on the different wheel-rail profile combinations, contacts with varying impact levels are generated over railhead. Although wear was assumed as the dominant damage mechanism under certain conditions, considering the above assumption, RCF damage was suggested to be prevalent when the contact parameters appear inside the specified region of the Shakedown Map. During the crack growth (as well as initiation), wear removed material from the surface of the railhead and shortens the depth of cracks. At the same time, the resulting wear changes the rail profile shape and in turn, alters the contact conditions and forces.

In this research, the interaction of wear was taken into account by subtracting the predicted wear depth from the predicted total RCF damage susceptibility to estimate the net crack depth. The predicted worn area was converted to depth on both rail gauge corner and crown of the railhead by using the equations presented in Chapter 7.4.  In addition, measured worn rail profiles were utilised to consider the variation in profile shape over time and their impact on the resulting wheel-rail forces. In order to represent the duty conditions experienced by rail each site in RCF predictions, the similar procedure as aforementioned in Chapter 7.2 was applied. The total number of simulations with different wheel-rail profile combinations used in the prediction accumulations were determined by considering the related scaling factor.

In order to validate the RCF predictions, the net crack depth results were correlated with the outputs from the MRX-RSCM device, this included the surface damage map and depth measurements. While the location comparison plots provided in Appendix B the opportunity to observe the relationship between predicted and measured cracks, the depth comparison plots presented the differences in terms of crack severity.

When the results in all track categories were considered, it was noted that the model produced reasonable predictions, as the results were relatively small under lower MGT levels (first inspection≈12 MGT and second inspection≈32 MGT). The results also seemed to be agreed with the previous research mentioned that homogeneous traffic could cause early initiation and relatively rapid crack growth compared to mixed traffic lines. The initial crack formation (Phase 1) was occurred between 5-10 MGT and the crack growth was given as 3.33 mm/100 MGT in the rapid transit system (Heyder & Brehmer, 2014).  In addition, it helped to identify which contact conditions were more responsible for the changes. For instance, while higher wear rates occurred on the gauge corner of the rail which made the tread contacts more susceptible to RCF damage in the first inspections, the worn rails generated more conformal contacts resulted in a decrease in contact pressures and hence cracks started to develop on the gauge corner of the rail and some of the cracks continue to propagate on the mid of the railhead.

As a result, it was suggested that the new RCF prediction method provided certain improvements to the accuracy of RCF damage predictions. For instance, both depth and longitudinal and lateral location of crack can be predicted and correlated using the NDT measurements. On the contrary to previous models' results, the RCF cracking was predicted in various type of track characteristics with different tonnage levels. The sites with major and minor cracking could be distinguished by using the new methodology. However, the difference between the measured and predicted crack depths were high in certain cases and there were sometimes large gaps that occurred particularly in the lateral

crack location predictions over railhead. The reasons for these deficiencies may be summarised as follows:

- Different material responses under successive wheel passages and decay in the ratchetting rate as well as the contribution of other factors such as fluid mechanism, thermal and residual stresses can affect the crack development and made it more difficult to predict the further position and orientation of RCF cracks. Although the research conducted several calibrations to predict the changes in crack depth measurements and used track irregularity information and worn rail-wheel profiles to increase the accuracy of RCF predictions in terms of both severity and locations, certain discrepancies between the measurements were generated. To further improve the accuracy, the research suggested the use of FASTSIM, as it can present the changes in contact stress distributions and local stresses peak values. Nonetheless, the other non-Hertzian models and more comprehensive tangential models were mentioned to be still not applicable in extended track distances (Burgelman et al., 2015).
- Although the research applied similar scaling factors in both RCF and wear predictions (as both ratchetting failure region is considered), the further approximation of scaling factors is required to represent the changes crack growth rate in different phases.
- The grinding which can also be seen on the site photos might have an effect on the reduction of crack severities (depths) and change in crack positions. This influence should be considered in damage predictions by including the post-grinding profile in the simulations, as it also modified the profile shape and the decreasing further amount of removed material from the predicted net crack depths.
- The uncertainty in the actual flangeway clearances lead to poor agreements between the predictions and measurements. This information should be obtained from field.
- As it was given in the computed wear depth conversion equations, the $R^2$ levels were approximately 70-80%. Whilst it was found as acceptable for most of the cases, they should be revised in certain cases such as unlubricated curve tracks.

Furthermore, a further study is conducted to provide guidance on LUL's maintenance strategy. To demonstrate the changes in the predictions for similar time/MGT under different profile shapes, the model was applied to certain high and low rail sites. It was found that RCF and wear depth predictions changed as the rail profile shapes alter over time. Additionally, the recommendations for the use of higher steel grade rails R 350HT and anti-head check profile CEN 60E2 were given. While the harder steel produced higher RCF predictions, the anti-head check profile generated considerably lesser predictions on the high rail site. But, the use of harder steel seemed to be more advantageous on the low rail site.

# Chapter 9    Conclusions and Recommendations

This chapter provides the main conclusions of this research. In respect to these outputs, recommendations for future research are provided in the subsequent section.

## 9.1  Conclusions

The research motivation was to understand and predict the susceptibility of rails to damage on underground-metro systems. Previous studies have mainly focused on predicting damage on mainline tracks and the damage models, such as the WLRM, were developed and validated considering the characteristics of these routes. However, due to high traffic demand and limited maintenance periods, rail damage management is a crucial concern for the metro systems and in recent years, LUL have increased efforts to improve their rail inspection and optimise maintenance strategy. They are currently using several NDT techniques during rail inspection to detect emerging defects and monitor the growth of these and previously recorded defects. This includes the use of the MRX-RSCM system which uses magnetic flux leakage based sensors to measure the crack depths on the rail surface. This is a key parameter in the severity assessment and future maintenance planning (e.g. grinding interval).

In this research, the rail inspection data acquired from various NDT techniques was analysed in detail to understand the damaging mechanisms and to identify the critical sites. The successive NDT measurements allowed to quantify the severity and location of the damage on the rail and also provided the unique opportunity to develop and further validate the proposed damage models. With the use of crack depth in validations, the accuracy of predictions was improved and the new methods were able to successfully show the damage susceptibility of tracks with various characteristics such as high and low rails of curves (both checked and un-checked) and tangent tracks.

The following section presents a summary of main conclusions and key findings drawn from each objective:

The current RCF damage prediction models were evaluated whether they can be applied to LUL tracks including their assumptions and gaps. The WLRM and the Shakedown Map were selected due to their integration with vehicle dynamics simulations and successes in real track conditions. Nevertheless, both of the models also contain several assumptions and produced certain deficiencies in the previous studies that were clarified in Chapter 2.

During the research, a significant volume of data consisted of different rail inspection outputs, defect data sheet (UT and visual inspection) and MRX-RSCM measurements as well as, rail and wheel profiles, track geometry data (from TRV output), speed profile,

track tonnage data and maintenance history including track lubricator positions and re-railing dates were provided by LUL. This information was very beneficial and it was used to accomplish each objective. Additionally, it helped to prepare detailed Vampire vehicle dynamics route simulations which made this research different from the other studies.

In the Objective 1, the analysis of the field defect data was conducted to *understand the dominant damage mechanisms on the studied lines and identify the key factors that promote RCF crack growth.* The Bakerloo and Jubilee lines were particularly studied in which both of them have curvaceous track geometry but, check rails were installed when the curve radius less than 200 m on the Bakerloo line. Different vehicle types operated on both of the lines and the Jubilee line is operated under ATO mode with running speeds up to 90 km/h whereas, the Bakerloo line uses manual mode operation with relatively lower speeds. The following objectives were found from this analysis provided in Chapter 3:

- Shelling and squat type of defects were the most prevalent in both of the lines. While squats mostly observed on shallower curves and tangent tracks of the over-ground section in Jubilee line, they mainly occurred on sharper curves in the tunnel section of the Bakerloo line. Gauge corner shelling was primarily observed on the high rail, whereas shelling on the top of running surface of the low rail was observed particularly on the Jubilee line.

- Although the MRX-RSCM data showed certain distance discrepancy, it provided useful information for observing the severity of RCF cracking on the entire lines.

- A higher number of defects were recorded in traction areas and lubricated/over-ground sections which potentially supported the finding of the previous RCF modelling studies stated that the traction direction which drives the fluid entrapment mechanisms, gave an increase in crack growth rates.

In the Objective 2; the applicability of the WLRM to LUL was assessed in Chapter 5 to *Evaluate the effectiveness of current rail damage prediction model under the influence of significant factors particularly observed on metro lines and the comparison of its predictions with the field data.*

In the first part of the Objective 2, the changes in 'signed Tγ' results were demonstrated under the factors such as additional traction/braking forces, curve radius, different friction coefficient, track irregularity levels and wheel-rail profile shapes.

- In comparison to previous WLRM results, the changing infrastructure characteristics and the additional traction forces resulting from the start-stop nature of traffic in metro lines gave rise to higher risk levels at all contacts. The sharper curves including the check-curved tracks, the reduction of friction coefficient due to lubrication as well as different profile shapes affected Tγ levels substantially. Therefore, the study suggested that all of these factors need to be taken into account to increase the accuracy of

damage predictions. The total number of passages should be accumulated considering the range of duty conditions observed by the rail in reality.

To address the second part of Objective 2, the damage predictions were also compared with field crack observations/measurements. The locations with high levels of 'signed Tγ' were used to indicate locations with a high susceptibility to damage and were compared with the field defects at these locations.

- Although the high 'signed Tγ' values provided good correlations with several measured crack locations, it sometimes overestimated the damage rates at locations where no damage was observed particularly on high rails. In addition, the signing of Tγ under traction direction led to underestimation especially on low rails. Therefore, it was concluded that the use of this parameter led to both over- and under-estimations in predicting RCF damage locations. In order to overcome these problems and to increase accuracy, it was proposed to investigate further the following key areas:
  - Interaction between RCF and wear; The poor correlation of 'signed Tγ' values with no reported defects might be resulting from an exceedance of the wear rate over the crack propagation rate.
  - 'Signed Tγ' assumption: To prevent underestimations, the 'raw Tγ' and the different creep force angles were proposed to take into account.
  - Consideration of other damage prediction parameters; As the energy term might not be sufficient to individually describe the overall changes at the wheel-rail contact, the Shakedown Map parameters were suggested to be used in further investigations.

In the objective 3, the proposed methodology was conducted in Chapter 6 to *Investigate the variations in the key contact parameters between the sites with and without reported RCF defects in order to identify the conditions that are contributing to the observed damage and propose improvements to rail damage prediction models.*

- The relationship between the selected damage prediction parameters: 'raw Tγ', creep force angle (θ) region, contact stress ($P_0$) and traction coefficient (T/N) and their comparisons between the sites with reported and no reported RCF defects showed that while contacts on reported sites had moderate contact stresses with relatively higher T/N and Tγ levels, the occurrence of higher contact stresses with various Tγ levels on no reported RCF sites suggested that increased wear rates on these sites may contribute to the removal of the initiated cracks through wear. As both of the model parameters helped to differentiate these sites, a combined Shakedown Map and Tγ approach was developed; while the Shakedown Map was utilised as a qualitative analysis to classify which contacts are more susceptible to wear or RCF damage, the energy (Tγ) values was used to quantify the damage predictions with successive wheel passages.

- Wear damage prediction method: Based on the research results and previous study findings which stated that the higher normal loads resulted in thick plastically deformed layers gave rise to wear in the experiments, the upper ratchetting and the LCF failure region on the Shakedown Map was selected. Subsequently, the BRR wear function was suggested to use to find the worn area.
- RCF crack depth prediction method: Similar to research findings, the previous studies mentioned that the shear forces caused from high traction/braking were driving factors for RCF damage. Thus, the ratchetting failure with higher traction levels (and with moderate contact stresses) was associated with RCF susceptibility. Subsequently, a new RCF crack depth prediction model was used.
- Both the indicated regions in the Shakedown Map and the new RCF crack depth prediction model were developed based on the iterative process by linking the predictions with MiniProf wear measurements and consecutive crack depth measurements reported by the MRX-RSCM system.

In the Objective 4, the new wear and RCF depth prediction methods were applied to the selected RCF monitoring sites to *Validate the proposed model predictions using NDT measurements*.

In the wear predictions provided in Chapter 7, when the contacts lay inside the specified wear risk region on the Shakedown Map, the BRR function was applied to predict the total worn area. These compared with field measurement from MiniProf. The initial prediction results showed significantly higher predictions than the actual measurements. As it may be expected from the wear curves with third body layers, the use of (dry) BRR function resulted in larger values. In addition, the decay in ratchetting rates as well as the changes in the wear rates over time with the steady state wear regime were also responsible. Based on the iterative process, scaling factors had to be applied but, this clearly showed that the most of the energy produced did not transform to any RCF or wear damage in rails.

The new wear prediction method was applied to rails under five different track categories (i-ii); high and low rails on R>200 m curved tracks, (iii-iv); high and low rails on R<200 m checked-curved tracks and (v) tangent tracks. The majority of cases demonstrated good correlations between predicted and measured areas. The results can be summarised as follows:

- Differences between the predictions and measurements were relatively small on both high and low rails of R> 200 m curved tracks.
- Damage locations were also successfully predicted; whereas the large gauge corner wear was estimated on high rails, the top/head wear on the crown of low rails was estimated which produced by the relocation of running band in these rails.

However, the new method produced certain over-and under-estimations in the following locations:

Under-estimation: The non-conformal shape (sharp gauge corner radius) of the BH rails possibly limited the predictions on the gauge region higher and resulted in lower predictions. The predictions were also smaller in tangent tracks due to smaller shakedown parameters and T$\gamma$ values.

Over-estimation: The predictions in certain high and low rails of checked curved tracks were considerably higher than the field measurements. As the changes in flangeway clearances in reality between the check and running rails were unknown and can vary considerably, the simulations with and without check rail contact were considered which gave rise to larger results. The results were also higher on older rails. Although a further scaling factor was used after 30 MGT to reflect the decrease in ratchetting rate and steady-state wear regime, the predictions became higher compared to measured values.

In the RCF crack depth predictions provided in Chapter 8, when the contacts lay inside the specified RCF risk region of the Shakedown Map, the new RCF crack depth prediction model was applied. The predictions were correlated with the two outputs from the MRX-RSCM system: surface damage map and depth measurements. Since the wear is removing material form the surface of the rails and shortens the depth of the cracks, its interaction was considered by subtracting the predicted wear depth from the predicted total RCF damage susceptibility to estimate the net crack depth. These net crack depth correlations with the field crack depth measurements were again presented in five different track categories. The results can be summarised as follows:

- The new method provided reasonable predictions in the lower tonnage levels and the results were relatively smaller under lower MGT levels (first inspection≈12 MGT and second inspection≈32 MGT). There was generally a good agreement between the regions of intense damage predictions and severe measured cracking in all the track categories. Conversely, the less severe damage predictions correlated with the sites with no observed damage, which was particularly evident on tangent tracks.

- Changes in RCF crack severity over time/MGT and the interaction of wear were able to shown by using the proposed method. While the higher flange contact stresses removed the initiated cracking on the gauge region of higher rails, the milder tread contact stresses gave rise to RCF on the crown of the rail in the first set of comparisons.

- The second set comparisons showed mixed results. For instance, whereas some cracks started to initiate on the gauge region of high rails, some cracks on the crown of the railhead were either removed or could continue to propagate towards field side.

- Regarding the low rails, the moderate contact stresses generated on the crown of the railhead gave rise to RCF cracking as seen in the both comparison results.

- Site visits were also conducted to verify the predictions and measurements. Although the predictions affected wider regions over railhead, good correlations were also noted with field observations such as cracks were predicted close to regions where head checks were recorded on RCF-BAK-4 site and gauge side lipping on RCF-BAK-8.

Nevertheless, certain deficiencies and gaps occurred particularly in the second prediction of the lateral crack locations over railhead. The reasons for these deficiencies can be summarised as follows:

- Due to decay in the ratchetting rates stemming from the changes in the plastic deformation history in the deeper layers and the effect of other factors such as fluid mechanism, thermal and residual stresses in crack growth, it became harder to predict the further position and orientation of cracks.
- Again, the uncertainty in check rail positions and the use of both with and without simulation cases resulted in higher predictions.

Furthermore, an additional study was conducted to answer the second part of the *Objective 4*: *provide guidance on future LUL's maintenance strategy*. As the research helped to show the changes in RCF and wear predictions over successive inspection cycles, it was suggested that the proposed methods can allow to predict the condition of rails prior to next inspection and hence, they can advise the amount of material which should be removed by grinding. To show the influence of changing profile shapes (in order to reflect variations throughout the rail life), the estimations were conducted for similar MGT levels on the selected new-light-severe worn high and low rail profiles. Additionally, the use of higher steel grade rails R350HT and anti-head check profile CEN 60E2 were evaluated. While the anti-head check profile generated lesser damage on the high rail, the harder rail seemed to be more advantageous on the low rail site.

With respect to the proposed RCF and wear damage prediction methods and their validation using successive NDT measurements, certain contributions' to current knowledge were made. For instance, some of the assumptions especially in the WLRM were improved and the previous inaccurate predictions with the Shakedown Map in the literature were addressed. Firstly, the new model was developed and validated considering the contact conditions on different operating environments; underground-metro systems. Secondly, 'the 'signed Tγ' assumption was removed and to find an optimum solution between under- and over-estimations, the selected damage prediction parameters were compared on sites with and without reported RCF defects. Thirdly, the interaction of wear with RCF was re-defined by using other contact parameters: contact stress and traction coefficient rather than Tγ only in the modelling. With the help of iterative process, a combined Shakedown Map and Tγ approach was developed and validated using site measurements in the selected RCF monitoring sites. The crack depths were predicted in

consecutive NDT measurements which is a key parameter used in the crack severity assessment. Additionally, another detection output: surface damage maps allowed to observe and validate the changes in RCF damage propagation and its interaction with wear over railhead. Since these predictions and validations conducted on the several sites with various track characteristics, it is suggested that the accuracy in rail damage predictions were improved which will also help to optimise future maintenance planning and to move towards condition-based maintenance

## 9.2 Recommendations on future work

Although the development of the new combined Shakedown Map and Tγ approach in the damage predictions provides opportunity to improve several assumptions in the current models, there were still certain deficiencies in both RCF and wear damage estimations. This require potential further investigations as listed in the following:

- While the consideration of only ratchetting region helped to neglect a large number of contacts with various energy levels which were produced from successive wheel passages, the defined scaling factors had to be applied to both the RCF and wear predictions. But, to consider the decay in ratchetting rates and to represent the changes in wear and crack growth rates in different phases, the rails should be continued to inspect in certain intervals in these "RCF Monitoring Sites" and damage predictions and validations should be conducted throughout the rail life. This may help to improve the approximation of scaling factors and hence, to make more accurate predictions.

- The future research should use the new wear curves for third body layers. But, it should be noted that they were also developed using twin disc testing therefore, certain variations can be generated in the field conditions.

- The previous studies and validation results demonstrated that the creep forces as well as the contact stress distributions in the modelling should be considered to improve the accuracy. In order to compare global and local contact outputs, FASTSIM was used in conjunction with VAMPIRE. Tables 9.1 and 9.2 present the Tγ distributions (as well as adhesion and slip regions) and their cumulative sum for the breaking points 15, 65 and 175 N at both tread and flange contacts. As it can be seen, the values in each grid element were considerably smaller than their cumulative results. While the 175 N tread contact case and all the flange contacts were in full slip condition, the 15 N and 65 N contact cases were in partial slip. However, although there were not large differences observed between cumulative local and global outputs, the FASTSIM calculation approximately 15 % lower at 175 N tread contact. The flexibility parameters caused a reduction in the creepages and hence, creep forces were differed in this code. But, the new breaking points should be determined using these local values and their correlation

with the field measurements should be conducted. It should be also noted that this will definitely increase the post-processing times compared to Vampire.

- Besides the tangential problem, the relatively quicker non-Hertizan (non-elliptical) contact models should be used to accurately predict both contact position and dimensions which will also help to better predict the lateral location of damage over railhead.

Table 9.1: Tγ values at tread contacts with global and local outputs
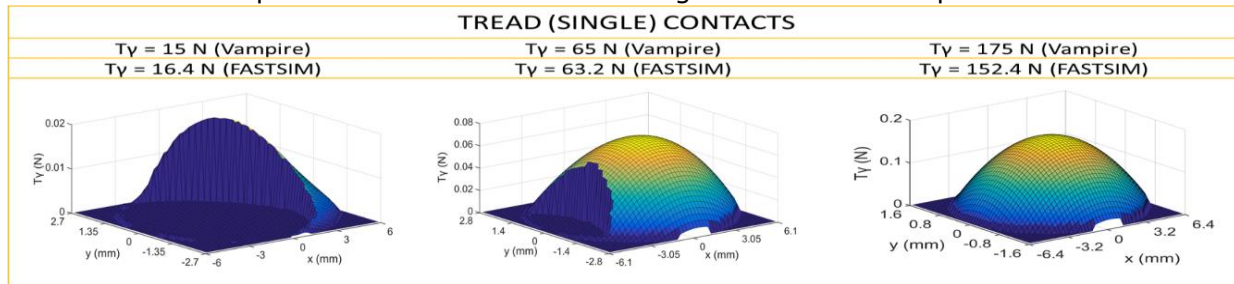


Table 9.2: Tγ values at flange contacts with global and local outputs
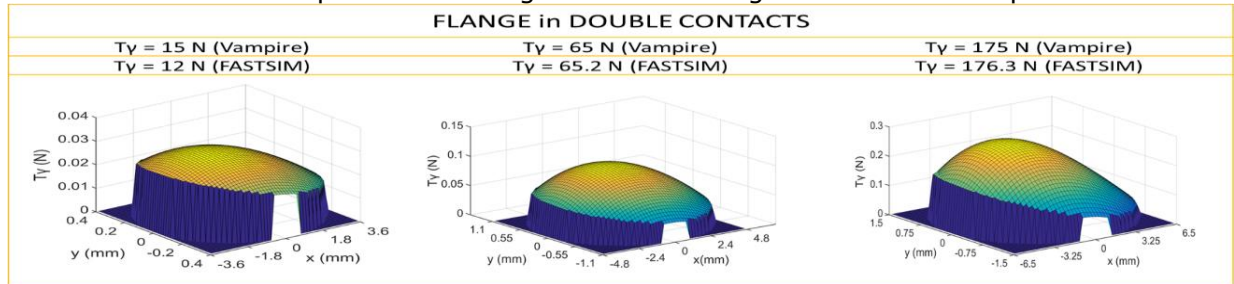


- The new methods should be also tested on different routes such as main and freight lines including under different steels and the predictions should be compared with the field measurements.

In addition to the above recommendations, the certain following suggestions are required to improve modelling inputs:

- The changes in dynamic behaviour of vehicles (e.g: degraded vehicle suspension) and greater distribution of wheel-rail profiles shapes should be taken into account.
- In respect to grinding, the post-ground profiles should be considered and the depth of removed material should be included in the wear depth predictions.
- Although the research spent a large amount of time analysing excessive volumes of (historical) NDT data and to increase its reliability to use in model validations, more rapid methods are needed to quickly examine the rail inspection results from various NDT techniques in large railway networks. Recently, the use of machine learning and/or artificial intelligence has been suggested to reduce this post-processing time. With respect to these advances, the damage prediction models can be applied to the online data and necessary maintenance actions can be determined more rapidly.

# REFERENCES

Ayasse, J. B., & Chollet, H. (2006). Wheel–rail contact. In S. Iwnicki (Ed.), *Handbook of railway vehicle dynamics* (pp. 86-120).

Beagley, T. M. (1976). Severe wear of rolling/sliding contacts. *Wear, 36*(3), 317-335.

Ben-Akiva, F.-Y. S. a. M. (1996). Modelling Rail Fatigue Behaviour with Multiple Hazards. *Journal of Infrastructure systems 2*, 73-82.

Bevan, A. (2011). *Further Devolopment of the WLRM Damage Parameter* (T775-01 project report). Retrieved from

Bevan, A., Jaiswal, J., Smith, A., & Ojeda Cabral, M. (2018). Judicious selection of available rail steels to reduce life-cycle costs. *Proceedings of the Institution of Mechanical Engineers, Part F: Journal of Rail and Rapid Transit*, 95440971880263. doi:10.1177/0954409718802639

Bogdański, S., & Brown, M. (2002). Modelling the three-dimensional behaviour of shallow rolling contact fatigue cracks in rails. *Wear, 253*(1), 17-25.

Bogdański, S., & Lewicki, P. (2008). 3D model of liquid entrapment mechanism for rolling contact fatigue cracks in rails. *Wear, 265*(9), 1356-1362.

Bolton, P. J., & Clayton, P. (1984). Rolling—sliding wear damage in rail and tyre steels. *Wear, 93*(2), 145-165.

Bolton, P. J., Clayton, P., & McEwen, I. J. (1982). Wear of Rail and Tire Steels Under Rolling/Sliding Conditions. *ASLE TRANSACTIONS, 25*(1), 17-24.

Bosso, N., Spiryagin, M., Gugliotta, A., & Somà, A. (2013). *Mechatronic modeling of real-time wheel-rail contact*: Springer.

Bower, A. F. (1988). The influence of crack face friction and trapped fluid on surface initiated rolling contact fatigue cracks. *Journal of tribology, 110*(4), 704-711.

Bower, A. F., & Johnson, K. L. (1991). Plastic flow and shakedown of the rail surface in repeated wheel-rail contact. *Wear, 144*(1), 1-18.

Brünger, O., & Dahlhaus, E. (2008). Railway Timetable & Traffic–Analysis, Modelling. *Simulation, Eurail press*, 58-82.

Burgelman, N., Sichani, M. S., Enblom, R., Berg, M., Li, Z., & Dollevoet, R. (2015). Influence of wheel–rail contact modelling on vehicle dynamic simulation. *Vehicle System Dynamics, 53*(8), 1190-1203.

Burstow, M. (2004). Whole life rail model application and development–Continued development of an RCF damage parameter. *T115 project report, RSSB*.

Burstow, M. (2006). *Background to the Tγ RCF damage function* Retrieved from

Burstow, M. (2009). *Proposed new WLRM damage functions for alternative rail steels*. Retrieved from

Burstow, M., Fletcher, D., Franklin, F., & Kapoor, A. (2008). *Management and Understanding of Rolling Contact Fatigue:WP1 Mechanisms of Crack Initiation*. Retrieved from

Carroll, R. (2006). *Surface metallurgy and rolling contact fatigue of rail.* University of Sheffield,

Carroll, R., & Beynon, J. (2007). Rolling contact fatigue of white etching layer: Part 1. Crack morphology. *Wear, 262*(9-10), 1253-1266. doi:10.1016/j.wear.2007.01.003

Chatterjee, P., Degrande, G., Jacobs, S., Charlier, J., Bouvet, P., & Brassenx, D. (2003). *Experimental results of free field and structural vibrations due to underground railway traffic.* Paper presented at the 10th International Congress on Sound and Vibration.

Chattopadhyay, G., Reddy, V., & Larsson-Kråik, P. O. (2005). Decision on economical rail grinding interval for controlling rolling contact fatigue. *International Transactions in Operational Research, 12*(6), 545-558.

DeltaRail. (2014). Vampire Pro V6.30 Help Manual. . UK:: DeltaRail Group Ltd.

Dembosky, M. (2004). *Rolling contact fatigue(RCF) in the UK system- the emerging solution.* Paper presented at the Permanent Way Institution Journal and Report of Proceedings.

Dirks, B., & Enblom, R. (2011). Prediction model for wheel profile wear and rolling contact fatigue. *Wear, 271*(1), 210-217. doi:10.1016/j.wear.2010.10.028

Dirks, B., Enblom, R., Ekberg, A., & Berg, M. (2015). The development of a crack propagation model for railway wheels and rails. *Fatigue & Fracture of Engineering Materials & Structures, 38*(12), 1478-1491. doi:10.1111/ffe.12318

Dollevoet, R. (2010). *Design of an Anti Head Check profile based on stress relief.* (Doctor of Philosophy ), University of Twente, The Netherlands.

Donzella, G., Mazzù, A., & Petrogalli, C. (2009). Competition between wear and rolling contact fatigue at the wheel—rail interface: some experimental evidence on rail steel. *Proceedings of the Institution of Mechanical Engineers, Part F: Journal of Rail and Rapid Transit, 223*(1), 31-44.

Dubourg, M., & Lamacq, V. (2002). A predictive rolling contact fatigue crack growth model: onset of branching, direction, and growth—role of dry and lubricated conditions on crack patterns. *Journal of tribology, 124*(4), 680-688.

Eadie, D. T., Elvidge, D., Oldknow, K., Stock, R., Pointner, P., Kalousek, J., & Klauser, P. (2008). The effects of top of rail friction modifier on wear and rolling contact fatigue: Full-scale rail–wheel test rig evaluation, analysis and modelling. *Wear, 265*(9), 1222-1230. doi:10.1016/j.wear.2008.02.029

Ekberg, A., Åkesson, B., & Kabo, E. (2014). Wheel/rail rolling contact fatigue–Probe, predict, prevent. *Wear, 314*(1), 2-12.

Ekberg, A., Kabo, E., & Andersson, H. (2001). *Predicting rolling contact fatigue of railway wheels*: Chalmers tekniska högsk.

Enblom, R., & Berg, M. (2008). Impact of non-elliptic contact modelling in wheel wear simulation. *Wear, 265*(9), 1532-1541.

Evans, J., & Iwnicki, S. (2002). *Vehicle dynamics and the wheel/rail interface.* Paper presented at the Proceedings of the IMechE Seminar on Wheels on rails–an update, London, UK.

Evans, J., Lee, T., & Hon, C. (2008). Optimising the wheel/rail interface on a modern urban rail system. *Vehicle System Dynamics, 46*(S1), 119-127.

Fischmeister, E., Rossmanith, H., Loibnegger, F., Linsbauer, H., Mittermayr, P., & Oberhauser, A. (2009). *From rail surface cracks to rail breaks–Recent investigations and results of research at the Wiener-Linien Metro System.* Paper presented at the 8th International Conference on Contact Mechanics and Wear of Rail/Wheel Systems (CM2009). Florence, Italy.

Fletcher, D., Hyde, P., & Kapoor, A. (2004). Growth of multiple rolling contact fatigue cracks driven by rail bending modelled using a boundary element technique. *Proceedings of the Institution of Mechanical Engineers, Part F: Journal of Rail and Rapid Transit, 218*(3), 243-253.

Fletcher, D., Hyde, P., & Kapoor, A. (2008). Modelling and full-scale trials to investigate fluid pressurisation of rolling contact fatigue cracks. *Wear, 265*(9), 1317-1324.

Fletcher, D., & Kapoor, A. (2006). Rapid method of stress intensity factor calculation for semi-elliptical surface breaking cracks under three-dimensional contact loading. *Proceedings of the Institution of Mechanical Engineers, Part F: Journal of Rail and Rapid Transit, 220*(3), 219-234.

Frank, E. (1981). *Locations of lubricators.* Paper presented at the Proceedings of the First Rail and Wheel Lubrication Symposium.

Franklin, F., Chung, T., & Kapoor, A. (2003). Ratcheting and fatigue-led wear in rail–wheel contact. *Fatigue & Fracture of Engineering Materials & Structures, 26*(10), 949-955.

Garnham, J., Fletcher, D., Davis, C., & Franklin, F. (2011). Visualization and modelling to understand rail rolling contact fatigue cracks in three dimensions. *Proceedings of the Institution of Mechanical Engineers, Part F: Journal of Rail and Rapid Transit, 225*(2), 165-178.

Glavin, W., Aspebakken, J., & Besch, G. (1989). Heavy haul: the Burlington Northern perspective.

Grassie, S. (2005). Rolling contact fatigue on the British railway system: treatment. *Wear, 258*(7), 1310-1318.

Grassie, S. (2011). *Squats and studs similarities and differences*. Paper presented at the presented at the (IHHA) International Heavy Haul Association Calgary, Canada.

Grassie, S., Fletcher, D., Hernandez, E., & Summers, P. (2011). Studs: a squat-type defect in rails. *Proceedings of the Institution of Mechanical Engineers, Part F: Journal of Rail and Rapid Transit*, 0954409711421462.

Greenwood-Engineering. (2010). *Miniprof© user's manual* Retrieved from

Haidemenopoulos, G., Zervaki, A., Terezakis, P., Tzanis, J., Giannakopoulos, A., & Kotouzas, M. (2006). Investigation of rolling contact fatigue cracks in a grade 900A rail steel of a metro track. *Fatigue & Fracture of Engineering Materials & Structures, 29*(11), 887-900.

Hardwick, C., Lewis, R., & Eadie, D. T. (2014). Wheel and rail wear—Understanding the effects of water and grease. *Wear, 314*(1-2), 198-204. doi:10.1016/j.wear.2013.11.020

Harvey, R. F., & McEwen, I. J. (1986). *The Relationship Between Wear Number and Wheel/Rail Wear in the Laboratory and the Field* (TM-VDY-001). Retrieved from

Heyder, R., & Brehmer, M. (2014). Empirical studies of head check propagation on the DB network. *Wear, 314*(1-2), 36-43. doi:10.1016/j.wear.2013.11.035

Hopkinson, I. (2016). Visualising the London Underground with tableau. Retrieved from https://blog.scraperwiki.com/2014/04/visualising-the-london-underground-withtableau

Hyde, P. (2011). *Numerical Techniques for Optimising Rail Grinding.* (Doctor of Philosophy), Newcastle University

Innotrack. (2008a). *D1.2.2 Track Sections and Track Irregularities*

*Analysis of DB Sites* (Project no. TIP5-CT-2006-031415). Retrieved from

Innotrack. (2008b). *D4.4.1 Rail Inspection Technologies* (Project no. TIP5-CT-2006-031415). Retrieved from

Innotrack. (2009a). *D4.1.4 Rail Degradation Algorithms* (Project no. TIP5- CT-2006-031415O). Retrieved from

Innotrack. (2009b). *D4.3.5 Simulation of Material Deformation and RCF* (Project no. TIP5-CT-2006-031415). Retrieved from

Iwnicki, S., Björklund, S., & Enblom, R. (2009). Wheel–rail contact mechanics. In *Wheel–Rail Interface Handbook* (pp. 58-92): Elsevier.

Johnson, K. L. (1989). The strength of surfaces in rolling contact. *Proceedings of the Institution of Mechanical Engineers, Part C: Mechanical Engineering Science, 203*(3), 151-163.

Johnson, K. L. (1990). A graphical approach to shakedown in rolling contact. In *Applied Stress Analysis* (pp. 263-274): Springer.

Johnson, K. L. (2000). *Plastic deformation in rolling contact*: Springer.

Jones, C. P., Tyfour, W. R., Beynon, J. H., & Kapoor, A. (1997). The effect of strain hardening on shakedown limits of a pearlitic rail steel. *211*(2), 131-140. doi:10.1243/0954409971530978

Kaewunruen, S. (2015). *Identification and prioritization of rail squat defects in the field using rail magnetisation technology.* Paper presented at the SPIE Smart Structures and Materials+ Nondestructive Evaluation and Health Monitoring.

Kalker, J. J. (2013). *Three-dimensional elastic bodies in rolling contact* (Vol. 2): Springer Science & Business Media.

Kaneta, M., & Murakami, Y. (1991). Propagation of semi-elliptical surface cracks in lubricated rolling/sliding elliptical contacts. *Journal of tribology, 113*(2), 270-275.

Kapoor, A., Beynon, J. H., Fletcher, D. I., & Loo-Morrey, M. (2004). Computer simulation of strain accumulation and hardening for pearlitic rail steel undergoing repeated contact. *The Journal of Strain Analysis for Engineering Design, 39*(4), 383-396. doi:10.1243/0309324041223935

Kapoor, A., Schmid, F., & Fletcher, D. I. (2002). Managing the critical wheel/rail interface. *Railway Gazette International, 158*(1).

Keer, L., & Bryant, M. (1983). A pitting model for rolling contact fatigue. *Journal of Tribology, 105*(2), 198-205.

Klecha, S. (2013). *Rail surface Crack Measurement (RSCM) Operator Propelled Unit (OPU)*. Retrieved from

Knothe, K., & Le The, H. (1984). A contribution to the calculation of the contact stress distribution between two elastic bodies of revolution with non-elliptical contact area. *Computers & Structures, 18*(6), 1025-1033. doi:http://dx.doi.org/10.1016/0045-7949(84)90147-0

Kumar, S., Espling, U., & Kumar, U. (2008). Holistic procedure for rail maintenance in Sweden. *Proceedings of the Institution of Mechanical Engineers, Part F: Journal of Rail and Rapid Transit, 222*(4), 331-344.

Larijani, N. (2014). *Anisotropy in pearlitic steel sub jected to rolling contact fatigue - mo delling and experiments.* (Doctor of Philosophy), Chalmers University of Technology, Goteborg, Sweden.

Lewis, R., Dwyer-Joyce, R. S., Olofsson, U., Pombo, J., Ambrósio, J., Pereira, M., . . . Kth. (2010). Mapping railway wheel material wear mechanisms and transitions. *Proceedings of the Institution of Mechanical Engineers, Part F: Journal of Rail and Rapid Transit, 224*(3), 125-137. doi:10.1243/09544097JRRT328

Lewis, R., & Olofsson, U. (2004). Mapping rail wear regimes and transitions. *Wear, 257*(8-jul), 721.

Lewis, R., & Olofsson, U. (2009). *Wheel-rail interface handbook*: Elsevier.

Li, Z., Zhao, X., Esveld, C., Dollevoet, R., & Molodova, M. (2008). An investigation into the causes of squats—Correlation analysis and numerical modeling. *Wear, 265*(9), 1349-1355.

LUL, L. U. (2013). S1158 Track Inspection and Maintenance Standard. In. London, UK.

LUL, L. U. (2015). S1159 Track Dimensions and Tolerances. In. London.

Magel, E. (2011). *Rolling Contact Fatigue: A Comprehensive Review* (No. DOT/FRA/ORD-11/24). Retrieved from United States:

Magel, E. (2016). *Validation of Electromagnetic Walking Stick Rail Surface Crack Measuring Systems* (No. AST-R-LR-0102). Retrieved from United States:

Magel, E. (2017). *A Survey of Wheel/Rail Friction* (No. DOT/FRA/ORD-17/21). Retrieved from United States:

Magel, E., Roney, M., Kalousek, J., & Sroba, P. (2003). The blending of theory and practice in modern rail grinding. *Fatigue & Fracture of Engineering Materials & Structures, 26*(10), 921-929.

Marich, S., Kerr, M., & Fogarty, R. (2001). *Optimising Trackside Lubrication for the Wheel/Rail System.* Paper presented at the RTA Conference.

McEwen, I. J., & Harvey, R. F. (1986). *Interpretation of Wheel/Rail Wear Numbers* (TM-VDY-004). Retrieved from

Mitchell, B. (2003). *Jubilee Line extension: from concept to completion*: Thomas Telford.

MRX. (2011). *Rail Surface Crack Measurement Manual*. Retrieved from

Nan, H. (2011). *Modelling Driving Behaviour in OpenTrack.* TU Delft, Delft University of Technology,

Nawaz, M. U. (2015). Estimation of Running Resistance in Train Tunnels.

Olofsson, U. (2009). Adhesion and friction modification. In R. Lewis & U. Olofsson (Eds.), *Wheel–Rail Interface Handbook* (pp. 510-527): Elsevier.

Olofsson, U., Zhu, Y., Abbasi, S., Lewis, R., & Lewis, S. (2013). Tribology of the wheel–rail contact–aspects of wear, particle emission and adhesion. *Vehicle System Dynamics, 51*(7), 1091-1120.

Olver, A. (2005). The mechanism of rolling contact fatigue: an update. *Proceedings of the Institution of Mechanical Engineers, Part J: Journal of Engineering Tribology, 219*(5), 313-330.

Papaelias, M. P., Roberts, C., & Davis, C. (2008). A review on non-destructive evaluation of rails: state-of-the-art and future development. *Proceedings of the Institution of Mechanical Engineers, Part F: Journal of Rail and Rapid Transit, 222*(4), 367-384.

Pearce, T. G., & Sherratt, N. D. (1991). Prediction of wheel profile wear. In *Mechanics and Fatigue in Wheel/Rail Contact* (pp. 343-351): Elsevier.

Plu, J., Bondeux, S., Boulanger, D., & Heyder, R. (2009). Application of fracture mechanics methods to rail design and maintenance. *Engineering Fracture Mechanics, 76*(17), 2602-2611.

Pombo, J., Ambrósio, J., Pereira, M., Lewis, R., Dwyer-Joyce, R., Ariaudo, C., & Kuka, N. (2011). Development of a wear prediction tool for steel railway wheels using three alternative wear functions. *Wear, 271*(1), 238-245. doi:10.1016/j.wear.2010.10.072

Ponter, A., Chen, H., Ciavarella, M., & Specchia, G. (2006). Shakedown analyses for rolling and sliding contact problems. *International Journal of Solids and Structures, 43*(14), 4201-4219. doi:10.1016/j.ijsolstr.2005.05.046

Ponter, A., Hearle, A., & Johnson, K. (1985). Application of the kinematical shakedown theorem to rolling and sliding point contacts. *Journal of the Mechanics and Physics of Solids, 33*(4), 339-362.

Profillidis, V. A. (2000). *Railway engineering*.

Qiu, H., Pei, Y., & Jin, Y. (1996). An experimental investigation into the influences of plastical deformation on rail steel wear. *TRIBOLOGY-BEIJING-, 16*, 80-84.

Ringsberg, J. (2001). Life prediction of rolling contact fatigue crack initiation. *International Journal of Fatigue, 23*(7), 575-586. doi:10.1016/S0142-1123(01)00024-X

Ringsberg, J. (2005). Shear mode growth of short surface-breaking RCF cracks. *Wear, 258*(7), 955-963.

Ringsberg, J., & Bergkvist, A. (2003). On propagation of short rolling contact fatigue cracks. *Fatigue & Fracture of Engineering Materials & Structures, 26*(10), 969-983.

Ringsberg, J., Loo-Morrey, M., Josefson, B. L., Kapoor, A., & Beynon, J. H. (2000). Prediction of fatigue crack initiation for rolling contact fatigue. *International Journal of Fatigue, 22*(3), 205-215. doi:10.1016/S0142-1123(99)00125-5

Schilke, M. (2013). *Degradation of Railway Rails from a Materials Point of View.* (Doctor of Philosophy), Chalmers University of Technology, Göteborg, Sweden.

Schilke, M., Larijani, N., & Persson, C. (2014). Interaction between cracks and microstructure in three dimensions for rolling contact fatigue in railway rails. *Fatigue & Fracture of Engineering Materials & Structures, 37*(3), 280-289.

Scott, D. (2009). Managing the wheel-rail interface: Europe Metro experience on the London Underground:Victoria Line. In R. Lewis & U. Olofsson (Eds.), *Wheel-rail interface handbook*: Elsevier.

Shackleton, P. (2009). An optimised wheel-rail contact model for vehicle dynamics simulation.

Shackleton, P., & Iwnicki, S. (2008). Comparison of wheel–rail contact codes for railway vehicle simulation: an introduction to the Manchester Contact Benchmark and initial results. *Vehicle System Dynamics, 46*(1-2), 129-149.

Shevtsov, I. Y. (2008). *Wheel/rail interface optimisation*: TU Delft, Delft University of Technology.

Sichani, M. (2013). *Wheel-rail contact modelling in vehicle dynamics simulation.* KTH Royal Institute of Technology, Stockholm,Sweeden

Sichani, M., Enblom, R., & Berg, M. (2014). Comparison of non-elliptic contact models: towards fast and accurate modelling of wheel–rail contact. *Wear, 314*(1), 111-117.

Sinclair, J. (2004). *Friction modifiers, in "Vehicle track interaction: identifying and implementing solutions".* Paper presented at the IMechE Seminar, February 17th.

Six, K., Meierhofer, A., Trummer, G., Bernsteiner, C., Marte, C., Müller, G., . . . Rosenberger, M. (2017). Plasticity in wheel–rail contact and its implications on vehicle–track interaction. *Proceedings of the Institution of Mechanical Engineers, Part F: Journal of Rail and Rapid Transit, 231*(5), 558-569. doi:10.1177/0954409716673118

Stichel, S., Mohr, H., Ågren, J., & Enblom, R. (2008). Investigation of the risk for rolling contact fatigue on wheels of different passenger trains. *Vehicle System Dynamics, 46*(1), 317-327. doi:10.1080/00423110801939188

TfL, T. f. L. (2017). London's transport - a history. Retrieved from https://tfl.gov.uk/corporate/abouttfl/culture-and-heritage/londons-transport-a-history/london-underground#on-this-page-0

Thelen, G., & Lovette, M. (1996). A parametric study of the lubrication transport mechanism at the rail-wheel interface. *Wear, 191*(1-2), 113-120.

Tillberg, J., Larsson, F., & Runesson, K. (2009). A study of multiple crack interaction at rolling contact fatigue loading of rails. *Proceedings of the Institution of Mechanical Engineers, Part F: Journal of Rail and Rapid Transit, 223*(4), 319-330.

Tunna, J., Sinclair, J., Perez, J. J. P. o. t. I. o. M. E., Part F: Journal of Rail, & Transit, R. (2007). A review of wheel wear and rolling contact fatigue. *221*(2), 271-289.

Tyfour, W. A. (1995). *Interaction between wear and rolling contact fatigue in pearlitic rail steels.* (Doctoral Degree), University of Leicester,

UIC, I. U. o. R. (2002). Rail defects. In. France: UIC.

Valenta, G., Varga, T., & Loibnegger, F. (2013). *Investigations of rail fractures at vienna underground and measures to reduce them.* Paper presented at the ECF13, San Sebastian 2000.

Vickerstaff, A. (2015). *Predict and Prevent:The future of wheelset management on London Underground*. Paper presented at the presented at the 21 Wheel-Rail Interaction Conference.

Vickerstaff, A. (2016). *A Holistic approach to WRI Management on London Underground*. Paper presented at the presented at the 22 Wheel-Rail Interaction Conference.

Vollebregt, E. (2014). Numerical modeling of measured railway creep versus creep-force curves with CONTACT. *Wear, 314*(1-2), 87-95.

Vollebregt, E., Iwnicki, S., Xie, G., & Shackleton, P. (2012). Assessing the accuracy of different simplified frictional rolling contact algorithms. *Vehicle System Dynamics, 50*(1), 1-17.

Way, S. (1935). Pitting due to rolling contact. *J. appl. Mech, 2*(2), 49-58.

Wilson, L. J. (2006). Performance measurements of rail curve lubricants.

Yan, W., & Fischer, F. (2000). Applicability of the Hertz contact theory to rail-wheel contact problems. *Archive of applied mechanics, 70*(4), 255-268.

Zaazaa, K. E., & Schwab, A. L. (2009). *Review of Joost Kalker's wheel-rail contact theories and their implementation in multibody codes.* Paper presented at the ASME 2009 International Design Engineering Technical Conferences and Computers and Information in Engineering Conference.

Zerbst, U., Lundén, R., Edel, K.-O., & Smith, R. A. (2009). Introduction to the damage tolerance behaviour of railway rails–a review. *Engineering fracture mechanics, 76*(17), 2563-2601.

Zhao, X. (2012). *Dynamic Wheel/Rail Rolling Contact at Singular Defects with Application to Squats.* (Doctor of Philosophy), Delft University of Technology,

Zhong, W., Hu, J. J., Shen, P., Wang, C. Y., & Lius, Q. Y. (2011). Experimental investigation between rolling contact fatigue and wear of high-speed and heavy-haul railway and selection of rail material. *Wear, 271*, 2485-2493.

# APPENDIX A

**Scaling factor calculation for total number of simulations**

Based on the tonnage of each inspection, scaling factors were defined as a result of iterative process and applied to the total number of (simulation) passages with different wheel-rail profiles combinations. The following formulas show the usage of total number simulations for different MGT levels based on the Figure 7.2.

Bakerloo line:

If $\quad x_{MGT\ level} < 15\ t$

$$x_{MGT\ level} = weight\ (Total\ number\ of\ all\ axle\ wheel\ passages_x)_{vehicles+passengers}$$

$$\frac{\sum 5\%\ (NN) + 38\%(NW1) + 38\%(NW2) + 19\%(NW3)}{Total\ number\ of\ all\ axle\ wheel\ passages_x} = \ x_{MGT\ level} * 1\%$$

If $15\ t < x_{MGT\ level} < 30\ t$

$$y_{MGT\ level} = x_{MGT\ level} - 15 = weight\ (Total\ number\ of\ all\ axle\ wheel\ passages_y)_{vehicles+passengers}$$

$$\frac{\sum 5\%\ (NN) + 38\%(NW1) + 38\%(NW2) + 19\%(NW3)}{Total\ number\ of\ all\ axle\ wheel\ passages_x} = \ x_{MGT\ level} * 1\%$$

$$\frac{\sum 5\%\ (WN) + 38\%(WW1) + 38\%(WW2) + 19\%(WW3)}{Total\ number\ of\ all\ axle\ wheel\ passages_y - Total\ number\ of\ all\ axle\ wheel\ passages_x} = \ y_{MGT\ level} * 1\%$$


If $\quad x_{MGT\ level} > 30\ t$

$$y_{MGT\ level} = x_{MGT\ level} - 15 = weight\ (Total\ number\ of\ all\ axle\ wheel\ passages_y)_{vehicles+passengers}$$

$$\frac{\sum 5\%\ (NN) + 38\%(NW1) + 38\%(NW2) + 19\%(NW3)}{Total\ number\ of\ all\ axle\ wheel\ passages_x} = \ x_{MGT\ level} * 1\%$$

$$\frac{\sum 5\%\ (WN) + 38\%(WW1) + 38\%(WW2) + 19\%(WW3)}{Total\ number\ of\ all\ axle\ wheel\ passages_y - Total\ number\ of\ all\ axle\ wheel\ passages_x}$$
$$= \ 30 * 1\% + (y_{MGT\ level} - 30) * 0.05\%$$

Jubilee line:

If $\quad x_{MGT\ level} < 15\ t$

$$x_{MGT\ level} = weight\ (Total\ number\ of\ all\ axle\ wheel\ passages_x)_{vehicles+passengers}$$

$$\frac{\sum 5\%\ (NN) + 47.5\%(NW1) + 28.5\%(NW2) + 19\%(NW3)}{Total\ number\ of\ all\ axle\ wheel\ passages_x} = \ x_{MGT\ level} * 1\%$$

If $15\,t < x_{MGT\ level} < 30\,t$

$$y_{MGT\ level} = x_{MGT\ level} - 15 = weight\ (Total\ number\ of\ all\ axle\ wheel\ passages_y)_{vehicles+passengers}$$

$$\frac{\sum 5\%\ (NN) + 47.5\%(NW1) + 28.5\%(NW2) + 19\%(NW3)}{Total\ number\ of\ all\ axle\ wheel\ passages_x} =\ x_{MGT\ level} * 1\%$$

$$\frac{\sum 5\%\ (WN) + 38\%(WW1) + 38\%(WW2) + 19\%(WW3)}{Total\ number\ of\ all\ axle\ wheel\ passages_y - Total\ number\ of\ all\ axle\ wheel\ passages_x} =\ y_{MGT\ level} * 1\%$$


If $x_{MGT\ level} > 30\,t$

$$y_{MGT\ level} = x_{MGT\ level} - 15 = weight\ (Total\ number\ of\ all\ axle\ wheel\ passages_y)_{vehicles+passengers}$$

$$\frac{\sum 5\%\ (NN) + 47.5\%(NW1) + 28.5\%(NW2) + 19\%(NW3)}{Total\ number\ of\ all\ axle\ wheel\ passages_x} =\ x_{MGT\ level} * 1\%$$

$$\frac{\sum 5\%\ (WN) + 47.5\%(WW1) + 28.5\%(WW2) + 19\%(WW3)}{Total\ number\ of\ all\ axle\ wheel\ passages_y - Total\ number\ of\ all\ axle\ wheel\ passages_x}$$
$$=\ 30 * 1\% + (y_{MGT\ level} - 30) * 0.05\%$$

# APPENDIX B

**Crack depth and location comparisons with MRX-RSCM measurements**

The following figures present the crack depth and location comparisons with the MRX-RSCM measurements. The information given in the top provides the name of the site, its distance, track characteristics, inspection details such time and tonnage of the first and second measurements. In the first plot, the measured surface damage maps were overlaid with the model predictions over railhead and second plot provides a comparison of the predicted and measured crack depths. The colour scales presented in the crack location comparison plots (sub-plot 1) demonstrate the predicted net crack depth values, with the white areas (grey in the MRX-RSCM surface damage map) indicating regions where the estimated RCF damage was zero which means that the damage was either removed through wear or no damaging contacts were predicted in this region. Similar to the MRX-RSCM data, a dark blue colour represents a relatively small estimated crack depth, whereas a red colour indicates a much larger depth. On these figures, certain regions are highlighted to indicate the correlations between the simulation and measurement results, with black rectangles highlighting the predictions that correlate well with the measured damage and red circles show the uncorrelated regions.

| Track Ch. | Case No | RCF-BAK-1 in B068BNBLO Rail Installation: 04/05/2015 | LCS Distance : 313-367 | Site Visit dated 20/07/2017 (45.6 MGT) |
|---|---|---|---|---|
| | 1 | MRX-RSCM_1: 14/11/2015 (194 days: 11.4 MGT) | Simulation Distance : 8+011-8+065 | Shelling at Running Surface at Ch.335 (8033-8035) |
| | 2 | MRX-RSCM_2: 30/09/2016 (515 days: 30.3 MGT) | Average Curve Radius: 305 m Rail Profile:FB | Corrugation was also observed along this site |

| MRX-RSCM 1 RCF CRACK LOCATION PREDICTION COMPARISON | |
| MRX-RSCM 1 RCF CRACK DEPTH PREDICTION COMPARISON | |
| MRX-RSCM 2 RCF CRACK LOCATION PREDICTION COMPARISON | |
| MRX-RSCM 2 RCF CRACK DEPTH PREDICTION COMPARISON | |
| FIELD OBSERVATIONS | Shelling on the Running Surface at Ch.335 (8+030-8+035). Corrugation on this site. |

Figure Appendix B 1: Comparison of RCF predictions with MRX-RSCM measurements on high rail case of RCF-BAK-1 site

| Track Ch. | Case No | RCF-BAK-4 in B068BSBLO Rail Installation:20/04/2015 | LCS Distance : 362-416 | Site Visit dated 20/07/2017 (46.3 MGT) |
|---|---|---|---|---|
| | 3 | MRX-RSCM_1: 14/11/2015 (194 days: 11.6 MGT) | Simulation Distance : 2+965-3+020 | Head Checks on Gauge Corner at Ch.370 (2+973) |
| | 4 | MRX-RSCM_1: 30/09/2016 (515 days: 31.3 MGT) | Average Curve Radius: 440 m Rail Profile:FB | |

| MRX-RSCM 1 RCF CRACK LOCATION PREDICTION COMPARISON |  |
|---|---|
| MRX-RSCM 1 RCF CRACK DEPTH PREDICTION COMPARISON |  |
| MRX-RSCM 2 RCF CRACK LOCATION PREDICTION COMPARISON |  |
| MRX-RSCM 2 RCF CRACK DEPTH PREDICTION COMPARISON |  |
| FIELD OBSERVATIONS | Head Check on the Gauge Corner at Ch.370 -375 (2+973-2+978)<br> |

Figure Appendix B 2: Comparison of RCF predictions with MRX-RSCM measurements on high rail case of RCF-BAK-4 site

| Track Ch. | Case No | RCF-BAK-8 in B134BNBLO Rail Installation:28/10/2014 | LCS Distance : 290-326 | Site Visit dated 19/07/2017 (56.5 MGT) |
|---|---|---|---|---|
| | 5 | MRX-RSCM_1: 13/11/2015 (381 days: 22.5 MGT) | Simulation Distance :1+892 - 1+928 | Lipping on Gauge Corner at Ch.305 (1+907) |
| | 6 | MRX-RSCM_1: 14/11/2016 (748 days: 44.2 MGT) | Average Curve Radius: 285 m Rail Profile:FB | |

| | |
|---|---|
| MRX-RSCM 1 RCF CRACK LOCATION PREDICTION COMPARISON |  |
| MRX-RSCM 1 RCF CRACK DEPTH PREDICTION COMPARISON |  |
| MRX-RSCM 2 RCF CRACK LOCATION PREDICTION COMPARISON |  |
| MRX-RSCM 2 RCF CRACK DEPTH PREDICTION COMPARISON |  |
| FIELD OBSERVATIONS | Lipping on Gauge Corner at Ch.305 -310 (1+907-1+912)  |

Figure Appendix B 3: Comparison of RCF predictions with MRX-RSCM measurements on high rail case of RCF-BAK-8 site

| Track Ch. | Case No | RCF-JUB-1 in F044JNBLO Rail Installation:10/12/2014 | LCS Distance : 246-282 | Site Visit dated 18/07/2017 (83.8 MGT) |
|---|---|---|---|---|
| | 7 | MRX-RSCM_1: 28/04/2016 (505 days: 44.5 MGT) | Simulation Distance: 16+144 - 16+180 | No defects were observed. |
| | | | Average Curve Radius: 430 m Rail Profile:FB | |

| MRX-RSCM 1 RCF CRACK LOCATION PREDICTION COMPARISON |  |
|---|---|
| MRX-RSCM 1 RCF CRACK DEPTH PREDICTION COMPARISON |  |
| FIELD OBSERVATIONS | The site was recently ground. No defects were observed.  |

Figure Appendix B 4: Comparison of RCF predictions with MRX-RSCM measurements on high rail case of RCF-JUB-1 site
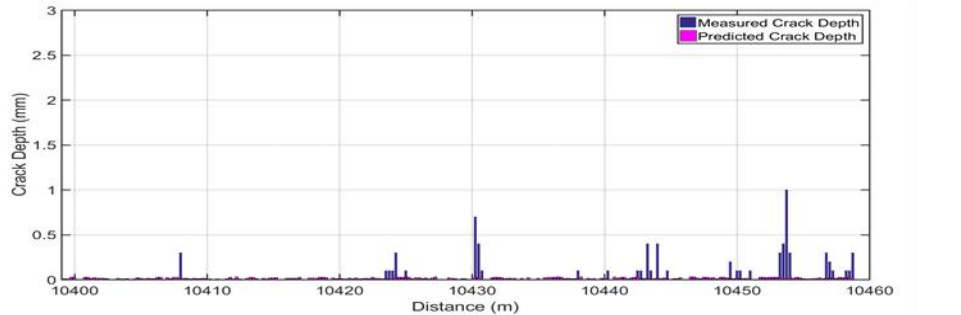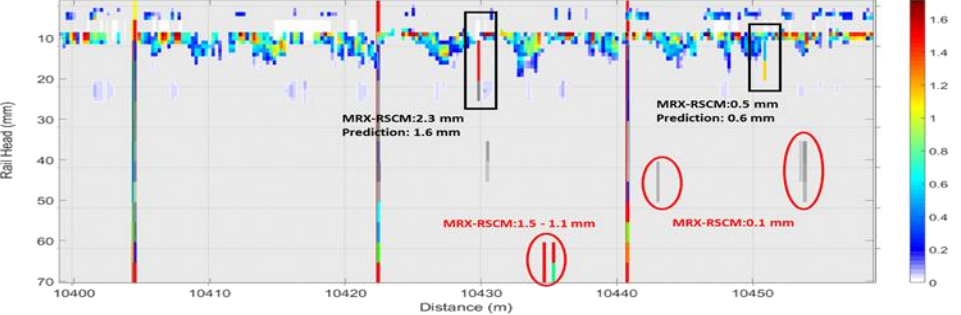
| Track Ch. | Case No | RCF-BAK-6 in B062BNBLO Rail Installation:17/06/2015 | LCS Distance : 129-188 | No Site Visit |
|---|---|---|---|---|
| | 8 | MRX-RSCM_1: 11/11/2015 (147 days: 8.6 MGT) | Simulation Distance :10+399 - 10+459 | |
| | 9 | MRX-RSCM_1: 10/10/2016 (481 days: 28.3 MGT) | Average Curve Radius: 362 m Rail Profile:FB | |

| MRX-RSCM 1 RCF CRACK LOCATION PREDICTION COMPARISON |  |
|---|---|
| MRX-RSCM 1 RCF CRACK DEPTH PREDICTION COMPARISON |  |
| MRX-RSCM 2 RCF CRACK LOCATION PREDICTION COMPARISON |  |
| MRX-RSCM 2 RCF CRACK DEPTH PREDICTION COMPARISON |  |
| FIELD OBSERVATIONS | No Site Visit |

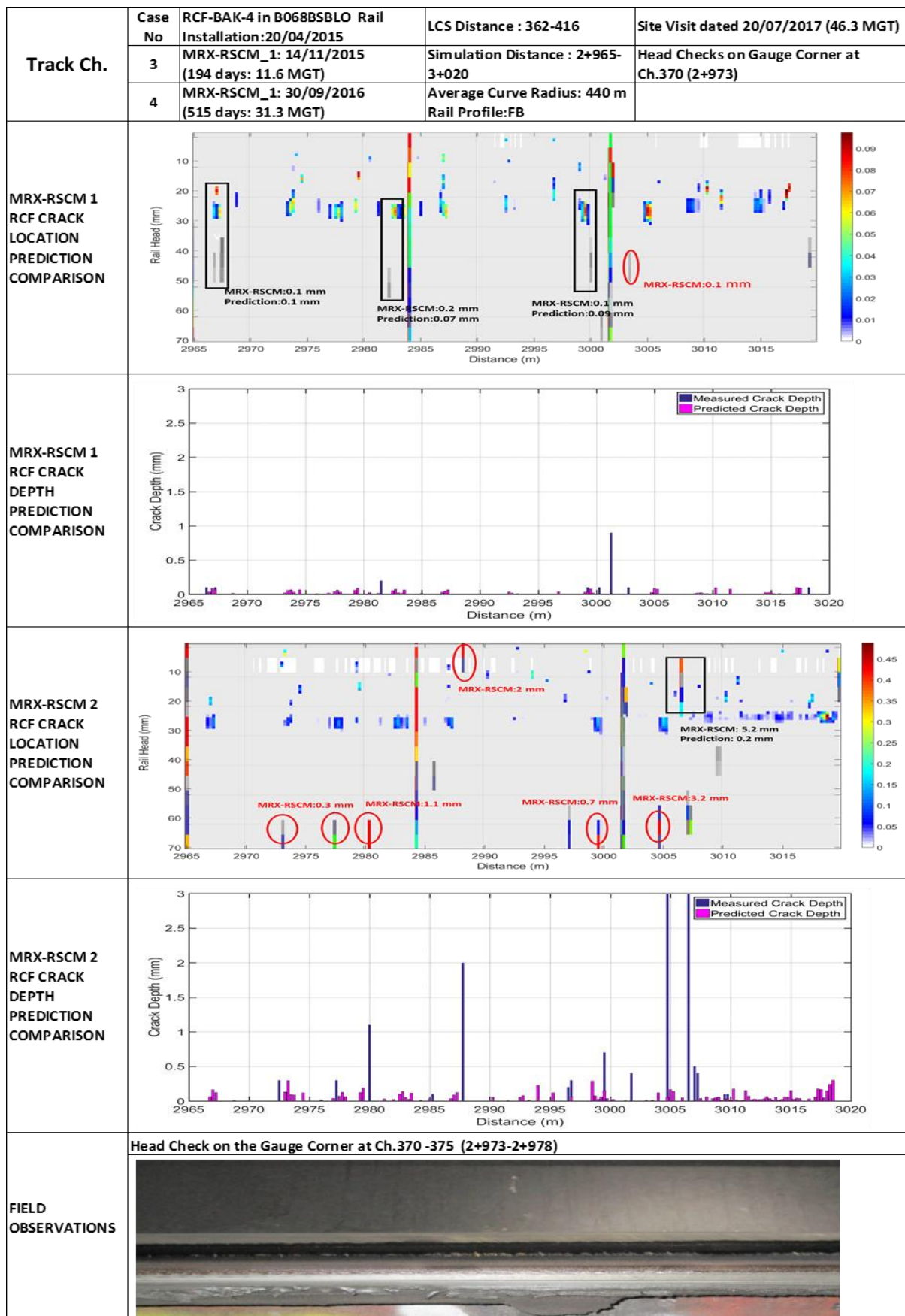Figure Appendix B 5: Comparison of RCF predictions with MRX-RSCM measurements on high rail cases of RCF-BAK-6 site

| Track Ch. | Case No | RCF-BAK-5 in B068BSBLO Rail Installation:16/04/2015 | LCS Distance : 320 - 356 | Site Visit dated 20/07/2017 (46.5 MGT) |
|---|---|---|---|---|
| | 1 | MRX-RSCM_1: 14/11/2015 (212 days: 12.5 MGT) | Simulation Distance: 2+923 - 2+959 | No Defects were observed. |
| | 2 | MRX-RSCM_2: 30/09/2016 (533 days: 31.5 MGT) | Average Curve Radius: 440 m Rail Profile:FB | |

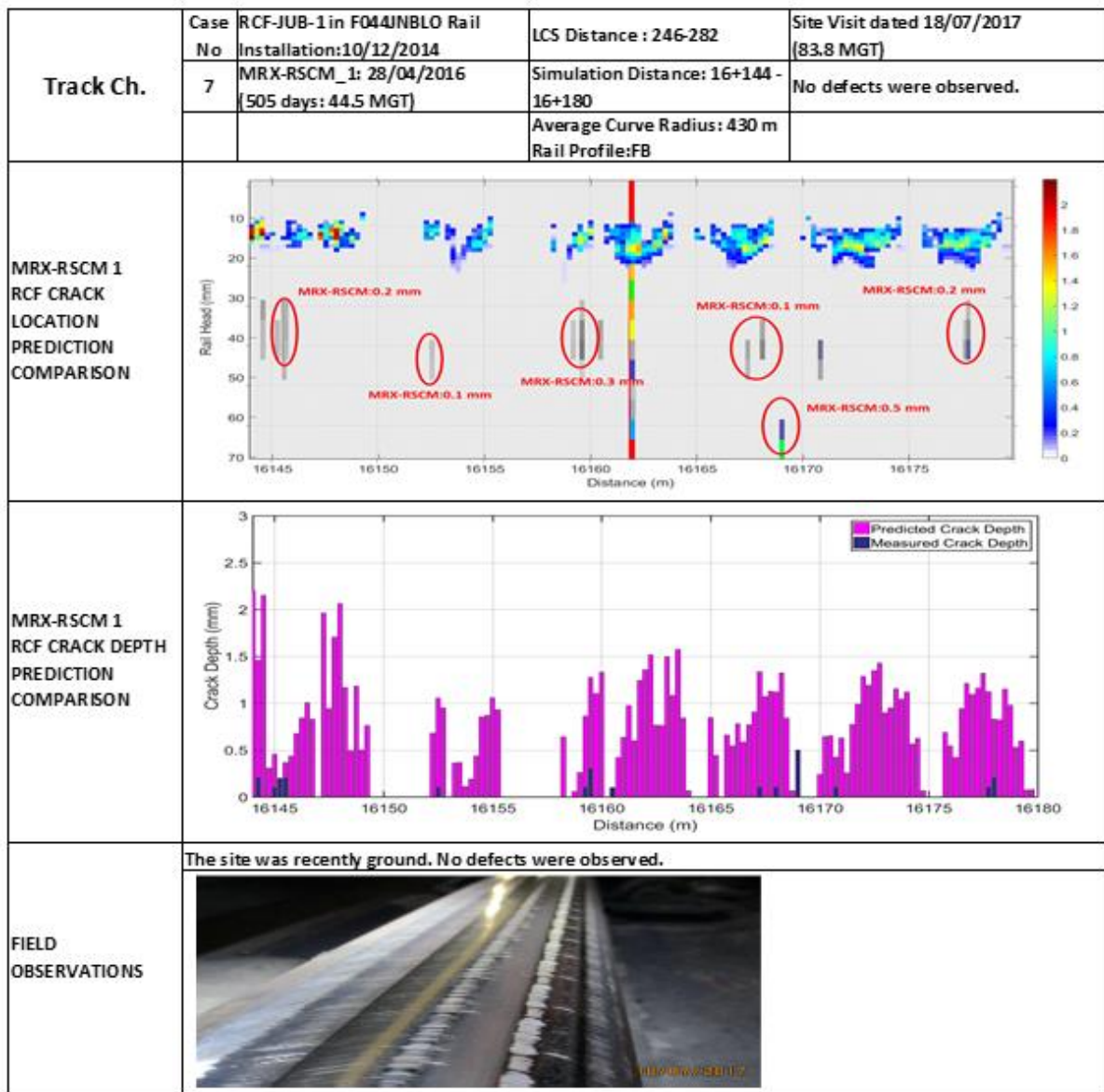| MRX-RSCM 1 RCF CRACK LOCATION PREDICTION COMPARISON |  |
|---|---|
| MRX-RSCM 1 RCF CRACK DEPTH PREDICTION COMPARISON |  |
| MRX-RSCM 2 RCF CRACK LOCATION PREDICTION COMPARISON |  |
| MRX-RSCM 2 RCF CRACK DEPTH PREDICTION COMPARISON |  |
| FIELD OBSERVATIONS | No defects were observed.  |

Figure Appendix B 6: Comparison of RCF predictions with MRX-RSCM measurements on low rail cases of RCF-BAK-5 site
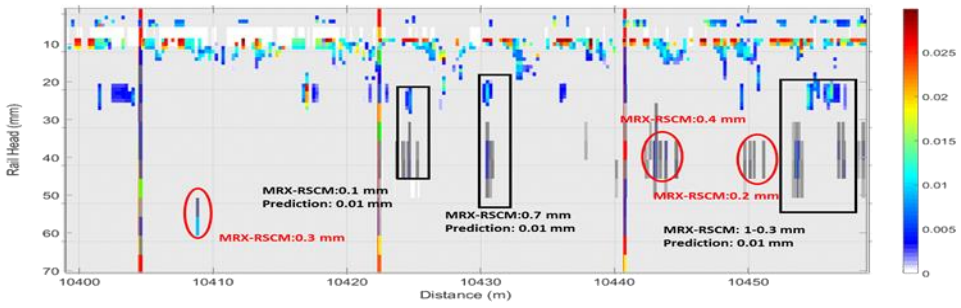
| Track Ch. | Case No | RCF-BAK-9 in B068BNBLO Rail Installation:29/04/2015 | | LCS Distance : 100 - 154 | No Site visit |
|---|---|---|---|---|---|
| | 3 | MRX-RSCM_1: 14/11/2015 (199 days: 11.7 MGT) | | Simulation Distance: 7+798 - 7+852 | |
| | 4 | MRX-RSCM_2: 30/09/2016 (520 days: 30.6 MGT) | | Average Curve Radius: 285 m Rail Profile:BH | |

| MRX-RSCM 1 RCF CRACK LOCATION PREDICTION COMPARISON |  |
|---|---|
| MRX-RSCM 1 RCF CRACK DEPTH PREDICTION COMPARISON |  |
| MRX-RSCM 2 RCF CRACK LOCATION PREDICTION COMPARISON |  |
| MRX-RSCM 2 RCF CRACK DEPTH PREDICTION COMPARISON |  |
| FIELD OBSERVATIONS | No Site Visit |

Figure Appendix B 7: Comparison of RCF predictions with MRX-RSCM measurements on low rail cases of RCF-BAK-9 site
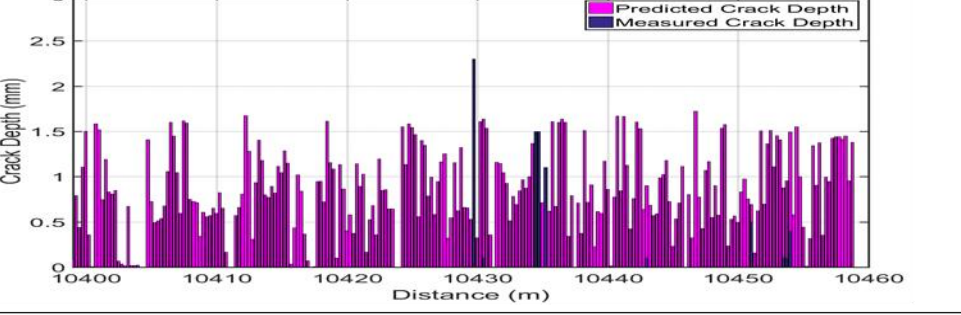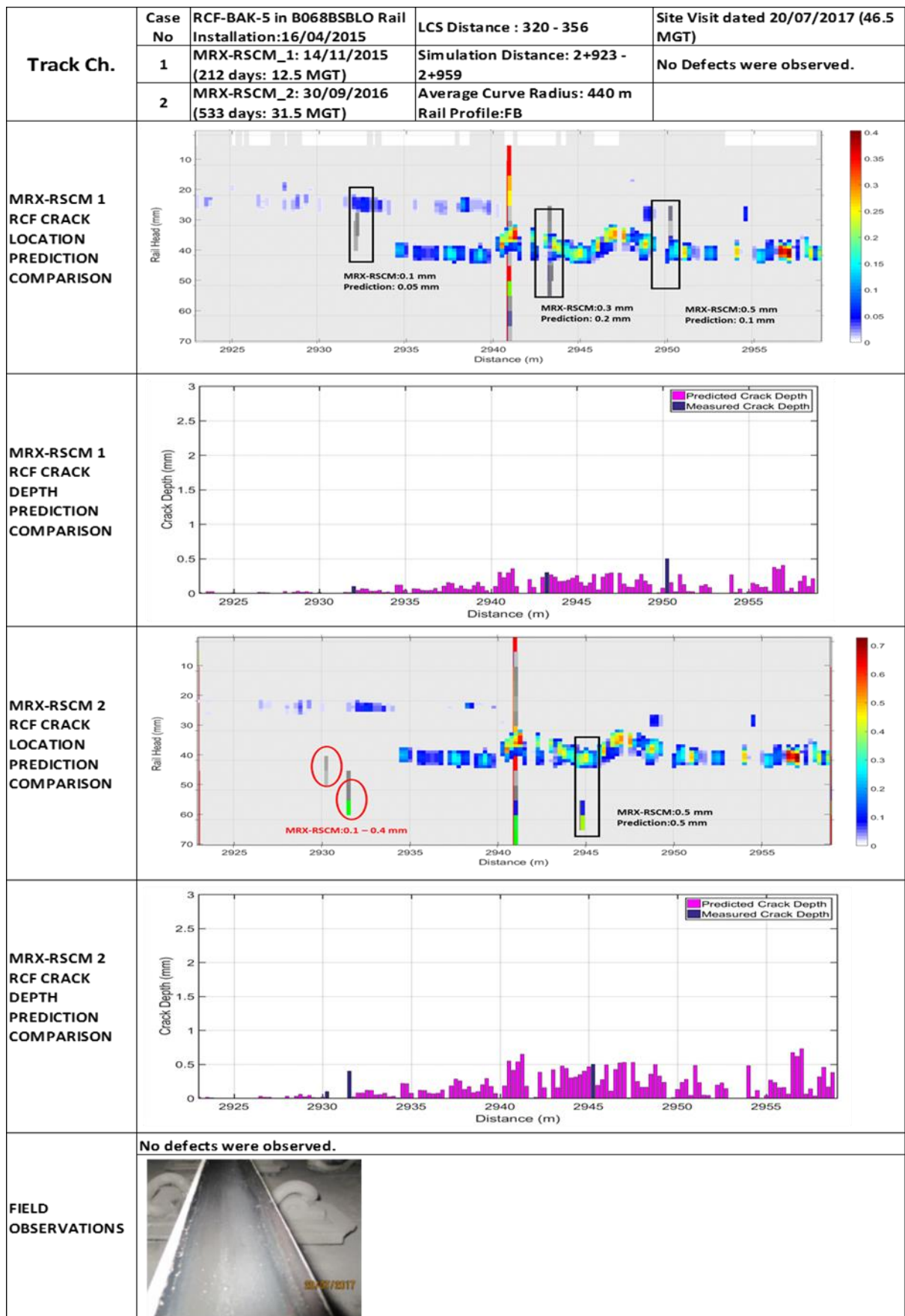
| Track Ch. | Case No | RCF-BAK-7 in B134BNBLO Rail Installation:28/10/2014 | LCS Distance : 225 - 279 | Site Visit dated 19/07/2017 (56.5 MGT) |
|---|---|---|---|---|
| | 5 | MRX-RSCM_1: 13/11/2015 (381 days: 22.5 MGT) | Simulation Distance: 1+827 - 1+881 | |
| | 6 | MRX-RSCM_2: 14/11/2016 (748 days: 44.2 MGT) | Average Curve Radius: 285 m Rail Profile:FB | |

| MRX-RSCM 1 RCF CRACK LOCATION PREDICTION COMPARISON |  |
|---|---|
| MRX-RSCM 1 RCF CRACK DEPTH PREDICTION COMPARISON |  |
| MRX-RSCM 2 RCF CRACK LOCATION PREDICTION COMPARISON |  |
| MRX-RSCM 2 RCF CRACK DEPTH PREDICTION COMPARISON |  |
| FIELD OBSERVATIONS | No defects and lipping on the field side was observed.  |

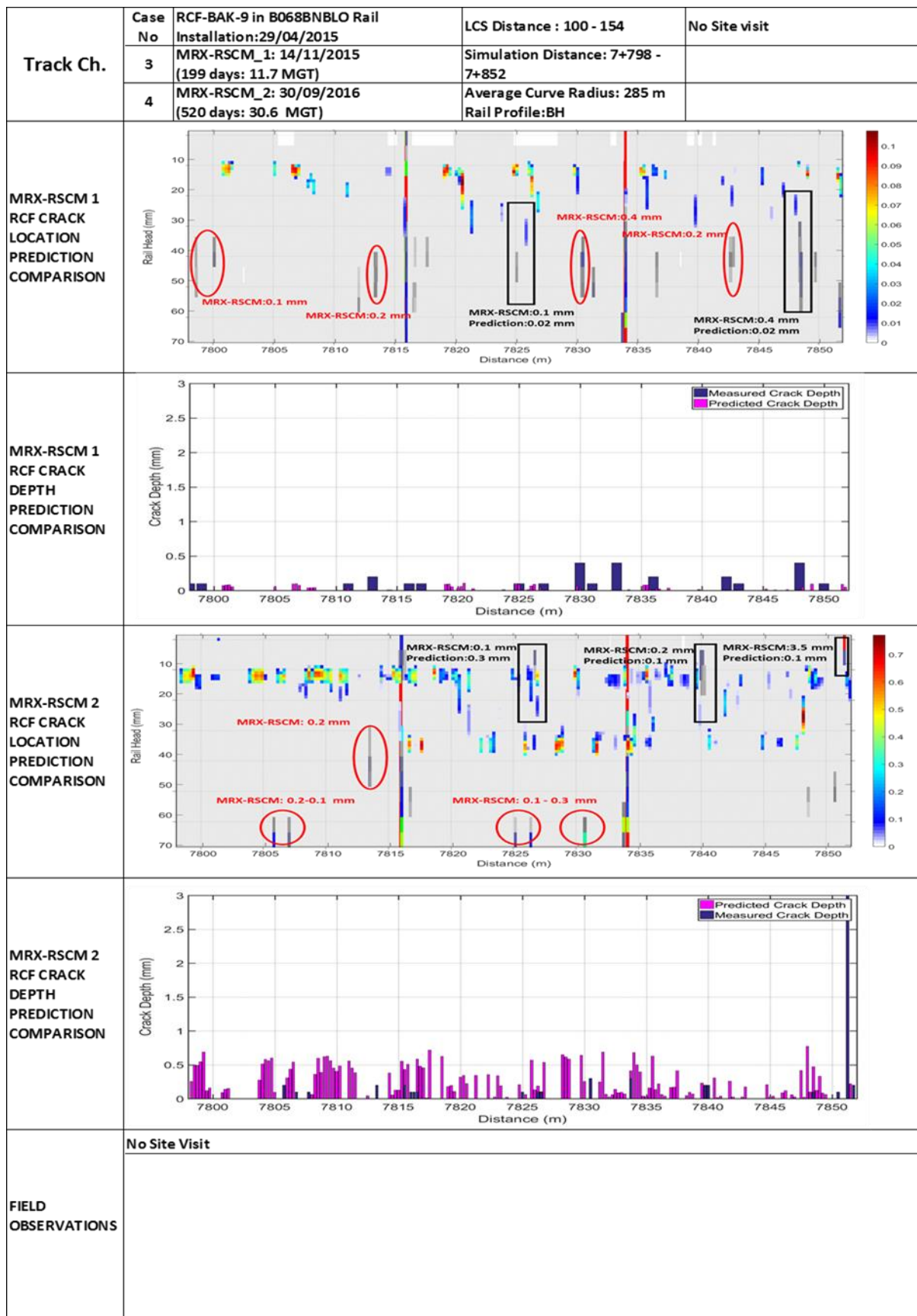Figure Appendix B 8: Comparison of RCF predictions with MRX-RSCM measurements on low rail cases of RCF-BAK-7 site

| Track Ch. | Case No | RCF-JUB-2 in B114JNBLO Rail Installation:20/04/2014 | LCS Distance : 433 - 451 | No site visit |
|---|---|---|---|---|
| | 7 | MRX-RSCM_1 :22/03/2016 (702 days: 59.5 MGT) | Simulation Distance: 19+430 - 19+448 | |
| | | | Average Curve Radius: 265 m Rail Profile:FB | |

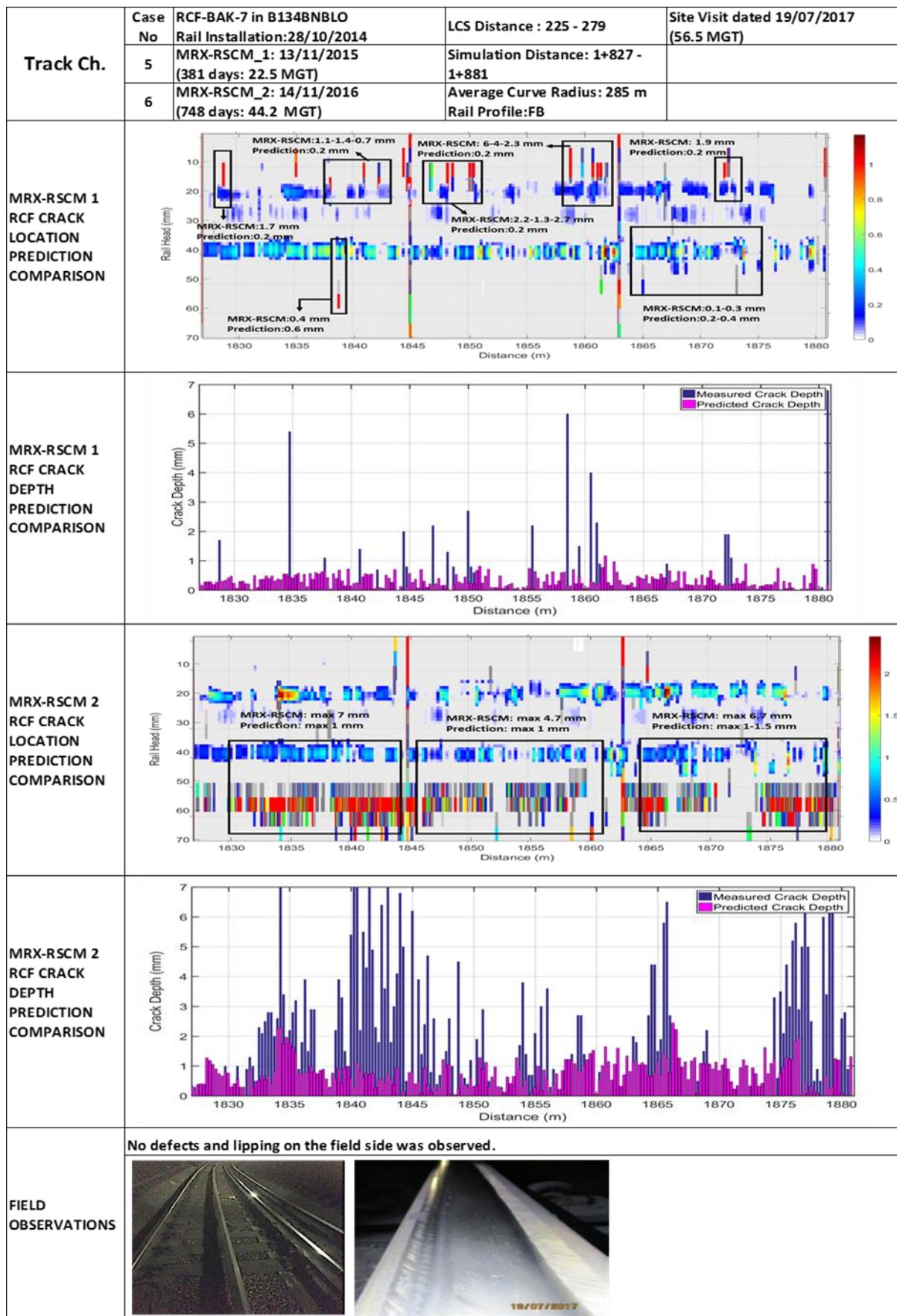| MRX-RSCM 1 RCF CRACK LOCATION PREDICTION COMPARISON |  |
|---|---|
| MRX-RSCM 1 RCF CRACK DEPTH PREDICTION COMPARISON |  |
| FIELD OBSERVATIONS | No site visit |

Figure Appendix B 9: Comparison of RCF predictions with MRX-RSCM measurements on low rail cases of RCF-JUB-2 site

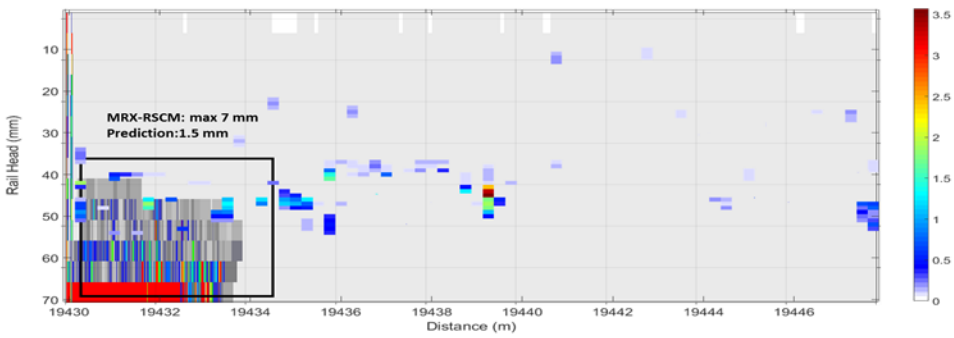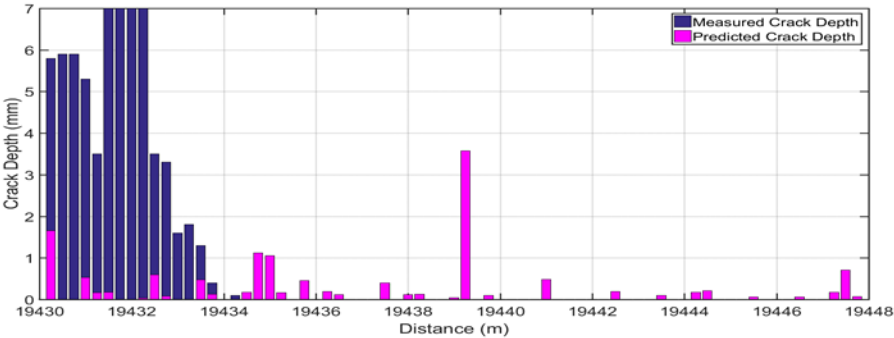| Track Ch. | Case No | RCF-BAK-2 in B122BSBLO Rail Installation:20/03/2015 | LCS Distance : 510 - 564 | Site Visit dated 21/07/2017 (48.2 MGT) |
|---|---|---|---|---|
| | 1 | MRX-RSCM_1: 17/11/2015 (242 days: 14.3 MGT) | Simulation Distance: 5+689 - 5+743 | Generally, no severe defects were observed. |
| | 2 | MRX-RSCM_2: 03/10/2016 (563 days: 33.3 MGT) | Average Curve Radius: 200 m Rail Profile:FB | Head checks were found at Ch.~ 520 |

| | |
|---|---|
| MRX-RSCM 1 RCF CRACK LOCATION PREDICTION COMPARISON |  |
| MRX-RSCM 1 RCF CRACK DEPTH PREDICTION COMPARISON |  |
| MRX-RSCM 2 RCF CRACK LOCATION PREDICTION COMPARISON |  |
| MRX-RSCM 2 RCF CRACK DEPTH PREDICTION COMPARISON |  |
| FIELD OBSERVATIONS | Generally, no severe defects were observed. Gauge corner cracks were found at Ch.~520 (5+699) with the help of MPI testing  |

Figure Appendix B 10: Comparison of RCF predictions with MRX-RSCM measurements on high rail cases of RCF-BAK-2
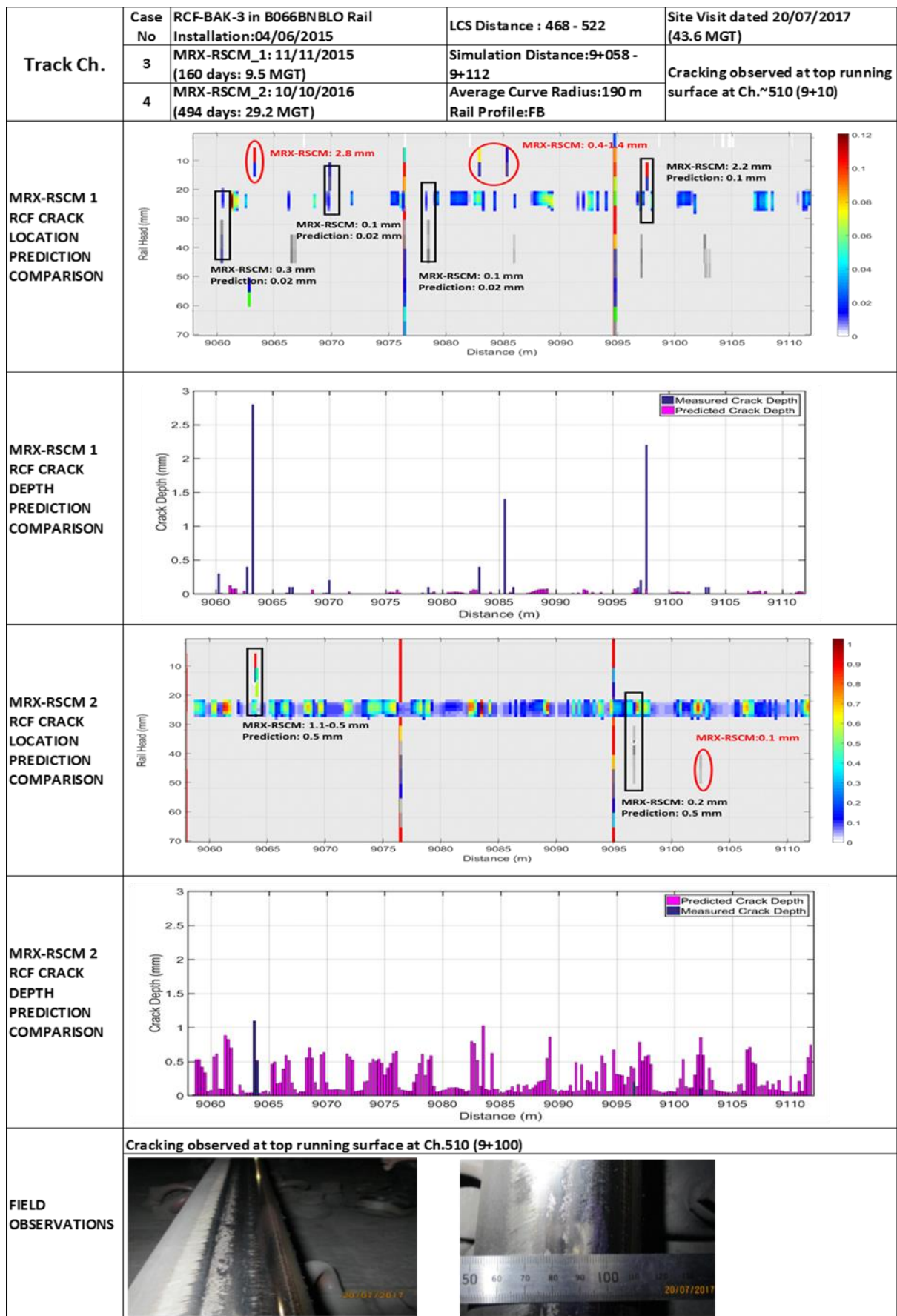
| Track Ch. | Case No | RCF-BAK-3 in B066BNBLO Rail Installation:04/06/2015 | LCS Distance : 468 - 522 | Site Visit dated 20/07/2017 (43.6 MGT) |
|---|---|---|---|---|
| | 3 | MRX-RSCM_1: 11/11/2015 (160 days: 9.5 MGT) | Simulation Distance:9+058 - 9+112 | Cracking observed at top running surface at Ch.~510 (9+10) |
| | 4 | MRX-RSCM_2: 10/10/2016 (494 days: 29.2 MGT) | Average Curve Radius:190 m Rail Profile:FB | |



**MRX-RSCM 1 RCF CRACK LOCATION COMPARISON**

**MRX-RSCM 1 RCF CRACK DEPTH PREDICTION COMPARISON**

**MRX-RSCM 2 RCF CRACK LOCATION PREDICTION COMPARISON**

**MRX-RSCM 2 RCF CRACK DEPTH PREDICTION COMPARISON**

**FIELD OBSERVATIONS**

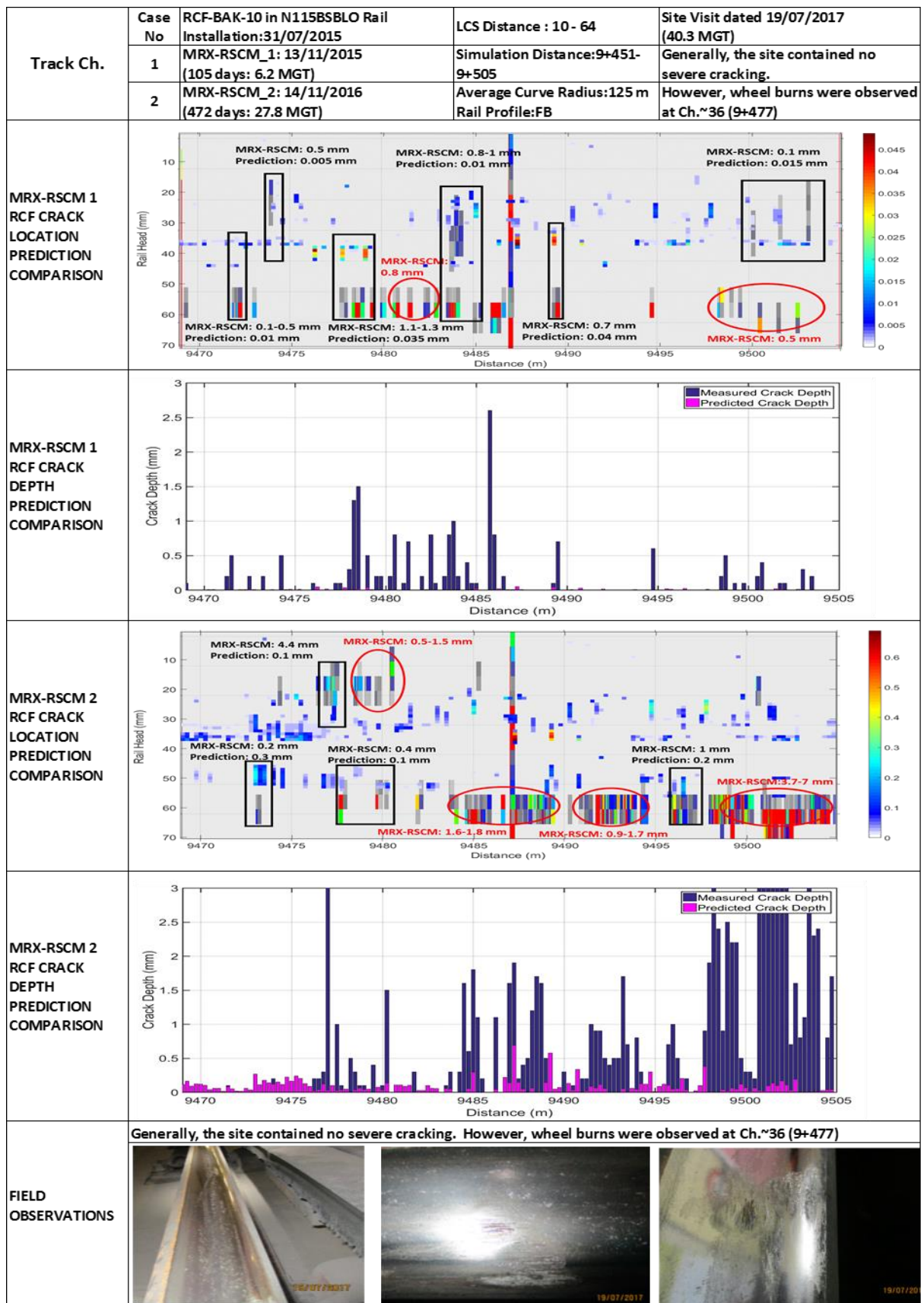Cracking observed at top running surface at Ch.510 (9+100)

Figure Appendix B 11: Comparison of RCF predictions with MRX-RSCM measurements on high rail cases of RCF-BAK-3

| Track Ch. | Case No | RCF-BAK-10 in N115BSBLO Rail Installation:31/07/2015 | LCS Distance : 10 - 64 | Site Visit dated 19/07/2017 (40.3 MGT) |
|---|---|---|---|---|
| | 1 | MRX-RSCM_1: 13/11/2015 (105 days: 6.2 MGT) | Simulation Distance:9+451-9+505 | Generally, the site contained no severe cracking. |
| | 2 | MRX-RSCM_2: 14/11/2016 (472 days: 27.8 MGT) | Average Curve Radius:125 m Rail Profile:FB | However, wheel burns were observed at Ch.~36 (9+477) |

**MRX-RSCM 1 RCF CRACK LOCATION PREDICTION COMPARISON**



**MRX-RSCM 1 RCF CRACK DEPTH PREDICTION COMPARISON**



**MRX-RSCM 2 RCF CRACK LOCATION PREDICTION COMPARISON**



**MRX-RSCM 2 RCF CRACK DEPTH PREDICTION COMPARISON**



**FIELD OBSERVATIONS**

Generally, the site contained no severe cracking. However, wheel burns were observed at Ch.~36 (9+477)



Figure Appendix B 12: Comparison of RCF predictions with MRX-RSCM measurements on low rail cases of RCF-BAK-10
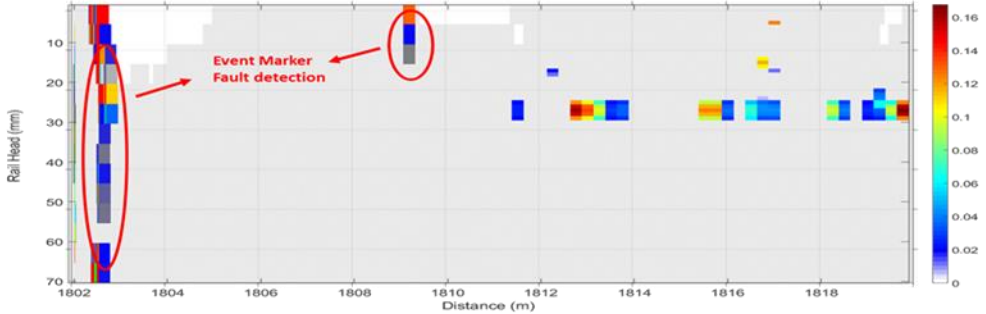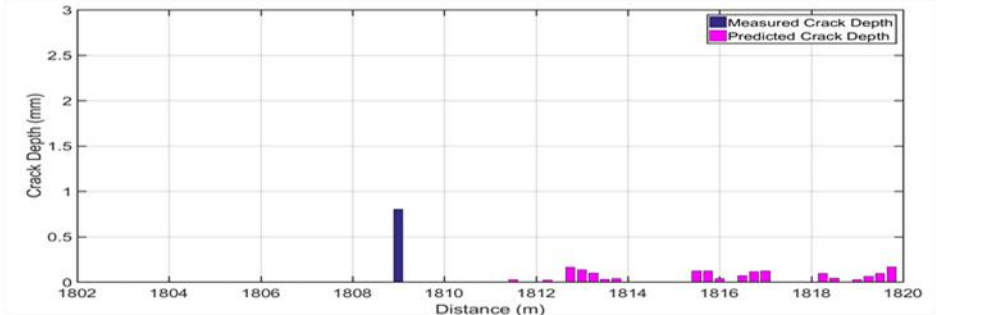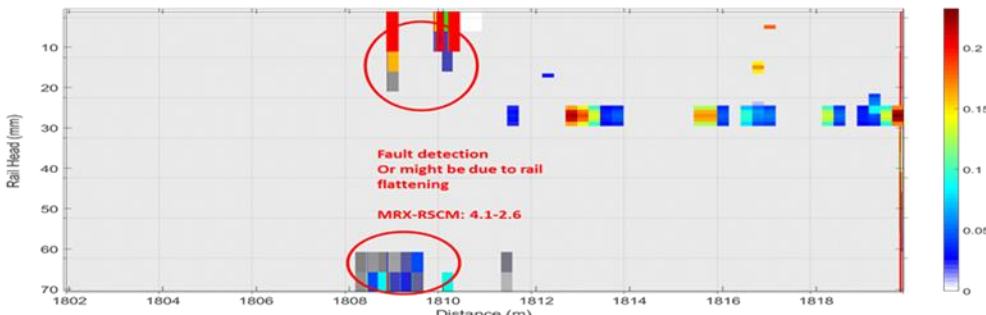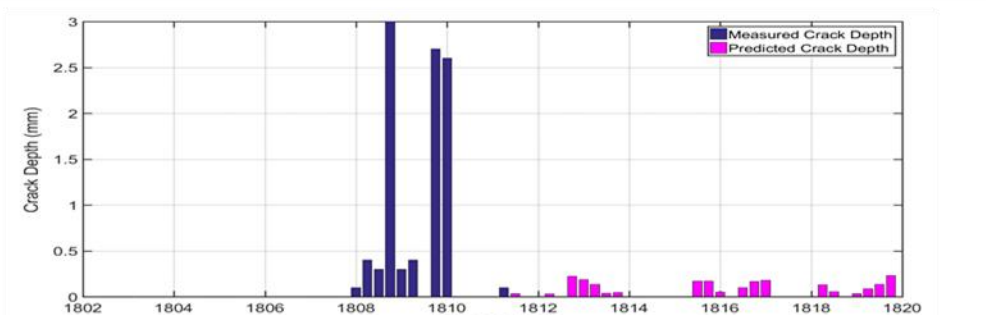
226

| Track Ch. | Case No | RCF-BAK-8 in B134BNBLO Rail Installation:28/10/2014 | LCS Distance : 200 - 218 | Site Visit dated 19/07/2017 (56.5 MGT) |
|---|---|---|---|---|
| | 1 | MRX-RSCM_1: 13/11/2015 (381 days: 22.5 MGT) | Simulation Distance : 1+802 - 1+820 | No defects were observed. |
| | 2 | MRX-RSCM_1: 14/11/2016 (748 days: 44.2 MGT) | Rail Profile:FB | |

| | |
|---|---|
| MRX-RSCM 1 RCF CRACK LOCATION PREDICTION COMPARISON |  |
| MRX-RSCM 1 RCF CRACK DEPTH PREDICTION COMPARISON |  |
| MRX-RSCM 2 RCF CRACK LOCATION PREDICTION COMPARISON |  |
| MRX-RSCM 2 RCF CRACK DEPTH PREDICTION COMPARISON |  |
| FIELD OBSERVATIONS | No defects were observed. |

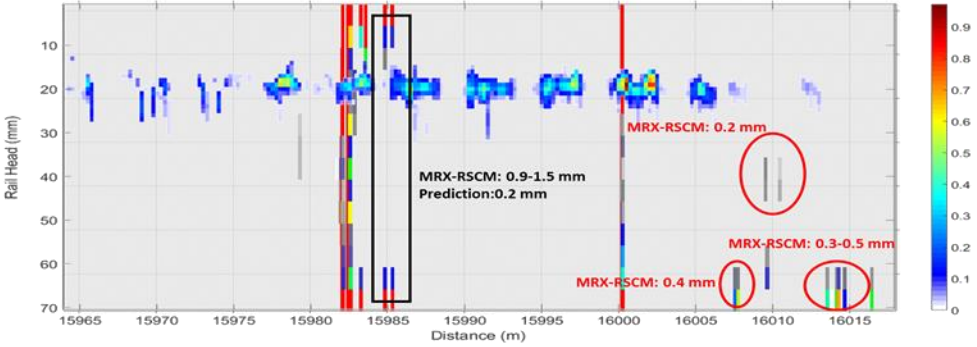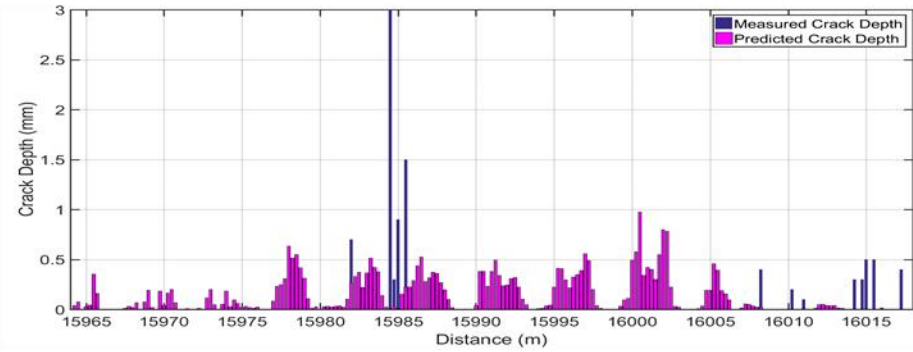Figure Appendix B 13: Comparison of RCF predictions with MRX-RSCM measurements on rail cases of RCF-BAK-8

| Track Ch. | Case No | RCF-JUB-1 in F044JNBLO Rail Installation:10/12/2014 | LCS Distance : 73-128 | Site Visit dated 18/07/2017 (83.8 MGT) |
|---|---|---|---|---|
| | 3 | MRX-RSCM_1: 28/04/2016 (505 days: 44.5 MGT) | Simulation Distance: 15+964 - 16+018 | No defects were observed. |
| | | | Rail Profile:BH | |

| MRX-RSCM 1 RCF CRACK LOCATION PREDICTION COMPARISON |  |
|---|---|
| MRX-RSCM 1 RCF CRACK DEPTH PREDICTION COMPARISON |  |
| FIELD OBSERVATIONS | No defects were observed.<br> |

Figure Appendix B 14: Comparison of RCF predictions with MRX-RSCM measurements on rail cases of RCF-JUB-2

| Track Ch. | Case No | RCF-JUB-3 in B112JNBLO Rail Installation:20/08/2014 | LCS Distance : 637-655 | No site visit |
|---|---|---|---|---|
| | 4 | MRX-RSCM_1: 22/03/2016 (580 days: 48.9 MGT) | Simulation Distance: 21+738+21+756 | |
| | | | Rail Profile:FB | |

| MRX-RSCM 1 RCF CRACK LOCATION PREDICTION COMPARISON |  |
|---|---|
| MRX-RSCM 1 RCF CRACK DEPTH PREDICTION COMPARISON |  |
| FIELD OBSERVATIONS | No Site visit |

Figure Appendix B 15: Comparison of RCF predictions with MRX-RSCM measurements on rail cases of RCF-JUB-3